



ScuDo
Scuola di Dottorato ~ Doctoral School
WHAT YOU ARE, TAKES YOU FAR

Doctoral Dissertation
Doctoral Program in Mechanical Engineering (29th Cycle)

Light-weight Design of Vehicle Roof Panel for Stiffness and Crash Analyses

By

Soroosh Borazjani

Supervisor:

Prof. Giovanni Belingardi

Doctoral Examination Committee:

Prof. S. Abrate , Referee, Southern Illinois University

Prof. C. De Marco , Referee, Università di Malta

Prof. M. Gobbi , Referee, Politecnico di Milano

Prof. S. Patil , Referee, National University of Singapore

Prof. D. Paolino , Referee, Politecnico di Torino

Politecnico di Torino
2016

Declaration

I hereby declare that, the contents and organization of this dissertation constitute my own original work and does not compromise in any way the rights of third parties, including those relating to the security of personal data.

Soroosh Borazjani

2016

* This dissertation is presented in partial fulfillment of the requirements for **Ph.D. degree** in the Graduate School of Politecnico di Torino (ScuDo).

*I would like to dedicate this thesis to my loving parents (REZA & PARVANEH)
and my forever love (SAHAR)*

Acknowledgment

I would like to acknowledge my Ph.D. supervisor Professor Giovanni Belingardi for his support, guidance, advice and insight throughout the research.

I would also like to thank the committee members for their valuable advice and comments.

Abstract

Vehicle crashworthiness refers to proper designing of the vehicle structure to reduce the risk of death and injury during the vehicle accidents. In the recent years, due to the enforcement of new EU normative, the interest of all the car manufacturers in producing lightweight vehicles is progressively increased as the combustion engine optimization has already used most of the improvements they had and the residual ones are becoming more and more difficult and costly. Based on this auto industry's interest, lightweight materials such as composite have absorbed lots of attention due to their superior characteristic of high stiffness to weight ratio.

In this thesis, efforts have been made to present a broad research on the lightweight design of vehicle roof panel for stiffness and crash analyses. The first part of the analyses belongs to the vehicle chassis static and dynamic stiffness analyses via the finite element code with the specific focus on substituting the steel roof panel with the lightweight materials of aluminum and composites. The structural response of the vehicle roof panel, made of different solutions, in full frontal crash with respect to NHTSA standard has been investigated at the second step. The effects of increasing the vehicle roof panel thickness at the both steps have been tested and compared for different solutions. At the third step an innovative design solution for the vehicle roof structure has been developed and tested in rollover crash analysis. In order to perform this task, After determining the performance of tubes made of steel, composite and composite foam-filled solutions under the three points bending test and proving the efficiency of composite-foam design; the same idea is implemented on the vehicle roof panel during the roof quasi-static crush test.

Besides the composite solutions, the sandwich design consists of composite face-sheets and foam core are tested in the roof crushing test based on the FMVSS

216 standard. After assessment of the sandwich roof panel in crushing test, the geometrical optimization of the foam core is implemented to determine the optimum design with respect to vehicle strength-to-weight ratio and mass reduction percentages. Besides different foam core configurations that have been tested, the final optimization have been implemented using the foam core with various densities and also the optimum face-sheets thickness has been determined. At the last chapter, challenges of vehicle composite roof panel assembly have been discussed.

Results in the case of stiffness and frontal crash analyses at step one and step two proved that although the composite solutions have lower energy absorption capacity in comparison with the steel one, they have large contribution to the weight reduction of the vehicle roof panel and still stays in the acceptable range of structural performance. Using the new design of sandwich solutions in roof crushing test have proved that while theses designs have reduced the vehicle roof panel weight by 68%, they have the same structural performance as the steel solution and could be considered as interesting solutions. Evaluating the behavior of the vehicle roof structure made of different solutions with various configurations under distinct analyses of stiffness and crashworthiness will help to improve the vehicle roof structure performance.

Contents

1. Introduction.....	1
1.1 Background.....	1
1.2 Importance of crashworthiness and composite material	2
1.3 Problem statement	2
1.4 Aims and objectives	3
1.5 Overview of the thesis	3
1.6 References	6
2. Light-weight Materials for Automotive Industry	7
2.1 Introduction	7
2.2 Lightweight steels in automotive industry	10
2.3 Aluminum alloys in automotive industry	12
2.4 Magnesium alloys in automotive structures	15
2.5 Thermoplastics and Thermoset for lightweight automotive structures .	17
2.6 Composite materials	18
2.6.1 Introduction.....	18
2.6.2 Composite manufacturing processes	22
2.7 Conclusion.....	27
2.8 References	28
3. Crashworthiness and Composite.....	31
3.1 Introduction	31
3.2 Vehicle crashworthiness assessment	32
3.3 Vehicle structure collapse modes	37

3.4 Test methodologies.....	38
3.4.1 Quasi-static test.....	38
3.4.2 Impact Test	38
3.5 Structures energy absorption metrics	38
3.6 Composite crashworthiness	40
3.6.1 Introduction.....	40
3.6.2 Catastrophic failure modes	41
3.6.3 Progressive failure modes	41
3.6.4 Parameters affecting the energy absorption of composite structure	44
3.6.5 Hooke's law for linear isotropic material	46
3.6.6 General format of Hooke's law for different types of materials.....	47
3.6.7 Failure theories of a lamina	53
3.7 Conclusion.....	58
3.8 References	58
4. Light-weight Design: Detailed Comparison of Roof Panel Solutions at Stiffness Analyses.....	62
4.1 Introduction	62
4.2 Automotive panels' behavior under loading	62
4.2.1 Bending stiffness of a panel.....	64
4.2.2 Oli canning resistance	66
4.2.3 Dent resistance	68
4.2.4 Shear rigidity of a panel.....	68
4.2.5 First bending frequencies.....	70
4.3 Framework of developing benchmark for vehicle roof panel	71
4.3.1 Vehicle roof panel benchmark	71
4.3.2 Optimizing strategies for roof panel thickness	73
4.3.3 Vehicle roof panel benchmark with respect to the modified panels' thickness	75

4.4 Vehicle body stiffness	77
4.4.1 Vehicle body bending stiffness	77
4.4.2 Vehicle body torsion stiffness.....	78
4.5 Load path analysis by simple structural surfaces (SSSs) model	79
4.5.1 Vehicle load path analysis during bending	80
4.5.2 Vehicle load path analysis during torsion.....	83
4.6 Finite element analysis formulation	87
4.6.1 The Implicit Method	88
4.6.2 The Explicit Method	88
4.7 Finite element modeling of composite structures with LS-DYNA	89
4.8 Toyota Yaris chassis stiffness analyses	95
4.9 Results and discussion	101
4.9.1 Bending load path analysis	102
4.9.2 Torsion load path analysis	102
4.9.3 Stiffness analyses results	104
4.10 Conclusion.....	107
4.11 References	108
5. Light-weight Design: Detailed Comparison of Roof Panel Solutions at Frontal Crash Analysis	111
5.1 Introduction	111
5.2 State of the art.....	111
5.3 Vehicle load path during frontal crash	114
5.4 Vehicle finite element model preparation for frontal crash.....	115
5.5 Results and discussion	116
5.5.1 Verifying the accuracy of model.....	117
5.5.2 Section forces and section displacement	118
5.5.3 Energy distribution	122
5.6 Conclusion.....	124

5.7 References	125
6. Crashworthiness Analysis of the Innovative Composite-sandwich based Vehicle Roof Structure	128
6.1 Introduction	128
6.2 General framework for modeling material progressive damage and failure in ABAQUS.....	135
6.2.1 Simulation of progressive failure analysis of metallic structures in ABAQUS.....	135
6.2.2 Simulation of progressive failure analysis of composite structures in ABAQUS.....	140
6.2.3 Modeling crushable foam in ABAQUS.....	145
6.3 Progressive failure analysis of tubes at three-points bending loading	148
6.3.1 Progressive failure analysis of thin-walled steel tube.....	149
6.3.2 Progressive failure analysis of thin-walled composite tube.....	152
6.3.3 Progressive failure analysis of composite foam-filled tube.....	158
6.3.4 Comparison of the tubes performance with respect to materials energy absorption	162
6.4 Test procedure and development of full vehicle finite element model	163
6.5 Material selection for sandwich solution.....	168
6.6 Results and discussion	173
6.6.1 Velocity dependency.....	173
6.6.2 Windscreens contribution to the vehicle roof structure strength ..	174
6.6.3 Comparison of the main vehicle BIW components energy absorption	175
6.6.4 Comparison of stiffness response between different designs of the roof panels	176
6.7 Conclusions	185
6.8 References	186
7. Assembly challenges of vehicle composite roof panel	193
7.1 Challenging issues of composite car roof panel production.....	193

7.2 Important notes on designing composite roof panel and attaching process to vehicle chassis.....	194
7.3 Composite roof panel assembly process.....	196
7.4 Conclusion.....	198
7.5 References.....	198
8. Conclusion.....	199
8.1 Overview of the thesis objectives.....	199
8.2 Findings.....	199

List of Figures

Figure 1.1: Methodology flowchart	4
Figure 2.1: Global estimated materials for automotive industry.....	8
Figure 2.2: Automotive steel strength/ductility ladder	11
Figure 2.3: Strength/ductility for the third generation of AHSS.....	12
Figure 2.4: History of vehicle aluminum content in North America	13
Figure 2.5: Automotive application of aluminum alloys	13
Figure 2.6: Audi R8 aluminum frame	14
Figure 2.7: Magnesium applications in automotive industry during history...	17
Figure 2.8: Schematic of composite structure	19
Figure 2.9: Composite typical stress-strain diagram.....	19
Figure 2.10: Comparison of composite a. Elastic modulus vs. Density-b. Strength vs. Cost-c. Stiffness vs. Strength.....	21
Figure 2.11: Schematic of various formats available for the reinforcing fiber	21
Figure 2.12: Comparison of composite production processes rate and applications	22
Figure 2.13: Hand lay-up composite manufacturing.....	23
Figure 2.14: Hand lay-up composite manufacturing.....	23
Figure 2.15: Sheet molding compound (SMC) composite manufacturing	24
Figure 2.16: Bulk Molding Compound (BMC) composite manufacturing.....	25
Figure 2.17: Resin Transfer Molding (RTM) composite processing	26
Figure 2.18: Pultrusion process	26
Figure 2.19: Schematic pictures of filament winding	27
Figure 3.1: Distribution of crash positions.....	33
Figure 3.2: Distribution of frontal crash positions	33
Figure 3.3: Schematic of load paths during different types of impact	34

Figure 3.4: Schematic of full frontal crash test34

Figure 3.5: Schematic of 20% frontal offset crash.....35

Figure 3.6: Schematic of 40% frontal offset crash.....35

Figure 3.7: Schematic of side crash test36

Figure 3.8: Schematic of rear crash test36

Figure 3.9: Schematic of roof crush test37

Figure 3.10: Axial collapse mode.....38

Figure 3.11: Bending collapse mode.....38

Figure 3.12: Example of the force-displacement curve for a composite specimen39

Figure 3.13: Comparison of metallic specimen folding and composite specimen fracture.....40

Figure 3.14: Typical load–displacement profiles of catastrophic and progressive axial compressive failures.....41

Figure 3.15: Crushing characteristics of transverse shearing failure mode42

Figure 3.16: Crushing characteristics of lamina bending failure mode43

Figure 3.17: Crushing characteristics of brittle fracturing failure mode.....43

Figure 3.18: Crushing characteristics of local buckling failure mode44

Figure 3.19. Transformation of coordinate axes for 1–2 plane of symmetry for a monoclinic material.....48

Figure 3.20: A unidirectional lamina as a monoclinic material with fibers, arranged in a rectangular array.....50

Figure 3.21: A unidirectional lamina as a transversely isotropic material with fibers arranged in a square array.....52

Figure 4.1: The concepts of stiffness and strength.....63

Figure 4.2: Curved panel behavior under the normal loading.....64

Figure 4.3: Roof panel dimensions65

Figure 4.4: Roof linear bending stiffness analysis65

Figure 4.5: Panel deformation under normal loading (steel panel).....	66
Figure 4.6: Typical force-displacement curve including oil canning load.....	67
Figure 4.7: Dynamic yield stress for steel.....	68
Figure 4.8: Roof linear shear stiffness analysis.....	69
Figure 4.9: Nodal force during shear analysis.....	69
Figure 4.10: Nodal displacement during shear analysis.....	70
Figure 4.11: Panel modal analysis boundary condition	70
Figure 4.12: Plate under the bending load.....	74
Figure 4.13: Vehicle bending stiffness and strength	78
Figure 4.14: Vehicle torsion stiffness and strength.....	78
Figure 4.15: Baseline model.....	80
Figure 4.16: Baseline model – bending loads	80
Figure 4.17: Payload distribution	81
Figure 4.18: Baseline model – bending case, end and edge loads	81
Figure 4.19: Vehicle in pure torsion	84
Figure 4.20: Frontal structure.....	84
Figure 4.21: Forces on dash panel.....	85
Figure 4.22: Parcel shelf.....	85
Figure 4.23: Edge forces in the standard sedan in the torsion load case.....	86
Figure 4.24: Sideframe.....	87
Figure 4.25: Vehicle finite element model.....	96
Figure 4.26: Schematic of composite lay-up.....	97
Figure 4.27: Chassis finite element model	98
Figure 4.28: Bending analysis.....	99
Figure 4.29: Torsional analysis	99
Figure 4.30: Torsion angle calculation.....	100
Figure 4.31: Chassis with steel roof first bending mode –34.4 Hz	101

Figure 4.32: Chassis with steel roof first torsion mode–20.2 Hz.....	101
Figure 4.33: Modal frequencies (Hertz).....	104
Figure 4.34: Light-weight index concept.....	105
Figure 5.1: Vehicle energy absorption during frontal crash.....	114
Figure 5.2: Vehicle finite element model including connectors and joints...	115
Figure 5.3: Vehicle finite element model.....	116
Figure 5.4: Images of vehicle frontal crash deformation at three subsequent time and comparison with a picture of the real crash test.....	117
Figure 5.5: Rigid wall reaction force	118
Figure 5.6: Full vehicle model force-displacement curve.....	118
Figure 5.7: LHB longitudinal force vs time	119
Figure 5.8: RHB longitudinal force vs time.....	119
Figure 5.9: LHB longitudinal displacement vs time	120
Figure 5.10: RHB longitudinal displacement vs time	121
Figure 5.11: Wrinkles at roof through frontal crash at t=90 ms.....	121
Figure 5.12: Vehicle total energy dissipation.....	123
Figure 5.13: Roof internal energy dissipation.....	123
Figure 5.14: Roof internal energy dissipation with modified thickness	124
Figure 6.1: Passenger vehicle occupant deaths by vehicle type, 1975-2014.	129
Figure 6.2: Vehicle roof crush tests	130
Figure 6.3: IIHS vehicle roof crashworthiness margins.....	132
Figure 6.4: Typical uniaxial stress-strain response of a metal specimen.....	135
Figure 6.5: Material stress-strain curve regarding to progressive damage degradation.....	138
Figure 6.6: Schematic of composite stress-strain curve in linear damage evolution	143
Figure 6.7: Damage variable definition based on equivalent displacement..	144

Figure 6.8: Crushable foam model with volumetric hardening: yield surface and flow potential in the p–q stress plane.....	147
Figure 6.9: Crushable foam model with isotropic hardening: yield surface and flow potential in the p–q stress plane.....	148
Figure 6.10: Tube three-points bending test configuration	149
Figure 6.11: Mesh sensitivity analysis of steel tube	151
Figure 6.12: Metallic tube deformation under bending load-front view.....	151
Figure 6.13: Metallic tube deformation under bending load-top view	152
Figure 6.14: Composite lay-up configuration	152
Figure 6.15: Mesh sensitivity analysis of composite tube	154
Figure 6.16: Value of Hashin's fiber compressive damage initiation criterion of 4th layer (HSNFCCRT).....	154
Figure 6.17: Value of Hashin's fiber tensile damage initiation criterion of 4th layer (HSNFTCRT).....	155
Figure 6.18: Value of Hashin's matrix compressive damage initiation criterion of 4th layer (HSNMCCRT).....	155
Figure 6.19: Value of Hashin's matrix tensile damage initiation criterion of 4th layer (HSNMTCRT).....	156
Figure 6.20: Value of fiber compressive damage variable of 4 th layer (DAMAGEFC)	156
Figure 6.21: Value of fiber tensile damage variable of 4 th layer (DAMAGEFT).....	157
Figure 6.22: Value of matrix compressive damage variable of 4 th layer (DAMAGEMC).....	157
Figure 6.23: Value of matrix tensile damage variable of 4 th layer (DAMAGEMT)	158
Figure 6.24: Value of shear damage variable of 4 th layer (DAMAGESHR)	158
Figure 6.25: SEM picture of EPP foam internal structure	159
Figure 6.26: Schematic of composite foam-filled tube	159

Figure 6.27: Typical stress-strain curve of foam structure under the compression load	160
Figure 6.28: EPP foam 45 Kg/m ³ stress-strain curve.....	161
Figure 6.29: EPP foam density vs. compressive Young's modulus	161
Figure 6.30: Deformed shape of the foam core.....	162
Figure 6.31: Comparison of tubes energy absorption	163
Figure 6.32: FMVSS 216 experimental test configuration	164
Figure 6.33: Load case and boundary condition	164
Figure 6.34: Reference coordinate system rotating about the Z-X plane	165
Figure 6.35: Reference coordinate system rotating about the Z-Y plane	166
Figure 6.36: Different methods to model the windshield laminated glass....	167
Figure 6.37: Schematic of sandwich panel.....	168
Figure 6.38: a. Original and b. exponentially extrapolated stress-strain curves for EPP 45 Kg/m ³	172
Figure 6.39: a. Original and b. exponentially extrapolated stress-strain curves for EPP 70 Kg/m ³	172
Figure 6.40: Dependency on velocity of the roof crush response.....	174
Figure 6.41: Windscreens effect on vehicle roof structure strength in roof crush test	175
Figure 6.42: Energy distribution in BIW components during the roof crush test.....	175
Figure 6.43: Roof panel solution configurations.....	176
Figure 6.44: Roof crush resistance comparison for the different solutions ..	177
Figure 6.45: Comparison of real and FEM roof crush test	178
Figure 6.46. a. Steel and b. composite roofs deformation.....	179
Figure 6.47. Solution type 3 deformation and failure.	179
Figure 6.48. Solutions a. Type 4- b. Type 5- c. Type 6- d. Type 7 deformation and failure	181

Figure 6.49: Roof crush resistance comparison for the solutions with EPP 70 Kg/m ³ foam core.....	183
Figure 6.50: Roof crush resistance comparison for the solutions with EPP 70 Kg/m ³ foam core and face-sheets thickness of 0.8 mm.....	184
Figure 7.1: Roof fiber lay-up orientation	194
Figure 7.2. Adhesive path on the roof panel	195
Figure 7.3. Roof feet	195
Figure 7.4. First step of pre-assembly of roof panel	196
Figure 7.5. Pre-assembly process of roof panel	196
Figure 7.6. Automated assembly first steps	197
Figure 7.7 Automated assembly second steps.....	197

List of Tables

Table 2.1: US cars Average vehicle weights.....	8
Table 2.2: Material distributions in typical automobiles.....	9
Table 2.3: Comparison of material properties used in vehicle.....	9
Table 2.4: Steels used in automotive industry.....	10
Table 2.5: Magnesium applications in non-automotive industry.....	15
Table 2.6: Property advantages of magnesium	16
Table 2.7: Material properties of thermoplastic polymers used in automobile	18
Table 3.1: Overview of European and United States crash tests for front events	35
Table 4.1: Steel and Aluminum material properties	71
Table 4.2: Composite material properties	72
Table 4.3: Strength parameters of composites	72
Table 4.4: Benchmark values of roof panels with the same thickness (1.2mm)	73
Table 4.5: Benchmark values of roof panels with the modified thickness	76
Table 4.6: Ls-Dyna available composite material model.....	90
Table 4.7: Reduced format of mat 54/55.....	92
Table 4.8: Material model 54/55 specifications	93
Table 4.9: Stiffness analyses results.....	106
Table 4.10: Modified stiffness analyses results	107
Table 6.1: Vehicle roof crush static test standards (FMVSS vs. updated FMVSS).....	131
Table 6.2: Vehicle roof crush static test standards (FMVSS vs. IIHS).....	131
Table 6.3: Steel AISI 1045 material properties.....	149
Table 6.4: Johnson-Cook plasticity model constants	149

Table 6.5: Johnson-Cook damage law parameters	150
Table 6.6: Composite elastic properties	153
Table 6.7: Strength parameters of composite material.....	153
Table 6.8: Fiber and matrix fracture toughness energies in both tensile and compressive directions.....	153
Table 6.9: Stress vs. strain.....	161
Table 6.10: Glass and PVB main material properties	167
Table 6.11: Composite material elastic properties	168
Table 6.12: Strength parameters of composite.....	169
Table 6.13: LS-DYNA available foam material models.....	170
Table 6.14. Solution results comparison (45 Kg/m ³ foam core) Part I.....	180
Table 6.15: Solution result comparison (45 Kg/m ³ foam core) Part II	182
Table 6.16: Solution result comparison (70 Kg/m ³ foam core) Part I.....	183
Table 6.17: Solutions results comparison (70 Kg/m ³ foam core) Part II.....	184

Chapter 1

Introduction

1.1 Background

Crashworthiness is the ability of a structure to protect its occupants during an impact. Crashworthiness analysis development of vehicles is divided into the two periods; the primary period from 1970 to 1985 and the second period from 1985 up to now. The primary period was dedicated to enhance the understanding of the crashworthiness phenomena. The first numerical method applying the spring-mass technique was used to analyze the vehicle components during the deformation including buckling and folding [1, 2].

It has been reported that the first vehicle crash model related to modeling of the vehicle front structure to the rigid barrier using beam and spring elements through an implicit software [3, 4].

Necessity to developing model capable of analyzing the stiffness of different components of the vehicle with accuracy and in a short period of time lead the researcher to develop the explicit finite element models capable of solving complex vehicle components. This method was considered as a huge development in crashworthiness analysis for car manufacturers.

Nowadays due to numerous restraints obligated by governmental organizations, vehicle manufacturers have to test their prototypes in different crash scenarios. While vehicles were only tested for frontal crash accident at the

first of numerical method development, today all car producers should test their vehicles through frontal, side, rear rollover etc. crash scenarios.

[5] Reported that the first application of composite material in crashworthiness had been tested for helicopters and Formula 1 vehicles as in chassis designed by McLaren in 1980 [6]. From 1980 up to now many researches have been done on analyzing composite materials for crashworthiness applications. These materials due to their superior characteristics of low weight and high stiffness-to-weight ratio have been applied in many industries.

1.2 Importance of crashworthiness and composite material

Numerical crashworthiness analyses provide the opportunity to test the vehicle structure with respect to different dictated obligations. The analyses help to test the full vehicle model in different scenarios using different material solutions. Having modelled the vehicle structure with numerical methods will reduce the huge cost of vehicle crashworthiness testing while with accurate simulation obtaining good results close to the real experimental test is quite possible.

Due to high interest of governments in using green materials to reduce the toxic gases emission, composite material can be a complete substitution for the traditional solutions such as metallic structures. In this thesis, it will be proved that using these materials along with the proper design of the structure will increase the energy absorption capacity of the vehicle structure and control the dissipated energy during the crash occurrence while reducing the vehicle components mass considerably.

1.3 Problem statement

A recent trend for auto industries is to produce lighter and lighter vehicles. In the near future vehicles have to be lighter to match requests about lower fuel consumption and CO₂ emissions, but at the same time provide maximum passenger safety. One way to decrease fuel consumption is through lightweight construction, but this should not cause any change in the safety of vehicle occupants. Vehicle bodies until now have consisted largely of a homogenous sheet steel structure with constant component sheet thicknesses, now the use of lighter materials such as aluminum and composites can be the alternatives for traditional steel. The use of these alternative materials asks for appropriate redesign of the structure.

1.4 Aims and objectives

In these researches the behavior of vehicle body when parts of the structure, specifically roof panel, redesigned with steel, aluminum, composites and sandwich materials has been investigated during the different scenarios of stiffness and crashworthiness analyses. The main objectives of the thesis are:

- 1) To study and improve the contribution of light-weight vehicle roof panels made of aluminum and composite materials to the vehicle chassis static and dynamic stiffness and present a method to optimize the panel thickness improving the roof panel structural efficiency.
- 2) To investigate the detailed response of vehicle roof structure regarding to applying metallic and light-weight solutions during the vehicle frontal crash and study the effects of panel thickness optimization on the response of the roof panels.
- 3) To develop an innovative design configurations made of composite and sandwich materials for the vehicle roof panel in the rollover crash test reducing the vehicle roof structure weight and providing maximum structural efficiency which is comparable to the steel solution.

1.5 Overview of the thesis

The overall methodology of the research is presented in Figure 1.1; Chapter 2 is dedicated to present the broad overview of using different types of light-weight materials in automotive industry. After interpreting the characteristics of light-weight steels, aluminum and magnesium, thermoplastics and thermosets, the advantages of the above-mentioned materials will be discussed. Finally a short comparison review of composite material properties to other solutions with respect to elastic modulus, density, strength, stiffness and cost will be presented. Interpretation regarding to different composite manufacturing process another advantages are presented at the last section of this chapter.

Chapter 3 generally belongs to presenting the information and regarding to vehicle crashworthiness assessment and behavior of composite material during crashworthiness. Having discussed the different types of vehicle standard safety tests, interpretation regarding to the most common vehicle structure collapse modes and the testing methods will be presented. The most important structure energy absorption metrics will be studied at the next section. Different types of composite material failure modes during the loading will be discussed and the parameters that affect the energy absorption of composite structure will be studied thoroughly. Finally theories related to different formats of Hooke's law for isotropic and non-isotropic materials will be presented and at last the most usual

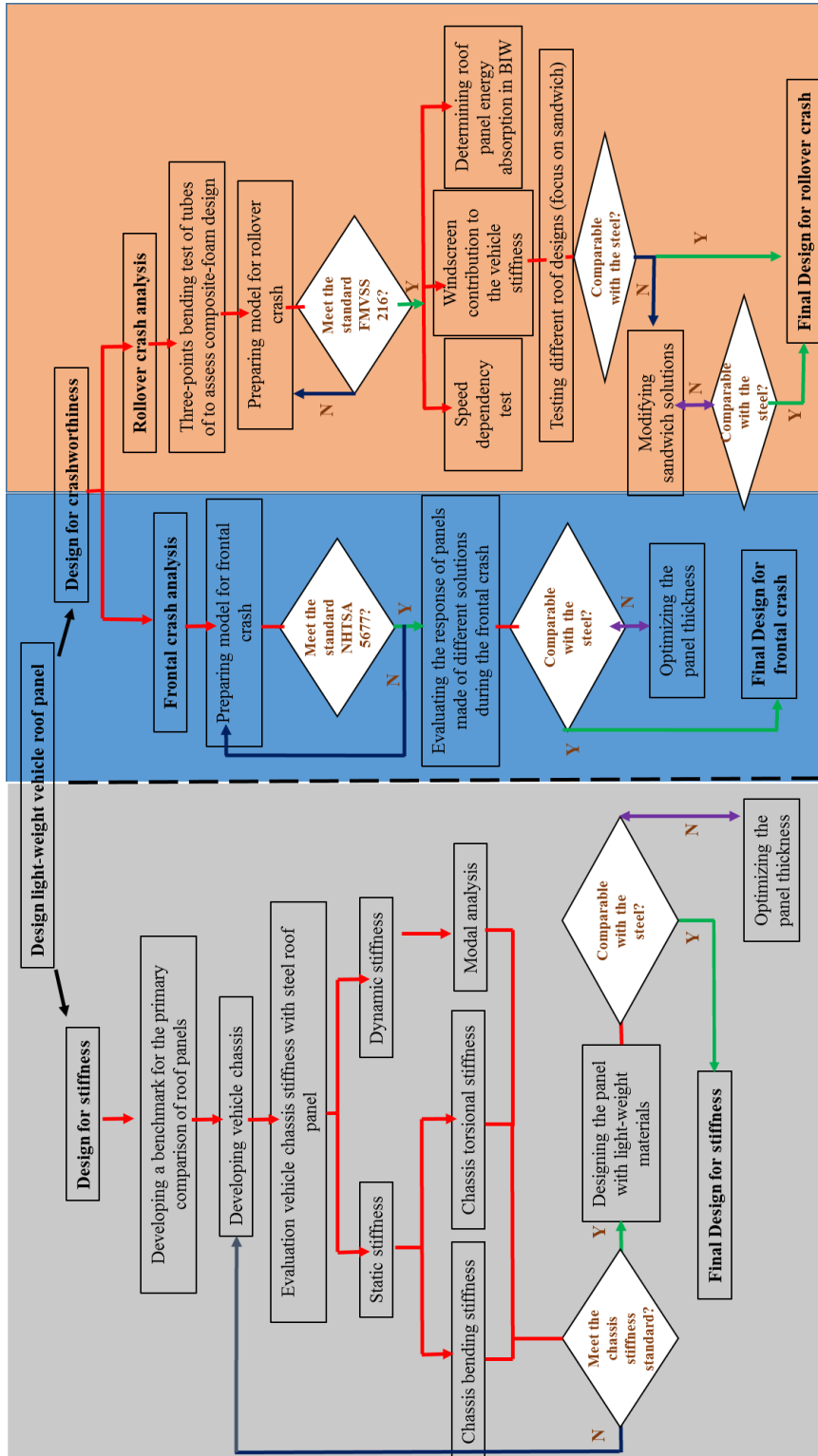


Figure 1.1: Methodology flowchart

theories of studying the composite material failure will be discussed.

Chapter 4 is presenting the first part of the research results regarding to comparison of the vehicle roof panel made of different solutions at stiffness analysis. At the first step, the benchmark of typical sedan roof panel will be developed with respect to the most important factors of designing automotive panels based on the primary and modified thicknesses of panels. After introducing the general framework for estimating the vehicle chassis bending and torsion stiffness value, load path analysis using the simple structural surfaces (SSSs) model during the bending and torsion loads will be discussed theoretically. In order to calculate the vehicle dynamic and static stiffness, the chassis of four-door sedan car (TOYOTA YARIS 2010) is developed using different material solutions for the roof structure. Different LS-DYNA material models for designing the composite structure will be introduced and compared and the complete procedure for modeling the composite roof structure will be described. Results related to load path analysis of the chassis during the bending and torsion loads obtained from SSSs and finite element method will be compared at the next step. After that vehicle stiffness results regarding to applying different material solutions for vehicle roof structure will be presented. As the last step results regarding to effect of increasing the composite layer thickness on the chassis stiffness values will be discussed.

In chapter 5 light-weight design of vehicle roof panel at frontal crash analysis with respect to different material solutions will be studied. The behavior of the vehicle roof structure though the frontal crash will be studied completely and the section forces and section displacements of vehicle roof structure with respect to different material solutions will be obtained and compared. The roof structure internal energy dissipation will be calculated and compared as a merit for energy absorption capacity. as the last step effect of increasing the roof panel thickness on energy absorption will be studied and results will be presented.

In chapter 6 an innovative design solution for the vehicle roof structure will be developed and tested in rollover crash analysis. After presenting the extensive theoretical interpretation related to modeling the failure of metallic, composite and sandwich structures in ABAQUS, the progressive failure analysis of thin-walled tubes made of steel, composite and composite foam-filled materials have been done through the three-points bending test. Modes of tubes deformation and failure have been presented for different solutions and energy absorption capacity of the tubes will be presented and compared by means of load-displacement

curves. After proving the efficiency of composite-foam design; the same idea will be implemented on the vehicle roof panel during the roof quasi-static crush test. The sandwich solutions will be designed and tested in the vehicle roof structure and the energy absorption capacity will be compared with the traditional solutions. The effect of using the sandwich core with higher density and increasing the sandwich face-sheets thickness will be discussed completely and the results will be presented.

In chapter 7, challenges of vehicle composite roof panel assembly in the production line have been discussed and at chapter 8 the overview of the conclusions and findings through the research will be presented once again.

1.6 References

- [1] Rapin, M.P., (1970). Vehicle Structural Crashworthiness in Proceedings of International Automobile Safety Conference Compendium, Detroit, Michigan, pp. 927-940.
- [2] Kamal, M.M. (1970). Analysis and Simulation of Vehicle to Barrier Impact, Society of Automotive Engineers. SAE Paper No. 700414.
- [3] Pifko, A.B. and Winter, R. (1981). Theory and Applications of Finite Element Analysis to Structural Crash Simulation. Computers & Structures, 13(1-3), pp. 277-285.
- [4] Winter, R., Mantus, M. and Pifko A.B. (1981). Finite Element Crash Analysis of a Rear Engine Automobile, 4th International Conference on Vehicle Structural Mechanics, SAE Publisher, pp. 55- 61.
- [5] Lukaszewicz, Dirk H.-J.A. (2013). Automotive Composite Structures for Crashworthiness. In Elmarakbi, A. (Eds), Advanced composite materials for automotive applications: Structural integrity and crashworthiness, Sunderland, UK, John Wiley & Sons.
- [6] Barnes, G., Coles, I., Roberts, R., Adams, D.O. and Garner, D.M.J. (2011). Crash Safety Assurance Strategies for Future Plastic and Composite Intensive Vehicles (PCIVs), Volpe National Transportation Systems Center, Cambridge, MA, USA.

Chapter 2

Light-weight Materials for Automotive Industry

2.1 Introduction

Nowadays, light-weight design has absorbed attentions in automotive industry due to its beneficial impacts such as reducing fuel consumption and CO₂ emission. In this chapter, the most important light-weight materials which are applicable to automotive industry will be pointed out; however the main focus in this thesis is on using metallic, composite and sandwich solutions. In USA, the average fuel economy is reported by the Corporate Average Fuel Economy (CAFE) standard, which measures the average fuel consumption expressed in miles per gallon (mpg); 1 mile per gallon equals to 0.43 km/liter. The history of vehicle weight changing is presented in Table 2.1 [1]. After decreasing the vehicle weight in 1986, adding additional parts to newly designed vehicles increased vehicle weight. For passenger cars, the CAFE standard increased from 18 mpg in 1978 to 27.5 mpg in 2009. It is predicted to increase the CAFE standard to 35 mpg in 2020. It is estimated that for every 10% reduction in vehicle weight, fuel consumption is reduced by 5 to 8% [1]. Reducing vehicle weight leads to decrease the power needed for acceleration and braking that creates an opportunity to design smaller engine, transmission and braking systems. Besides the fuel consumption, reducing vehicle weight causes greenhouse gases emission; reducing vehicle weight by 100 kg results in CO₂ reduction up to 12.5 g/km.

Table 2.1: US cars Average vehicle weights [1]

Year	Vehicle (curb) weight	
	kg	lb
1976	1839	4059
1986	1385	3057
1996	1600	3532
1999	1683	3716
2002	1742	3846
2004	1820	4018
2007	1775	3918
2009*	1701	3755
2015*	1631	3600

*Forecast

The global passenger automobile raw materials demand is presented in Figure 2.1. Today steel has the major part of materials used in vehicles as shown in Table 2.2 [2], so substituting steel with another materials needs to consider design characteristics, formability, corrosion, joining, cost and recycling of the alternative material. Properties of different materials applicable in vehicle structure and design are presented in Table 2.3 [2]. There are different materials available which can be good substitutions to the metallic structure such as high-strength steels, aluminum, magnesium and composites that will be presented in the next section.

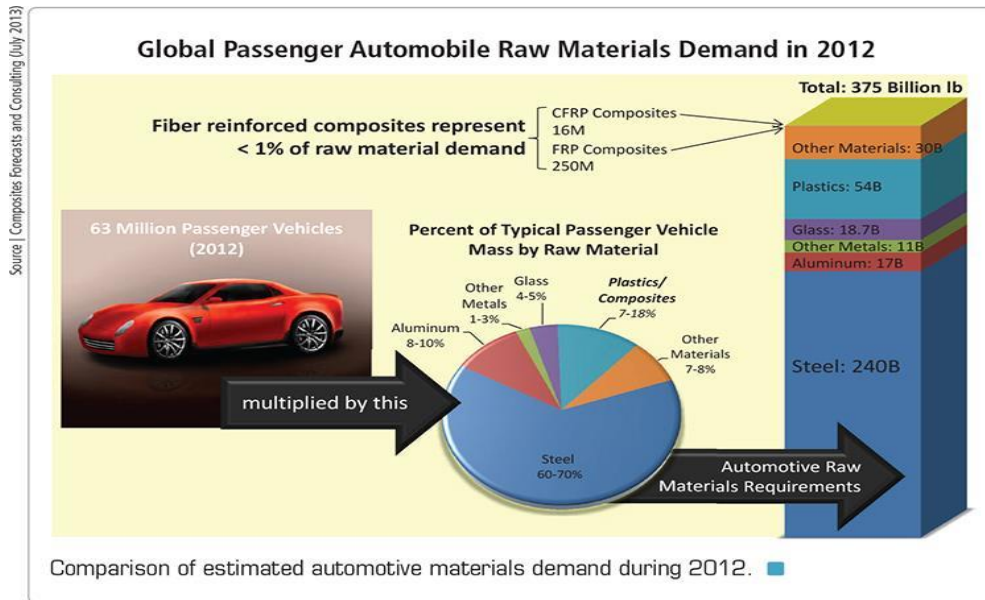


Figure 2.1: Global estimated materials for automotive industry (<http://www.transparencymarketresearch.com>)

Table 2.2: Material distributions in typical automobiles [2]

Material	Percentage of vehicle weight	Major areas of application
Steel	55	Body structure, body panels, engine and transmission components, suspension components, driveline components
Cast iron	9	Engine components, brakes, suspension
Aluminum	8.5	Engine block, wheel
Copper	1.5	Wiring, electrical components
Polymers (plastics) and polymer matrix composites	9	Interior components, electrical and electronic components, under-the hood components, fuel line components
Elastomers	4	Tires, trims, gaskets
Glass	3	Glazing
Other	10	Fluids, lubricants, etc.

Table 2.3: Comparison of material properties used in vehicle [2]

Material	Density (ρ) (g/cm ³)	Tensile modulus (E) (GPa)	Yield strength (S _y) (Mpa)	Tensile strength (S _t) (MPa)	Coeff. Of thermal expansion (10 ⁻⁶ /°C)
DQ Low carbon steel	7.87	207	186	317	11
DP 400/700 Steel	7.87	207	400	700	11
TRIP 450/800 Steel	7.87	207	450	800	11
5182-H24 Aluminum	2.7	70	235	310	23
6111-T62 Aluminum	2.7	70	320	360	23
AZ91 Magnesium	1.8	45	160	240	26
Ti-6Al-4V Titanium	4.43	114	827	896	9
304 Stainless steel	7.9	200	241	614	17
Nitronic 30 stainless steel	7.86	193	393	862	16
High strength CFRE (unidirectional)	1.55	138	-	1550	-
High modulus CFRE (unidirectional)	1.63	215	-	1240	-0.9 (L) 27 (T)
GFRE (unidirectional)	1.85	39	-	965	6 (L) 19 (T)
CFRE (quasi-isotropic)	1.55	45.5	-	579	0.9
Sheet molding compound (SMC-R50)	1.87	16	-	164	14.8

L is the longitudinal direction and T is the transverse direction

2.2 Lightweight steels in automotive industry

Several types of steel used in automotive industry to reduce mass and improve energy absorption in crash events as presented in Table 2.4 [2]. These steels are divided into three categories of low carbon and conventional types of high strength steels (HSS), first generation of advanced high strength steels (AHSS) and the third category consists of the second generation of AHSS.

For a long time, low carbon steels were the most common steels used in vehicle body panels and structural components due their superior characteristics of formability, weldability, high quality appearance after painting, ease of manufacturing and low cost. High strength low alloy (HSLA) steels are used for load carrying structural parts for which good weldability is needed. These steels use to produce as motor compartment rails, rocker side panels and rear longitudinal rails due to their good formability, high strength and affordable cost.

Table 2.4: Steels used in automotive industry [2]

Low carbon and conventional high strength steels (HSSs)
Low carbon steels (LC)
Solid solution strengthened (SSS)
Bake hardenable (BH)
High strength low alloy (HSLA)
First generation advanced high strength steels (AHSSs)
Dual phase (DP) – ferrite/martensite
High hole expansion (HHE) – ferrite/bainite
Stretch flangeable (SF)
Transformation induced plasticity (TRIP)
Complex phase (CP)
Fully martensitic (MS)
Boron heat treatable steels
Second generation advanced high strength steels
Twinning induced plasticity (TWIP)
Lightweight steels with induced plasticity (L-IP)

The term Advanced High Strength Steels (AHSS) generally refers to a wide range of steel grades that are part of the first generation of AHSS. This type of steel has other phases except ferrite which has changed its material mechanical, forming and even energy absorbing properties. Among all AHSS steels dual phase steels are the most commonly used in automotive applications. Twinning Induced Plasticity (TWIP) steels and Lightweight Steels with Induced Plasticity (L-IP) are the latest generation of Advanced High Strength Steels designed to provide the combination of very high tensile strengths and exceptional ductility. This steel generation consists of a face centered cubic austenite structure that is obtained through the use of very high levels of manganese. Strength comparison of HSS, first and second generations of advanced high strength steels is presented in Figure 2.2. The second generation of AHSS hugely increases the ductility to tensile strength ratio of steel in comparison with the conventional steel [2].

In order to fill the gap in strength/ductility ladder between the first and second generations of AHSS and propose the more cost of effective choice of AHSS, American Iron and Steel Institute (AISI) developed the third generation of steels. The comparison of strength/ductility ladder is presented in Figure 2.3 for the third generation of AHSS [2].

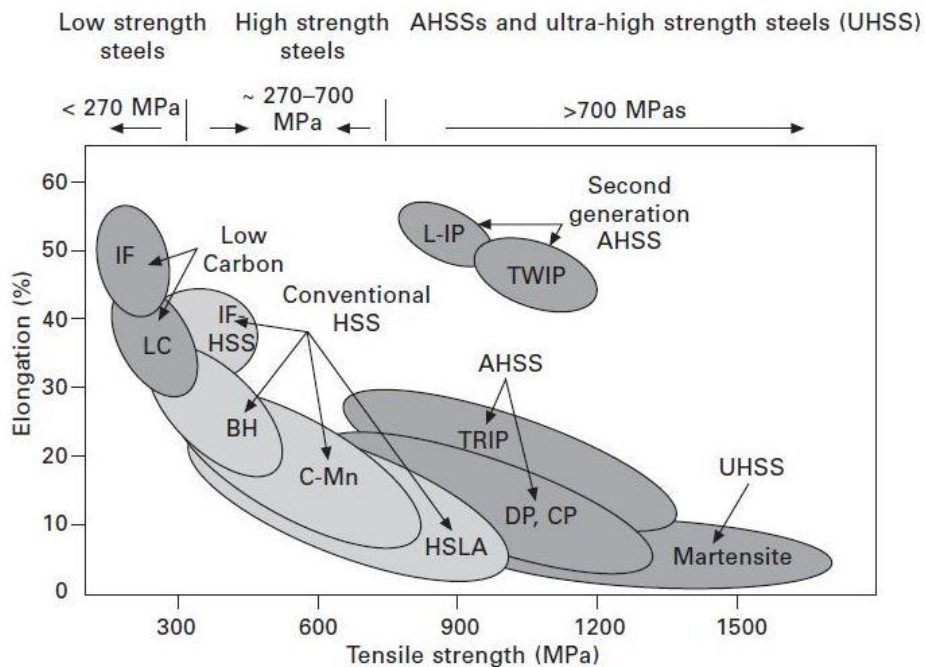


Figure 2.2: Automotive steel strength/ductility ladder [2]

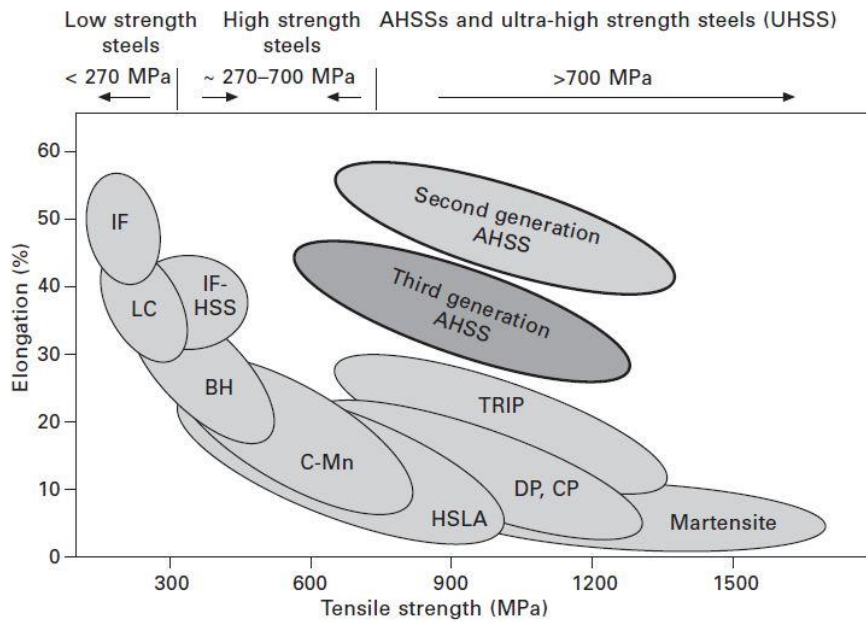


Figure 2.3: Strength/ductility for the third generation of AHSS [2]

2.3 Aluminum alloys in automotive industry

Aluminum with the density of 2.69 g/cm^3 and high deformability can be a good substitution for steel in automotive industry. Although the aluminum modulus of elasticity is low (69 GPa) in compare with that of steel (210 GPa), high deformability of aluminum alloys makes it possible to produce them in various forms of castings, extrusions, stampings, forgings, impacts, and machined components. Parts produced by casting and extrusion consolidate the product final form and this reduces the number of components necessary to produce a vehicle.

Figure 2.4 shows that North American automotive industries increased the usage of aluminum materials in vehicles from 36 kg in 1973 to 147 kg in 2007 [3-5]. Almost 100% of transmission cases, 60% of engine blocks and 60% of wheels are made of aluminum alloys.

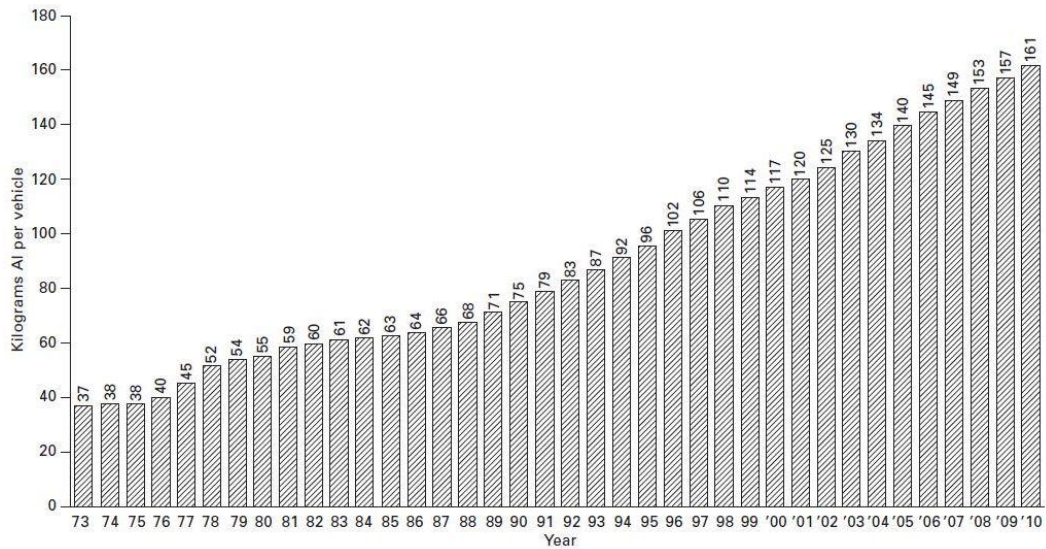


Figure 2.4: History of vehicle aluminum content in North America [3-5]

Applications of aluminum alloys in a typical automobile, without consideration of body design, are shown in Figure 2.5 [6]. Aluminum has a wide range of applications in vehicle body, as an example Audi built the R8 sport car made of full aluminum chassis with the weight of 210 kg and high torsional rigidity as shown in Figure 2.6 [7].

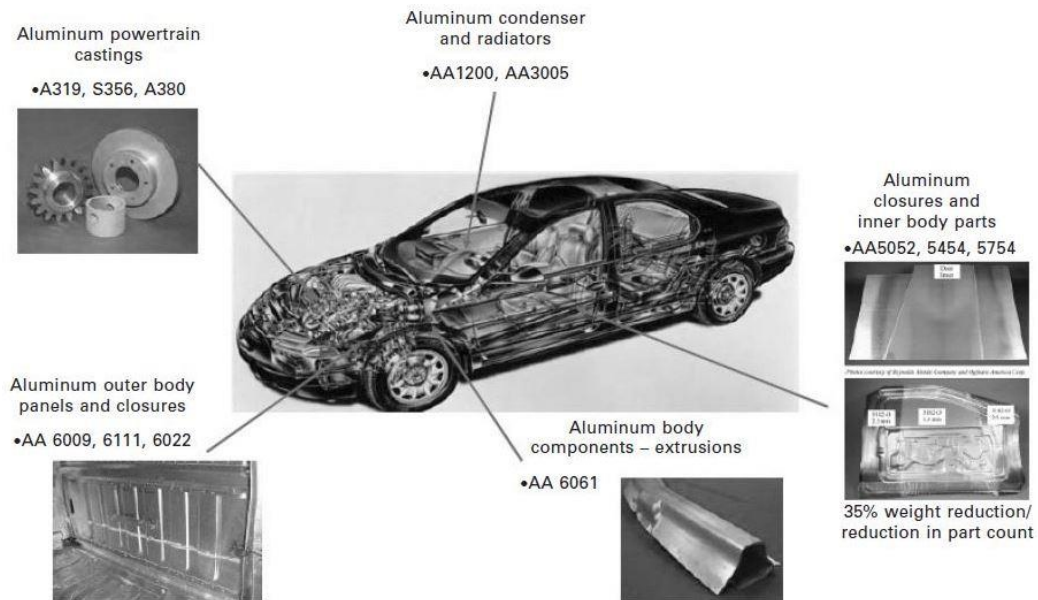


Figure 2.5: Automotive application of aluminum alloys [6]



Figure 2.6: Audi R8 aluminum frame [7]

Although aluminum is a suitable alternative for steel but substituting this material needs careful investigation in terms of design and applications in automobile. Parameters such as flexibility of design, light weighting efficiency, crashworthiness, manufacturing cost, maintenance cost, repair requirements and recyclability should be considered before substituting aluminum for any steel part [8]. Before considering aluminum as an alternative for steel it is necessary to compare their properties and characteristics as following [9]:

- ❖ Aluminum density is one-third that of steel.
- ❖ Aluminum elastic modulus is one-third that of steel.
- ❖ Aluminum hardness is lower than steel.
- ❖ Aluminum alloys specific fatigue strength, the highest stress that a material can withstand for a given number of cycles without breaking — called also endurance strength, is about one-half that of steel.
- ❖ Aluminum alloys thermal expansion coefficient is about 1.5 times greater than that of steel.
- ❖ Ductility, as measured by % elongation of aluminum alloys in the annealed condition, is about two-thirds less than that of annealed low carbon steel.
- ❖ Aluminum alloy sheet formability is lower than that of annealed low carbon sheet steel.

- ❖ Aluminum alloys can be used down to cryogenic temperatures without loss of ductility, while carbon steels suffer from embrittlement at low temperatures.
- ❖ Steel is strain rate sensitive while aluminum alloys are not.
- ❖ Unlike steel, aluminum and aluminum alloys are non-magnetic.
- ❖ Aluminum thermal and electrical conductivities are about four times that of steel.
- ❖ Damping characteristics of aluminum alloys and steel are similar.
- ❖ Corrosion resistance of aluminum is much higher than that of steel.
- ❖ Aluminum alloys can be used unfinished in many applications while steels require paint to prevent corrosion.
- ❖ Aluminum is harder to weld than steel.
- ❖ Recycling value of aluminum is higher than that of steel.

2.4 Magnesium alloys in automotive structures

The density of magnesium is 1.74 g/cc, which is one-third that of aluminum (Al) and less than one-fourth that of steel; magnesium is less dense than most glass fiber-reinforced automotive polymers while it has equal density to carbon fiber composites, although magnesium alloys can cost considerably less. The advantages of magnesium as a structural material are presented in Table 2.5 [10].

Table 2.5: Magnesium applications in non-automotive industry [10]

Military and Aerospace	Consumer products
Aircraft air frames	Power tools
Engines	Cameras
Transmission cases	Hand luggage
Missile skins and frames	Appliance parts
Electronic housings	Cell phones
	Portable computers

Due to high chemical reactivity of magnesium, it has a major role in non-automotive industries such as organic chemistry, pharmaceuticals, and electrochemical industry. Few applications of magnesium in non-automotive are presented in Table 2.6 [11].

Table 2.6: Property advantages of magnesium [11]

Property	Advantage
Specific strength	-Magnesium has a specific strength that is similar to cast iron, and similar or greater than many traditional automotive aluminum alloys and thus can provide more mass reduction relative to aluminum.
Specific stiffness	-Magnesium has a higher specific stiffness than many polymeric materials and composites, thus allowing improved mass reduction.
Fluidity	-The relatively high fluidity of magnesium allows extremely thin walled castings (1.5 mm), which enhances mass reduction opportunities.
Hot formability	-Wrought magnesium can be formed into very complex shapes using elevated temperature forming processes.
Machining	-Machining tools last longer with magnesium than aluminum, reducing costs. The only issue is added care required with machining chips.
Damping	-Magnesium alloys have excellent damping capability compared with other materials making them attractive
Low temperature properties	-Magnesium does not exhibit a brittle to ductile transition so it can be used at very low service temperatures

Although magnesium is not a popular material for automotive industry, few applications of this material is shown in Figure 2.7.

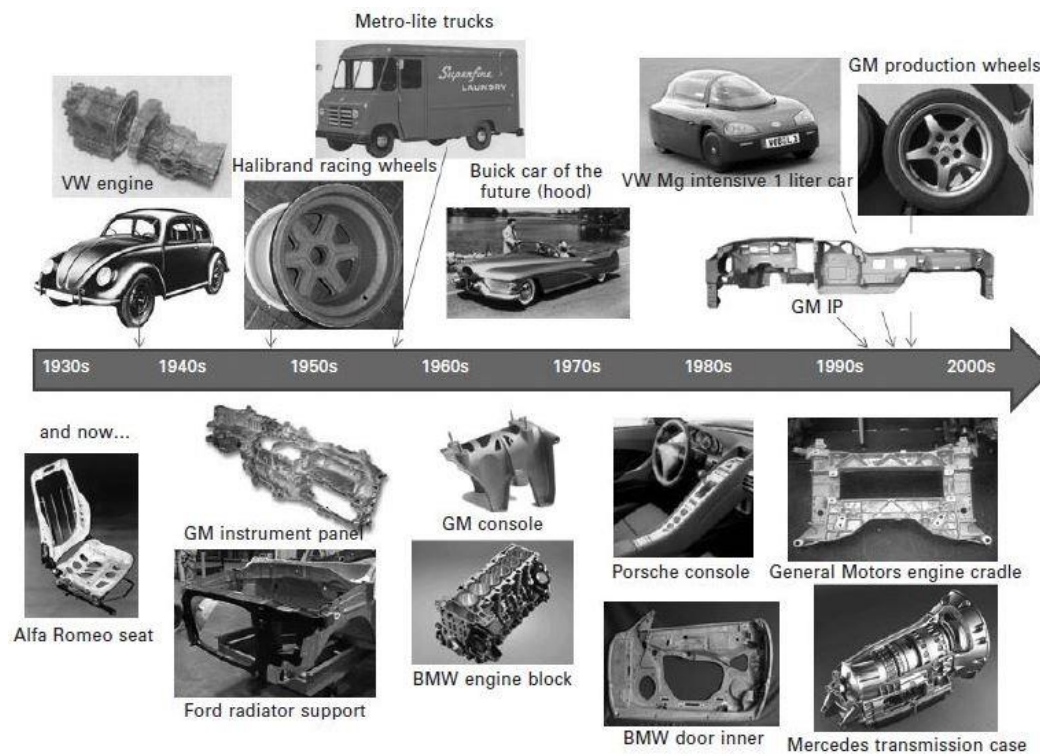


Figure 2.7: Magnesium applications in automotive industry during history [2]

2.5 Thermoplastics and Thermoset for lightweight automotive structures

Polymers are divided into two main categories; thermoplastics and thermosets. Thermoplastics are a class of polymers that can be softened and melted when they are heated. This is in contrast to the thermosets which cannot be melted by heating. Besides the higher recyclability of thermoplastics, they have higher ductility and impact resistance than thermosets along with lower production time. Thermoplastics are used in automobiles structure to satisfy many needs as shown in Table 2.7 [12, 13].

Thermoset polymer due to its lower viscosity than thermoplastic has the possibility of combining with long and continuous fibers to produce composite structures with high strength. These composite structures are widely found in vehicle parts such as bumper beams, fenders, hoods, roof panels, radiator supports, deck lids and exterior and interior body components.

Table 2.7: Material properties of thermoplastic polymers used in automobile [12, 13]

Polymer	Acronym	Amorphous or semi-crystalline	Density (g/cc)	Modulus (GPa)	Strength (MPa)	Strain to failure strength (%)	Notched Izod impact examples* (J/m)	Automotive application
High density polyethylene	HDPE	Semi-crystalline	0.96	1	20–30	–	20–750	Windshield washer fluid bottle, ducts, fuel tank
Polypropylene	PP	Semi-crystalline	0.90	1.3	30–40	30–200	20–70	Battery case, cooling fan blades, heating ducts, bumper beam, instrument panel, splash shields, interior consoles
Polycarbonate	PC	Amorphous	1.2	2.5	60	90–130	640–960	Head lamp lens, instrument panel carrier
Polymethyl methacrylate	PMMA	Amorphous	1.17–1.20	2.8	50–70	2–6	15–20	Tail lamp lens, instrument panel clusters
Acrylonitrile butadiene styrene	ABS	Amorphous	1.05–1.07	2.2	40	90–130	320	Bumper beam, instrument panel, wheel covers, mirror housing, interior consoles
Styrene maleic anhydride	SMA	Amorphous	1.05–1.15	2.8	35–60	2–30	25–650	instrument panel carrier
Polyamide-6 (nylon-6)	PA-6	Semi-crystalline	1.14	2.5	80	45	60	Intake manifold, resonator, engine throttle body, cooling fan blades
Polyamide-6,6 (nylon-6,6)	PA-6,6	Semi-crystalline	1.14	2.8	60–80	60	100	Intake manifold, resonator, switches, gears, cooling fan blades
Polyamide-4,6 (nylon-4,6)	PA-4,6	Semi-crystalline	1.18	3	99	25	98	Electrical connectors, switch body, charge-air coolers, chain tensioners
Polyoxymethylene (acetal)	POM	Semi-crystalline	1.41	2	61–70	25–75	65–85	Gears, window crank, seat belt components, door lock housings
Polyethylene terephthalate	PET	Amorphous	1.37	2	70	–	45	Electrical connectors, ignition coil bobbins
Polybutylene terephthalate	PBT	Semi-crystalline	1.31	1.7	55	55–60	65–70	Electrical connectors, fuse boxes, sensor housings, actuator cases, mirror housings
Polyphenylene sulfide	PPS	Semi-crystalline	1.34	3.3	69	1.6	16	Fuel rail, pump impellers, thermostat housing, throttle body, ignition coil bobbin

*In many of these applications, the polymer may be combined with fillers or short fiber reinforcements. The properties listed are without any fillers or short fiber reinforcements.

2.6 Composite materials

2.6.1 Introduction

Composites are the materials consist of different materials with various properties. The goal is that the composite material improve the defects of each constituent and creates new structure with better performance. The final product should be lighter along with higher strength. By weight, about 8% of today's automobile parts are made of composites including bumpers, body panels, and doors [14].

Composites consist of reinforcing phase and matrix as shown in Figure 2.8. The reinforcing phase provides the strength and stiffness. There are different fibers available at the market that the most common ones are carbon, glass and aramid. Comparison of typical stress-strain curve for composite fibers is shown in Figure 2.9 [15]. The reinforcement which is a fiber should be harder, stronger, and stiffer than the matrix. The continuous phase is the matrix, which is a polymer,

metal, or ceramic. Polymers have low strength and stiffness, metals have intermediate strength and stiffness but high ductility while ceramics have high strength and stiffness but are brittle. The matrix plays major roles such as maintaining the fibers in the proper direction and protecting them from abrasion. In polymer and metal matrix composites strong bond between the fiber and the matrix is formed in which the matrix transmits loads from the matrix to the fibers through shear loading at the interface. The goal to use ceramic matrix composites is to increase the toughness rather than the strength and stiffness; therefore a low interfacial strength bond is desirable [16].

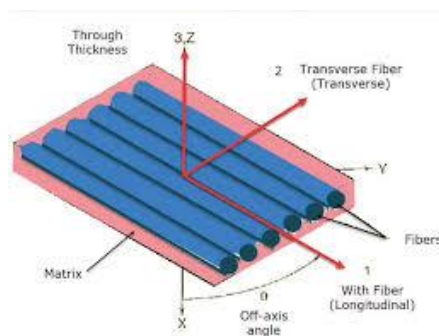


Figure 2.8: Schematic of composite structure

Detailed comparison of composite materials with metal and aluminum in terms of density, Young's modulus, specific strength and stiffness and cost are presented in Figure 2.10 [8]. It is observed that composite materials have higher production cost in compare with the other materials while they have lower density and similar strength and stiffness to metallic materials.

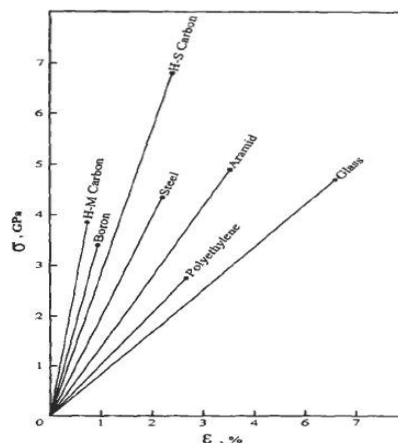
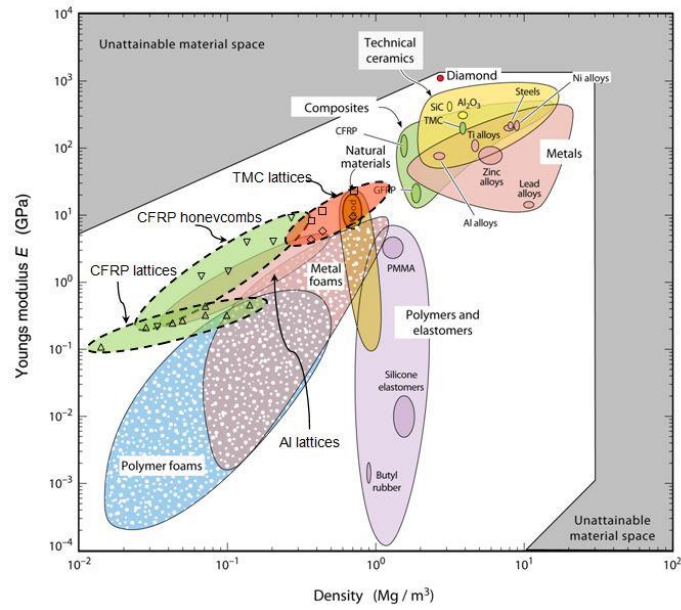
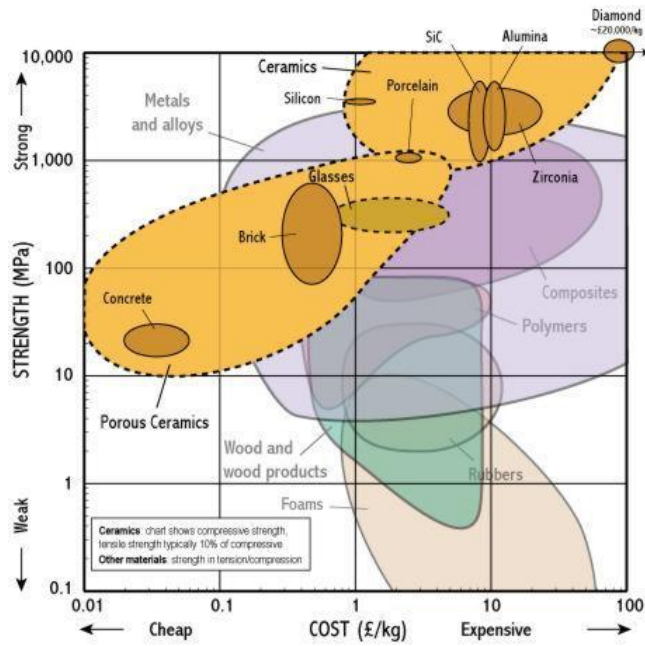


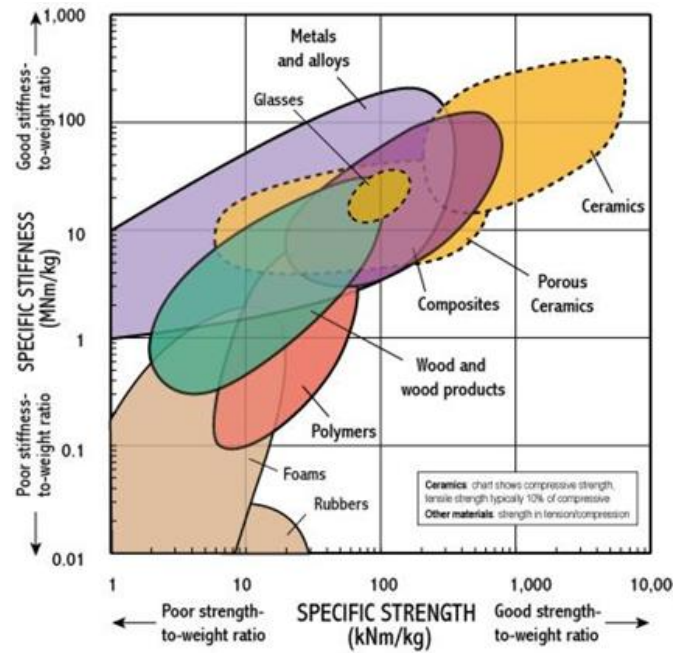
Figure 2.9: Composite typical stress-strain diagram [15]



a. Elastic modulus vs. Density



b. Strength vs. Cost



c. Stiffness vs. Strength

Figure 2.10: Comparison of composite a. Elastic modulus vs. Density-b. Strength vs. Cost-c. Stiffness vs. Strength [8]

Composite can use different formats of fiber reinforcement such as unidirectional fiber, fabric or woven format, short fibers, particulate and random fiber orientation as shown in Figure 2.11.

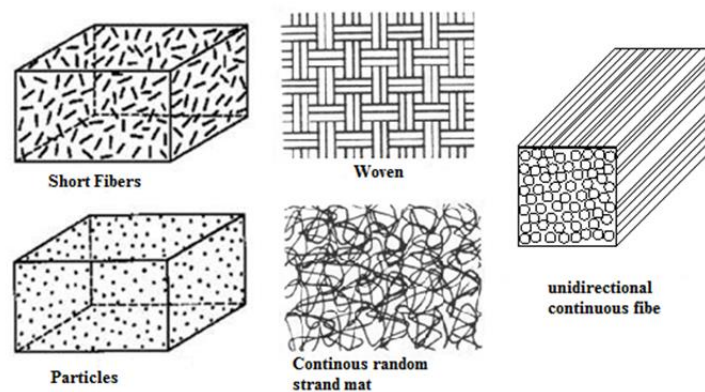


Figure 2.11: Schematic of various formats available for the reinforcing fiber

2.6.2 Composite manufacturing processes

Composite materials can be produced by different process such as hand lay-up, RTM, pultrusion, filament winding, SMC, BMC, etc. The production rate along with the applications of these processes are presented in Figure 2.12 [17]. The composite production processes are described in following:

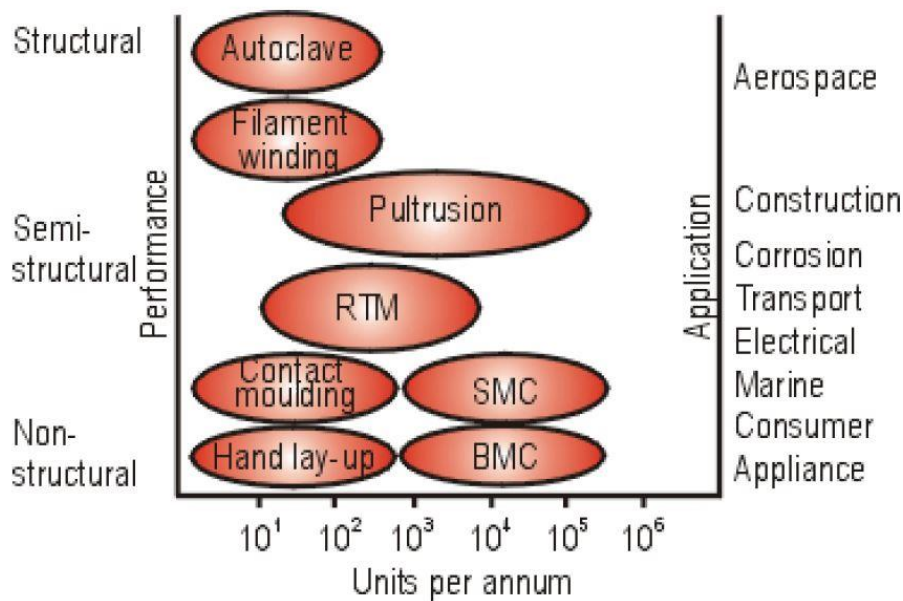


Figure 2.12: Comparison of composite production processes rate and applications [17]

2.6.2.1 Hand lay-up

Hand lay-up method is the simplest method in which reinforcing material and resin are laid into the mold and then compressed with the roller for the final shape. Using hand lay-up technique to manufacture composite materials has the advantages of low cost and possibility of producing small and large parts, while it has disadvantages of poor accuracy and high material waste. The schematic of hand lay-up process is shown in Figure 2.13.

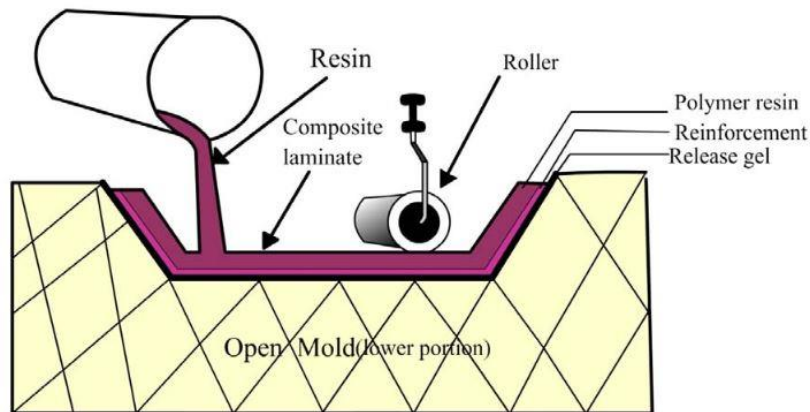


Figure 2.13: Hand lay-up composite manufacturing

2.6.2.2 Spray-up

In this technique as shown in Figure 2.14 [18], spray gun is used to combine fibers and resin simultaneously in the mold. The process of spraying chopped fibers and resin, in place of mat type reinforcements, into an open mold resulting in a part with one finished surface is called Spray-up. This method has the advantages of higher output than hand lay-up and possibility of producing parts in different size. Although this technique has higher production rate, it needs higher initial investment, more emission and material waste.

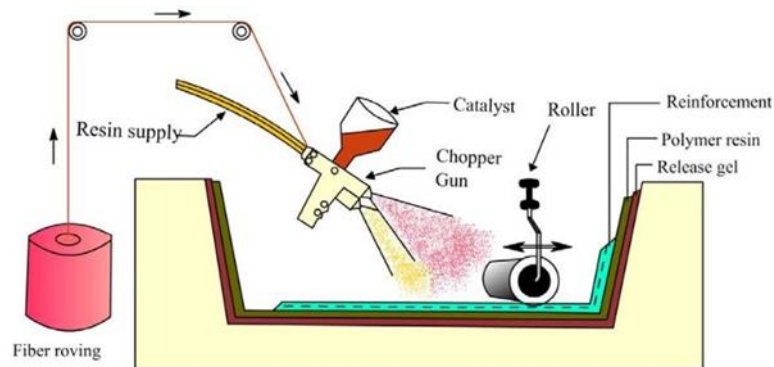


Figure 2.14: Hand lay-up composite manufacturing [18]

2.6.2.3 Sheet Molding Compound (SMC)

SMC (sheet molding compound) is a sheet of composites containing uncured thermosetting resins and short fibers and fillers. This composite consists of chopped glass fibers, fillers, additives, and polyester or vinylester resin. In this process, after all the ingredients of the resin paste are completely mixed, a resin is

placed on a polyethylene moving film through a metering device. Continuous strands of chopped glass fibers are dispersed over the moving resin paste and then another layer of resin paste is placed over dispersed fibers for good fiber combination. These polyethylene films remain until they are placed in a compression mold. Instead of glass fibers, carbon fibers or other fibers can be used. A heated compaction roller is then rolled up the complete sheet and then the sheet cut into any appropriate shapes suitable for shipping [19]. The schematic of SMC process is shown in Figure 2.15.

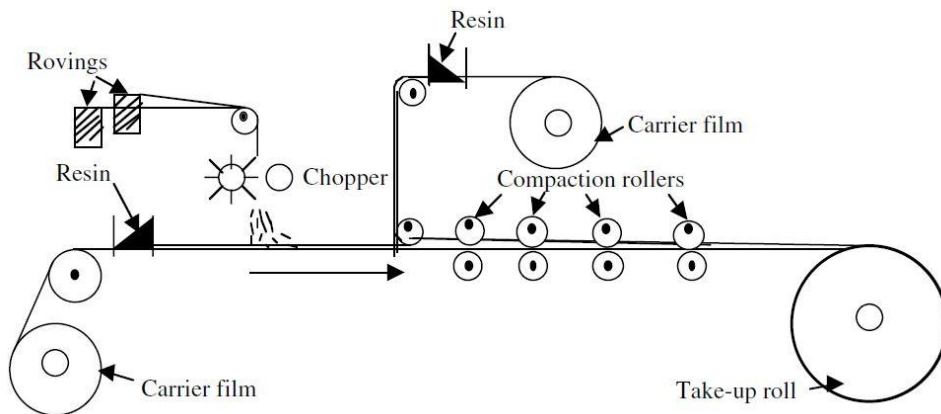


Figure 2.15: Sheet molding compound (SMC) composite manufacturing [19]

2.6.2.4 Bulk Molding Compound (BMC)

Bulk molding compound (BMC), which is also known as dough molding compound (DMC), is a compound that is prepared in log or rope format. In BMC process, after fibers are mixed with resins then the compound is prepared in log or rope format by extrusion process. The extruded part is cut depending on the requirement. BMC generally contains 15-20 % fiber in a polyester or vinylester resin with the length of 6 to 12 mm. BMC composite has weaker mechanical properties in compare with the SMC composite due to the lower fiber volume fraction and shorter fiber length. The schematic of BMC process is shown in Figure 2.16.

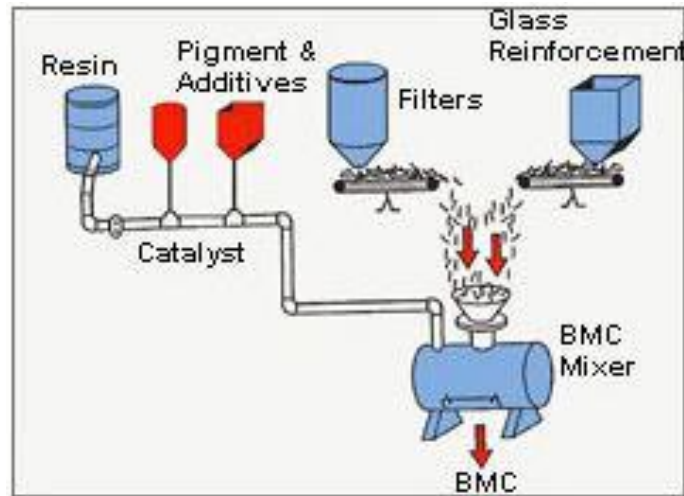


Figure 2.16: Bulk Molding Compound (BMC) composite manufacturing

2.6.2.5 Resin Transfer Molding (RTM)

RTM is a semi-automatic process which uses closed models and performs at low pressure. In this process many dry layers of woven roving are placed at the bottom of the mold and the liquid resin with low viscosity is led through in the mold cavity and then at the next step it would be cured. Resin transfer modeling process is shown in Figure 2.17. The advantages of this process can be classified as below [20]:

- Fabricating of complex structure.
- Smooth surface after processing.
- Design flexibility.
- Combining several parts into the unique one.

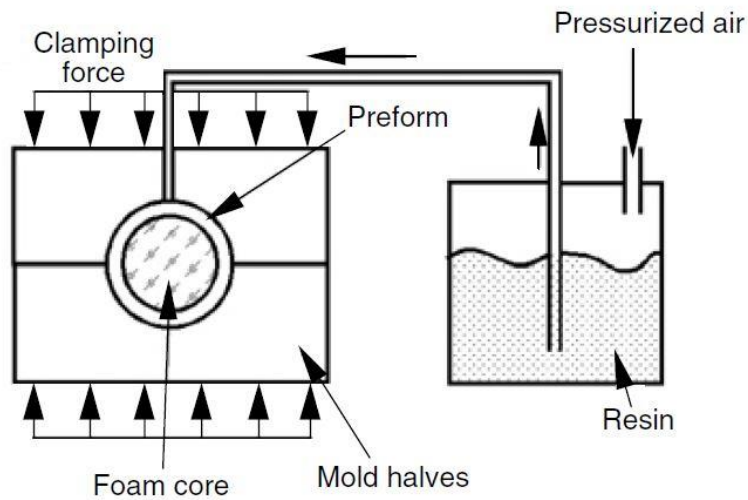


Figure 2.17: Resin Transfer Molding (RTM) composite processing [20]

2.6.2.6 Pultrusion

Pultrusion is a fabricating process that uses for shaping composite materials which have constant cross section area. As shown in Figure 2.18, during this process fibers are led into a resin bath and then reinforced fibers are led to the specific oven for curing and final shaping. Pultrusion is an automatic uninterrupted process which can be useful for fabricating complex shapes [21]. Pultrusion process can improve the essential characteristics of products such as corrosion resistance, chemical resistance, increasing strength and stability, increasing durability and decreasing weight [22].

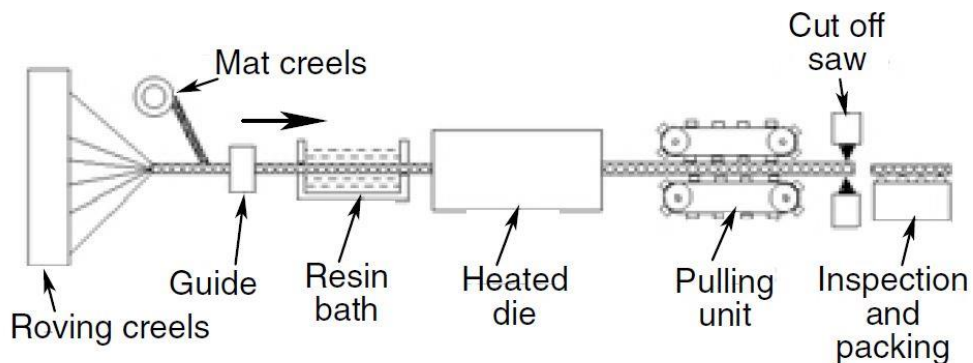


Figure 2.18: Pultrusion process

2.6.2.7 Filament winding process

Filament winding (Figure 2.19) is one of the oldest and most common process of fabrication in situation where we need precise fiber orientation. This technique uses for retrofitting products by using reinforced fibers and composite resins. In this process after proper tension is provided for filaments, they are wound over a mandrel. The mandrel rotates with the spinning wheel on a horizontal axis then carriage begins to move linearly forward and backward so fibers are laid down in the predetermined pattern. Diverse resins or fibers can be used in the process of filament winding depends on the desirable performance and provided cost. The most common fibers are carbon fibers, aramid fibers and glass fibers. At the subsequent process set fibers are coated with liquid resins and after specific processes (wet winding or prepreg winding) they are wound on the mandrel; then after the mandrel covered by the adequate thickness leaded through an oven for curing and solidifying the resin. According to desirable products and their applications, mandrel could be removed or became an integral part of the product [23-25].

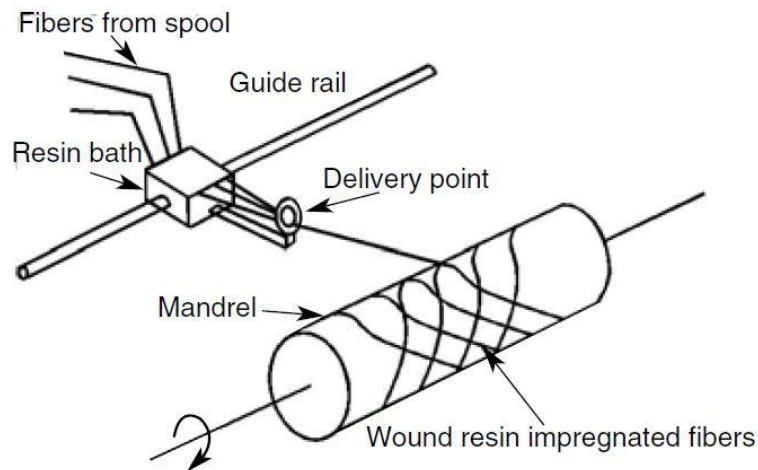


Figure 2.19: Schematic pictures of filament winding

2.7 Conclusion

Increasing greenhouse gases emission and fuel price enforce governments to set regulations to decrease these effects. It is estimated that for every 10% reduction in vehicle weight, fuel consumption is reduced by 5 to 8%. Based on these statistics lightening vehicle has a major role in reducing emissions and cost. In this chapter lightweight materials of advanced steel, aluminum, magnesium, thermoplastic, thermoset and composite materials and their applications in

automotive industry have been discussed thoroughly; however the main focus in this thesis is on using metallic, composite and sandwich solutions due to feasibility of the designs. Recently, composite as a material with low density and high stiffness gained a lot of attentions in automotive industry. In this chapter after composite materials have been compared in the terms of density, stiffness, elastic modulus and strength with the other solutions, the structure of composite material along with the method for producing it were investigated.

2.8 References

- [1] Brooke, L. and Evans, H. (2009). ‘Lighten up!’ *Automotive Engineering*, 117(3), pp. 16–22.
- [2] Horvath, C.D. (2010). Advanced steels for lightweight automotive structures. In P. K. Mallick (Eds), *Materials, design and manufacturing for lightweight vehicles* (pp. 35-78). USA: Elsevier.
- [3] The Aluminum Association Auto & Light Truck Group (ALTG): www.autoaluminum.org (Accessed September 2016).
- [4] Stempel, B., representing ALTG, ‘The Road Ahead Looks Brighter and Lighter,’ presentation made at the American Metal Market’s North American Aluminum Conference, June 26–27, 2007, Chicago, IL.
- [5] Schultz, R. (Ducker Worldwide North America), Ducker Worldwide Materials Growth Report, 2008, richards@ducker.com (Accessed September 2016).
- [6] Benedyk, J.C., ‘Automotive Aluminum Casting Trends and Developments,’ *Light Metal Age*, vol. 58, October, 2000, pp. 36–41.
- [7] AluDrive, Summer 2008, European Aluminium Association www.aluminium.org (Accessed September 2016).
- [8] Ashby, F. (2005). *Materials Selection in Mechanical Design*, Elsevier. Butterworth-Heinemann Linacre House, Jordan Hill, Oxford OX2 8DP 30 Corporate Drive, Burlington, MA 01803.
- [9] Benedyk, J.C. (2010). Aluminum alloys for lightweight automotive structures. In P. K. Mallick (Eds), *Materials, design and manufacturing for lightweight vehicles* (pp. 79-113). USA: Elsevier.

- [10] Powell, B.R., Krajewski, P.E. and Luo, A.A. Magnesium alloys for lightweight powertrains and automotive structures In P.K. Mallick (Eds), *Materials, design and manufacturing for lightweight vehicles* (pp. 114-173). USA: Elsevier.
- [11] Avedesian, M. and Baker, H. (1999). *ASM Specialty Handbook: Magnesium and Magnesium Alloys*, ASM International, Materials Park, Ohio.
- [12] Maxwell, J. (1994). *Plastics in the Automotive Industry*, Cambridge, Woodhead Publishing.
- [13] Lange, W. (2003). Polymers in automobile applications, in *Plastics and the Environment* (ed. Andrady A L), John Wiley & Sons.
- [14] Kaw, A.K. (2006). *Mechanics of Composite Materials-Second Edition*, CRC Press, Taylor and Francis Group, Boca Raton, Florida, USA.
- [15] Vasiliev, V.V., & Morozov, E. (2001). *Mechanics and analysis of composite materials* Elsevier, pp. 10-16.
- [16] Campbell, F.C. (2010). *Structural composite materials*, ASM International, Materials Park, Ohio.
- [17] <http://www.azom.com/article.aspx?ArticleID=352> (Accessed September 2016).
- [18] <http://www.frprawmaterial.com/frp-process.html> (Accessed September 2016).
- [19] Mazumdar, S. (2001). *Composites manufacturing: Materials, product, and process engineering*, CRC press.
- [20] Babu, M.S., Srikanth, G, Biswas, S. (2000). Composite fabrication by filament winding-an insight, Available from: <http://www.Tifac.org.in/news/acfil.html> (Accessed September 2016).
- [21] Carlone, P., Palazzo, G., & Pasquino, R. (2007). Pultrusion manufacturing process development: Cure optimization by hybrid computational methods. *Computers & Mathematics with Applications*, 53(9), pp. 1464-1471.

[22] Pultrusion: the process, product and applications, Reinforced Plastics november 1991, 0034-3617/91/\$3.50, Elsevier Science Publishers Ltd.

[23] Etamax engineering :www.etamax.com.au (Accessed September 2016).

[24] Shen, F.C. (1995). A filament-wound structure technology overview. *Materials Chemistry and Physics*, 42(2), pp. 96-100.

[25] Lossie, M., Peters, J., & Van Brussel, H. (1989). Design philosophy in filament winding. *CIRP Annals-Manufacturing Technology*, 38(1), pp. 175-178.

Chapter 3

Crashworthiness and Composite

3.1 Introduction

Crashworthiness is the ability of a structure to protect its occupants during an impact. Crashworthiness concept was first defined in aerospace industry around 1950 to measure the potential of the structure in crash events. The same meaning was defined in automotive industry which implies that crashworthiness is the ability of vehicle structure to provide enough cabin space for the passengers and decelerate the loads transmitted to them by deforming plastically. This means that the crash deceleration pulse should be below the upper range of human tolerance. If the peak of crash deceleration pulse happens early and decrease slowly, this pulse would be less harmful to the vehicle passengers. In this way it is quite crucial that the restraint system absorbs the energy as much as possible by a controllable plastic deformation.

The vehicle body should be stiff enough in the case of bending and torsion load insertion, beside it should have the minimum vibration frequency to reduce the vehicle harshness. In general vehicle structural crashworthiness can be viewed in the five different aspects of frontal, rear, side and roof crashworthiness and the designed restraint system. The front part of vehicle structure should be stiff to absorb the crash kinetic energy by plastic deformation; it should also prevent the vehicle body intrusion through the passenger cabin specifically in the case of crash with narrow objects. The rear part of the vehicle structure should be stiff to protect the passengers and the fuel tank. Vehicle side structure should be designed in a way that minimum intrusion occurs through the door during the crash. Vehicle roof panel should be stiff to provide sufficient space for the vehicle

occupants in the case of rollover, protecting them from severe head injury and the restraint system including energy-absorbing steering columns, seat belts, air bags and head restraints is necessary to protect the vehicle occupants from the collision inside the cabin in crash events [1].

In this chapter, besides the discussion about different types of vehicle crash, crashworthiness metrics will be introduced. Crashworthiness energy absorption characteristics and the typical modes of vehicle component deformation will be studied. Deformation modes of metallic and composite specimen's will be compared and parameters affecting the energy absorption capacity of composite material will be discussed. Stress-strain relations for isotropic and non-isotropic material structures will be derived and failure criteria of composite materials will be studied.

3.2 Vehicle crashworthiness assessment

Crashworthiness tests are categorized into the three main groups of component tests, sled tests, and full-scale vehicle model test. At the first step vehicle components are tested under the quasi-static and dynamic loading condition to investigate their energy absorption capacity and deformation modes. In a sled test, a vehicle buck representing the passenger compartment including its interior components such as the seat, instrument panel, steering system, seat belts, air bags and dummies is tested under the dynamic loads to evaluate the passenger response in a frontal and side impacts and measuring the crash deceleration pulse transmitted to dummies by setting sensors on them. The full-scale model test consists of the complete vehicle model and the rigid barrier; so the response the full model is measured during the vehicle impact to the rigid barrier and the vehicle restraint system is evaluated thoroughly [1].

Vehicle crash safety is divided into two main categories of active and passive safety. Active safety are the devices deigned to avoid the crash occurrence while passive safety goal is to reduce the damage of the vehicle structure to keep the occupants as safe as possible. Active safety related to applying devices such as ABS (Antilock Braking System), traction control, electronic stability control, rollover-detection sensors, active suspension and forward collision warning systems, emergency brake assist, etc., while passive safety is involved in improving the crashworthiness of the vehicle body and applying restraint systems such as seat belt and airbag [2]. The vehicle passive safety is assessed through the governmental standard tests such as the Federal Motor Vehicle Safety Standards (FMVSS) in the USA. In addition new car assessment programs (NCAPs, e.g. Insurance Institute for Highway Safety, IIHS) are implemented to evaluate the

performance of all vehicles and rate the vehicles crashworthiness. Distribution of crash accidents without considering the rollover crashes, which is around 2% of the total number of crashes, is presented in Figure 3.1. As shown in Figure 3.2 while the majority of crashes cover only a small proportion of the vehicle front, full frontal impact amounts to 31.1% of all typical frontal crash accidents and this proves that every design should be prepared for different crash zones [3].

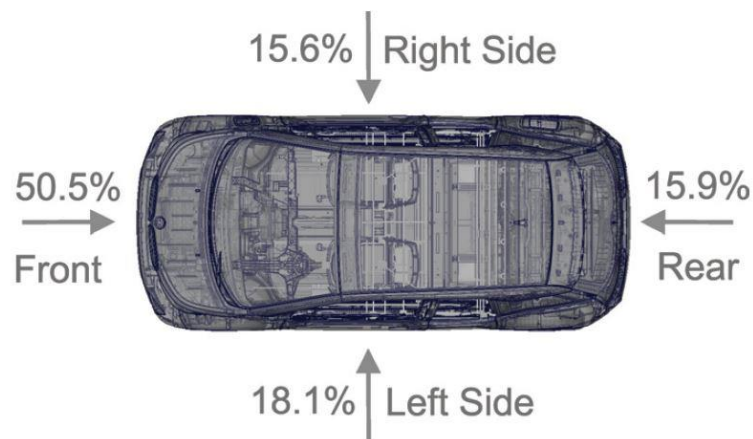


Figure 3.1: Distribution of crash positions [3]

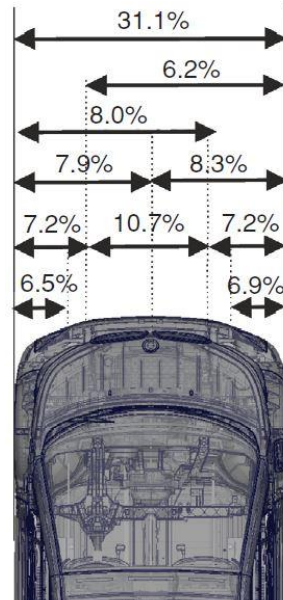


Figure 3.2: Distribution of frontal crash positions [3]

There are different standards available to assess the crashworthiness of vehicle structure that the main groups of them will discuss briefly. The load path which determine the force distribution through the vehicle structure for frontal, side and roof crash occurrences is presented in Figure 3.3.

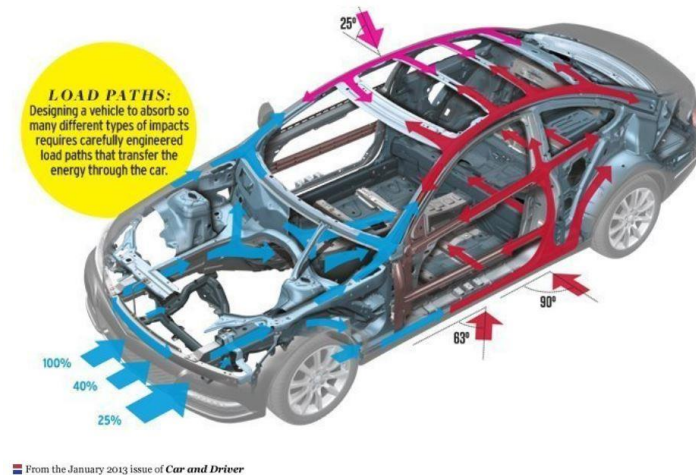


Figure 3.3: Schematic of load paths during different types of impact

FMVSS standard 208 as shown in Figure 3.4, related to assessment of vehicle frontal crash in collision with the rigid barrier with the initial velocity of 30 mph. In this test several load cells are set on the barrier face to monitor the impact force-time history and sensors on dummies to measure the crash pulses. This test can be done based on the NCAP requirements with the initial velocity of 35 mph. Another types of vehicle frontal crashworthiness assessment related to the vehicle frontal offset impact with 20 to 50 percent overlap with the initial velocity of 40 mph are shown in Figures 3.5 and 3.6. The other possibilities for evaluating the vehicle frontal crashworthiness is presented in Table 3.1.



Figure 3.4: Schematic of full frontal crash test



Figure 3.5: Schematic of 20% frontal offset crash

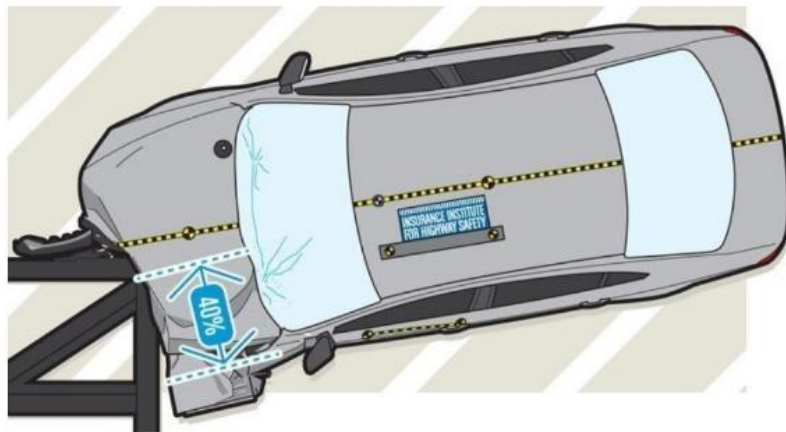


Figure 3.6: Schematic of 40% frontal offset crash

Table 3.1: Overview of European and United States crash tests for front events [4]

Test Name	ECE R94	EuroNCAP	FMVSS 208	FMVSS 208	FMVSS 301; 305	USNCAP	IIHS	IIHS
Load case	Offset front	Offset front	Full width front	Offset front	30° front	Full width frontal	Offset front	Small Overlap
Test Speed	56 km/h	64 km/h	32 - 56 km/h	40 km/h	48 km/h	56 km/h	64.4 km/h	64.4 km/h
Barrier	progressive	progressive	rigid	starr	rigid barrier	rigid barrier	progressive	rigid barrier
Impact Angle	0°	0°	0°	0°	0°	0°	0°	0°
Overlap	40 - 50%	40 - 50%	100%	40%	100%	100%	40%	25%
Belted / Unbelted	B	B	B & U	B	B	B	B	B
Symbol								

In FMVSS 214 for evaluating the performance of vehicle structure in the case of side crash, the moving barrier with the mass of 3000 pound and the initial

speed of 30 mph is impacted to the vehicle at the angle of 63° . The IIHS standard implements the test at the angle of 90° between the vehicle and the moving barrier. The schematic of side crash is shown in Figure 3.7.



Figure 3.7: Schematic of side crash test

In order to evaluate the performance of the vehicle rear part, the standard test of FMVSS 301 is implemented as shown in Figure 3.8. In this test the moving barrier with the mass of 4000 pound and initial speed of 30 mph is impacted to the stationary vehicle with the full tank to assess the major damage to the fuel tank.

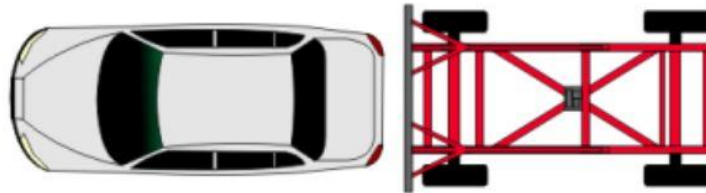


Figure 3.8: Schematic of rear crash test

The vehicle roof strength is measured through the FMVSS 216 test as shown in Figure 3.9. In this test the quasi-static load is subjected to the vehicle roof structure by a rigid puncher and the amount of intrusion and force-time history are recorded [5].

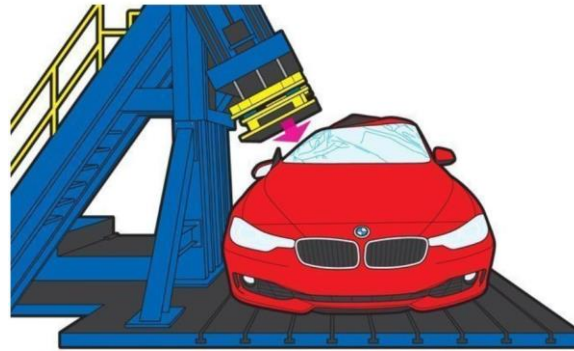


Figure 3.9: Schematic of roof crush test

3.3 Vehicle structure collapse modes

There are two main challenges of energy absorption and crash resistance in vehicle structures design through the crash tests. Vehicle structural members are usually considered as column or beam. In order to clarify the difference between the two concepts of structural members called column or beam, it is necessary to mention that the member which is loaded axially due to the compression load is called column and the member loaded by bending or combination of bending and axial loads is called beam. Pure axial deformation only occurs only in the case of full frontal and rear crashes or slightly off-angle impacts while most vehicle structures encounter with the combined axial and bending deformations during the crash. It is worth to note that, torsion is also another structural deformation mode which is quite likely during the crash. The sheet metal panels usually deform by irregular folding or crumpling [1].

Axial collapse mode is the most effective mechanism for energy absorption and it is the rarest type of deformation during the crash, while the bending mode leads to appearance of local hinges absorbs lower amount of energy. The axial and bending modes of metallic vehicle structures are shown in Figures 3.10 and 3.11.



Figure 3.10: Axial collapse mode [1]

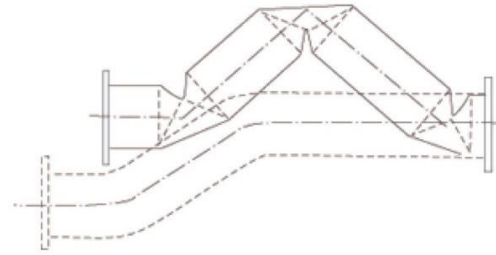


Figure 3.11: Bending collapse mode [1]

3.4 Test methodologies

In order to evaluate the behavior of material in the crush tests, the two typical tests of quasi-static and impact are implemented.

3.4.1 Quasi-static test

In quasi-static test the specimen is crushed at the constant speed. Although quasi-static test is not able to simulate the real crash condition due to not considering of material strain rate effects, because of simple and low cost set up is a common method to evaluate the energy absorption capacity of the structures. It is worth to mention that using quasi-static method, it is possible to capture the failure mechanism of the structure due to the long period of the procedure which is impossible in the case of impact test.

3.4.2 Impact Test

Impact test is implemented in order to simulate the actual crash condition. In this test in contrast to the quasi-static test, the speed is not constant and it decreases from the initial speed during the procedure; so it is able to consider all the strain-rate effects of material. This test is completed in just a fraction of second so it is necessary to use high speed camera and sensors to follow the test and this issue increases the cost of the impact test [6, 7].

3.5 Structures energy absorption metrics

In order to evaluate the crashworthiness of the structures, it is necessary to introduce the most important parameters for measuring the energy absorption of the components. The typical parameters are the specific energy absorption (SEA), the crush force efficiency (CFE) and the sustained crush stress (SCS). The SEA is calculated by Eq. 3.1:

$$SEA = \frac{W}{\rho A \delta} = \frac{\int_0^{\delta} F d\delta}{\rho A \delta} = SCS \quad \text{Eq. 3.1}$$

W is the total absorbed energy, ρ the material density, A the cross-section, δ the total crush displacement and F the crush force. In most cases F is also equal to the mean force as shown in Figure 3.12; the SEA is also referred to as the specific sustained crush stress (SSCS). The CFE is the ratio of maximum to mean force at Eq. 3.2, where the mean force can be calculated from the SEA or from the stable load after the initial peak as shown in Figure 3.12. The peak force is related to the elastic properties of the structure before fracture, while the mean force obtained during the stable permanent deformation in the structure leading to energy dissipation [4]. There is also a parameter called the load uniformity index (LU) which is inverse of CFE.

$$CFE = \frac{F_{\text{Mean}}}{F_{\text{Peak}}} = \frac{1}{LU} \quad \text{Eq. 3.2}$$

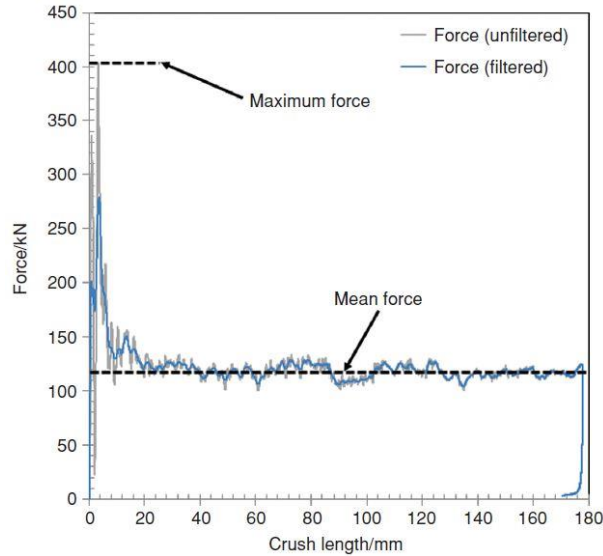


Figure 3.12: Example of the force-displacement curve for a composite specimen [4]

The ideal value of CFE is the one near the 1 and the reason is that the CFE value close to 1 shows that after the elastic deformation, the structure fails at the constant load with the peak load. Close mean force to the peak force means that

energy is dissipated in the structure with a controllable manner. For typical quasi-static tests the CFE values from 0.6 to 0.8 have been considered as optimum values for effective structures, while in dynamic tests this value as low as 0.4. The sustained crush stress as the other important crashworthiness factor is calculated by Eq. 3.3:

$$SCS = \frac{F_{Mean}}{A} \quad \text{Eq. 3.3}$$

3.6 Composite crashworthiness

3.6.1 Introduction

Composite materials show different behavior from what it was observed for metallic structures; instead of buckling and folding that observed in metallic structures due to the plastic deformation under the compression loading, composite structures fail through various mechanism modes due to their brittle nature. The comparison of metallic and composite tubes during axial compressive loading is presented in Figure 3.13 [4]. The failure mechanism of composite include of fiber fracture, matrix cracking, fiber-matrix debonding, delamination and interplay separation. Generally composite failure modes are divided into the two main categories of catastrophic and progressive modes.



Figure 3.13: Comparison of metallic specimen folding and composite specimen fracture [4]

3.6.2 Catastrophic failure modes

Composite catastrophic failure modes are not of interest for crashworthiness design of structures due to its low energy absorption. This is due to the fact that during the catastrophic failure a sudden increase in load to the peak value is followed by a low post failure load. The early rising of the load peak along with the low energy absorption turns this type of composite failure mode to the undesirable one [7, 8].

3.6.3 Progressive failure modes

As soon as progressive failure occurs in the composite structure, the peak load increases until the initiation of the failure and followed by a gradual decreasing trend. This manner helps to improve the energy absorption in structures faced with the progressive failure. Due to high energy absorption capacity during the progressive failure, there is no need to increase the structure weigh. Progressive failure is controlled by triggers in a stable manner. Triggers are stress concentrators that control the structure deformation and help to initiate the failure in a specific location, so they prevent the global buckling and appearance of the high peak load [7, 9]. The schematic of load-displacement history for the composite structure during the catastrophic and progressive failure is shown in Figure 3.14 [10]. The four modes of composite progressive crushing are presented at below.

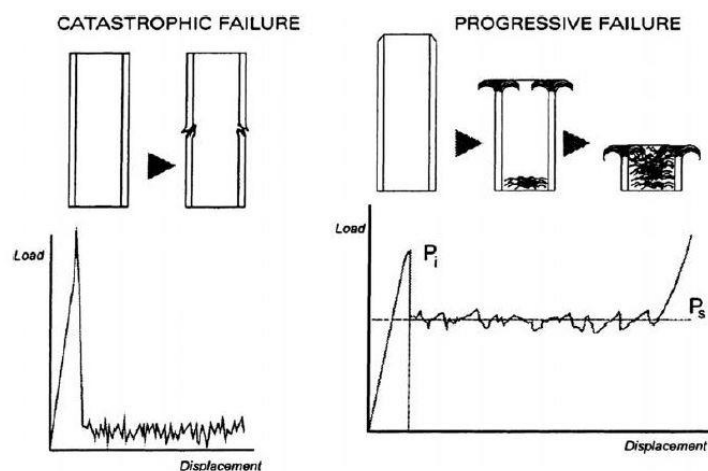


Figure 3.14: Typical load–displacement profiles of catastrophic and progressive axial compressive failures [10]

3.6.3.1 Transverse shearing or fragmentation mode

Through the transverse shearing or fragmentation failure mode as shown in Figure 3.15, a wedge-shaped laminate cross-section with one or multiple short interlaminar and longitudinal cracks forming the partial lamina bundles is created. cracks length and location depend on the material properties and the absorbed energy through the fracturing of the lamina bundles [8]. Lamina bundles as load resistant columns fragment causing the longitudinal and interlamina cracks length to be less than that of the lamina under the loading.

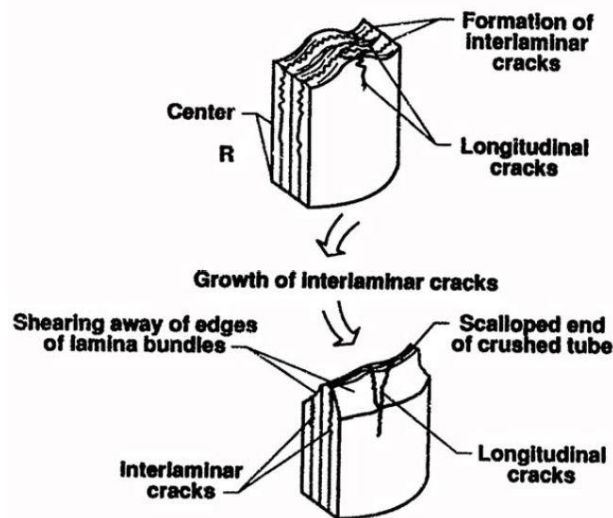


Figure 3.15: Crushing characteristics of transverse shearing failure mode [11]

3.6.3.2 Lamina bending or splaying mode

This failure mode is determined by long interlamina, intralamina and parallel to fiber cracks as shown in Figure 3.16. The main energy absorption mechanism is lamina bundles fracturing. The lamina bundles exhibit bending deformation or splaying and do not fracture as in the transverse shearing mode. When the laminas bend, two secondary energy absorption mechanisms, which are associated to friction, occur as a result of the sliding bundle and the loading surface.

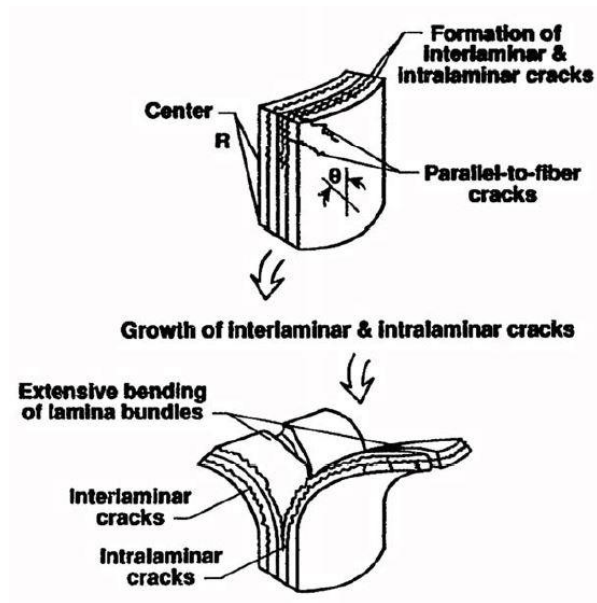


Figure 3.16: Crushing characteristics of lamina bending failure mode [11]

3.6.3.3 Brittle fracturing

The brittle fracturing mode is a combination of transverse shearing/fragmentation mode and lamina bending as shown in Figure 3.17. Interlamina cracks appeared in brittle fracturing mode are longer than those created in fragmentation mode but shorter than those in the lamina bending mode. In this way, the energy absorption mechanism is the mix of the two failure mechanisms.

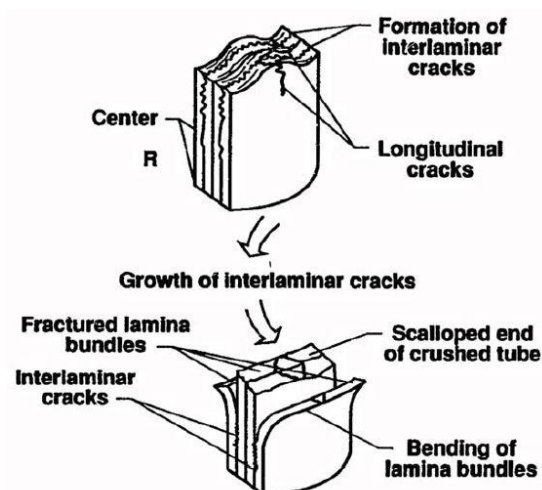


Figure 3.17: Crushing characteristics of brittle fracturing failure mode [11]

3.6.3.4 Local buckling or progressive folding

Local buckles caused by material plastic deformation are created in this failure mode as shown in Figure 3.18. In this failure mode, composite materials exhibit both brittle and ductile behaviors. Due to fiber and matrix plastic deformation and fiber splitting occurring in the material, most fiber-reinforced composites remain intact after being crushed. However, under high stress brittle fiber reinforced composites exhibit local buckling crushing mode while the matrix exhibit plastic deformation. Mechanisms like plastic yielding of the fiber and matrix control the crushing process for progressive folding.

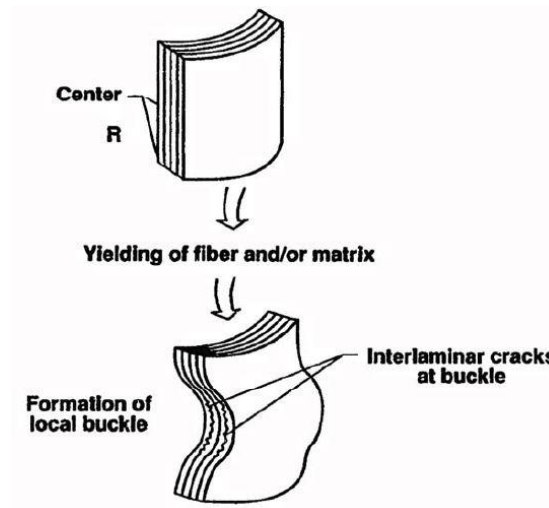


Figure 3.18: Crushing characteristics of local buckling failure mode [11]

3.6.4 Parameters affecting the energy absorption of composite structure

Energy absorption of composite structures during the loading can be affected by various parameters as they are described in the following [4].

3.6.4.1 Fiber Material

Different types of fiber such as carbon, glass, aramid, polyethylene are used in automotive industry. Also natural fibers such as cotton or hemp gained attention due to strict recycling requirements in vehicle industries. Glass and carbon fiber reinforced tubes tend to crush in brittle fracture, through splaying, fragmentation or a combination of the two while aramid, polyethylene and steel fiber reinforced structures are progressively folded due to ductile deformation.

3.6.4.2 Matrix Material

Thermoplastic matrixes due to their high fracture toughness is desirable for energy absorbing structures in comparison with thermoset matrixes [12]. So the matrix toughness is an important factor for constituting composite structures with higher SEA.

3.6.4.3 Fiber Volume Fraction

Generally by increasing the fiber volume fraction the energy absorption capacity of composite materials improves but not for all kinds of fibers. It has been reported that [13] the specific energy absorption for glass fiber rods, made of long or continues fibers, increased when the fiber volume fraction increased from 10 to 40%. In the case of using the chopped short fiber tubes [14], increasing fiber volume fraction beyond the certain level leads to decreasing the SEA.

3.6.4.4 Fiber Architecture

Fiber architecture refers to the effects of the fiber arrangement, such as unidirectional, woven or braided on the SEA of composite structures. It has been reported [15, 16] that woven and braided reinforced structures have higher SEA than those with unidirectional fibers. This behavior of the woven and braided materials is due to the through-thickness reinforcing effect of the individual layers crimp. During the progressive folding deformation, the plies are separated and then bent to the sides or crushed in the middle causing high SEA.

3.6.4.5 Trigger

Triggers are stress concentrators that control the structure deformation and help to initiate the failure in a specific location. Triggers are divided into the two categories of geometrical and non-geometrical. Geometrical grippers such as chamfer, bevels, grooves, and holes are used to initiate the progressive failure while non-geometric trigger means applying ply drops and fiber layup orientation in the specimen. Based on the results reported in [17], while the chamfer trigger yielded higher mean loads for round specimens, the tulip trigger yielded higher mean loads for rectangular specimens.

3.6.4.6 Geometry

The proportion of thickness to diameter of tubes (t/D) is an important geometrical factors that can affect the SEA due to determining the tendency of tubes for global or local buckling deformations. This parameter is measured for non-circular cross-section tubes by defining the proportion of tube thickness to contact area or the structure moment of inertia. It was approved that, the SEA increases when t/D ratio is between 0.05-0.1 and out of this range the SEA of composite structures reduces. This can be explained assuming unstable collapse below 0.05 and changes in crush zone morphology above 0.10. Also it is worth to mention that. Usually rounded tubes have higher specific energy absorption than the rectangular tubes and this can be explained with the more uniform loading of round

specimens and the hoop constraints imparted by transverse layers on the perimeter that can act to support axial fibers in the center of the layup.

3.6.4.7 Test Speed and Direction

Composite materials exhibit a strain stiffening behavior; during the progressive crushing, structures under dynamic loading absorb more energy than those under the quasi-static loading. Also it is necessary to take into consideration that structures under the axial compressive loading absorb more energy than those under the bending forces.

3.6.5 Hooke's law for linear isotropic material

For a linear isotropic material in a three-dimensional stress state, the Hooke's law stress-strain relationships at a point in an x - y - z orthogonal system can be expressed in matrix form as following in Eqs. 3.4 and 3.5 [18]:

$$\begin{bmatrix} \varepsilon_x \\ \varepsilon_y \\ \varepsilon_z \\ \gamma_{yz} \\ \gamma_{zx} \\ \gamma_{xy} \end{bmatrix} = \begin{bmatrix} \frac{1}{E} & \frac{-\nu}{E} & \frac{-\nu}{E} & 0 & 0 & 0 \\ \frac{-\nu}{E} & \frac{1}{E} & \frac{-\nu}{E} & 0 & 0 & 0 \\ \frac{-\nu}{E} & \frac{-\nu}{E} & \frac{1}{E} & 0 & 0 & 0 \\ 0 & 0 & 0 & \frac{1}{G} & 0 & 0 \\ 0 & 0 & 0 & 0 & \frac{1}{G} & 0 \\ 0 & 0 & 0 & 0 & 0 & \frac{1}{G} \end{bmatrix} \begin{bmatrix} \sigma_x \\ \sigma_y \\ \sigma_z \\ \tau_{yz} \\ \tau_{zx} \\ \tau_{xy} \end{bmatrix} \quad \text{Eq. 3.4}$$

$$\begin{bmatrix} \sigma_x \\ \sigma_y \\ \sigma_z \\ \tau_{yz} \\ \tau_{zx} \\ \tau_{xy} \end{bmatrix} = \begin{bmatrix} \frac{E(1-\nu)}{(1-2\nu)(1+\nu)} & \frac{\nu E}{(1-2\nu)(1+\nu)} & \frac{\nu E}{(1-2\nu)(1+\nu)} & 0 & 0 & 0 \\ \frac{\nu E}{(1-2\nu)(1+\nu)} & \frac{E(1-\nu)}{(1-2\nu)(1+\nu)} & \frac{\nu E}{(1-2\nu)(1+\nu)} & 0 & 0 & 0 \\ \frac{\nu E}{(1-2\nu)(1+\nu)} & \frac{\nu E}{(1-2\nu)(1+\nu)} & \frac{E(1-\nu)}{(1-2\nu)(1+\nu)} & 0 & 0 & 0 \\ 0 & 0 & 0 & G & 0 & 0 \\ 0 & 0 & 0 & 0 & G & 0 \\ 0 & 0 & 0 & 0 & 0 & G \end{bmatrix} \begin{bmatrix} \varepsilon_x \\ \varepsilon_y \\ \varepsilon_z \\ \gamma_{yz} \\ \gamma_{zx} \\ \gamma_{xy} \end{bmatrix} \quad \text{Eq. 3.5}$$

ν is the Poisson's ratio and G is the shear modulus which is a function of two elastic constants, E and ν , as in Eq. 3.6:

$$G = \frac{E}{2(1+\nu)} \quad \text{Eq. 3.6}$$

The 6×6 matrix in Equation 3.4 is called the compliance matrix $[S]$ of an isotropic material while 6×6 matrix in Equation 3.5, obtained by inverting the compliance matrix in Equation 3.4, is called the stiffness matrix $[C]$ of an isotropic material.

3.6.6 General format of Hooke's law for different types of materials

The stress–strain relationship for materials which are not linearly elastic and isotropic are more complicated than Equations 3.4 and 3.5 [18]. The most general stress–strain relationship for a three-dimensional body in a 1–2–3 Cartesian coordinate system is given as in Eqs. 3.7 and 3.8:

$$\begin{bmatrix} \sigma_1 \\ \sigma_2 \\ \sigma_3 \\ \tau_{23} \\ \tau_{31} \\ \tau_{12} \end{bmatrix} = \begin{bmatrix} C_{11} & C_{12} & C_{13} & C_{14} & C_{15} & C_{16} \\ C_{21} & C_{22} & C_{23} & C_{24} & C_{25} & C_{26} \\ C_{31} & C_{32} & C_{33} & C_{34} & C_{35} & C_{36} \\ C_{41} & C_{42} & C_{43} & C_{44} & C_{45} & C_{46} \\ C_{51} & C_{52} & C_{53} & C_{54} & C_{55} & C_{56} \\ C_{61} & C_{62} & C_{63} & C_{64} & C_{65} & C_{66} \end{bmatrix} \begin{bmatrix} \varepsilon_1 \\ \varepsilon_2 \\ \varepsilon_3 \\ \gamma_{23} \\ \gamma_{31} \\ \gamma_{12} \end{bmatrix} \quad \text{Eq. 3.7}$$

The 6×6 $[C]$ matrix is the stiffness matrix to determine the general strain–stress relationship for a three dimensional body in a 1–2–3 orthogonal Cartesian coordinate system and has 36 constants. By inverting Equation 3.7, the compliance matrix is obtained as in Eq. 3.8:

$$\begin{bmatrix} \varepsilon_1 \\ \varepsilon_2 \\ \varepsilon_3 \\ \gamma_{23} \\ \gamma_{31} \\ \gamma_{12} \end{bmatrix} = \begin{bmatrix} S_{11} & S_{12} & S_{13} & S_{14} & S_{15} & S_{16} \\ S_{21} & S_{22} & S_{23} & S_{24} & S_{25} & S_{26} \\ S_{31} & S_{32} & S_{33} & S_{34} & S_{35} & S_{36} \\ S_{41} & S_{42} & S_{43} & S_{44} & S_{45} & S_{46} \\ S_{51} & S_{52} & S_{53} & S_{54} & S_{55} & S_{56} \\ S_{61} & S_{62} & S_{63} & S_{64} & S_{65} & S_{66} \end{bmatrix} \begin{bmatrix} \sigma_1 \\ \sigma_2 \\ \sigma_3 \\ \tau_{23} \\ \tau_{31} \\ \tau_{12} \end{bmatrix} \quad \text{Eq. 3.8}$$

3.6.6.1 Anisotropic material

The anisotropic material has 21 independent elastic constants at a specific point. Once these constants are found for a particular point, the stress and strain relationship can be developed at that point.

3.6.6.2 Monoclinic material

If, in one plane of material symmetry one of the coordinate system direction is normal to the plane of material symmetry as direction 3 in Figure 3.19, then the stiffness matrix reduces to Eq. 3.9.

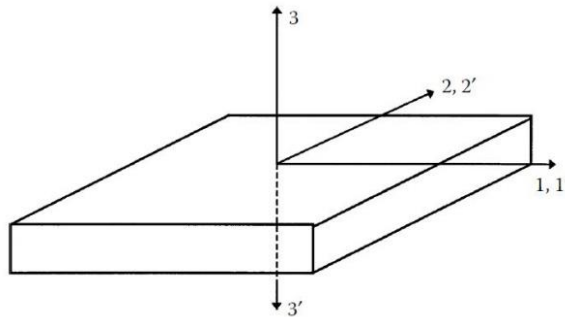


Figure 3.19. Transformation of coordinate axes for 1–2 plane of symmetry for a monoclinic material

$$[C] = \begin{bmatrix} C_{11} & C_{12} & C_{13} & 0 & 0 & C_{16} \\ C_{12} & C_{22} & C_{23} & 0 & 0 & C_{26} \\ C_{13} & C_{23} & C_{33} & 0 & 0 & C_{36} \\ 0 & 0 & 0 & C_{44} & C_{45} & 0 \\ 0 & 0 & 0 & C_{45} & C_{55} & 0 \\ C_{16} & C_{26} & C_{36} & 0 & 0 & C_{66} \end{bmatrix} \quad \text{Eq. 3.9}$$

where $C_{14}=0$, $C_{15}=0$, $C_{24}=0$, $C_{25}=0$, $C_{34}=0$, $C_{35}=0$, $C_{46}=0$, $C_{56}=0$.

The direction perpendicular to the plane of symmetry is called the principal direction. The monoclinic material has 13 independent elastic constants. Example of the monoclinic material is Feldspar which is the most abundant group of minerals in the earth's crust, forming about 60% of rocks. The compliance matrix also reduces as in Eq. 3.10.

$$[S] = \begin{bmatrix} S_{11} & S_{12} & S_{13} & 0 & 0 & S_{16} \\ S_{12} & S_{22} & S_{23} & 0 & 0 & S_{26} \\ S_{13} & S_{23} & S_{33} & 0 & 0 & S_{36} \\ 0 & 0 & 0 & S_{44} & S_{45} & 0 \\ 0 & 0 & 0 & S_{45} & S_{55} & 0 \\ S_{16} & S_{26} & S_{36} & 0 & 0 & S_{66} \end{bmatrix} \quad \text{Eq. 3.10}$$

3.6.6.3 Orthotropic material (orthogonally anisotropic)

If a material has three mutually perpendicular planes of material symmetry, then the nine independent elastic constants are present and the stiffness matrix is given by Eq. 3.11 and the compliance matrix by Eq. 3.12.

$$[C] = \begin{bmatrix} C_{11} & C_{12} & C_{13} & 0 & 0 & 0 \\ C_{12} & C_{22} & C_{23} & 0 & 0 & 0 \\ C_{13} & C_{23} & C_{33} & 0 & 0 & 0 \\ 0 & 0 & 0 & C_{44} & 0 & 0 \\ 0 & 0 & 0 & 0 & C_{55} & 0 \\ 0 & 0 & 0 & 0 & 0 & C_{66} \end{bmatrix} \quad \text{Eq. 3.11}$$

where $C_{16}=0$, $C_{26}=0$, $C_{36}=0$, $C_{45}=0$.

Examples of an orthotropic material is a single lamina made of continuous fiber composite arranged in a rectangular array as shown in Figure 3.20.

$$[S] = \begin{bmatrix} S_{11} & S_{12} & S_{13} & 0 & 0 & 0 \\ S_{12} & S_{22} & S_{23} & 0 & 0 & 0 \\ S_{13} & S_{23} & S_{33} & 0 & 0 & 0 \\ 0 & 0 & 0 & S_{44} & 0 & 0 \\ 0 & 0 & 0 & 0 & S_{55} & 0 \\ 0 & 0 & 0 & 0 & 0 & S_{66} \end{bmatrix} \quad \text{Eq. 3.12}$$

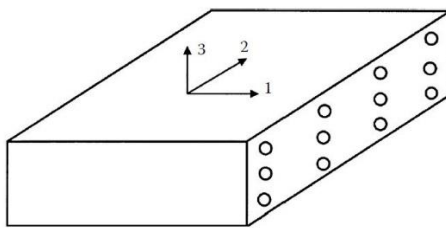


Figure 3.20: A unidirectional lamina as a monoclinic material with fibers, arranged in a rectangular array

3.6.6.4 Transversely isotropic material

Consider a plane of material isotropy in one of the planes of an orthotropic body. If direction 1 is normal to that plane (2–3) of isotropy, then the stiffness matrix is given by Eq. 3.13 and only five independent elastic constants remain.

$$[C] = \begin{bmatrix} C_{11} & C_{12} & C_{12} & 0 & 0 & 0 \\ C_{12} & C_{22} & C_{23} & 0 & 0 & 0 \\ C_{12} & C_{23} & C_{22} & 0 & 0 & 0 \\ 0 & 0 & 0 & \frac{C_{22}-C_{23}}{2} & 0 & 0 \\ 0 & 0 & 0 & 0 & C_{55} & 0 \\ 0 & 0 & 0 & 0 & 0 & C_{55} \end{bmatrix} \quad \text{Eq. 3.13}$$

where $C_{22} = C_{33}$, $C_{12} = C_{13}$, $C_{55} = C_{66}$, $C_{44} = \frac{C_{22} - C_{23}}{2}$

An example of transversely isotropic material is a unidirectional lamina in which the fibers are arranged in a square array or a hexagonal array as shown in Figure 3.21. In Figure 3.21, the fibers are in direction 1 and plane 2–3 will be considered as the plane of isotropy.

The compliance matrix reduces to Eq. 3.14 for transversely isotropic material.

$$[S] = \begin{bmatrix} S_{11} & S_{12} & S_{12} & 0 & 0 & 0 \\ S_{12} & S_{22} & S_{23} & 0 & 0 & 0 \\ S_{12} & S_{23} & S_{22} & 0 & 0 & 0 \\ 0 & 0 & 0 & 2(S_{22} - S_{23}) & 0 & 0 \\ 0 & 0 & 0 & 0 & S_{55} & 0 \\ 0 & 0 & 0 & 0 & 0 & S_{55} \end{bmatrix} \quad \text{Eq. 3.14}$$

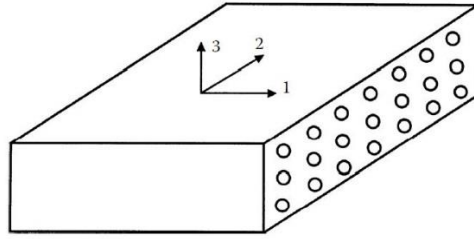


Figure 3.21: A unidirectional lamina as a transversely isotropic material with fibers arranged in a square array

3.6.6.5 Isotropic material

If an orthotropic body has all identical planes then it is called an isotropic material. It has only two independent constants and its stiffness matrix is reduced to Eq. 3.15:

$$[C] = \begin{bmatrix} C_{11} & C_{12} & C_{12} & 0 & 0 & 0 \\ C_{12} & C_{11} & C_{12} & 0 & 0 & 0 \\ C_{12} & C_{12} & C_{11} & 0 & 0 & 0 \\ 0 & 0 & 0 & \frac{C_{11}-C_{12}}{2} & 0 & 0 \\ 0 & 0 & 0 & 0 & \frac{C_{11}-C_{12}}{2} & 0 \\ 0 & 0 & 0 & 0 & 0 & \frac{C_{11}-C_{12}}{2} \end{bmatrix} \quad \text{Eq. 3.15}$$

where $C_{11} = C_{22}$, $C_{12} = C_{23}$, $C_{66} = \frac{C_{22} - C_{23}}{2} = \frac{C_{11} - C_{12}}{2}$.

and

$$C_{11} = \frac{E(1-\nu)}{(1-2\nu)(1+\nu)} \quad \text{Eq. 3.16}$$

$$C_{12} = \frac{\nu E}{(1-2\nu)(1+\nu)} \quad \text{Eq. 3.17}$$

Examples of isotropic material are the common materials such as steel, iron, and aluminum.

3.6.7 Failure theories of a lamina

In order to analyze the strength of composite layers, failure analyses should be applied. Different types of failure analyses can be used for evaluating the strength of composites. The theories are generally based on the normal and shear strengths of a unidirectional lamina.

Generally failure criteria are divided into two main branches: independent (non-interactive) criteria and interactive criteria. Although independent criteria such as maximum stress and maximum strain can be simply applied and investigate mode of failure, these analyses neglect the effects of stress interactions. Interactive criteria such as Tsai-Wu, Tsai-Hill, Chang and Hashin include stress interactions in failure mechanism and are applying for predicting first-ply failure [19].

There are two material axes in unidirectional lamina; the axis which is parallel to the fibers direction and the one perpendicular to the fibers direction. Thus, there are five strength parameters for a unidirectional lamina; compression and tension strength in fiber direction, compression and tension strength perpendicular to fiber direction and the shear strength. The five strength parameters of a unidirectional lamina are:

$(\sigma_1^T)_{\text{ult}}$ = Ultimate longitudinal tensile strength in direction 1

$(\sigma_1^C)_{\text{ult}}$ = Ultimate longitudinal compressive strength in direction 1

$(\sigma_2^T)_{\text{ult}}$ = Ultimate transverse tensile strength in direction 2

$(\sigma_2^C)_{\text{ult}}$ = Ultimate transverse compressive strength in direction 2

$(\tau_{12})_{\text{ult}}$ = Ultimate in-plane shear strength in plane 12

3.6.7.1 Maximum stress failure theory

This theory is related to the maximum normal stress theory by Rankine and the maximum shearing stress theory by Tresca [18]. The stresses acting on a lamina are divided into the normal and shear stresses in the local axes. Using Eq. 3.18 it is possible to transform the given global stresses or strains of a lamina to the corresponding ones in the material axes; where [T] is called the transformation matrix. If normal or shear stresses in the local axes of a lamina is equal to or

beyond the corresponding ultimate strengths of the unidirectional lamina, then it is possible to predict the failure in a lamina as shown in Eq. 3.19:

$$\begin{bmatrix} \sigma_x \\ \sigma_y \\ \sigma_z \end{bmatrix} = [T]^{-1} \begin{bmatrix} \sigma_1 \\ \sigma_2 \\ \sigma_z \end{bmatrix} \quad \text{Eq. 3.18}$$

The lamina is failed if the following unequal are violated.

$$\begin{aligned} -(\sigma_1^C)_{\text{ult}} < \sigma_1 < (\sigma_1^T)_{\text{ult}}, \text{ or} \\ -(\sigma_2^C)_{\text{ult}} < \sigma_2 < (\sigma_2^T)_{\text{ult}}, \text{ or} \\ -(\tau_{12})_{\text{ult}} < \tau_{12} < (\tau_{12})_{\text{ult}} \end{aligned} \quad \text{Eq. 3.19}$$

3.6.7.2 Maximum strain failure theory

This theory is based on the maximum normal strain theory by St. Venant and the maximum shear stress theory by Tresca. The strains applied to a lamina are resolved to strains in the local axes. If normal or shearing strains in the local axes of a lamina equal or exceed the corresponding ultimate strains of the unidirectional lamina then the failure occurs [18]. Failure occurs in lamina if Eq. 3.20 is violated.

$$\begin{aligned} -(\varepsilon_1^C)_{\text{ult}} < \varepsilon_1 < (\varepsilon_1^T)_{\text{ult}}, \text{ or} \\ -(\varepsilon_2^C)_{\text{ult}} < \varepsilon_2 < (\varepsilon_2^T)_{\text{ult}}, \text{ or} \\ -(\gamma_{12})_{\text{ult}} < \gamma_{12} < (\gamma_{12})_{\text{ult}} \end{aligned} \quad \text{Eq. 3.20}$$

3.6.7.3 Tsai-Wu failure criterion

This failure theory is based on the total strain energy failure theory of Beltrami. Satisfying the following equality (Eq. 3.21) is essential for Tsai-Wu theory to predict failure in an orthotropic lamina under plane stress condition:

$$F_1\sigma_{11} + F_2\sigma_{22} + F_6\tau_{12} + F_{11}\sigma_{11}^2 + F_{22}\sigma_{22}^2 + F_{66}\tau_{12}^2 + 2F_{12}\sigma_{11}\sigma_{22} \geq 1 \quad \text{Eq. 3.21}$$

Elastic characteristics should be defined with four independent elastic constants ($E_{11}, E_{22}, G_{12}, \nu_{12}$). Strength properties are divided into five independent strength properties:

X_t = longitudinal tensile strength

Y_t = transverse tensile strength

X_c = longitudinal compressive strength

Y_c = transverse compressive strength

S = in-plane shear strength

F_1, F_2 are the strength coefficients and are given by, it should be considered that F_1, F_2, F_{11}, F_{22} and F_{66} can be calculated by using the tensile, compressive and shear strength properties in the principal material directions.

$$F_1 = \frac{1}{X_t} - \frac{1}{X_c}, \quad F_2 = \frac{1}{Y_t} - \frac{1}{Y_c}, \quad F_6 = 0$$

$$F_{11} = -\frac{1}{X_t X_c}, \quad F_{22} = -\frac{1}{Y_t Y_c}, \quad F_{66} = -\frac{1}{S^2}$$

F_{12} is a strength interaction term between σ_{11} and σ_{22} which can be determined with a suitable biaxial test. Since it is not always easy to perform biaxial tests, it is necessary to determine an approximate range of value for F_{12} . The approximate range of F_{12} is as following in Eq. 3.22:

$$-\frac{1}{2}\sqrt{F_{11}F_{22}} \leq F_{12} \leq 0 \quad \text{Eq. 3.22}$$

The lower limit of Eq. 3.19 is frequently used for F_{12} [19-23].

3.6.7.4 Tsai-Hill failure criterion

This theory is based on the distortion energy failure theory of Von-Mises' distortional energy yield criterion for isotropic materials as applied to anisotropic materials. Distortion energy is a part of the total strain energy caused by changing in shape of a body. It is supposed that as soon as the distortion energy becomes greater than the failure distortion energy of the material failure occurs.

Tsai-Hill failure criterion can be explained as below [23, 24]:

$$F_{11}\sigma_{11}^2 + F_{22}\sigma_{22}^2 + F_{66}\tau_{12}^2 + 2F_{12}\sigma_{11}\sigma_{22} \geq 1 \quad \text{Eq. 3.23}$$

The strength parameters F_{11} , F_{22} , F_{66} and F_{12} are given by

$$F_{11} = \frac{1}{X^2}, \quad F_{22} = \frac{1}{Y^2}, \quad F_{66} = \frac{1}{S^2}, \quad F_{12} = -\frac{1}{2} \left(\frac{1}{X^2} + \frac{1}{Y^2} \right).$$

3.6.7.5 Chang-Chang failure criterion

The Chang-Chang failure criterion with degraded parameters are reported in Eqs. 3.24-3.27 [25].

- for the tensile fiber mode,

$$\sigma_{11} > 0 \quad \text{then} \quad e_f^2 = \left(\frac{\sigma_{11}}{X_t} \right)^2 + \beta \left(\frac{\sigma_{12}}{S} \right) - 1 \quad \left. \begin{array}{l} \geq 0 \text{ failed} \\ < 0 \text{ elastic} \end{array} \right\} \quad \text{Eq. 3.24}$$

if failure condition is reached then degradation of the elastic coefficients takes place according to

$$E_1 = E_2 = G_{12} = \nu_{21} = \nu_{12} = 0$$

- for the compressive fiber mode,

$$\sigma_{11} < 0 \quad \text{then} \quad e_c^2 = \left(\frac{\sigma_{11}}{X_c} \right)^2 - 1 \quad \left. \begin{array}{l} \geq 0 \text{ failed} \\ < 0 \text{ elastic} \end{array} \right\} \quad \text{Eq. 3.25}$$

if failure condition is reached then degradation of the elastic coefficients takes place according to

$$E_1 = \nu_{21} = \nu_{12} = 0$$

- for the tensile matrix mode,

$$\sigma_{22} > 0 \quad \text{then} \quad e_m^2 = \left(\frac{\sigma_{22}}{Y_t} \right)^2 + \left(\frac{\sigma_{12}}{S} \right)^2 - 1 \quad \left\{ \begin{array}{l} \geq 0 \text{ failed} \\ < 0 \text{ elastic} \end{array} \right\} \quad \text{Eq. 3.26}$$

if failure condition is reached then degradation of the elastic coefficients takes place according to

$$E_2 = \nu_{21} = 0 \rightarrow G_{12} = 0$$

- for the compressive matrix mode,

$$\sigma_{22} < 0 \quad \text{then} \quad e_d^2 = \left(\frac{\sigma_{22}}{2S} \right)^2 + \left[\left(\frac{Y_c}{2S} \right)^2 - 1 \right] \frac{\sigma_{22}}{Y_c} + \left(\frac{\sigma_{12}}{S} \right)^2 - 1 \quad \left\{ \begin{array}{l} \geq 0 \text{ failed} \\ < 0 \text{ elastic} \end{array} \right\} \quad \text{Eq. 3.27}$$

if failure condition is reached then degradation of the elastic coefficients takes place according to

$$E_2 = \nu_{21} = \nu_{12} = 0 \rightarrow G_{12} = 0$$

3.6.7.6 Hashin failure criterion

The hashin 3D failure criterion predicts the failure according to Eqs 3.28-3.31 [26].

-Tensile fiber mode

$$\left(\frac{\sigma_{11}}{X_t} \right) + \frac{1}{S^2} (\sigma_{12}^2 + \sigma_{13}^2) = 1 \quad \text{Eq. 3.28}$$

or

$$\sigma_{11} = X_t$$

-Compressive fiber mode

$$|\sigma_{11}| = X_c \quad \text{Eq. 3.29}$$

-Tensile matrix mode $\sigma_{22} + \sigma_{33} > 0$

$$\frac{1}{Y_t^2} (\sigma_{22} + \sigma_{33})^2 + \frac{1}{S_t^2} (\sigma_{23}^2 - \sigma_{22}\sigma_{33}) + \frac{1}{S^2} (\sigma_{12}^2 + \sigma_{13}^2) = 1 \quad \text{Eq. 3.30}$$

-Compressive matrix mode $\sigma_{22} + \sigma_{33} < 0$

$$\frac{1}{Y_c} \left[\left(\frac{Y_c}{2S_t} \right)^2 - 1 \right] (\sigma_{22} + \sigma_{33}) + \frac{1}{4S_t^2} (\sigma_{22} + \sigma_{33})^2 + \frac{1}{S_t^2} (\sigma_{23}^2 - \sigma_{22}\sigma_{33}) + \frac{1}{S^2} (\sigma_{12}^2 + \sigma_{13}^2) = 1$$

Eq. 3.31

in addition to the previous definitions, S_t represents the transverse shear strength, the allowable value of shear stress σ_{23} (the allowable value of σ_{13} is, as for σ_{12} , S).

3.7 Conclusion

Through this chapter different types of vehicle crash have been discussed and crashworthiness metrics have been introduced. Crashworthiness energy absorption characteristics and the typical modes of vehicle component deformation have been studied. Comparison of metallic and composite specimen's deformation modes has been discussed and parameters affecting the energy absorption capacity of composite material have been investigated. Composite materials do not deform plastically due to their brittle behavior while metallic structure has the possibility of folding plastically. Stress-strain relations for isotropic and non-isotropic material structures are calculated based on Hook's law. Various failure criteria of composite materials were presented and the material properties degradation were studied based on them.

3.8 References

- [1] Du Bois, P., Chou, C.C., Fileta, B.B., Khalil, T.B., King, A.I., Mahmood, H. F., et al. (2004). Vehicle crashworthiness and occupant protection.
- [2] Deb, A. (2010). Crashworthiness design issues for lightweight vehicles. In Mallick, P.K. (Eds), *Materials, design and manufacturing for lightweight vehicles* (pp. 332-355), Elsevier, USA.

- [3] Bakker, J. <http://gidas.org/en/willkommen> (Accessed July 2014).
- [4] Lukaszewicz, Dirk H.-J.A. (2013). Automotive Composite Structures for Crashworthiness. In Elmarakbi, A. (Eds), *Advanced composite materials for automotive applications: Structural integrity and crashworthiness*, Sunderland, UK, John Wiley & Sons.
- [5] <http://www.caranddriver.com/features/crash-course-how-current-impact-tests-make-cars-safer-feature> (Accessed October 2016).
- [6] Tobby, E., & Bahaadini, A. (2015). Design, analysis and verification of composite components subjected to crash load cases, master thesis, Blekinge Institute of Technology Karlskrona, Sweden.
- [7] Jacob, G.C. (2006). Automotive crashworthiness of adhesively bonded carbon fiber polymer composite structures. Ph.D. thesis, University of Tennessee, Knoxville.
- [8] Lazarus, S.D. (2004). Energy absorption for crashworthiness in carbon-fiber braided composite structures, PhD thesis, Cranfield University.
- [9] Thornton, P.H. (1979). Energy Absorption in Composite Structures. *Journal of Composite Materials*, 13(3), pp. 247–262.
- [10] Jimenez, M.A., Miravete, A, Larrode, E, Revuelta, D. (2000). Effect of trigger geometry on energy absorption in composite profiles. *Composite Structure*, vol. 48, pp. 107–11.
- [11] Farley G.L. and Jones R.M. (1989). Energy-absorption capability of composite tubes and beams, DTIC Document.
- [12] Cauchi Savona, S. and Hogg, P.J. (2006). Effect of fracture toughness properties on the crushing of flat composite plates. *Composite Science and Technology*, vol. 66, pp. 2317–2328.
- [13] Tao, W.H., Robertson, R.E. and Thornton, P.H. (1993). Effects of material properties and crush conditions on the energy absorption of fiber composite rods. *Composite Science and Technology*, vol. 47, pp. 405–418.
- [14] Jacob, G.C., Starbuck, J.M., Fellers, J.F. and Simunovic, S. (2005). Effect of fiber volume fraction, fiber length and fiber tow size on the energy absorption of

chopped carbon fiber-polymer composites. *Polymer Composites*, 26(3), pp. 293–305.

[15] Kim, J.S., Yoon, H.J. and Shin, K.B. (2011). A study on crushing behaviors of composite circular tubes with different reinforcing fibers. *International Journal of Impact Engineering*, 38(4), pp. 198–207.

[16] Bisagni, C., Di Pietro, G., Fraschini, L. and Terletti, D. (2005). Progressive crushing of fiber-reinforced composite structural components of a formula one racing car. *Composite Structures*, 60(4), pp. 391–402.

[17] Palanivelu, S., Van Paepegem, W., Degrieck, J. et al. (2010). Experimental study on the axial crushing behavior of pultruded composite tubes. *Polymer Testing*, 29(2), pp. 224–234.

[18] Kaw, A. K. (2005). *Mechanics of composite materials* CRC press, pp. 79-90.

[19] Onder, A. (2007). First failure pressure of composite pressure vessels. Master of Science Thesis, Graduate School of Natural and Applied Sciences of Dokuz Eylül University, Izmir.

[20] Chandrashekhara, K. (2008). Modeling of Composite Hydrogen Storage Cylinders using Finite Element Analysis, Technical report.

[21] Bhavya, S., Kumar, P. R., & Kalam, S. A. (2012). Failure analysis of a composite cylinder. *IOSR Journal of Mechanical and Civil Engineering (IOSR-JMCE)*, 3(3), pp. 1-7.

[22] Sinha, M., & Pandit, S. (2012). Maximum stress and burst pressure analysis of CFRP composite pressure vessel. *International Journal of Emerging trends in Engineering and Development*, 4(2), pp. 714-721.

[23] Xu, P., Zheng, J., & Liu, P. (2009). Finite element analysis of burst pressure of composite hydrogen storage vessels. *Materials & Design*, 30(7), pp. 2295-2301.

[24] Reddy, J., & Pandey, A. (1987). A first-ply failure analysis of composite laminates. *Computers & Structures*, 25(3), pp. 371-393.

[25] *Ls-dyna theory manual*, Hallquist J. O. (Ed.), California: Livermore Software Technology Corporation, 2006.

- [26] Paris, F., & Jackson, K.E. (2001). A study of failure criteria of fibrous composite materials, NASA/CR-2001-210661.

Chapter 4

Light-weight Design: Detailed Comparison of Roof Panel Solutions at Stiffness Analyses

4.1 Introduction

In this chapter, the general idea is to study the contribution of light-weight vehicle roof panel in the total vehicle stiffness and present a method to optimize the thickness which improves the vehicle structure efficiency.

After developing a benchmark for vehicle roof panel with respect to the most important factors of designing automotive panels, the chassis load path analysis under the bending and torsion loads will be done theoretically and numerically. Next, the chassis static and dynamic stiffness analyses based on the standards will be implemented. Then, the roof panel thickness with respect to the chassis weight and stiffness will be optimized for different material solutions.

4.2 Automotive panels' behavior under loading

Before starting to develop a benchmark for the vehicle roof panel it would be useful to mention about the difference of stiffness and strength; stiffness is defined when the small and elastic deformations occur due to the loading. Stiffness is defined only in elastic regions for the structures as the slope of the

load vs deflection curve as shown in Figure 4.1. Strength implies that no part of the structure will lose its function when it is subjected to loads [1, 2]. In other words, the strength implies to the maximum load where some permanent deformation is expected as shown in Figure 4.1.

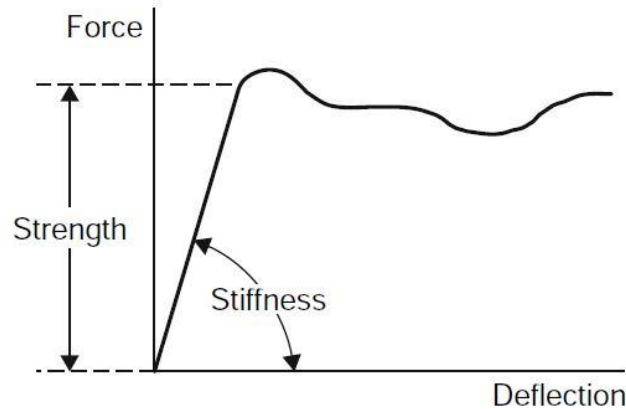


Figure 4.1: The concepts of stiffness and strength

The curved panel under the normal load shows different behavior as shown in Figure 4.2; at the first part of the graph, panel shows linear elastic behavior under the loading and the normal stiffness of the panel can be calculated as a proportion of subjected load to the respective vertical deformation. As loading increases, the panel curvature is inverted and this inversion can be soft in which the panel surface maintains its contact with the load puncher or it can be hard in which the panel surface loses its contact with the puncher and snaps over. The load which causes the hard snap over in panels is referred as critical buckling load or oil-canning resistance load. Dent resistance is measured as the minimum energy that causes permanent deformation in panels. Also the shear rigidity of the panel, which is defined as the proportion of the shear load value to the respective displacement of the panel under the loading, and the first bending frequencies of the panel are determined. The theoretical formula will be presented at the following section [2].

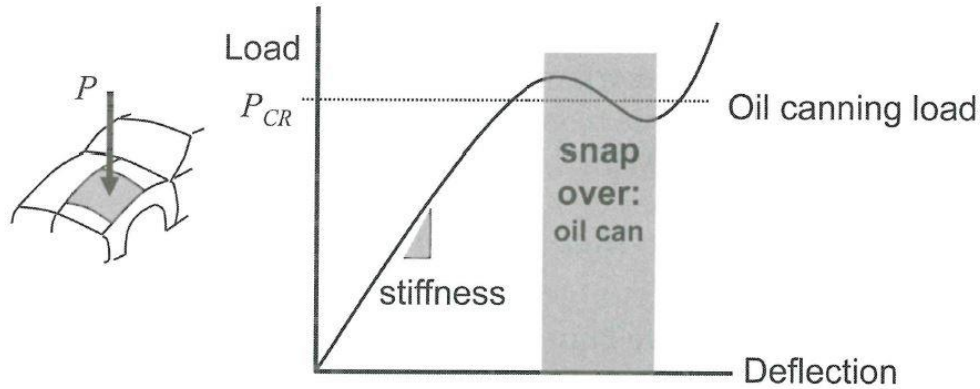


Figure 4.2: Curved panel behavior under the normal loading [2]

4.2.1 Bending stiffness of a panel

Bending stiffness of the automotive panels are estimated by FEM based on the proportion of the subjected load amount to the panel deformation value in elastic region of material behavior. The roof panel dimensions are clear in Figure 4.3. In the case of roof panel consideration, the roof panel is subjected to the distributed load (in order to prevent stress concentration) while the roof edges are constrained as shown in Figure 4.4. However there are some theoretical formulation by which it is possible to estimate the bending stiffness of automotive panels as presented at Eq. 4.1 [2]:

$$K = \frac{B}{R} \frac{Et^2}{\sqrt{1-\nu^2}} \quad \text{Eq.4.1}$$

where R is the spherical radius, B is a constant equals to 2.309, E is the Young's modulus, ν is the Poisson's ratio and t is the panel thickness.

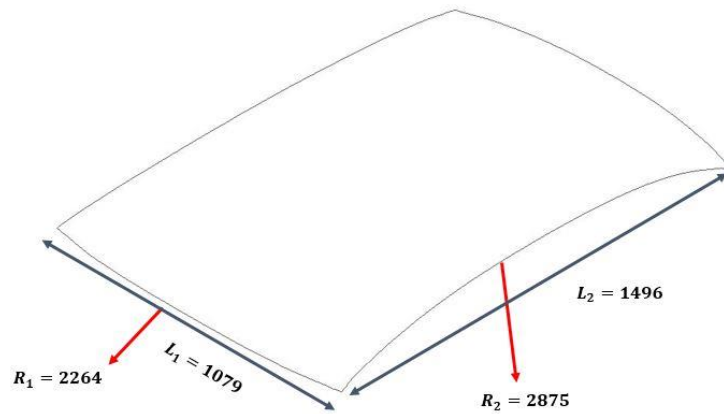


Figure 4.3: Roof panel dimensions

Due to the fact that most of the automotive panels are doubly curved panels, it is necessary to calculate the equivalent radius as in Eq. 4.2 to substitute in Eq. 4.1:

$$\frac{1}{R_{EQ}} = \frac{\left(\frac{L_1^2}{R_1}\right) + \left(\frac{L_2^2}{R_2}\right)}{2L_1L_2} \quad \text{Eq. 4.2}$$

where R_1 and R_2 are radii of panel curvature in orthogonal directions and L_1 and L_2 are rectangular panel dimensions.

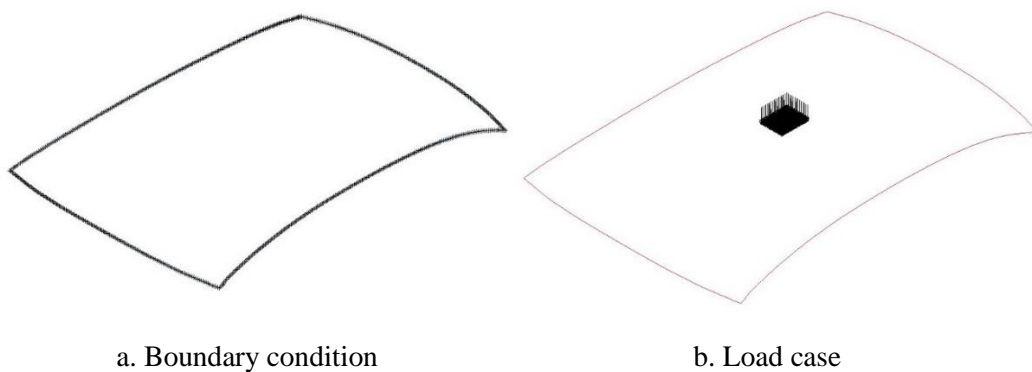


Figure 4.4: Roof linear bending stiffness analysis

The bending stiffness of the panel is calculated using FEM by applying 1N normal load to the roof panel and calculation of the resultant displacement as shown in Figure 4.5.

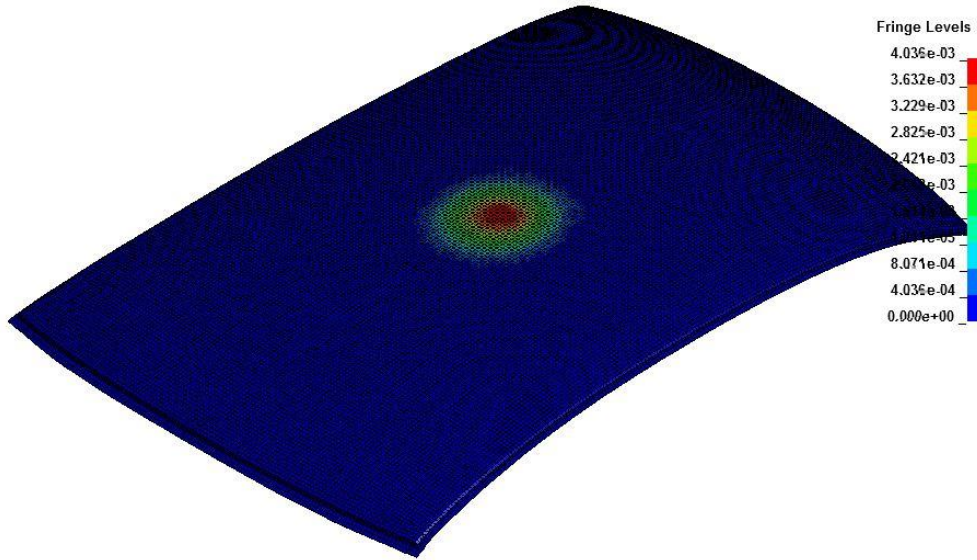


Figure 4.5: Panel deformation under normal loading (steel panel)

4.2.2 Oli canning resistance

Oil canning is local elastic buckling which is created by a sudden reversed curvature on the surface when the panel is pressed by hand. Since it is an elastic deformation, it does not leave any permanent depression as shown in Figure 4.6. The critical buckling load can be calculated as follows in Eq. 4.3 [2]:

$$P_{CR} = \frac{CR_{CR} \pi^2 E t^4}{L_1 L_2 (1 - \nu^2)} \quad \text{Eq. 4.3}$$

where

$$C = 0.645 - 7.75 \times 10^{-7} L_1 L_2 \quad \text{Eq. 4.4}$$

$$R_{CR} = 45.929 - 34.183\lambda + 6.397\lambda^2 \quad \text{Eq. 4.5}$$

$$\lambda = \frac{1}{2} \sqrt{\frac{L_1 L_2}{t}} \sqrt{\frac{12(1-\nu^2)}{R_1 R_2}} \quad \text{Eq. 4.6}$$

And the panel lengths and curvatures are valid just in the following range:

$$\left\{ \begin{array}{l} \frac{R_1}{L_1} \text{ and } \frac{R_2}{L_2} > 2 \\ \frac{1}{3} < \frac{L_1}{L_2} < 3 \\ L_1 L_2 < 0.774 \text{m}^2 \end{array} \right\}$$

However, due to the above-mentioned limitations, the oil canning resistance is calculated for a part of roof resulted from the panel section cut and not through the whole panel length.

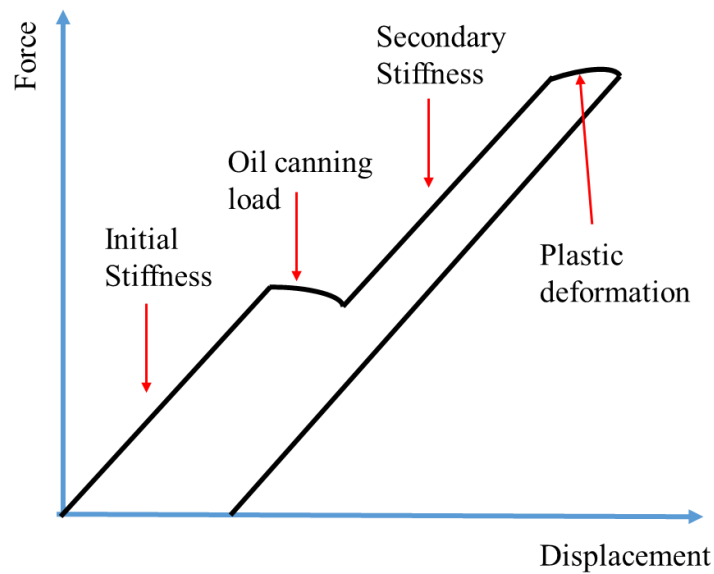


Figure 4.6: Typical force-displacement curve including oil canning load (<http://www.azom.com/article.aspx?ArticleID=1629>)

4.2.3 Dent resistance

Denting is a permanent deformation and it occurs when the local stresses in the dented region exceed the yield strength of the material. The dent resistance energy is calculated based on Eq. 4.7 [2]:

$$W = 56.8 \frac{(\sigma_{YD} t^2)^2}{K} \quad \text{Eq. 4.7}$$

where K and t are the panel normal stiffness and thickness respectively and σ_{YD} is the yield strength of material at a dynamic strain rate. The ratio of dynamic to static yield strength of steels at various strain rates is shown in Figure 4.7 [2]. This value for the considered steel is 298 MPa.

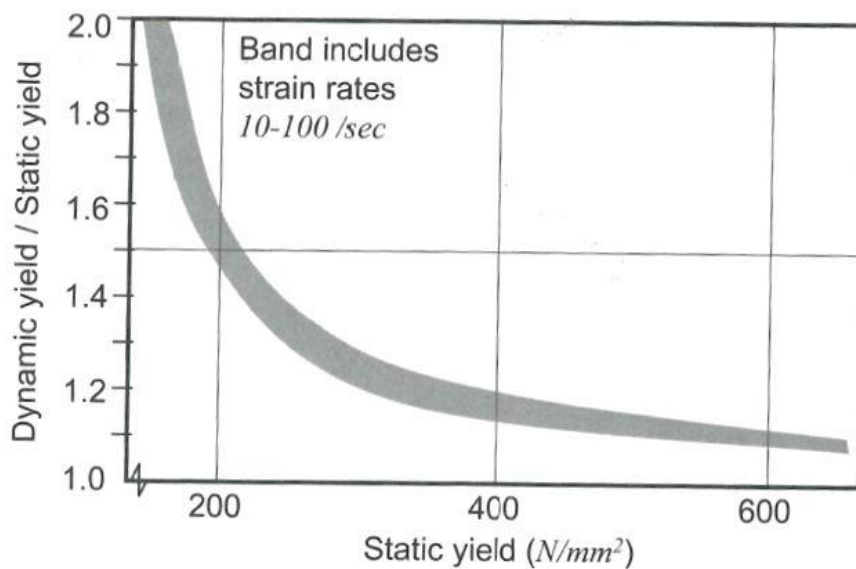


Figure 4.7: Dynamic yield stress for steel

4.2.4 Shear rigidity of a panel

The shear rigidity of the panel is estimated by applying the shear load at the roof edge while the other edge is constrained as shown in Figure 4.8.

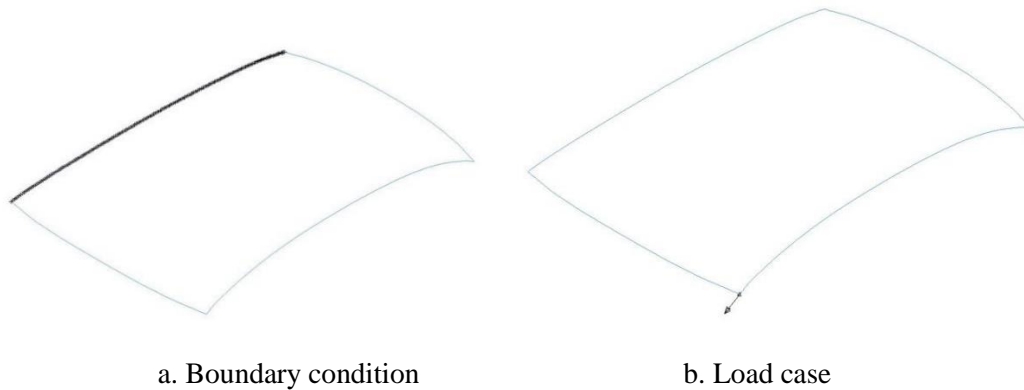


Figure 4.8: Roof linear shear stiffness analysis

However the approximate shear rigidity of the roof panel can be calculated by Eq. 4.8 as follows [2]:

$$(Gt) = \left(\frac{F}{\delta} \right) \left(\frac{b}{a} \right) \quad \text{Eq. 4.8}$$

where Gt is the effective shear rigidity of a panel, a is the panel dimension side in which loading occurs and b is the adjacent side dimension.

The nodal force and displacement of a particular node of the roof panel after the shear loading is presented in Figures 4.9 and 4.10.

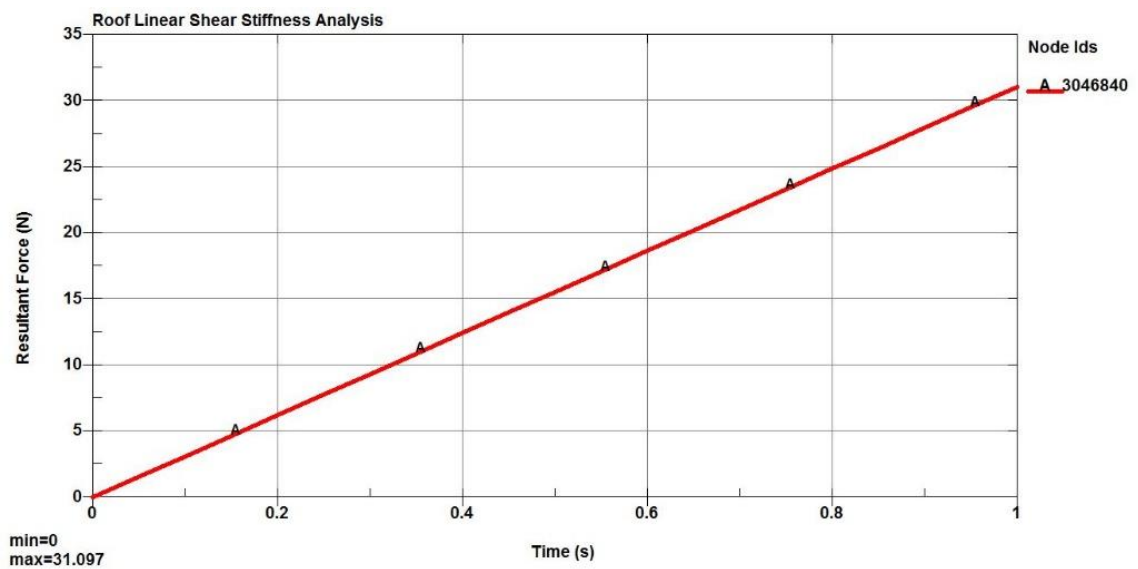


Figure 4.9: Nodal force during shear analysis

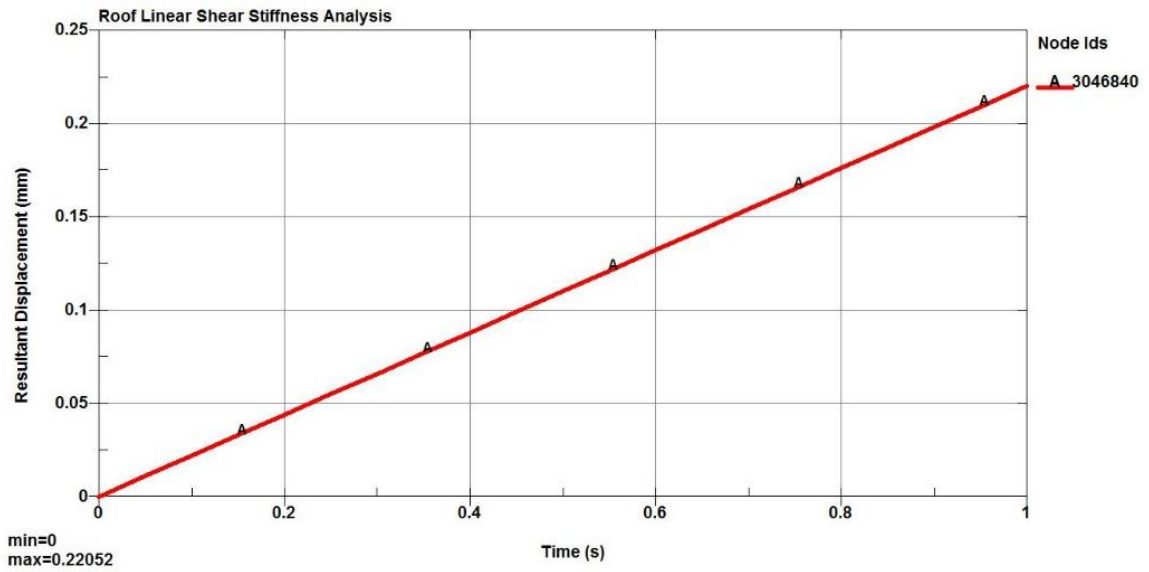


Figure 4.10: Nodal displacement during shear analysis

4.2.5 First bending frequencies

The modal analysis of the vehicle roof panel has been implemented regarding to two types of boundary conditions named “single sided constraint” and “double sided constraints” [3] as shown in Figure 4.11.

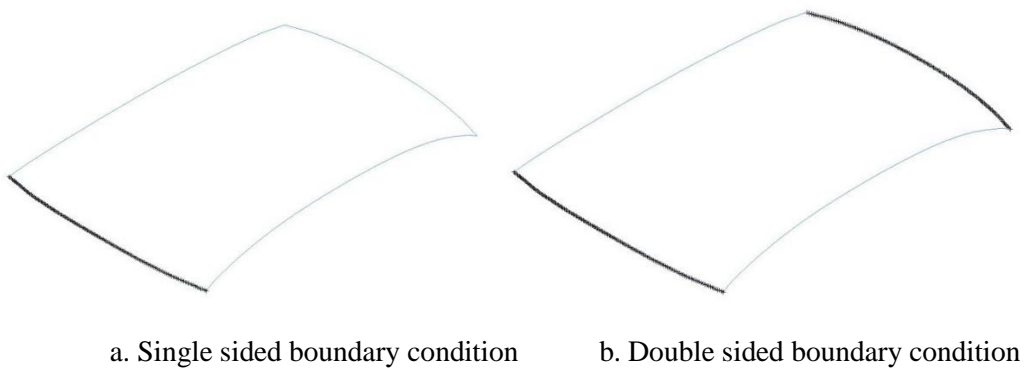


Figure 4.11: Panel modal analysis boundary condition

4.3 Framework of developing benchmark for vehicle roof panel

After describing the requirements for evaluating the behavior of vehicle roof panel under normal loadings, now it is time to develop the benchmark for the roof panel with respect to different material solutions. At the first step, the benchmark for the roof panel with the same thickness but different material properties is presented. At the next step, the new benchmark regarding to panels with modified thickness will be presented and compared.

4.3.1 Vehicle roof panel benchmark

After estimating bending and shear stiffness, critical buckling load, dent resistance and first bending frequencies, the benchmark of the TOYOTA YARIS 2010 roof panel with respect to the stiffness and the material solutions cost is presented in Table 4.4. It is worth to mention that, longitudinal Young's modulus of composite materials has been considered to calculate the pre-scribed factors. The considered Young's modulus used in theoretical formulation for steel, aluminum, unidirectional carbon fiber, woven carbon fiber and unidirectional glass fiber are 200, 71, 127, 53.6 and 31.2 GPa respectively. The properties of different material solutions are presented in Tables 4.1-4.3.

Table 4.1: Steel and Aluminum material properties

	ρ (kg/m ³)	E (GPa)	ν	σ_Y (MPa)
Steel	7890	200	0.3	220
Al 6082-T6	2710	71	0.33	270

Table 4.2: Composite material properties

	ρ (Kg/m3)	E_1 (GPa)	E_2 (GPa)	ν_{12}	G_{12} (GPa)	G_{23} (GPa)	G_{13} (GPa)
Carbon/Epoxy- Woven [4]	1450	53.6	55.2	0.04	2.85	1.425	2.85
Carbon/Epoxy - Unidirectional [5]	1520	127	8.41	0.02	4.21	4.21	4.21
Glass/Epoxy- Unidirectional [6]	1850	31.2	9.36	0.29	5	5.5	5.5

Table 4.3: Strength parameters of composites [4-6]

	X_t (MPa)	X_c (MPa)	Y_t (MPa)	Y_c (MPa)	S (MPa)
Carbon/Epoxy- Woven	642	618	652	556	84
Carbon/Epoxy – Unidirectional	2200	1470	48.9	199	154
Glass/Epoxy- Unidirectional	483	409	34.9	92.2	73.3

The gap between the theoretical and FEM results of composite solutions is due to the fact that first of all, the Eq. 4.1 is an empirical equation which was originally developed for isotropic material; secondly another reason is that probably the effective Young's modulus of composite material is less than that of considered in theoretical formulations.

Table 4.4: Benchmark values of roof panels with the same thickness (1.2mm)

Material	Steel	Aluminum	Uni. carbon	Woven carbon	Uni. glass
Bending stiffness (N/mm)-FEM	248	90	121	27	25
Bending stiffness (N/mm)-Theoretical	279	100	169	73	43
Shear rigidity (N/mm)-FEM	102	37	23	16	11
oil canning resistance (N)-Theoretical	461	166	284	123	72
Dent resistance (N.mm)-Theoretical	4.5E+4	-	-	-	-
The first four eigenvalue frequencies (Hz)-single sided constraint	2-3-18-19	2-3-18-19	2-3-21-23	2-3-19-21	1-2-12-13
The first four eigenvalue frequencies (Hz)-double sided constraints	61-70-76-122	62-71-77-124	70-81-82-127	62-73-74-110	41-47-51-81
Mass (Kg)	15.7	5.4	3.0	2.9	3.7
Mass + Non-structural mass (Kg)	31.7	21.4	19	18.9	19.7
Cost (\$)	35	60	500	550	400

4.3.2 Optimizing strategies for roof panel thickness

Thickness of roof panels made of different solutions has been increased based on two methods:

- 1- Increasing the panel thickness based on the proportion of the normal stiffness of panels made of different material solutions as presented at Eq. 4.1 (with respect to the steel solution as a reference); from now on this method is called as M1.
- 2- Increasing the panel thickness based on the equation for calculating the maximum deflection of the rectangular plate as shown in Figure 4.12 by Eqs. 4.9-4.12 [7]; from now on this method is called as M2.

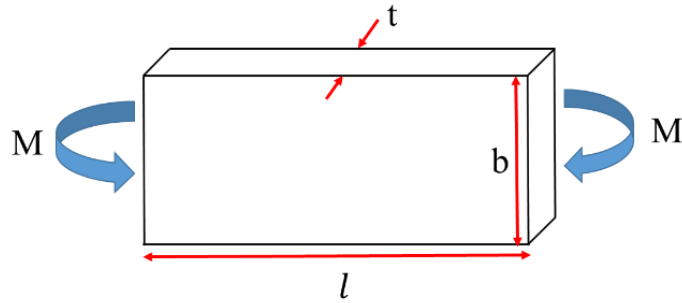


Figure 4.12: Plate under the bending load [7]

Due to the fact that the roof panel has small curvatures, it can be approximated as a rectangular plate and the maximum deflection is estimated for a steel plate as in Eq. 4.9:

$$\delta_{\max,1} = \frac{Ml^2}{8E_1I_1}, \text{ where } I_1 = \frac{bt_1^3}{12} \quad \text{Eq. 4.9}$$

If the steel solution is replaced with the other solutions then the Eq. 4.9 is replaced with the Eq. 4.10 as follows:

$$\delta_{\max,2} = \frac{Ml^2}{8E_2I_2}, \text{ where } I_2 = \frac{bt_2^3}{12} \quad \text{Eq. 4.10}$$

In order to avoid excessive deformation of roof panel, the maximum deflection of aluminum and composite panels should not be greater than the reference steel panel. Therefore Eq. 4.9 and Eq. 4.10 should be equated as follows to determine the desired thickness for the roof panel made of different solutions.

$$\frac{Ml^2}{8E_1I_1} = \frac{Ml^2}{8E_2I_2} \quad \text{Eq. 4.11}$$

$$\frac{t_2}{t_1} = \sqrt[3]{\frac{E_1}{E_2}} \quad \text{Eq. 4.12}$$

4.3.3 Vehicle roof panel benchmark with respect to the modified panels' thickness

At the updated benchmark, results regarding the stiffness values and bending frequencies along with the estimated cost for all the material solutions with optimized thickness are presented as in Table 4.5.

Increasing thickness increases the panel stiffness values and bending frequencies as it is obvious in Table 4.5; however, as mentioned before the gap between the results of theoretical and FEM methods is due to the fact that equation developed for calculating the bending stiffness of a panel is exact for isotropic material and another reason is the difference between the longitudinal and effective Young's modulus of the composite solutions.

After developing the benchmark for vehicle roof panel and calculating the metrics for the panel, now it is time to evaluate behavior of the roof panel in the full vehicle model through various load cases and determine the contribution of light-weight vehicle roof panel in the total vehicle stiffness.

Table 4.5: Benchmark values of roof panels with the modified thickness

Material	Aluminum	Uni. carbon	Woven carbon	Uni. glass
Thickness-M1-(mm)	2.00	1.54	2.34	3.04
Thickness-M2-(mm)	1.70	1.40	1.86	2.23
Bending stiffness (N/mm)-FEM-M1	210	198	88	135
Bending stiffness (N/mm)-FEM-M2	157	161	58	72
Bending stiffness (N/mm)-Theoretical-M1	279	279	279	279
Bending stiffness (N/mm)-Theoretical-M2	201	230	177	150
Shear rigidity (N/mm)-FEM-M1	130	39	59	92
Shear rigidity (N/mm)-FEM-M2	88	32	39	49
The first four eigenvalue frequencies (Hz)-single sided constraint-M1	3-3-21-22	3-4-23-24	3-4-23-24	2-3-16-17
The first four eigenvalue frequencies (Hz)-single sided constraint-M2	3-3-20-21	3-4-22-24	3-4-22-23	2-2-15-15
The first four eigenvalue frequencies (Hz)-double sided constraints-M1	70-78-86-130	73-84-85-128	70-80-81-115	52-56-61-88
The first four eigenvalue frequencies (Hz)-double sided constraints-M2	68-75-83-128	71-83-84-128	67-78-79-113	48-53-58-86
Mass (Kg)-M1	9.0	3.9	5.6	9.3
Mass (Kg)-M2	7.6	3.5	4.5	6.8
Mass + Non-structural mass (Kg)-M1	25	19.9	21.6	25.3
Mass + Non-structural mass (Kg)-M2	23.6	19.5	20.5	22.8
Cost (\$)-M1	100	640	1060	1010
Cost (\$)-M2	85	580	845	740

4.4 Vehicle body stiffness

Structural stiffness has an important effect on the riding and safety performance of vehicles. Body as the primary part of vehicle that embeds the passengers and various vehicle systems, should be stiff enough to protect the passengers. Structural stiffness is divided into the two categories of static and dynamic stiffness. Static stiffness is related to the study of deforming body under the static and quasi-static loads, it is traditionally subdivided into bending and torsional stiffness. Bending and torsional stiffness are measuring the response of body structure against flexural and torsional loads, they have huge impact on the handling and comfort characteristics of vehicle. Dynamic stiffness is related to the study of vibrational characteristics of chassis which refers to vehicle internal noise, vibration and harshness (NVH) specifications and in the customer perspective the vehicle riding comfort [8].

In this section, the theoretical formations for calculating the bending and torsional stiffness of a chassis are presented.

4.4.1 Vehicle body bending stiffness

During the static bending test, forces are applied at the front seat locations, while the body is fully constrained at front and rear shock towers, as shown in Figure 4.13. The static bending stiffness K_b is defined equal to the ratio of the applied load F to the average vertical displacement δ of the two load points along the rocker panel and tunnel beams according to Eq. 4.13. The maximum load- F_s - (see Figure 4.13) after which that plastic deformation begins is called vehicle bending strength.

$$K_b = \frac{F}{\delta} \text{ (N/mm)} \quad \text{Eq. 4.13}$$

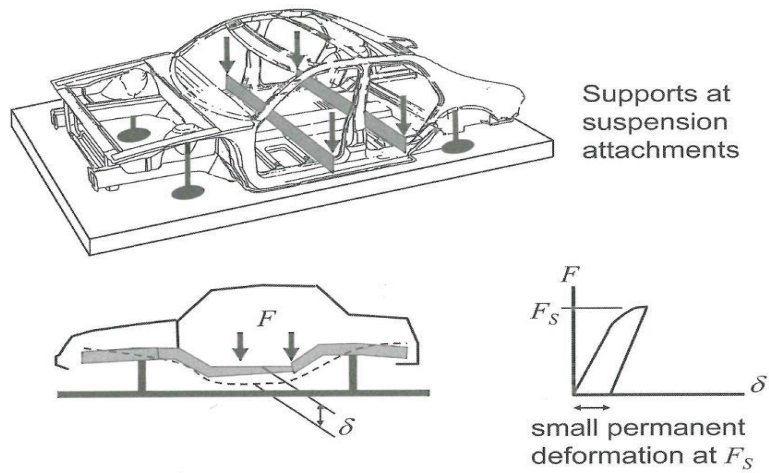


Figure 4.13: Vehicle bending stiffness and strength [2]

4.4.2 Vehicle body torsion stiffness

In the case of the static torsion test, a static torque is applied around the longitudinal axis of the body, to the body-in-white at the front shock towers, whereas the rear shock towers are fully constrained, as shown in Figure 4.14. The torsion stiffness, K_t is defined as the ratio of the applied torsion Moment (T) to the rotation angle Φ of the vehicle at the load points according to Eq. 4.14.

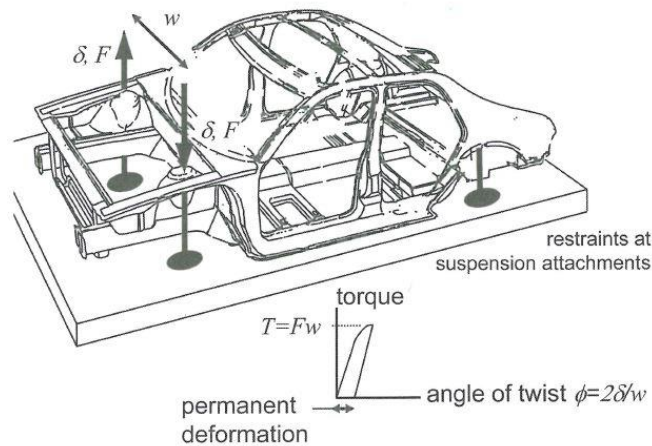


Figure 4.14: Vehicle torsion stiffness and strength [2]

$$K_t = \frac{T}{\phi} \text{ (N.m/deg), where } T=Fw \tag{Eq. 4.14}$$

4.5 Load path analysis by simple structural surfaces (SSSs) model

Although vehicle in the road are subjected to different load cases, the major load cases are bending and torsion loads. The load path caused by both bending and torsion loads can be determined using the simple structural surfaces (SSSs) model [1]. The standard sedan shown in Figure 4.15, considered as a ‘closed box’ passenger compartment, including front and rear bulkheads, side-frames, floor, roof and windscreen that are assumed as plane surfaces. In order to determine the load path it is necessary to consider the following SSSs parts in the standard sedan as shown in Figure 4.15.

1. and 2. Front and rear transverse floor beams.
3. and 4. Inner wing panels.
5. Dash panel.
6. Front parcel shelf.
7. and 8. Rear quarter panels.
9. Panel behind the rear seats.
10. Rear parcel shelf.
11. Floor panel
12. and 13. Left and right-hand side-frames.
14. Windscreen frame.
15. Roof panel.
16. Backlight or rear window frame.

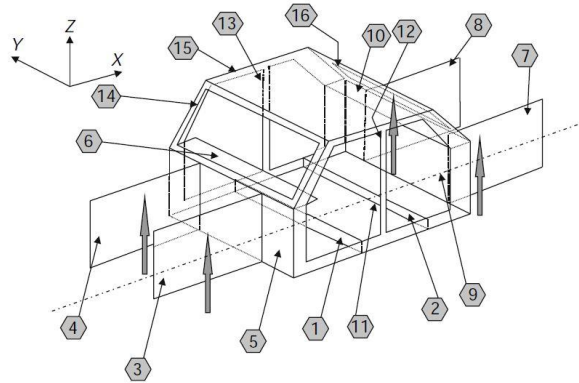


Figure 4.15: Baseline model [1]

4.5.1 Vehicle load path analysis during bending

The main bending loads inserted to the sedan are shown in Figure 4.16. The main bending loads are power-train (F_{pt}), the front and rear passenger's seats (F_{pf} , F_{pr}) and the luggage (F_l).

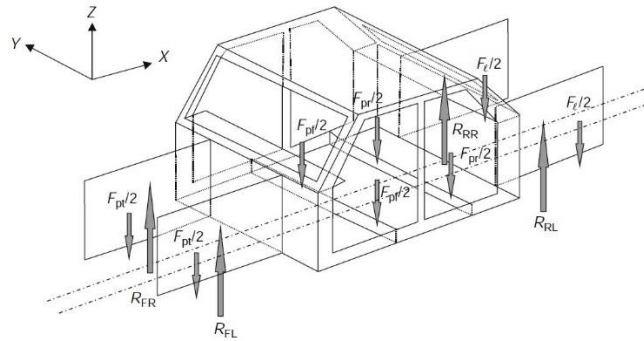


Figure 4.16: Baseline model – bending loads [1]

If the sedan viewed in side elevation (Figure 4.17), it can be considered as a rigid body. According to the equilibrium equations; by taking moments about rear and front suspension mounting, the front and rear suspension reaction forces are obtained with Eqs. 4.15 and 4.16.

$$R_F = \frac{F_{pt}(L + l_{pt}) + F_{pf}(L - l_{pf}) + F_{pr}(L - l_{pr}) - F_l l_l}{L} \quad \text{Eq. 4.15}$$

$$R_R = \frac{F_{pf} l_{pf} + F_{pr} l_{pr} + F_l(L + l_l) - F_{pt} l_{pt}}{L} \quad \text{Eq. 4.16}$$

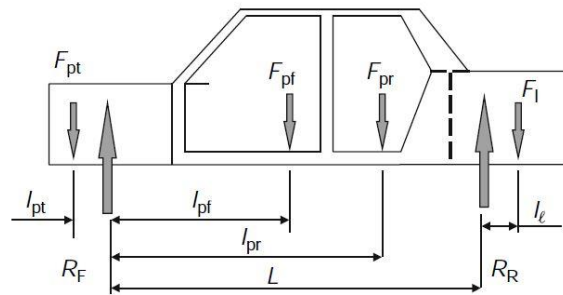


Figure 4.17: Payload distribution [1]

By considering the sedan model in the ‘exploded’ view shown in Figure 4.18, it is easily possible to calculate all the loads in substructures based on equilibrium equations. By deriving the equilibrium equations, the edge and end loads obtained by Eqs. 4.17 to 4.31.

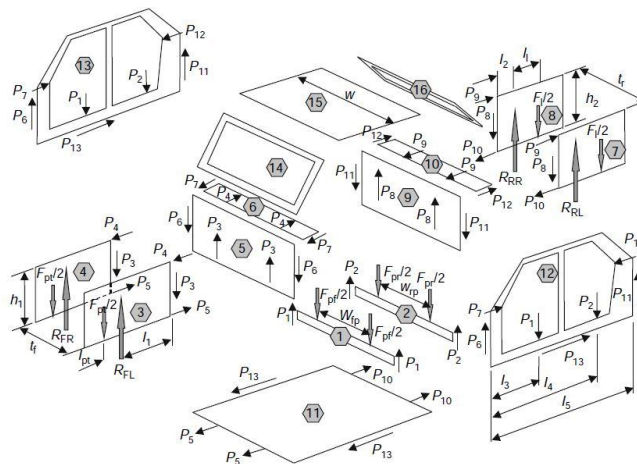


Figure 4.18: Baseline model – bending case, end and edge loads [1]

By resolving the forces vertically and horizontally about the vehicle longitudinal centerline and taking the moments about the front and rear lower corners the following loads are obtained:

for substructure (1) the loads are determined by:

$$P_1 = F_{pf}/2 \tag{Eq. 4.17}$$

for substructure (2) the loads are determined by:

$$P_2 = F_{pr}/2 \quad \text{Eq. 4.18}$$

for substructures (3 and 4) the loads are determined by:

$$P_3 = R_{FL} - F_{pt}/2 \quad \text{Eq. 4.19}$$

$$P_4 = \frac{\left\{ R_{FL}l_1 - \frac{F_{pt}(l_l + l_{pt})}{2} \right\}}{h_1} \quad \text{Eq. 4.20}$$

$$P_5 = P_4 \quad \text{Eq. 4.21}$$

for substructure (5) the loads are determined by:

$$P_6 = P_3 \quad \text{Eq. 4.22}$$

for substructure (6) the loads are determined by:

$$P_7 = P_4 \quad \text{Eq. 4.23}$$

for substructures (7 and 8) the loads are determined by:

$$P_8 = R_{RL} - F_l/2 \quad \text{Eq. 4.24}$$

$$P_9 = \frac{\left\{ R_{RL}l_2 - \frac{F_l(l_1 + l_2)}{2} \right\}}{h} \quad \text{Eq. 4.25}$$

$$P_{10} = P_9 \quad \text{Eq. 4.26}$$

for substructure (9) the loads are determined by:

$$P_{11} = P_8 \quad \text{Eq. 4.27}$$

for substructure (10) the loads are determined by:

$$P_{12} = P_9 \quad \text{Eq. 4.28}$$

for substructure (11) reaction forces P_5 from the inner front wing panels and forces P_{10} from the rear quarter panel are applied to this panel but these forces are not necessarily equal so additional forces P_{13} are required acting at the sides which react on the side-frames. The loads are determined by:

$$2P_{13} = 2(P_{10} - P_5) \quad \text{Eq. 4.29}$$

for substructures (12 and 13) the loads have been determined by Eqs. 4.17, 4.18, 4.22, 4.23, 4.27, 4.28 and 4.29, however it is necessary to check the accuracy of the equations by the following relation:

$$P_6 - P_1 - P_2 + P_{11} = 0 \quad \text{Eq. 4.30}$$

$$P_7 + P_{13} - P_{12} = 0 \quad \text{Eq. 4.31}$$

It should be noted that windscreen frame (14), roof panel (15) and backlight (16) substructures are not subjected to any load during the bending loading in the SSSs model.

4.5.2 Vehicle load path analysis during torsion

The vehicle is subjected to torsion loading on the road when a wheel on one side strikes a bump. This loading caused by vertical displacement in the wheel axel. Although this displacement subjects the combination of bending and torsion loading to the vehicle, the pure torsion load is considered. The Equal and opposite R_{FT} loads are applied to the front suspension towers as R_{RT} loads at rear suspension towers leading to the equal couple of T about the vehicle centerline as shown in Figure 4.19. The SSS edge loads in the case of torsion loading are indicated by Q ; so it is possible to consider the combination of bending and torsion loading effects by estimating P and Q . The torque T is calculated by Eq. 4.32:

$$T = R_{FT}S_F = R_{RT}S_R \quad \text{Eq. 4.32}$$

Hence

$$R_{FT} = T/S_F, R_{RT} = T/S_R$$

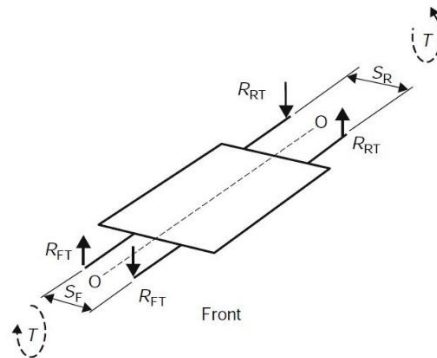


Figure 4.19: Vehicle in pure torsion [1]

For Front and rear inner fenders, as shown in Figure 4.20, the loads are determined based on moment equilibrium equation by Eqs. 4.33-4.35:

$$R_{FT}L_1 = P_{FT}h_1 \quad \text{Eq. 4.33}$$

thus

$$P_{FT} = \frac{TL_1}{S_F h_1} \quad \text{Eq. 4.34}$$

$$P_{RT} = \frac{TL_2}{S_R h_2} \quad \text{Eq. 4.35}$$

where L_2 = loaded length and h_2 = height of rear inner fender

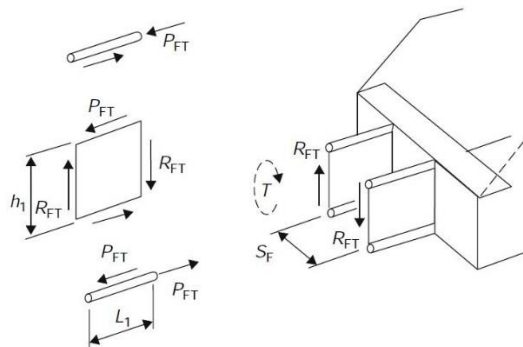


Figure 4.20: Frontal structure [1]

when the torque T is applied to the engine bulkhead the force P_{FT} can obtain by Eq. 4.36 as shown in Figure 4.21:

$$P_{FT}S_F = T \tag{Eq. 4.36}$$

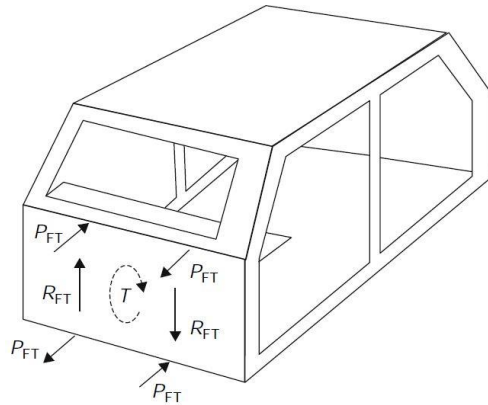


Figure 4.21: Forces on dash panel [1]

The parcel shelf carrying the couple $P_{FT}S_F$ out to the sideframe at the mid A-pillars as shown in Figure 4.22. The end forces Q_{X1} form a couple to balance this couple, thus:

$$Q_{X1}B = P_{FT}S_F, Q_{X1} = P_{FT}S_F/B \tag{Eq. 4.37}$$

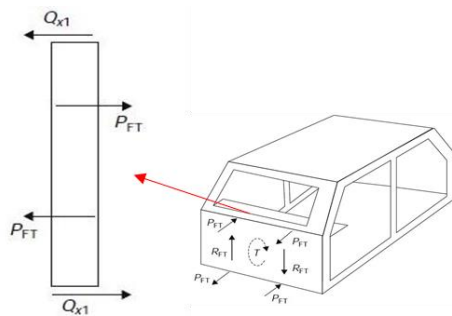


Figure 4.22: Parcel shelf [1]

By similar reasoning the rear parcel shelf reaction forces Q_{X2} are:

$$Q_{X2} = P_{RT}S_R/B \tag{Eq. 4.38}$$

The exploded view of the SSS edge forces in the passenger compartment is shown in Figure 4.23.

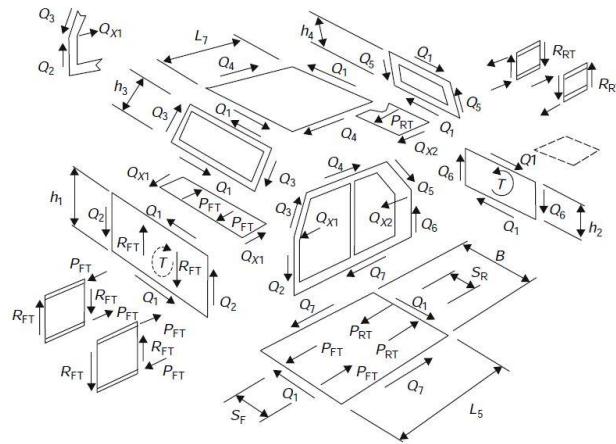


Figure 4.23: Edge forces in the standard sedan in the torsion load case [1]

The load path for the other passenger compartment parts are calculated from Eqs. 4.39-4.45:

$$Q_1 h_1 + Q_2 B$$

Eq. 4.39- front bulkhead

$$-Q_1 h_3 + Q_3 B$$

Eq. 4.40- windshield

$$-Q_1 L_7 + Q_4 B$$

Eq. 4.41- roof

$$-Q_1 h_4 + Q_5 B$$

Eq. 4.42- backlight

$$Q_1 h_2 + Q_6 B$$

Eq. 4.43- rear bulkhead

$$Q_1 L_5 - Q_7 B = P_{FT} S_F + P_{RT} S_R$$

Eq. 4.44- floor

$$-r_2 Q_2 + r_3 Q_3 + r_4 Q_4 + r_5 Q_5 - r_6 Q_6 + r_7 Q_7 = Q_{X1} (h_1 - Z) + Q_{X2} (h_2 - Z)$$

Eq. 4.45-sideframe

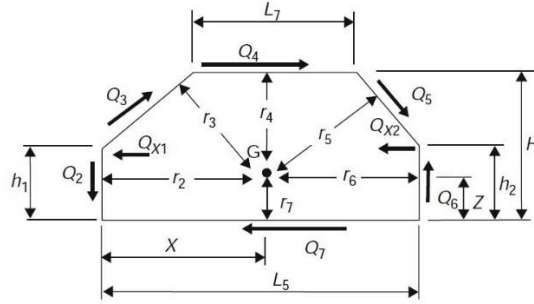


Figure 4.24: Sideframe [1]

It is much clear if the above equations are written in matrix format as below:

$$\begin{bmatrix} L_5 & 0 & 0 & 0 & 0 & 0 & -B \\ h_1 & B & 0 & 0 & 0 & 0 & 0 \\ -h_3 & 0 & B & 0 & 0 & 0 & 0 \\ -L_7 & 0 & 0 & B & 0 & 0 & 0 \\ -h_4 & 0 & 0 & 0 & B & 0 & 0 \\ h_2 & 0 & 0 & 0 & 0 & B & 0 \\ 0 & -r_2 & r_3 & r_4 & r_5 & -r_6 & r_7 \end{bmatrix} \begin{bmatrix} Q_1 \\ Q_2 \\ Q_3 \\ Q_4 \\ Q_5 \\ Q_6 \\ Q_7 \end{bmatrix} = \begin{bmatrix} P_{FT}S_F + P_{RT}S_R \\ T \\ 0 \\ 0 \\ 0 \\ T \\ Q_{X1}(h_1 - Z) + Q_{X2}(h_2 - Z) \end{bmatrix} \begin{matrix} \text{floor} \\ \text{front bulkhead} \\ \text{windshield} \\ \text{roof} \\ \text{backlight} \\ \text{rear bulkhead} \\ \text{sideframe} \end{matrix}$$

Equilibrium matrix
Edge forces
Input forces

4.6 Finite element analysis formulation

The differential equations are derived from the virtual work principles [9]. The virtual work principle states that the work done by external loads is equal to the ones by internal loads. By applying the virtual work principle into a finite element volume V_e , the Eq. 4.46 is derived [10]:

$$\delta(U)^e = \delta W^e \tag{Eq. 4.46}$$

$\delta(U)^e$ is the work done by the internal loads and δW^e is the work done by the external loads. By completely deriving the above formula, the structure equations of motion can be derived as:

$$[M] \left\{ \ddot{D} \right\} + [C] \left\{ \dot{D} \right\} + \{ R^{int} \} = \{ R^{ext} \} \tag{Eq. 4.47}$$

$[M]$ and $[C]$ are system structural mass and damping matrixes respectively; $\{R^{int}\} = [K]\{D\}$ is the internal load vector and $\{R^{ext}\}$ is the external load vector. $\{D\}$, $\{\dot{D}\}$ and $\{\ddot{D}\}$ are the nodal displacements, velocities and accelerations respectively. It worth to mention that the stiffness matrix $[K]$ is not constant for the non-linear problems such as crashworthiness and is a function of displacement and time.

Based on the direct integration methods, the time derivatives in Eq. 4.47 ($\{\dot{D}\}$, $\{\ddot{D}\}$) is replaced by differences of displacement $\{D\}$ at various portions of time. In this way the equation is written as:

$$[M]\{\ddot{D}\}_n + [C]\{\dot{D}\}_n + \{R^{int}\}_n = \{R^{ext}\}_n \quad \text{Eq. 4.48}$$

n implies to $n\Delta t$ time and Δt is the time step. To solve the Eq. 4.48, there are the two possible methods of implicit and explicit that will describe as follows.

4.6.1 The Implicit Method

In the implicit method, $\{D\}$ is defined as:

$$\{D\}_{n+1} = f\left(\{\dot{D}\}_{n+1}, \{\ddot{D}\}_{n+1}, \{D\}_n, \dots\right) \quad \text{Eq. 4.49}$$

In order to determine the time derivatives of $\{D\}_{n+1}$, it is necessary to implement several iterations. During each iteration, equations including of mass, damping and stiffness matrixes should be resolved; if the model is the complex one then several iterations needed to solve the equation which makes this method is very expensive. The implicit method is unconditionally stable under some circumstances and it allows for large time steps to be used but it is not suitable for crash analysis that occurs in portion of a second [10].

4.6.2 The Explicit Method

In the explicit method, $\{D\}$ is defined as:

$$\{D\}_{n+1} = f\left(\{D\}_n, \{\dot{D}\}_n, \{\ddot{D}\}_n, \{D\}_{n-1}, \dots\right) \quad \text{Eq. 4.50}$$

This method requires knowledge of the complete history of the information consisting of displacements and their times derivatives at time $n\Delta t$ and earlier to calculate the displacements at time step $n + 1$. The explicit method is conditionally stable, according to the length of the time step which itself depends on the smallest element size in the mesh. This method is very suitable for nonlinear dynamic problems occur in short periods of time such as crash problems [11].

4.7 Finite element modeling of composite structures with LS-DYNA

Composites are orthotropic linear elastic materials characterized by a quite complicated failure surface because of the different failure mechanisms that could take place. During the failure, material elastic properties are degraded, and this behaviour can be reproduced by means of different degradation methods. The resulting constitutive models are generally divided into the two main categories: the progressive failure models (PFM) and the continuum damage mechanics models (CDM). PFM is a strength-based degradation law that uses the ply discount method to degrade the material properties. After the ply applied stresses have exceeded the specific strength values, the material mechanical properties are immediately dropped from undamaged status to fully damaged status. In other words, progressive failure model is considered as a ply-by-ply failure model in which once all plies have failed the whole element is deleted [5]. CDM describes the gradual deterioration of the elastic properties of the material through the use of internal damage variables [12].

The finite element code LS-DYNA presents various composite material models including both PFM (MAT22, MAT54/55 and MAT59) and CDM (MAT58 and MAT158, MAT161/162 and MAT261/262). The comparison of different material models which can be used to model composite materials is presented in Table 4.6 [13, 14].

Table 4.6: Ls-Dyna available composite material model

Material Card	Failure Criteria	Elements	Specifications
MAT22 Composite Damage	Reduced Chang-Chang	Thin and Thick Shells, Solid, SPH	Brittle model, PFM, No damage effects
MAT54/55 Enhanced Composite Damage	54: Chang-Chang 55: Chang-Chang and Tsai-Wu	Thin Shell	Crashfront algorithm, PFM, Strength-based failure, Damage effects
MAT58 Laminated Composite Fabric	Reduced Hashin	Thin and Thick Shells	Smooth stress strain relation, CDM, Crashfront algorithm
MAT59 Composite Failure Model	Reduced Tsai-Wu	Thin and Thick Shells, Solid, SPH	Crashfront algorithm, PFM-Smooth stress strain relation, No damage effects, Fabric shear behaviour control, Plasticity based
MAT114 Layered Linear Plasticity	User Subroutine and Plastic to Strain Criteria	Thin and Thick Shells	Elastoplastic model, Strain rate effects
MAT116 Composite Layup	No Failure	Thin Shell	Composite lay-ups Elastic response, Input pre-integration done inside LSDYNA
MAT117/118 Composite Matrix/ Composite Direct	No Failure	Thin Shell	Elastic response, Input pre-integration done outside LSDYNA, Stiffness matrix coefficients imported directly from the experimental data Similar to MAT58, Viscous stress tensor for eliminating spurious stress oscillations, Strain rate effects, CDM, Viscoelastic material
MAT158 Rate Sensitive Composite Fabric	Reduced Hashin	Thin and Thick Shells	Extra licence Required for translation and connection to MSC, Delamination Modelling, CDM, Strain rate effects
MAT161/162 Composite MSC/ Composite DMG MSC	Hashin	Solid	
MAT221 Orthotropic Simplified Damage	Reduced Chang-Chang	Solid, SPH	Developed of MAT22, Damage Effects
MAT261/262 Laminated Fracture Daimler Pinho/ Laminated Fracture Daimler Camanho	261: Pinho 262: Camanho	Thin and Thick Shells, Solid	CDM, Non-linear shear behavior, Crashfront algorithm, Shear plasticity hardening parameter

MAT 54/55 has been selected between the available material models to model the composite structure. This material model predicts composite structures failure based on the Chang-Chang or the Tsai-Wu failure criteria. It is based on four concurrent failure modes. When failure limit condition is reached in one of the four failure modes, the related orthotropic elastic material properties (i.e. Young's modulus, Poisson's ratios and shear modulus) are set to zero. The Chang-Chang and the Tsai-Wu failure criteria with degraded parameters are reported in Eqs. 3.24-3.27 in chapter three.

The Material model 54/55, Mat Enhanced Composite Damage, consists of different sections that are used to define in detail the constitutive material properties, material coordinate system, damage factors, strain to failure parameters, failure criteria, shear stress weighting factor, material strength parameters and element deletion option as shown in Table 4.7. Unfortunately, LS-DYNA manual does not provide complete description of the theoretical background that is under those material card parameters and there are only few papers available that discuss these parameters. Although a complete description can be found in [5] it is worth to present here a brief description for some parameters in the material card relevant for our particular study. The constitutive material inputs include the elastic material properties such as the Young and shear modulus and Poisson ratio in longitudinal (fiber) and transverse (matrix) directions which are completely described in [5] and the material coordinate system parameters - that will be described later - moreover there is the important factor ALPH that is used in the shear stress-strain relations as reported in Eq. 4.51. In Eq. 4.51, α (APLH in the material card) is a weighting factor for the non-linear shear stress term.

$$2\varepsilon_{12} = \frac{1}{G_{12}}\tau_{12} + \alpha\tau_{12}^3 \quad \text{Eq. 4.51}$$

The damage initiation factors with respect to failure criteria have already been discussed in the chapter three. The damage factors FBRT and YCFAC are the strength reduction parameters used to degrade the undamaged fiber strength of the remaining plies once the matrix failure has occurred. The FBRT parameter shows the reduction percentage of the tensile strength from its undamaged value ($X_t \cdot \text{FBRT}$) and the YCFAC parameter uses the undamaged matrix compressive strength to determine the damaged compressive fiber strength ($X_c = \text{YCFAC} \cdot Y_c$). It is worth to mention that the selected range of the FBRT parameter is between 0-1



Table 4.8: Material model 54/55 specifications

Variable	Definition
MID	Material identification number
RO	Mass density
EA	Young's modulus in longitudinal direction, E_a
EB	Young's modulus in transverse direction, E_b
(EC)	Young's modulus in normal direction, E_c
PRBA	Minor Poisson's ratio, ν_{ba}
PRBC	Minor Poisson's ratio, ν_{bc}
(PRCB)	Minor Poisson's ratio, ν_{cb}
GAB	Shear modulus G_{ab}
GBC	Shear modulus G_{bc}
GCA	Shear modulus G_{ca}
(KF)	Bulk modulus of failed material. (Not used)
AOPT	Material direction option
A1, A2, A3	Components of vector A, for AOPT=2
MANGLE	Material angle, for AOPT=0.
V1, V2, V3	Components of vector V, for AOPT=3
D1, D2, D3	Components of vector D, for AOPT=2
DFAILM	Maximum strain for matrix straining in both tension and compression
DFAILS	Maximum tensorial shear strain
TFAIL	Time step size for element deletion
ALPH	Shear stress parameter for non-linear term
SOFT	Softening reduction factor for material strength in crashfront elements
FBRT	Softening parameter for fiber tensile strength after failure has

	occurred in compressive matrix mode
YCFAC	Reduction factor for compressive fiber strength after failure has occurred in compressive matrix mode
DFAILT	Maximum strain for fiber tension
DFAILC	Maximum strain for fiber compression
EFS	Effective failure strain
XC	Longitudinal compressive strength
XT	Longitudinal tensile strength
YC	Transverse compressive strength
YT	Transverse tensile strength
SC	Shear strength
CRIT	Failure criteria to use (MAT54 Chang-Chang criterion, MAT55 Tsai-Wu criterion)
BETA	Weighing factor for shear term in tensile fiber mode
PFL	Percentage of layer needed to fail until crashfront is initiated and strength is reduced in neighboring elements
EPSF	Damage initiation transverse shear strain
EPSR	Final rapture transverse shear strain
TSMMD	Transverse shear maximum damage
SOFT2	Optional orthogonal softening reduction factor. When active, SOFT becomes parallel reduction factor
SLIMT1-2	Factor to determine minimum stress limit after maximum stress occurred for fiber & matrix tension
SLIMC1-2	Factor to determine minimum stress limit after maximum stress occurred for fiber & matrix compression
SLIMS	Factor to determine minimum stress limit after maximum stress occurred for shear
NCYRED	Number of cycles for stress reduction from maximum to minimum stress
SOFTG	Softening reduction factor for transverse shear stiffness for crashfront elements
LCXC	Load curve ID for XC vs strain rate. Will override parameter XC
LCXT	Load curve ID for XT vs strain rate. Will override parameter XT
LCYC	Load curve ID for YC vs strain rate. Will override parameter YC
LCYT	Load curve ID for YT vs strain rate. Will override parameter YT
LCSC	Load curve ID for SC vs strain rate. Will override parameter SC
DT	Strain rate averaging option

There are different methods for modelling composite materials in LS-DYNA. The old method was proposed many years ago by using the keyword *INTEGRATION_SHELL. In this method a user-defined thickness integration with the inputs of relative thickness coordinates and weighting factors have been used. A more recent method, which is categorized as a zone-based modelling concept, is using the keyword *PART_COMPOSITE. There is no need to define a section, instead it is necessary to define thickness and fiber direction for each integration point. Where there is the necessity for extra adjusting of the fiber orientation, this keyword could be integrated with the keyword *ELEMENT_SHELL_BETA. The fiber orientation is a result of the material Axis Option parameter (AOPT) and ϕ_i ($\beta + \beta_i$) parameters. Before defining the fiber orientation, it is strongly recommended to define coherently the normal direction for all the elements. This is quite important because the element surface normal is used to define the sequence of element node numbering which in turn is significantly important to define the primary element direction. Combination of AOPT and β determines the element reference system, while β_i determines the material (fiber) direction. The complete procedure for adjusting the fiber direction is described in the LS-DYNA user manual [13]. There is also a new method available using the keyword *ELEMENT_SHELL_COMPOSITE, which is a ply-based method, in this case there is no need to apply the keyword *INTEGRATION_SHELL_BETA.

The use of the *ELEMENT_SHELL_COMPOSITE keyword is strongly recommended in the case of arbitrary draping of fiber angle from region to region [15].

4.8 Toyota Yaris chassis stiffness analyses

The FEM model of TOYOYA YARIS 2010 has been selected as it is available from the National Crash Analysis Centre (NCAC) provided by George Washington University in the United States [16]. This FEM model of passenger vehicle is the result of a reverse engineering procedure performed at NCAC by systematically disassembling the vehicle part by part. Each part is scanned to obtain its geometry and material data are obtained through coupon testing of samples taken from vehicle parts [17]. Figure 4.25 shows the finite element model of the vehicle that consists of 974388 elements and 1009131 nodes. The FE model of the roof structure consists of 26000 shell elements and 26288 nodes.

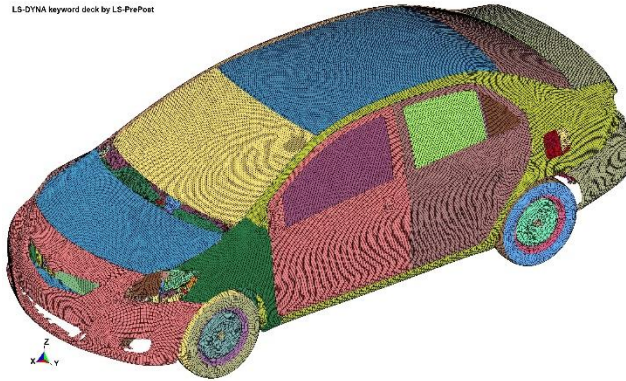


Figure 4.25: Vehicle finite element model

The original thickness of the roof panel is 1.2 mm and in the case of using composite material it is equal to the summation of the four layer thickness. Each layer has one integration point through the thickness (NIP=4). The schema of composite lay-up is shown in Figure 4.26. MAT24, Piecewise Linear Plasticity, has been used to model the roof with traditional material solutions, while Mat 54/55 has been chosen to model the composite roof panel. MAT24 is an elastoplastic material model that can analyze failure based on plastic strain as an alternative possibility. This material model is capable of taking into account the strain-rate effects by using different methods. The Cowper-Symonds model, which scales the yield stress, has been applied to describe the strain rate sensitivity of the two metallic materials, however, as it is well known, aluminum has very low sensitivity to the strain-rate. In the case of modelling the composite structure, when composite shell has layers of dissimilar materials it is generally recommended to activate the laminate shell theory option. This option corrects the wrong assumption of constant shear strain through the thickness of the shell; this parameter is very important when modelling sandwich structure because it helps to prevent a too stiff behaviour of the structure. The two types of linear shell element formulation 18 and fully integrated element type 16 have been used to model the metallic and composite roof panels respectively. Possible Hourglass (HG) modes, which are nonphysical, zero-energy modes of deformation, should be taken under careful control. As it is well known “Hourglass modes” occur only in the case of reduced integration elements. LS-DYNA has various algorithms to prevent hourglass modes, Stiffness-based HG control (types 4 and 5) is generally

considered more effective than viscous HG control for structural parts, while type 8 HG control applies only to shell formulation 16. In order to entirely eliminate hourglass modes, it is necessary to use element formulations with full-integration or, eventually, selectively reduced (S/R) integration schemas [18]. In this case the two types of hourglass algorithms 4 and 8 are used to control the hourglass energy.

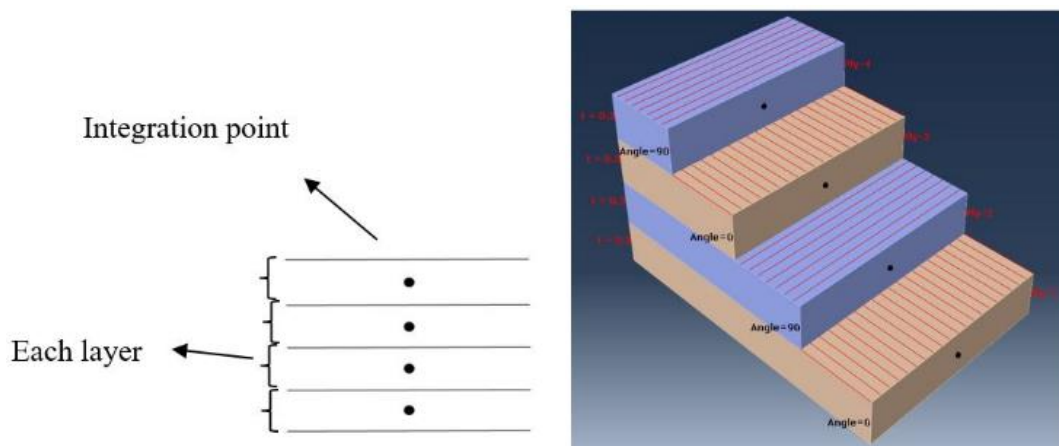


Figure 4.26: Schematic of composite lay-up

In order to perform modal, bending and torsion analyses of vehicle body, it is necessary to develop the chassis model as shown in Figure 4.27. The chassis model consists of shell elements and beam elements as connectors. One cumbersome but important task is to check carefully that all the chassis constraints have been included in the model. The sections that will be used for the analysis of the roof are defined at the roof pillars intersections as shown in Figure 4.27.

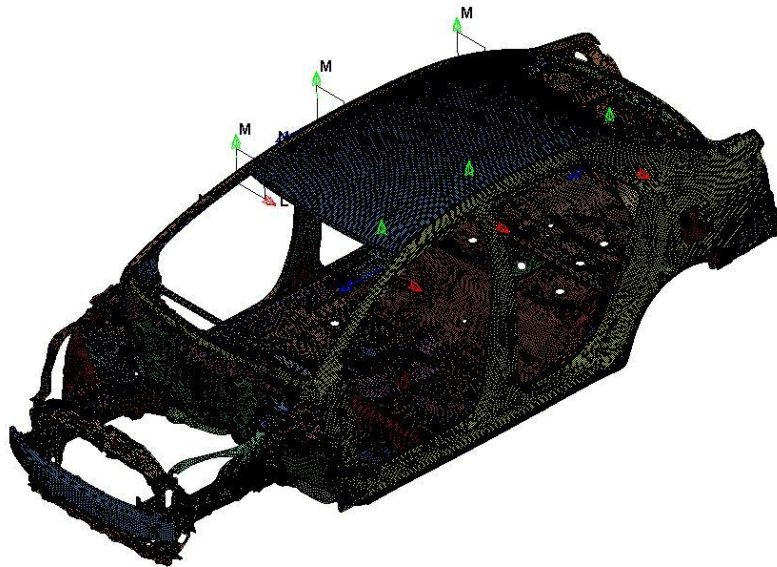


Figure 4.27: Chassis finite element model

Constrained_Nodal_Rigid_Body (CNRB) constraints and Spot_Weld models are used to simulate properly the joining between the various parts of the body to describe the whole structure. These analyses are of the implicit, linear analyses types. The first part of the stiffness analysis is the static analyses as shown in Figures 4.28 and 4.29. In the case of the static bending test, forces are applied at the front seat locations, while the body is fully constrained at front and rear shock towers, as shown in Figure 4.28. Rectangular shell beam has been designed based on SAE standard [19] to distribute the applied loads along the passengers' locations evenly and to avoid stress concentration at the load application points. The bending stiffness is calculated based on Eq. 4.13.

In the case of chassis static torsion test, as mentioned before, a torque is applied at the front shock towers while the rear shock towers are constrained as shown in Figure 4.29. The torsion angle of chassis is calculated based on Figure 4.30 and by Eq. 4.52 where d is the transverse distance between the reference nodes at shock towers at the initial position and ΔZ_i , ΔY_i are the vertical and horizontal displacements of the reference nodes respectively and the torsional stiffness is calculated based on Eq. 4.14.

Bending Analysis with Steel Roof

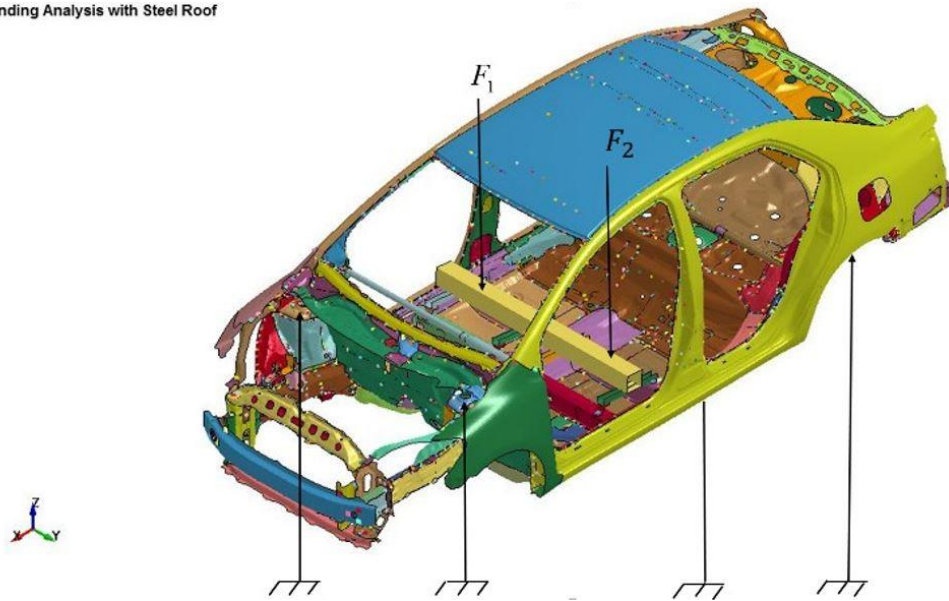


Figure 4.28: Bending analysis

Torsion Analysis with Steel Roof

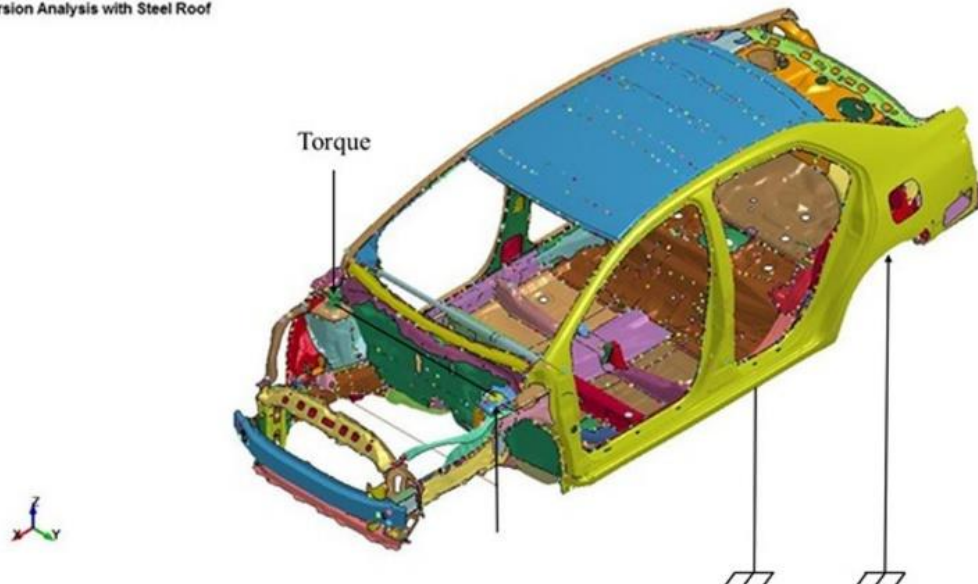


Figure 4.29: Torsional analysis

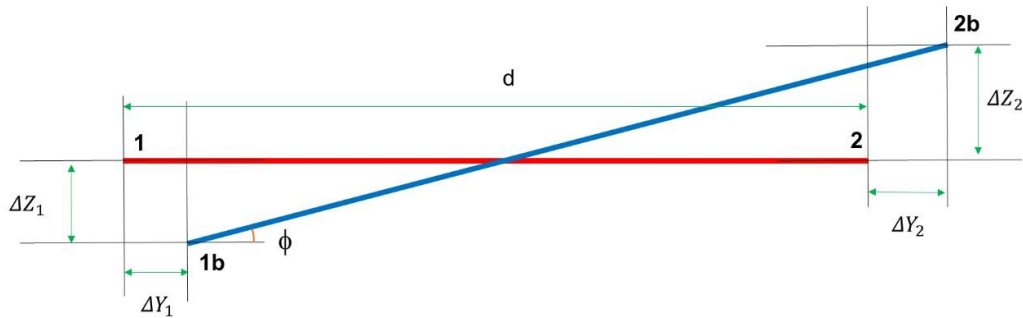


Figure 4.30: Torsion angle calculation

$$\phi = \text{tg}^{-1} \left(\frac{\Delta Z_1 + \Delta Z_2}{d + \Delta Y_2 - \Delta Y_1} \right) \quad \text{Eq. 4.52}$$

The second part of stiffness analysis is modal or dynamic analysis as shown in Figures 4.31 and 4.32 where the first bending modal shape and the first torsion modal shape are visible; it is worth noting that modal analysis in some cases can be quite useful for finding out some deficiencies in the mathematical model (for example parts separated from the chassis) and eliminating the non-realistic rigid body modes. In other words, sometimes modal analysis has been done before the static stiffness analyses.

The modal analysis of the structure is fundamental to study the NVH response of the vehicle. NVH is coming from the excitations due both to the vehicle riding on the road and to the thermal engine operation and is propagating through the structure. Further the comfort of the passenger into the passenger compartment is determined both by the acoustic eigenvalues of the compartment itself and by the vibration of the compartment walls.



Figure 4.31: Chassis with steel roof first bending mode –34.4 Hz



Figure 4.32: Chassis with steel roof first torsion mode –20.2 Hz

4.9 Results and discussion

At this section, firstly the results of load path analyses in the case of global bending and torsion loadings based on theoretical and simulation methods are presented and compared for the steel roof panel. Secondly, the results of different material solutions for stiffness analyses including modal, bending and torsional models are presented and finally results based on the modified roof panel thickness will be presented.

4.9.1 Bending load path analysis

Based on Eqs. 4.15 to 4.31, the only load subjected to the chassis is the loading on the front seats (F_{pf}) which is 6000 N. The results are as following:

$$R_F = F_{pf} (L - l_{pf})/L = 3568 \text{ N}$$

$$R_R = F_{pf} l_{pf}/L = 2432 \text{ N}$$

$$P_1 = P_3 = P_6 = 3000 \text{ N}$$

$$P_2 = P_4 = P_5 = P_7 = P_8 = P_9 = P_{10} = P_{11} = P_{12} = P_{13} = 0$$

Theoretical equations using SSSs model, mention that the vehicle “roof” is not under any specific loading during the global bending, while simulation presents another results. After implementing the bending stiffness analysis in Ls-Dyna, the distributed loads in roof panel obtained from the all defined sections in three directions of X, Y and Z and the average forces distribution are presented as following:

$$F_X = 300 \text{ N}$$

$$F_Y = 37 \text{ N}$$

$$F_Z = 80 \text{ N}$$

4.9.2 Torsion load path analysis

Based on Eqs. 4.32-4.45, by applying the torque equals to 1125.8 N.mm the equilibrium and input forces matrixes are as following:

$$\begin{bmatrix} 3128 & 0 & 0 & 0 & 0 & 0 & -1281 \\ 792 & 1281 & 0 & 0 & 0 & 0 & 0 \\ -762 & 0 & 1281 & 0 & 0 & 0 & 0 \\ -1496 & 0 & 0 & 1281 & 0 & 0 & 0 \\ -520 & 0 & 0 & 0 & 1281 & 0 & 0 \\ 770 & 0 & 0 & 0 & 0 & 1281 & 0 \\ 0 & -1557 & 833 & 675 & 702 & -1571 & 570 \end{bmatrix} = \text{Equilibrium Matrix}$$

$$\begin{bmatrix} 1184.8 \\ 1125.8 \\ 0 \\ 0 \\ 0 \\ 1125.8 \\ 2077.9 \end{bmatrix} = \text{Input Forces}$$

By multiplying the inverse of equilibrium matrix to input forces matrix, the edge forces are calculated as below:

$$\begin{bmatrix} 716 \\ 436 \\ 426 \\ 836 \\ 290 \\ 449 \\ 823 \end{bmatrix} = \begin{bmatrix} Q_1 \\ Q_2 \\ Q_3 \\ Q_4 \\ Q_5 \\ Q_6 \\ Q_7 \end{bmatrix} = \text{Edge Forces}$$

Q_1 and Q_4 are the transvers and longitudinal forces distributed through the roof panel based on SSSs model. Again these results have huge differences with the simulation findings; longitudinal and transvers forces distributed through the roof panel are reported as 91 N and 168 N by finite element method. The differences in results at the both loading case is quite expecting; the SSSs model just consists of the major parts not all of the them using only planar surfaces while

the original model consist of curvature shape shells connecting with constraints and beams that distributing the loadings in Z direction (through the thickness) too and reduce the load distribution through the panels. It is necessary to mention that the chassis used for these theoretical analyses is made of steel roof.

4.9.3 Stiffness analyses results

Results for modal analysis as presented in Figure 4.33 show that there are not big differences for the first bending and torsional frequencies of chassis with different material solutions. Static stiffness results as shown in Table 4.9 prove that chassis bending stiffness values are pretty close for all material solutions while there are considerable differences between the chassis torsional stiffness values. The steel solution has the highest value while the glass fiber/epoxy composite has the lowest value. This confirms the huge effect of the roof panel when the chassis is under the torsional loading. Results of stiffness values are in good agreement with the industrial reports for the passenger vehicles [2, 20, 21].

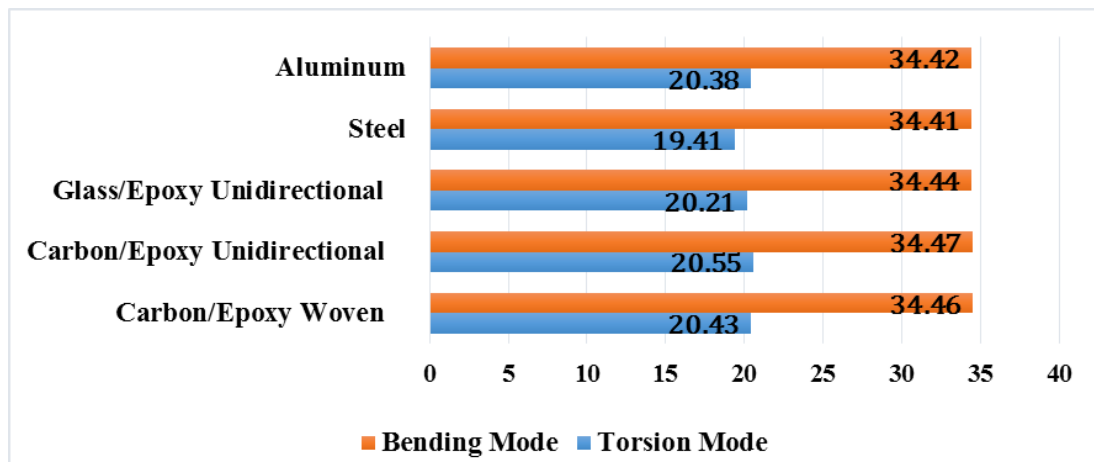


Figure 4.33: Modal frequencies (Hertz)

Light-weight index or body structure efficiency (LWI), is defined as the ratio of chassis mass to vehicle area A and to the torsional stiffness, it has been calculated according to Figure 4.34. This index is usually reported in industrial reports after stiffness analyses are accomplished for assessing the mass to stiffness ratio of BIW. It is clear that the lower the value of this index the lighter is the

solution, while maintaining similar values of the structural performance. Although the values reported in Table 4.9 are very close one to the other it is possible to note that the aluminum as well as the two carbon fiber composite solutions have the better results.

$$LWI = \frac{m}{A \times K_t}$$

m: Body mass (Kg)

A: Wheel base \times Track (m²)

K_t: Torsional stiffness (kNm/deg)

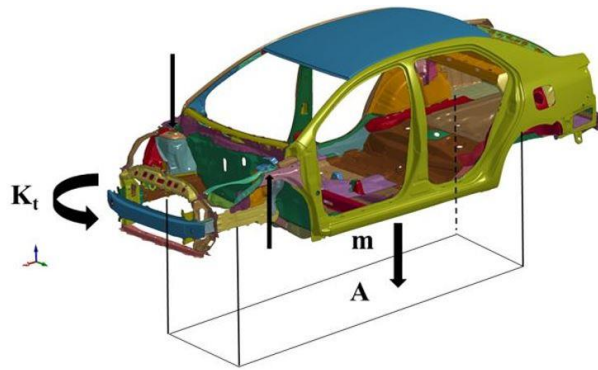


Figure 4.34: Light-weight index concept

Results for roof mass reduction percentages are presented in Table 4.9, together with the already mentioned bending and torsional stiffness, and light-weight indexes. It can be noted that in comparison with the reference steel solution there is a reduction of the roof weight of 32% in case of aluminum solution and of about 40% in case of the composite material solutions, considering non-structural mass (non-structural mass is the additional mass distributed on the roof panel) and without non-structural mass consideration, the roof panels' mass have been reduced by 66% and 81% for aluminum and composite with carbon fiber solutions respectively.

Table 4.9: Stiffness analyses results

Material	Bending Stiffness (N/mm)	Torsional Stiffness (Nm./deg)	Roof Mass Reduction Percentages with and without structural mass (%)	Light-Weight Index (Kg.deg/kN.m³)
Steel	7326	13286	-	5.61
Aluminum	7316	12914	32.57-65.80	5.56
Carbon/Epoxy Woven	7327	12743	40.40-81.65	5.58
Carbon/Epoxy Unidirectional	7326	12733	39.96-80.70	5.58
Glass/Epoxy Unidirectional	7328	12624	37.89-76.50	5.65

At the second step, thicknesses of roof panels except for the steel solution, which is assumed as the reference solution, have been increased based on the cubic root of their Young modulus rate to the steel one as described at section 4.3.2 and all the analyses have been performed again. The thickness of all solutions except the steel one has been increased based on the M2 method.

Stiffness results based on the modified thickness for each material solutions are presented in the Table 4.10. As it is conceived from Table 4.10, chassis torsional stiffness values increased by increasing roof thickness considerably. Light-weight index decreased by increasing roof thickness. Decreasing the light-weight index confirms the direct impact of thickness with the stiffness values. Using aluminum and unidirectional carbon fiber panels have lower light-weight indexes along with the mass reduction percentages of 25% and 38% for aluminum and composite solutions respectively (51% and 77% if non-structural mass is not considered).

Table 4.10: Modified stiffness analyses results

Material	Modified Roof Panel Thickness (mm)	Bending & Torsional Stiffness (N/mm-Nm./deg)	Roof Mass Reduction Percentages with and without structural mass (%)	Light-Weight Index (Kg.deg/kN.m³)
Steel	1.2	7326-13286	-	5.61
Aluminum	1.70	7319-13054	25.47-51.47	5.54
Carbon/Epoxy Woven	1.86	7344-12831	35.38-71.46	5.57
Carbon/Epoxy Unidirectional	1.40	7335-12813	38.40-77.58	5.56
Glass/Epoxy Unidirectional	2.23	7330-12822	27.92-56.37	5.63

4.10 Conclusion

In this chapter, the contribution of light-weight vehicle roof panel in the total vehicle stiffness has been studied and a method for optimizing the panel thickness which improves the vehicle structure efficiency has been presented.

At first, a benchmark for vehicle roof panel with respect to the most important factors of designing automotive panels has been developed. Then the chassis load path analysis under the bending and torsion loads has been done theoretically and numerically. The results have a big differences due to simplicity, unrealistic geometry of panels (planar faces) and lack of constraints, beams and joints of SSSs model which can affect the loading distribution pattern.

Next, the chassis static and dynamic stiffness analyses based on the standards have been implemented and the roof panel thickness with respect to the chassis weight and stiffness has been optimized for different material solutions. Results for modal analysis showed that there are not big differences for the first bending and torsional frequencies of chassis with different material solutions. Static stiffness results proved that chassis bending stiffness values are pretty close for all

material solutions while there are considerable differences between the chassis torsional stiffness values. The steel solution has the highest value while the glass fiber/epoxy composite has the lowest value. In order to have a trade-off between the chassis mass and stiffness, light-weight index has been defined. It is possible to note that the aluminum as well as the two carbon fiber composite solutions have lower light-weight indexes. It is important to mention that roof panels made of aluminum and carbon fibers reduced the panel mass (considering roof non-structural mass) by 32 % and 40% respectively.

Finally the thicknesses of roof panels except for the steel solution, have been increased based on the cubic root of their Young modulus rate to the steel one and all the analyses have been performed again. Chassis torsional stiffness values increased by increasing roof thickness considerably, while light-weight index decreased by increasing roof thickness and roof panels' mass have been reduced by 25% and 38% for aluminum and composite solutions respectively.

Part of the work described in this chapter has been published in "Lightweight design: Detailed comparison of roof panel solutions at crash and stiffness analyses, 2017 [22]" and "Light-Weight-Design: Detailed Comparison of Roof Panel Solutions at Crash and Stiffness Analyses, 2016 [23]".

4.11 References

- [1] Brown, J., Robertson, A.J., Serpento, S., Structural Design (2009). In Crolla, D.A. (Eds), *Automotive engineering: Powertrain, chassis system and vehicle body*, (pp. 525-566), Elsevier; Amsterdam; Boston: Oxford, U.K.; Burlington, Mass.: Butterworth-Heinemann.
- [2] Malen, D.E. (2011). *Fundamentals of automobile body structure design*. Warrendale, PA: SAE International.
- [3] Yang, Y., Zhao, G., Ma, D., & Xu, X. (2011). Mode calculation and testing of a car body in white. *Shock and Vibration*, vol. 18, pp. 289-298.
- [4] Obradovic, J., Boria, S., and Belingardi, G. (2011). Lightweight design and crash analysis of composite frontal impact energy absorbing structures. *Composite Structures*, vol. 94, pp.423-430.

- [5] Feraboli, P., Wade, B., Deleo, F., Rassaian, M., Higgins, M., Byar, A., (2011). LS-DYNA MAT54 modelling of the axial crushing of a composite tape sinusoidal specimen, *Composites Part A: Applied Science and Manufacturing*, vol. 42, pp. 1809-1825.
- [6] Belingardi, G., Beyene, A.T and Koricho, E.G. (2013). Geometrical optimization of bumper beam profile made of pultruded composite by numerical simulation. *Composite Structures*, vol. 102, pp.217-225.
- [7] Belingardi, G., Koricho, E.G., Martorana, B. (2013). Implementation of composite and recyclable thermoplastic materials for automotive bumper subsystem. *International Journal of Automotive Composites*, 1(1), pp. 67-89.
- [8] Keer, T., and Sturt, R. *Automotive Structures* (2007). In Melchers, R.E. and Hough, R. (Eds), *Modeling complex engineering structures in Automotive Structures*, (pp. 225-246), ASCE Press, Reston, VA, USA.
- [9] Zienkiewicz, O., *The finite element method*, McGraw-Hill, 1977.
- [10] Cook, R.D., Malkus, D.S., Plesha M.E., and Witt R.J. (2001). *Concepts and Applications of Finite Element Analysis*, Wiley.
- [11] Ibrahim, H.K. (2009). *Design Optimization of Vehicle Structures for Crashworthiness Improvement*, PhD thesis, Concordia University Montreal, Quebec, Canada.
- [12] Park, C.K, Kan, C.D, Hollowell, W.T, and Hill, S.I. Investigation of opportunities for light-weighting vehicles using advanced plastics and composites, Rep. DOT HS 811 692, National Highway Traffic Safety Administration, Washington, DC, 2012.
- [13] LS-DYNA Keyword User's Manual - Volume II. Material Models. Version R7.0. Livermore Software Technology Corporation, February 2016.
- [14] Ls-dyna theory manual, Hallquist J.O. (Ed.), California: Livermore Software Technology Corporation, 2006.
- [15] Stelzmann, U. and Hormann, M. Ply-based composite modelling with the new *ELEMENT_SHELL_COMPOSITE keyword, Proceedings of the 8th European LS-DYNA Users Conference, Strasbourg, May 2011.

- [16] NCAC. Finite element model archive. National Crash Analysis Centre, George Washington University, <http://www.ncac.gwu.edu/vml/models.html> (Accessed May 2014).
- [17] Bambach, M. (2014). Fiber composite strengthening of thin steel passenger vehicle roof structures. *Thin-Walled Structures*, vol. 74, pp.1-11.
- [18] <http://www.dynasupport.com/howtos/element/hourglass> (Accessed July 2014).
- [19] Jain A., (2014). Computational Analysis and Optimization of Torsional Stiffness of a Formula-SAE Chassis. SAE Paper No. 2014-01-0355.
- [20] Morello, L., Rossini L.R., Pia G. and Tonoli A. (2001). *The Automotive Body Volume II: System Design*, Springer, New York.
- [21] Happian-Smith, J. (2001). *An introduction to modern vehicle design* Elsevier, Woburn, MA.
- [22] Borazjani, S., Belingardi, G. (2017). Lightweight design: Detailed comparison of roof panel solutions at crash and stiffness analyses. *International Journal of Crashworthiness*, 22(1), pp. 49-62.
- [23] Light-Weight-Design: Detailed Comparison of Roof Panel Solutions at Crash and Stiffness Analyses, Borazjani, S., Belingardi, G., 1st International Conference on Impact Loading of Structures and Materials (ICILSM), Turin, 22/26 May 2016.

Chapter 5

Light-weight Design: Detailed Comparison of Roof Panel Solutions at Frontal Crash Analysis

5.1 Introduction

This chapter refers to modelling and evaluating the response of metallic roof panel as well as the composite ones during the vehicle full frontal crash. After some previous works related to crashworthiness applications of composite materials were reviewed, the preparation of vehicle finite element model with respect to metallic and composite roofs will be described. The simulation result of vehicle deformation mode during the impact will be compared with the real test to assure the accuracy of the simulation. Then, the behavior of roof panels made of different solutions will be evaluated by comparing the panel section forces and section displacements. Next, the internal energy dissipation through the roof panel during the crash will be compared for different material solutions and finally, the effect of increasing panel's thickness, based on the strategy described in previous chapter, on the panels' energy absorption will be studied.

5.2 State of the art

Several researches about the crashworthiness of composite materials were published. Belingardi et al. [1, 2] investigated the mechanical properties and impact resistance performance of the classical Glass Matrix reinforced

Thermoplastics (GMT) and the reinforced GMT (GMT_UD, GMTex) materials by quasi-static and dynamic tests. The results revealed that the reinforced GMT materials have higher strength and stiffness in comparison with the classical GMT. Also this research proved that the reinforced GMT materials have higher energy absorption efficiency and impact resistance while they have lower mass with respect to the classical GMT. The effectiveness of these materials for the vehicle bumper system were investigated by finite element codes. Boria et al. [3] investigated the mechanical properties of a full thermoplastic composite consists of the thermoplastic reinforcement and matrix. After performing tensile, compression, bending and shear tests to determine the mechanical properties of materials, thin-walled tubes were subjected under the axial static and dynamic loadings to assess the energy absorption capacity of tubes. The data were analyzed in terms of load–displacement curves, specific energy absorption (SEA), crush force efficiency (CFE), stroke efficiency (SE) and crushing stress. Results showed that the thermoplastic composite material are 3/4 times lower in energy absorption capacity in comparison with a common thermosets composite.

There are many published papers in which the composite tubes with regular cross sections ,rectangular and circular, have been tested [4, 5] under axial crash loading to compare the energy absorption capability of tubes and to demonstrate the suitability of the composite materials for this structural applications. There are researches [6-8] available offering non-standard cross-section for attenuators and tubes to improve the energy absorption of system. All these researchers have worked on various topologies and considered the effects of the laminate material properties, laminates stacking sequence, layer thickness and orientation on the energy absorption of the thin walled structures. The energy absorption capability of CFRP truncated conical structures made of high-strength carbon fibers embedded in an epoxy resin has been investigated through an experimental test by Boria et al. [9]. In this research cones models with different geometries, wall thickness, cone angle and internal diameters were tested. Results showed that for wall inclination angle of 5^0 , fronds have formed both internally and externally, while for greater inclination angles the frond has a tendency to form only inside the tube section. Results revealed that under the dynamic loading condition, energy absorption capacity and SAE values are less than those resulting from the corresponding quasi-static case. The possible reason has been reported as the difference between dynamic and static loading friction coefficient. It was shown that while increasing the cones wall laminate thickness and diameter have a direct impact on the energy absorption capacity of the sample, increasing the cone wall inclination has an opposite effect. Boria et al. [10] has done a research on the crashworthiness of a composite impact attenuator for a Formula SAE racing car to

assess deceleration values during crushing. The experimental test have been implemented using drop weight test machine while the simulation analysis have been done by the finite element code Ls-Dyna. The suitability of a progressive failure material model to simulate the quasi-static crushing of a composite specimen has been evaluated by Feraboli et al. [11]. Utilizing the commercial code LS-DYNA, he demonstrated that the achievement of successful simulation results requires extensive calibration of element size, contact definition, the definition of a load–penetration curve instead of the single contact’s constant penalty factor, and of the crush front softening parameters which are adopted for an element strength reduction algorithm. The model exhibited stable and progressive element failure and deletion, and was capable of capturing with accuracy the peak and average crush loads, as well as the overall load–displacement response. Feraboli’s studies determined that the SOFT crush front parameter is the most important parameter for determining the success of the simulation. Eshkoor et al. [12, 13] investigated the energy absorption response of triggered and non-triggered woven natural silk/epoxy composite rectangular tubes subjected to an axial quasi-static crushing test. In this research parameters such as peak load, energy absorption and specific energy absorption (SEA) were computed and compared. The analyses showed that the SEA values decreased a little with the increasing length of the composite specimen, while, due to the increment in the crush stroke, the total energy absorption increased with increasing length of the composite specimen. The peak load in the triggered specimens is nearly half of that in the non-triggered specimens, confirming the trigger effectiveness. Bambach et al. [14] worked on reinforcing thin-walled metal tubes with composite fibers. Composite reinforced tubes have been tested experimentally and studied analytically to demonstrate the suitability of application of these crush boxes in vehicle frontal crash. Bambach’s research showed the substantial improvements in vehicle crash performance and energy absorption system. Avalle et al. [15] has done a broad research on light-weight design of vehicle bonnet. In this work, different shape of designs and materials such as aluminum and thermoplastic were suggested and tested. Results revealed that although the thermoplastic solution contributes to vehicle weight reduction, it does not meet the stiffness performance standards. On the other hand, aluminum was introduced as a promising solution which 32% contributes to the weight reduction. Then the head injury criterion (HIC) value were reported for different bonnet solutions and the new methods for measurement of the translational and the rotational accelerations has been developed. Crashworthiness analysis of vehicle door using composite material as a new alternative has been investigated

by Belingardi and Jindong [16]. The conventional steel door was redesigned by using inner and outer composite panels and replaced with the composite reinforcing pane. Numerically modelling the side impact test, the energy absorption of vehicle door and the force transmitted to the dummy were measured and compared with the steel door as a reference. Results showed that the suggested design has an acceptable performance with respect to occupation safety merits, while it reduced the vehicle door mass by 32%. In this chapter, efforts have been made to evaluate the response of vehicle in case of full frontal crash with specific focus on roof panel material solutions and thickness.

5.3 Vehicle load path during frontal crash

During the crash occurrence, different parts of vehicle body undergo to large deformation. The reaction force flows through the vehicle body following different paths as shown in Figure 5.1. The frontal energy absorption area consists of the bumper, front part of the engine hood and crash boxes. The middle energy absorption area consists of the longitudinal front rail beams, fender, rear part of the engine hood and engine and suspension frames. At the crash moment, a first part of the kinetic energy has been absorbed by the frontal area, the remaining part of the energy is flowing through the hood, frontal rail beams and sub-frames and a portion of that energy is absorbed by these components. These energy absorptions are due to large plastic folding and bending deformation of the structural components through the crash. Once again the remaining energy is distributed through the passengers' cabin structure, and in this by the roof, which should absorb the rest of energy amount to be dissipated. At the same time, the cabin structure should prevent large intrusions, not only because of the reduction of the survival space but also because of direct impact against passengers' bodies [17, 18].

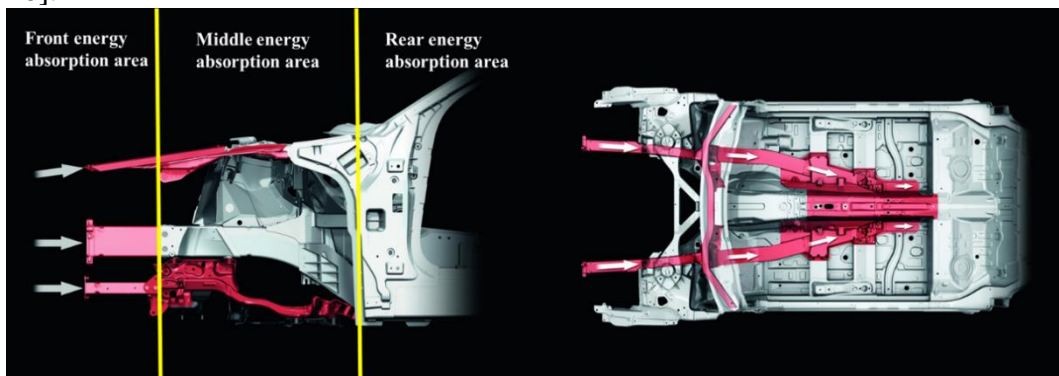


Figure 5.1: Vehicle energy absorption during frontal crash [17, 18]

5.4 Vehicle finite element model preparation for frontal crash

As it described in chapter 4, the FEM model of TOYOYA YARIS 2010 has been downloaded from the National Crash Analysis Centre (NCAC) provided by George Washington University. The vehicle model has the following statistics including connectors and joints as shown in Figure 5.2:

- 772- parts
- 950560- shell elements
- 19319- solid elements
- 4497- beam elements
- 974511- total number of elements
- 2862- spot welds
- 14- joints
- 998318- nodes

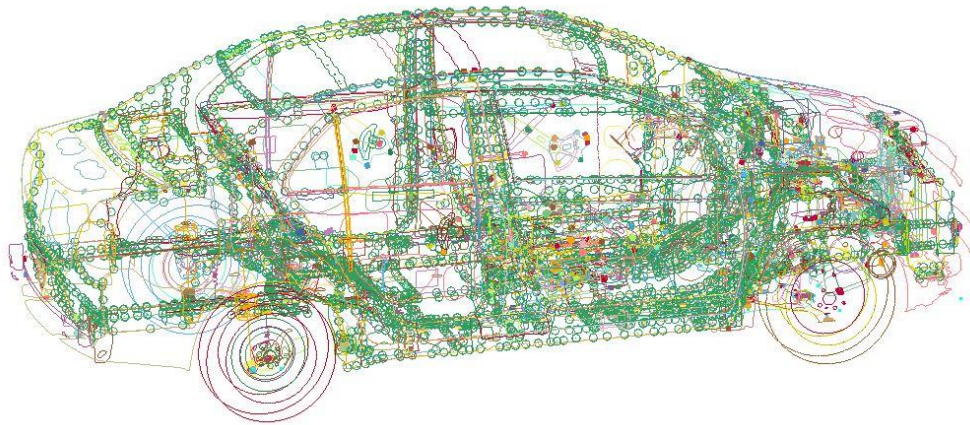


Figure 5.2: Vehicle finite element model including connectors and joints

The two contact algorithms of `Contact_Automatic_Single_Surface` and `Contact_Interior` have been used to model the contact between the vehicle and rigid barrier and vehicle internal parts respectively. The frontal crash test is done

based on the National Highway Traffic Safety Administration (NHTSA) standard 5677 that sets a full width impact against a rigid barrier at the initial velocity of 56.3 km/hr. LS-DYNA Explicit package along with mass scaling method have been used due to presence of large deformation and nonlinearities and to speed up the analysis. The sections that will be used for the analysis of the roof are defined at the roof pillars intersections. Figure 5.3 shows the finite element model of the vehicle along with the defined sections and the material coordinate system of the roof in the case of use of composite material. The FE model of the roof structure consists of 26000 shell elements with the thickness of 1.2 mm has been modelled. Mat 24, Piecewise Linear Plasticity and Mat 54/55 have been used to model the conventional and composite roof panels respectively. Material properties of traditional and composite solutions along with the complete simulation procedure of roof panels were described in the previous chapter. The same composite lay-up has been applied to model the composite panel.

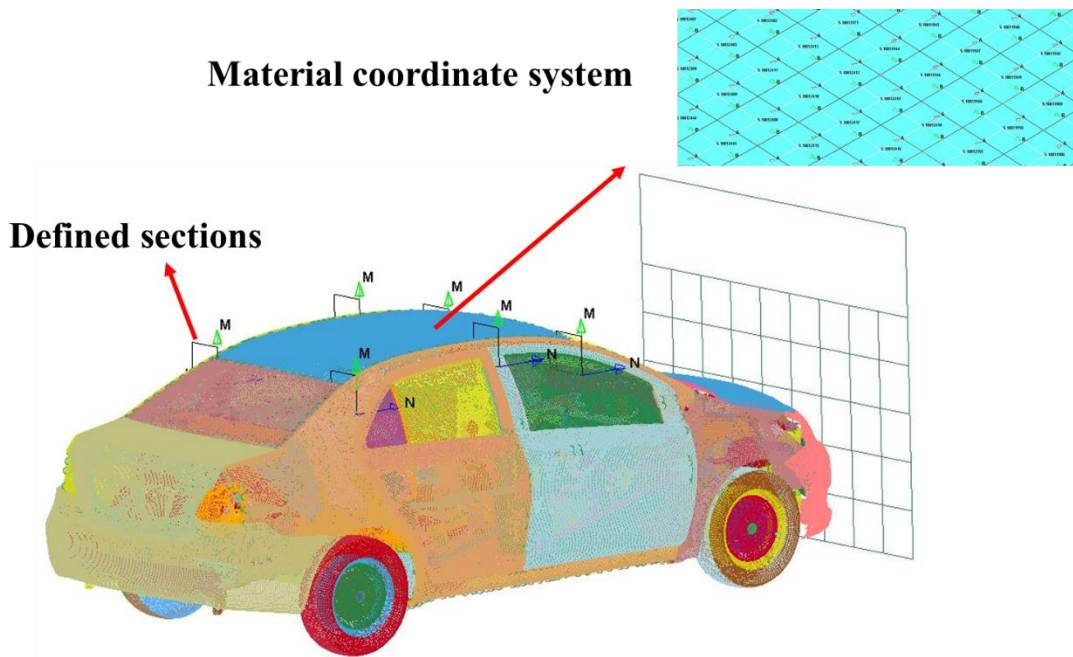


Figure 5.3: Vehicle finite element model

5.5 Results and discussion

First, the deformation mode of vehicle finite element model during the impact will be compared with real crash test to verify the accuracy of modeling. Second,

results related to panel section forces and section displacements will be presented and compared for different material solutions. Third, the curve related to time history of internal energy dissipation of roof panel made of different materials will be presented and finally, the effects of increasing thickness on the roof panel's energy absorption will be discussed.

5.5.1 Verifying the accuracy of model

Figure 5.4 shows the time history of vehicle frontal crash at three instants of time; the picture of real vehicle crash test is also shown in Figure 5.4 for sake of comparison. It can be observed that the numerical simulation results are well representative of the real crash test results.

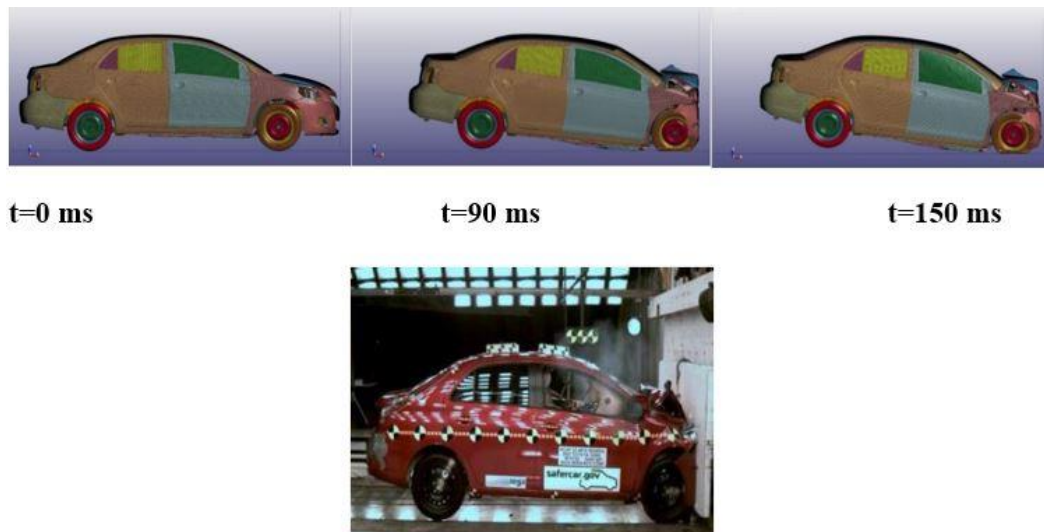


Figure 5.4: Images of vehicle frontal crash deformation at three subsequent time and comparison with a picture of the real crash test

Before presenting the results related to loading distribution through the roof panel, the rigid wall reaction force and the full model force-displacement curves through the frontal crash are presented as shown in Figures 5.5 and 5.6 respectively; they are in good agreement with the TOYOTA YARIS industrial report results [19].

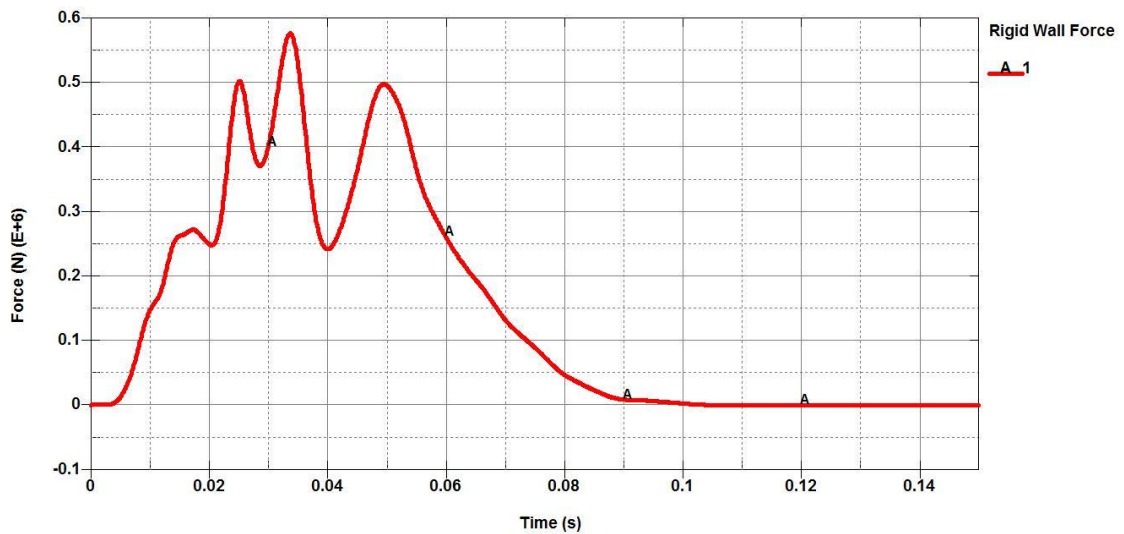


Figure 5.5: Rigid wall reaction force

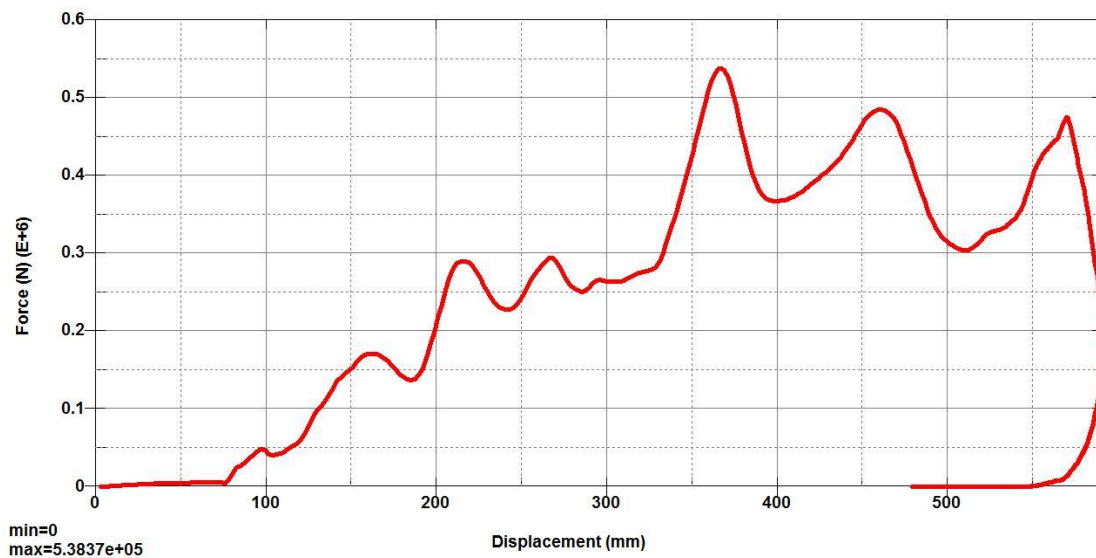


Figure 5.6: Full vehicle model force-displacement curve

5.5.2 Section forces and section displacement

In Figures 5.7-5.10 the resulting time histories of the longitudinal force (Figures 5.7 and 5.8) and of the x-displacement (Figures 5.9 and 5.10) are presented for two of the selected sections, in particular the two sections on the left and right hand roof rail at the intersection with the B-pillar (LHB-RHB). As shown in

Figures 5.7 and 5.8 the trend of longitudinal force is almost the same for all material solutions. Figure 5.7 shows that during the first 90 milliseconds the roof panel is under compressive force and absorbs energy but after 90 milliseconds the direction of section force has changed due to the spring-back behavior of the vehicle structure during the rebounding from the rigid wall. The direction of the section force in RHB has changed after around 80 milliseconds as shown in Figure 5.8. It is important to mention that the composite solutions properties are the same as what it has been reported in Tables 4.1-4.3.

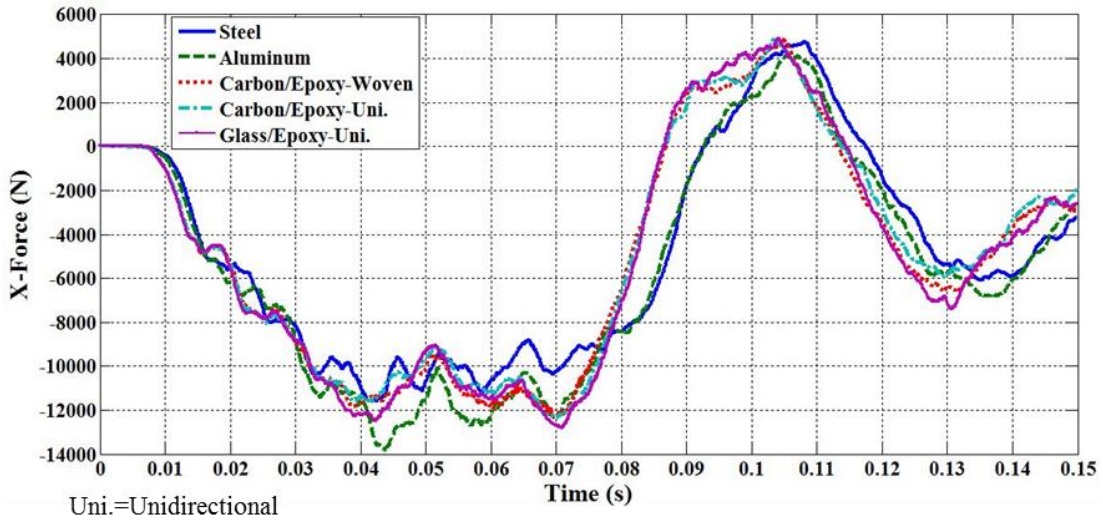


Figure 5.7: LHB longitudinal force vs time

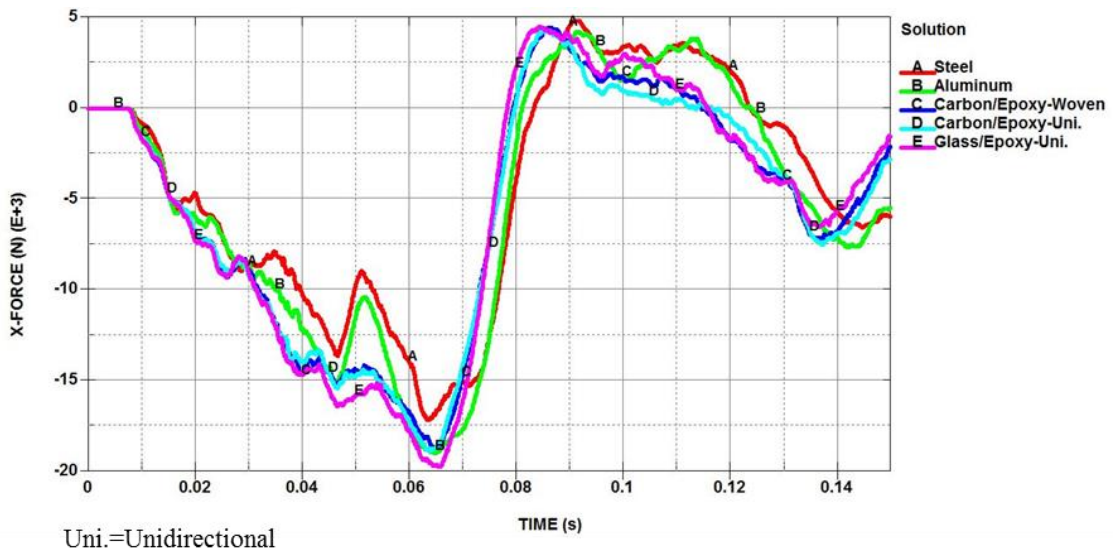


Figure 5.8: RHB longitudinal force vs time

The curves shown in Figures 5.9 and 5.10 are related to the displacement of the centroid of the selected sections. It is important to specify that the displacement is given by the sum of two parts: the rigid translation of the roof with the rest of the vehicle and the roof deformation. Although the trend and the values are similar, it is possible to see that the three composite material solutions exhibit lower values with respect to the metallic solutions, this difference is probably due to the different nature of the energy absorption mechanisms (that is mainly brittle fracture for the composite materials and plastic deformation for the metallic materials) and different modes of elastic buckling during the longitudinal force subjection. This difference in roof longitudinal deformation confirms the difference in the energy distribution through the roof panels as the composite solutions are less stiff than the traditional metallic solutions.

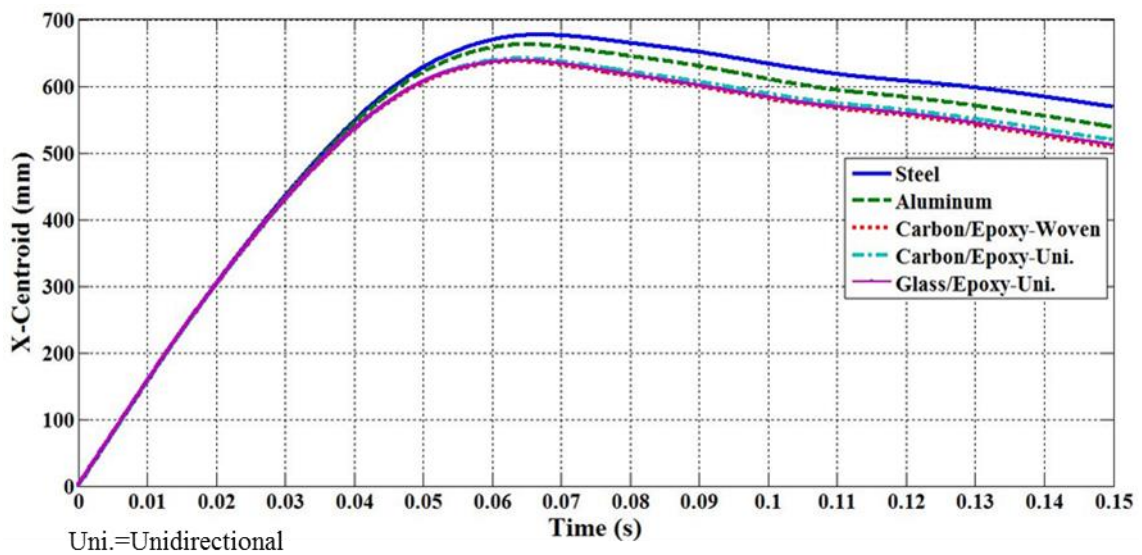


Figure 5.9: LHB longitudinal displacement vs time

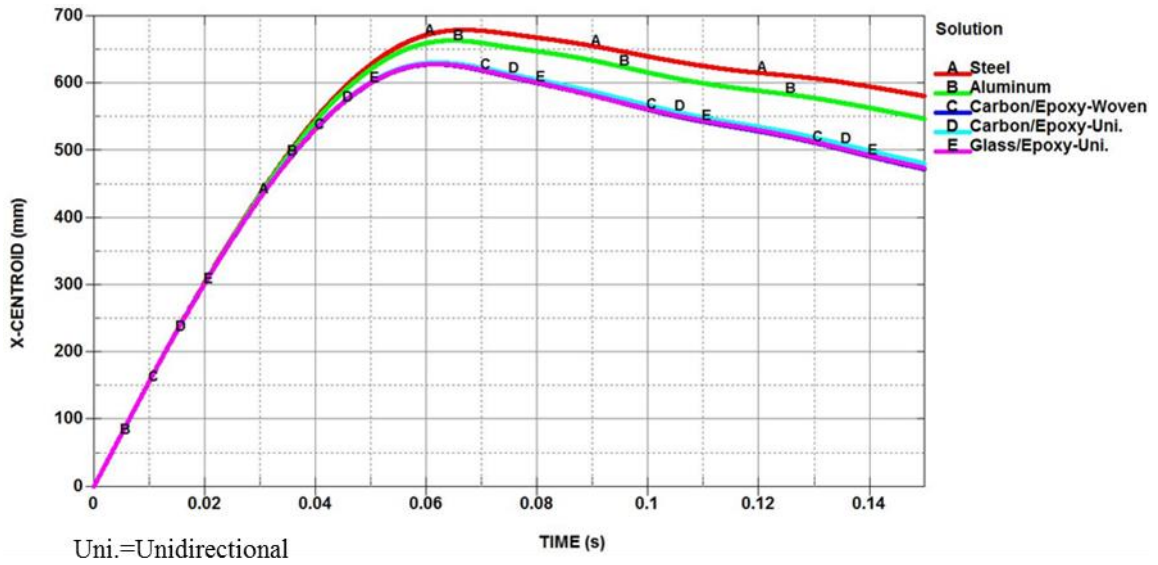


Figure 5.10: RHB longitudinal displacement vs time

The comparison of the roof deformed shape, based on the two material solutions of composite and metallic roofs, is presented in Figure 5.11. As it is depicted, during the frontal crash wrinkles appeared at the roof and cause deformation. These waves have a higher amplitude in the case of the composite roof than in the case of the metallic one due to composite’s brittle behavior and different modes of elastic buckling. Resistance to this type of deformation depends on the energy absorption capacity of the selected material and, as it was expected, the composite solution absorbs less amount of energy.

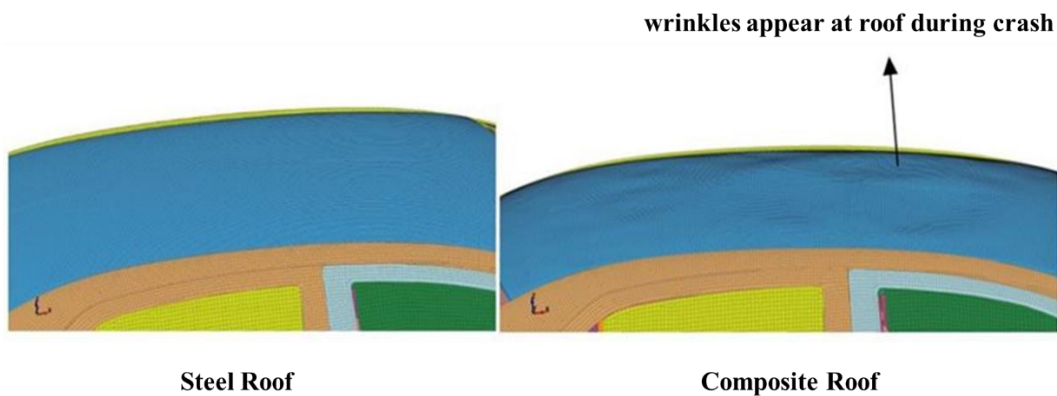


Figure 5.11: Wrinkles at roof through frontal crash at t=90 ms

5.5.3 Energy distribution

The total energy balance of the vehicle during the impact can be calculated by Eq. 5.1:

$$E_T = E_I + E_K + E_C + E_{RW} + E_{DAMP} + E_{HG} \quad \text{Eq. 5.1}$$

where E_T is the total energy, E_I is the internal energy, E_K is the kinetic energy, E_C is the contact energy, E_{RW} is the rigid wall energy, E_{DAMP} is the system damping energy and E_{HG} is the hourglass energy.

The internal energy is calculated based on Eq. 5.2 as follows:

$$E_I = E_S + E_{PD} \quad \text{Eq. 5.2}$$

where E_S is elastic strain energy and E_{PD} is work done in permanent deformation [20].

Figure 5.12 shows the vehicle total energy dissipation during the crash and this result is in a good agreement with the TOYOTA YARIS report [19]. Figure 5.13 is dealing with the roof panel internal energy dissipation for different material solutions. Since full integrated elements have been used to model roof panels, the hourglass energy is zero and due to the fact that there is no permanent deformation in roof panel in full frontal crash E_{PD} is equal to zero and internal energy is equal to elastic strain energy. The highest values of internal energy are for steel and aluminum solutions. Composites have less amount of internal energy absorption due to their brittle nature, lower compressive strengths and different modes of elastic buckling. It is quite well visible that up to 50 ms the curves are well superimposed then for the two metallic material solutions a further increment, larger for the steel solution, followed by a stabilization are visible, while for the composite material solutions it is possible to notice a progressive reduction of the internal deformation energy. This is due to the wrinkles occurred at the composite roof panels resulting in non-stabilized energy dissipation reduction.

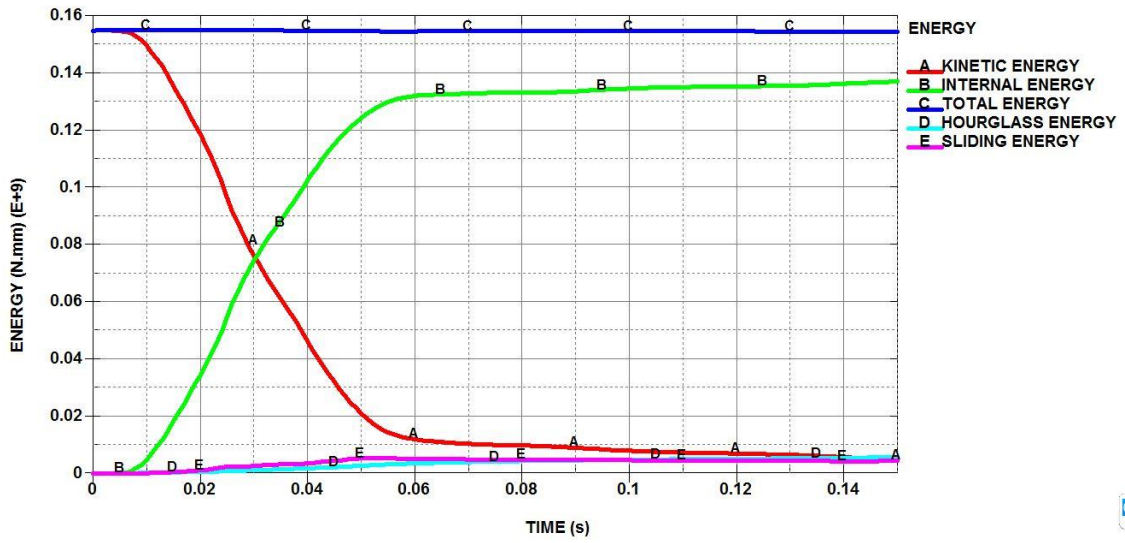


Figure 5.12: Vehicle total energy dissipation

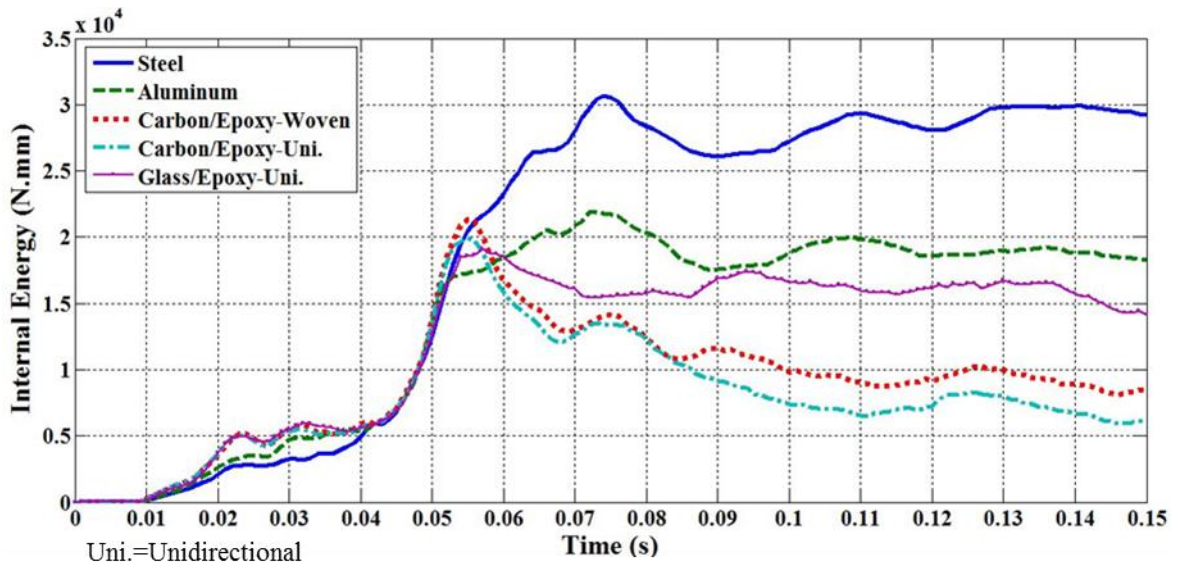


Figure 5.13: Roof internal energy dissipation

As it described in chapter 4, thicknesses of roof panels except for the steel solution, which is assumed as the reference solution, have been increased based on the equal bending stiffness approach [21]. Increasing thicknesses has substantial effects on the energy absorption of the roof panel as it is shown in Figure 5.14. If a comparison is made between the values of this Figure with those

of the previous Figure 5.13, it is possible to note that for all the material solutions the energy absorption has been increased except for the steel (that is the reference solution) and for the woven carbon fiber. This is probably because the Mat 54/55 material model is designed for modelling unidirectional fiber and is less accurate for the woven fibers. The maximum energy absorption increment has been obtained for the aluminum solution (+9 %) while for the unidirectional carbon fiber solution is 4% and less than 1% for the unidirectional glass fiber one.

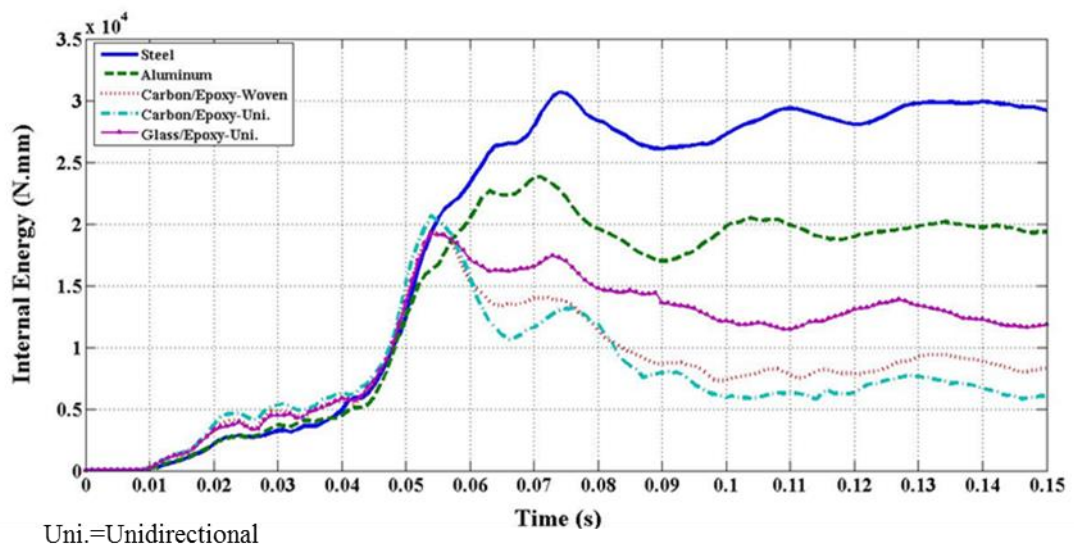


Figure 5.14: Roof internal energy dissipation with modified thickness

5.6 Conclusion

In this chapter, efforts have been made to present some results of a broad research about the vehicle roof behaviour during the frontal crash with the specific focus on the material solutions and roof shell thickness. The Toyota Yaris finite element model available on-line has been considered and modified appropriately for the study. At first, roofs with the same thickness and different material solutions have been examined. Results for two of the selected sections prove that, as it was expected, the traditional solutions of steel and aluminum absorb more energy than the composite ones. This is due to their ability of large plastic deformation. Next, the thickness of roof has been increased according to the equal bending stiffness criteria, i.e. proportionally to the ratio of material Young modulus. After repeating the crash analyses, energy-absorption capacity of roof system has been raised around 9% for the aluminum and 4% for the unidirectional carbon fiber solutions

and the ability of roof panel for deformation have been improved. Based on the presented results for modified panel thickness, aluminum and unidirectional carbon fiber solutions it comes out that the composite solutions give comparable stiffness. Although with lower energy absorption capacity of the roof in comparison with the steel solutions but they have large contribution, up to 40%, to the weight reduction of vehicle roof panel along with the acceptable structural performance. Therefore composite material solution can be a valuable substitution for the steel roof panel. This chapter helps to have a detailed information about the response of vehicle roof panel made of different solutions during the frontal crash.

Part of the work described in this chapter has been published in “Lightweight design: Detailed comparison of roof panel solutions at crash and stiffness analyses, 2017 [22]” and “Light-Weight-Design: Detailed Comparison of Roof Panel Solutions at Crash and Stiffness Analyses, 2016 [23]” and “Light-Weight Design Application: Design of a composite vehicle roof and analysis in the frontal crash, 2015 [24].

5.7 References

- [1] Belingardi, G., Beyene, A.T., & Jichuan, D. (2016). Energy absorbing capability of GMT, GMTex and GMT-UD composite panels for static and dynamic loading—Experimental and numerical study. *Composite Structures*, vol. 143, pp. 371-387.
- [2] Belingardi, G., Beyene, A., Koricho, E., & Martorana, B. (2015). Alternative lightweight materials and component manufacturing technologies for vehicle frontal bumper beam. *Composite Structures*, vol. 120, pp. 483-495.
- [3] Boria, S., Scattina, A., & Belingardi, G. (2016). Experimental evaluation of a fully recyclable thermoplastic composite. *Composite Structures*, vol. 140, pp. 21-35.
- [4] Ochelski, S., and Gotowicki, P. (2009). Experimental assessment of energy absorption capability of carbon epoxy and glass-epoxy composites. *Composite Structures*, vol. 87, pp. 215-224.
- [5] Boria, S., and Belingardi, G. (2012). Numerical investigation of energy absorbers in composite materials for automotive applications. *International Journal of Crashworthiness*, vol. 17, pp. 345-356.

- [6] Kathiresan M., Manisekar K., and Manikandan V. (2014). Crashworthiness analysis of glass fiber/epoxy laminated thin walled composite conical frusta under axial compression. *Composite Structures*, vol. 108, pp. 584-599.
- [7] Obradovic, J., Boria, S., and Belingardi, G. (2011). Lightweight design and crash analysis of composite frontal impact energy absorbing structures. *Composite Structures*, vol. 94, pp. 423-430.
- [8] Wang, J., Yang, N., Zhao, J., Wang, D., Wang, Y., and Li, K. (2016). Design and experimental verification of composite impact attenuator for racing vehicles. *Composite Structures*, vol. 141, pp. 39-49.
- [9] Boria, S., Scattina, A., & Belingardi, G. (2015). Axial energy absorption of CFRP truncated cones. *Composite Structures*, vol. 130, pp. 18-28.
- [10] Boria, S., Obradovic, J., & Belingardi, G. (2015). Experimental and numerical investigations of the impact behaviour of composite frontal crash structures. *Composites Part B: Engineering*, vol. 79, pp. 20-27.
- [11] Feraboli, P., Wade, B., Deleo, F., Rassaian M., Higgins M., Byar A. (2011). LS-DYNA MAT54 modelling of the axial crushing of a composite tape sinusoidal specimen. *Composites Part A: Applied Science and Manufacturing*, vol. 42, pp. 1809-1825.
- [12] Eshkoo, R., Oshkoo, S.A., Sulong, A., Zulkifli R., Ariffin A.K., and Azhari, C.H. (2013). Comparative research on the crashworthiness characteristics of woven natural silk/epoxy composite tubes, *Materials & Design*, vol. 47, pp. 248-257.
- [13] Eshkoo, R., Ude, A., Oshkoo, S.A., Sulong, A., Zulkifli, R., Ariffin, A.K., and Azhari C.H. (2014). Failure mechanism of woven natural silk/epoxy rectangular composite tubes under axial quasi-static crushing test using trigger mechanism. *International Journal of Impact Engineering*, vol. 64, pp. 53-61.
- [14] Bambach, M. (2013). Fiber composite strengthening of thin-walled steel vehicle crush tubes for frontal collision energy absorption. *Thin-Walled Structures*, vol. 66, pp. 15-22.

- [15] Avalle, M., Belingardi, G., & Scattina, A. (2013). Numerical and experimental investigation of a lightweight bonnet for pedestrian safety. *International Journal of Crashworthiness*, 18(1), pp. 29-39.
- [16] Belingardi, G., & Jindong, J. (2016). Crashworthiness evaluation of composite vehicle side door with an innovative design. *International Journal of Automotive Composites*, 2(1), pp. 75-93.
- [17] Chunyu, W., and Bing, W. (2007). Research on car frame structure crashworthiness by application of FEA method, *Autom. Eng.* vol. 4, pp. 41-46.
- [18] Shen, H., Qiao, X., Chen, H. BIW Safety Performance Research Based on Vehicle Frontal Crash, *Proceedings of the FISITA 2012 World Automotive Congress, 2012, Lecture Notes in Electrical Engineering* 197.
- [19] NCAC, "Development and Validation of a Finite Element Model for a 2010 Toyota Yaris Sedan" NCAC 2011-T-001, prepared for FHWA, 2011.
- [20] Lund, E.G, Jecmenica, M., Melteig, O., Robbersmyr, K.G., Karimi, H.R. (2015). Development and validation of a nonlinear dynamic impact model for a notch impact, *The International Journal of Advanced Manufacturing Technology*, 80(9), pp. 1945–1955.
- [21] Belingardi, G., Koricho, E.G., Martorana, B. (2013). Implementation of composite and recyclable thermoplastic materials for automotive bumper subsystem. *International Journal of Automotive Composites*, 1(1), pp. 67-89.
- [22] Borazjani, S., Belingardi, G. (2017). Lightweight design: Detailed comparison of roof panel solutions at crash and stiffness analyses. *International Journal of Crashworthiness*, 22(1), pp. 49-62.
- [23] Light-Weight-Design: Detailed Comparison of Roof Panel Solutions at Crash and Stiffness Analyses, Borazjani, S., Belingardi, G. 1st International Conference on Impact Loading of Structures and Materials (ICILSM), Turin, 22/26 May 2016.
- [24] Light-Weight Design Application: Design of a composite vehicle roof and analysis in the frontal crash- Borazjani, S., Belingardi, G. NUAKA I MOTORNA VOZILA SCIENCE AND MOTOR VEHICLES- International Automotive Conference, Belgrade, Serbia-2015.

Chapter 6

Crashworthiness Analysis of the Innovative Composite-sandwich based Vehicle Roof Structure

6.1 Introduction

The high rate of crash accidents fatalities urged the car manufacturer companies to improve the safety of vehicles. It is reported that around 33000 people died in United States due to different type of accidents in 2010 [1]. It is quite important to mention that although rollover crashes allocate small portion of total crashes, around 2.1%, this is the most deadly type of crash. Unfortunately 35% of people involved in rollover crashes died, that is around 7600 people. Since, even if passengers are fastening their seatbelts (but in this particular case seatbelts are less effective due to their particular geometry), there is a high chance of fatalities, 31%, in rollover accidents, it is vital to design the vehicle roof component structure with an high standard of safety [1].

This chapter aims to develop an innovative design solution for the vehicle roof structure in rollover crash analysis. In the first section of this chapter, after reviewing the fracture modeling procedure of steel, composite and foam materials, progressive failure analysis of thin-walled tubes made of steel, composite and composite foam-filled materials will modeled. Deformation and failure modes of tubes will be presented and discussed for different solutions to show the efficiency

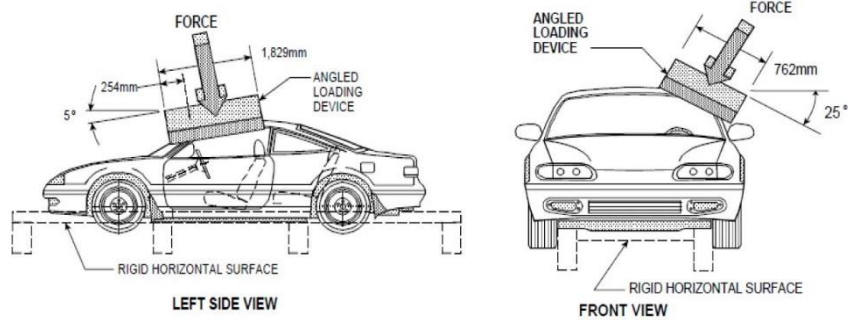
of composite-foam design solution. In the second section, the preparation of vehicle finite element model for rollover quasi-static test will be discussed. Then, after implementing the velocity dependency test, the contribution of windscreens to the vehicle stiffness will be shown. The next step is showing the importance of vehicle roof panel between the main BIW components in the case of energy absorption. Fulfilling these tasks, designs made of steel, composite and sandwich solutions for the roof panel will be presented and their efficiency will be evaluated. The last step is optimizing the sandwich solutions regarding to face-sheets thickness and foam core density.



Figure 6.1: Passenger vehicle occupant deaths by vehicle type, 1975-2014 [1]

In spite of the existence of various roof crush tests, government institutions are pushing even higher safety margins. There are different types of static and dynamic roof crush tests, Figure 6.2, such as the Federal Motor Vehicle Safety Standard (FMVSS) 216 [2], Inverted Vehicle Drop Dynamic Test (Society of Automotive Engineering, SAE, J996) [3] and Dolly Rollover Test (SAE J2114) [4] that are aimed to evaluate the vehicle roof structure performance. The initial rules of FMVSS prescribed that the vehicle roof should sustain a force equal to 1.5 times the unloaded vehicle weight (UVW). The new updated standard, FMVSS 216a, [5] increased this margin by considering the force to be applied to the vehicle roof structure equal to 3 times the UVW with the new obligation of making test on both driver and passenger sides, the comparison of the FMVSS 216 and FMVSS 216a standards is presented in Table 6.1. There is also more conservative type of vehicle roof crush test standard which is considering the

applied load equal to 4 times UVW, set by Insurance Institute for Highway Safety (IIHS) [6] as shown in Table 6.2.



Static roof crush test (FMVSS 216)

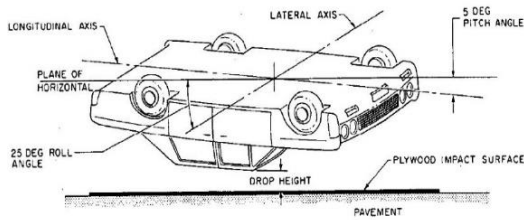


FIG. 1—INVERTED VEHICLE DROP TEST DROP POSITION

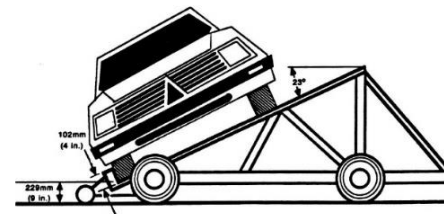


FIGURE 1—DOLLY ROLLOVER FIXTURE

Inverted vehicle drop dynamic test (SAE J996)

Dolly rollover test (SAE J2114)

Figure 6.2: Vehicle roof crush tests

Table 6.1: Vehicle roof crush static test standards (FMVSS vs. updated FMVSS) [6]

Test Parameter	FMVSS 216 Current Standard	FMVSS 216a Final Rule
Required Load	1.5 times UVW or 5,000 lbs - whichever is less (GVWR of 6,000 lbs or less)	3.0 times UVW (GVWR of 6,000 lbs or less) 1.5 times UVW (GVWR of 6,000 to 10,000 lbs)
Required Maximum Displacement	5 inches	5 inches or contact up to 50 lbs with Head Positioning Fixture (HPF)
Interior Fixture Placement	Not required	HPF is placed in each front occupant position
Load Location	Driver or Passenger Side	Driver and Passenger Sides
Platen Angle Monitoring	No tolerance specified	Must stay within $\pm 0.5^\circ$ of original pitch (5°) and roll (25°) platen angles throughout test.
Load Rate	Up to 0.5 inches/second	
Test Platen	30 inches x 72 inches	
Vehicle Tie-Down	Vehicle supported off of suspension with sills or chassis frame secured to I-beam structures with epoxy. Note: Prior to 2006, FMVSS 216 required vehicles to be supported off the suspension with the sills or chassis frame secured to a tie down fixture with chains and binders.	
Vehicle and Test Platen Orientation	5° (pitch) and 25° (roll); forward-most point on roof 10 inches from edge of platen and initial contact point aligned with the longitudinal centerline of platen.	

Table 6.2: Vehicle roof crush static test standards (FMVSS vs. IIHS) [6]

Test Parameter	FMVSS 216a	IIHS
Intent of Test	Legal requirement	Not required by law; testing done for consumer informational purposes
Test Load	3.0 x UVW	4.0 x UVW
Load Location	Driver and Passenger side	Driver or Passenger side
Maximum Displacement	5 inches	10 inches (rating is based on first five inches)
Load Rate	Up to 0.5 inches/sec	0.2 inches/sec
Tie Down	Support sills through I-beam structures and epoxy	Support sills through I-beam structures that clamp to pinch weld
Vehicle Attitude	$0^\circ \pm 0.5^\circ$ measured at sill	$\pm 0.5^\circ$ of the angle measured at sill of vehicle on a flat surface. Angle is also adjusted according to platen longitudinal angle if it is \pm 5°
External Instrumentation	Head Positioning Fixture	None

IIHS standard test acceptable margins for vehicle roof crashworthiness during the quasi-static test are presented in Figure 6.3. As mentioned before, strength-to-weight ratio of beyond 4 will satisfy the requirements.

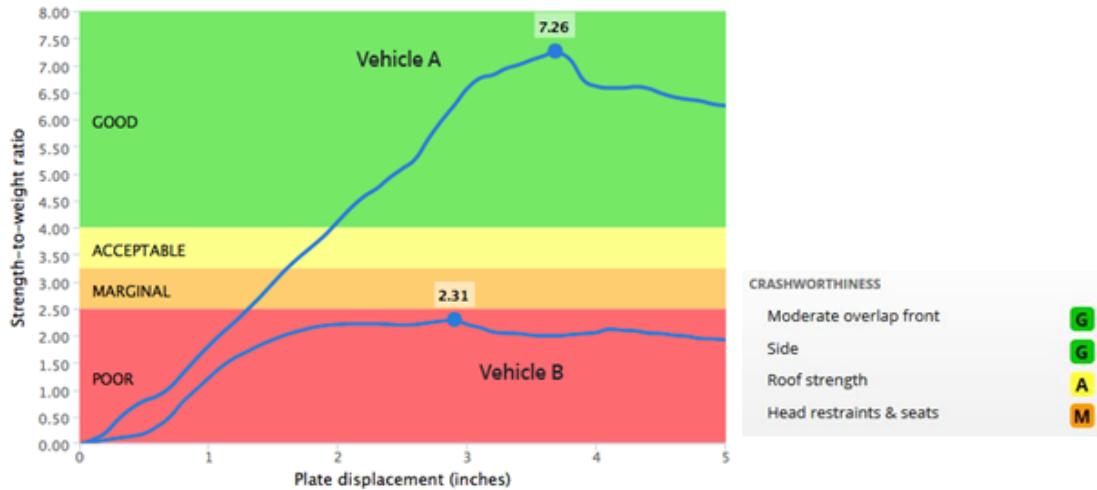


Figure 6.3: IIHS vehicle roof crashworthiness margins (<http://www.iihs.org>)

Composites as energy absorber, light-weight and anti-corrosion materials are the perfect substitutions for metallic structure specifically in the case of impact. Although these materials have not the possibility for plastic deformation due to their brittle nature, they have high stiffness and strength to weight ratios. Several works have been done on investigating the energy absorption and crashworthiness of composite and sandwich structures. Mamalis et al. [7] studied the collapse modes of sandwich panels made of composite face-sheets and a foam core under axial compression force. Three collapse modes were observed. The first collapse mode occurred with foam core shear failure and sandwich fragmentation. The second mode was characterized by face-sheets delamination and buckling and the third one was the progressive crushing mode. It was proved that the third mode is the most important type of sandwich collapse mode due to energy absorption capacity of the structure; it depends on the foam core properties. Many papers such as [8-10] studied sandwich tubes under tension and compression. Tarlochan et al. [10] tested sandwich structures made of different cores and face-sheets materials and designs under axial loading. Tubes made with a sandwich structure with composite skin reinforcement made of carbon, glass or Kevlar fibers along with Expanded Polystyrene (EPS) or Polyurethane (PU) cores have been tested. These studies have demonstrated that carbon fiber and EPS are the best solution

for face-sheet and core respectively. There are some papers available in which innovative designs have been presented. Zhang et al. [11] designed honeycomb sandwich circular tube to improve energy absorption efficiency. This design is made of two circular aluminum tubes filled in between with a core shaped as a large-cell lattice. It was found that the buckling of lattices controls the folding of the outer and inner tubes which results in an increment of the plastic deformation of the tube. It was observed that the intrusion of the folded tube walls into the honeycomb cell gaps, strengthen the crashworthiness of the honeycomb cell. Zangani et al. [12] proposed the foam-filled twin-walled composite hollow box sections with internal reinforcement. Progressive failure of the suggested tubes in respect to different corner designs and arrangements of the corrugation configuration inside the foam core were studied experimentally and numerically. Strain rate effects on the material properties of foam structure has been determined by quasi-static test just at low strain rates in [13]. Also damage and failure of the considered foam structure have been studied under the drop tests and obtained experimental results have been compared with numerical results.

Li et al. [14] evaluated the crashworthiness of hollow and foam-filled circular tubes under three-points bending test. During test the failure modes of hollow, foam-filled single and foam-filled double tubes were observed and the total energy absorption, the specific energy absorption and the energy –absorbing effectiveness factor were determined. This research proved that the foam-filled double tubes has higher resistance to the bending load and absorbed the highest energy. Steeves and Fleck [15] investigated the collapse modes of sandwich structures consisting of woven glass fiber face-sheet and PVC foam core under bending load by experiment and simulation. Different types of collapse modes such as face-sheet microbuckling and indentation, core shearing and crushing were observed depending on the sandwich geometry and foam core density. Collapse modes of sandwich structures with respect to the slenderness ratio of the beam and the relative thickness of face-sheet to core were investigated. Damage indentation of sandwich structure with rigid foam core under compressive load has been investigated and tested by Rizov et al. [16]. Typical dimensions of the damaged zone on the sandwich face-sheet have been measured and load-displacement curves have been obtained. Using finite element codes residual stress and strains after unloading were calculated and compared with the experimental results. Johnson and Li [17] investigated the effects of puncher nose shape and the foam core density on the indentation of sandwich structures. It was

found that the foam core density has a high influence on the energy absorption of sandwich structures.

Previous works have discussed different methods in order to increase the strength of vehicle roof structure during rollover crash. Mao et al. [18] strengthened the vehicle roof structure by increasing roof components thickness, placing steel tubes inside the initial design and foam filling of the roof panel based on the requirements of the FMVSS 216 and inverted dynamic tests standards; simulations have been done with the finite element code LS-DYNA. Although these techniques increased the vehicle weight from 1% to 2.3%, they could increase the energy absorption of roof components. Pan and Zhu [19] proposed surrogate-based design to optimize the roof strength efficiency. Different types of computational optimization methods such as kriging, radial basis function, support vector regression and various weighted average surrogates have been tried to select the most effective optimization method. After having applied different optimization algorithms, weighted surrogate method proved the highest efficiency by raising the crush resistance force of 41.7% while the vehicle weight reduced by 5.3%. A new design of thermoplastic countermeasure concept to reinforce vehicle roof structure has been introduced in [20]. Countermeasure concept modifies the original structure by adding longitudinal ribs along the bending direction stiffened by cross ribs to strengthen local buckle points. The proposed design presented in a full plastic countermeasure and a plastic/metal hybrid countermeasure placed inside the B-Pillar. The efficiency of the design has been evaluated by numerical simulation and it was shown that while achieving the same strength of the traditional steel design, countermeasure concept reduced the structure weight by 40-50%. Rahul and Mirdamadi [21] improved the roof structure stiffness by adding structural foam inside the vehicle body structure. After having observed the efficiency of the design, the model was optimized to maximize the roof structure strength and minimize the vehicle mass. Bambach [22] has proposed to improve the vehicle roof system performance by using bonded composite metal structures. After roof crush quasi-static tests, his studies showed that the suggested model has the potential to contribute to higher roof strengths and light-weighting of vehicles.

6.2 General framework for modeling material progressive damage and failure in ABAQUS

The framework of material failure for different materials in ABAQUS is presented in Figure 6.4 for a metallic sample under the uniaxial loading. During the material failure process, material loses the load-carrying capacity results from the material stiffness degradation. Failure analysis of material in abaqus is divided to the three main phases. The first phase (a-b) is related to the linear elastic behavior of the material. To model the elasticity behavior of different types of material, the elastic Young's modulus and Poisson's ratio are required. At the second phase (b-c) plastic behavior with the strain hardening of the material occurs; from point c up to point d is related to the damage response of the material under the loading. c is considered as the point of damage initiation which is considered based on the defined failure criterion. Degradation of material stiffness at the third phase (c-d) is obtained by the damage evolution law and d is the point of complete rupture of the material. It is worth to mention that without the damage consideration of the material, the response of the material would be at the d' direction [23].

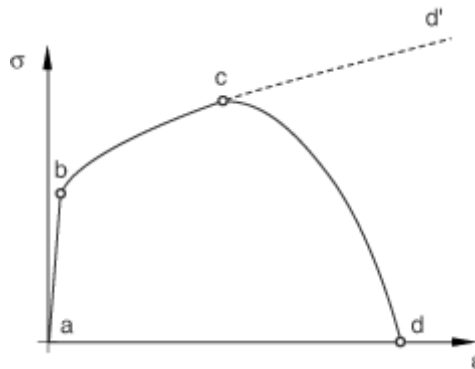


Figure 6.4: Typical uniaxial stress-strain response of a metal specimen [23]

6.2.1 Simulation of progressive failure analysis of metallic structures in ABAQUS

The elasticity behavior of ductile material is defined using elastic material properties while plastic models are implemented to predict plastic deformation of the metallic structures. As soon as the material damage begins beyond the yield strength of the material, damage initiation and evolution criteria are needed to fully capture the realistic behavior of the structure.

6.2.1.1 Modeling plasticity behavior of metals with Johnson-Cook model

In order to study the plasticity behavior of metallic structures, the Johnson-Cook plastic model is used. Johnson-Cook plasticity models is one of the most efficient model capable of considering the effects of strain hardening, strain-rate (viscosity) and thermal softening [24].The Johnson-Cook plasticity model is represented by the Eq. 6.1:

$$\bar{\sigma} = \underbrace{\left[A + B \left(\bar{\epsilon}^{pl} \right)^n \right]}_{\text{Strain hardening effect}} \underbrace{\left[1 + C \ln \left(\frac{\dot{\bar{\epsilon}}^{pl}}{\dot{\bar{\epsilon}}_0} \right) \right]}_{\text{Strain-rate (viscosity) effect}} \underbrace{\left[1 - \left(\frac{T - T_{room}}{T_m - T_{room}} \right)^m \right]}_{\text{Thermal softening effect}} \quad \text{Eq. 6.1}$$

Where

$\bar{\sigma}$ = equivalent plastic stress

$\bar{\epsilon}^{pl}$ & $\dot{\bar{\epsilon}}^{pl}$ = equivalent plastic strain & equivalent plastic strain rate

$\dot{\bar{\epsilon}}_0$ = reference equivalent plastic strain rate

A: Johnson-Cook yield strength

B: Johnson-Cook hardening coefficient

C: Johnson-Cook strain rate constant

n & m: Johnson-Cook strain hardening exponent & Johnson-Cook softening exponent

6.2.1.2 General framework of ductile damage initiation criteria for metallic structures

In order to study the fracture mechanisms of the metallic structures, the two damage initiation failure criteria of ductile and shear criteria have been defined in ABAQUS. Ductile fracture caused by nucleation, growth, and coalescence of voids; and shear fracture due to shear band localization can be modelled [25]. In the case of bending of metallic tubes for this research only the ductile criterion is considered.

The ductile damage criterion predicts the damage initiation based on assumption that the equivalent plastic strain at the damage onset, $\bar{\epsilon}_D^{pl}$ is a function of strain rate and stress triaxiality Eq. 6.2:

$$\bar{\epsilon}_D^{pl} \left(\eta, \dot{\bar{\epsilon}}^{pl} \right) \quad \text{Eq. 6.2}$$

The stress triaxiality is defined as $\eta = -p/q$, where p is the pressure stress, q is the Von Mises stress and $\dot{\bar{\epsilon}}^{pl}$ is the equivalent plastic strain rate. The damage initiates if a scalar damage parameter ω_D as below exceeds 1:

$$\omega_D = \int \frac{d\bar{\epsilon}^{pl}}{\bar{\epsilon}_D^{pl}(\eta, \dot{\bar{\epsilon}}^{pl})} = 1 \quad \text{Eq. 6.3}$$

6.2.1.3 Johnson-Cook damage initiation criterion

Johnson-Cook damage model [26] is a specific form of the ductile damage initiation criterion in which d_1 - d_5 are representative of five failure parameters as Eq. 6.4:

$$\bar{\epsilon}_D^{pl} = \left[d_1 + d_2 \exp(-d_3 \eta) \right] \left[1 + d_4 \ln \left(\frac{\dot{\bar{\epsilon}}^{pl}}{\dot{\bar{\epsilon}}_0} \right) \right] \left[1 + d_5 \frac{T - T_0}{T_m - T_0} \right] \quad \text{Eq. 6.4}$$

where T , T_m and T_0 are the current, melting and the transition temperature respectively.

6.2.1.4 Damage evolution of metallic structures based on effective plastic displacement and the fracture energy

The damage evolution law determines the rate of material stiffness degradation after the damage initiation criterion has been satisfied. In the case of ductile materials the material stiffness is degraded considering the scalar damage variable of D ; once the damage begins the stress tensor is updated according to the Eq. 6.5 [23]:

$$\sigma = (1 - D) \bar{\sigma} \quad \text{Eq. 6.5}$$

where $\bar{\sigma}$ is the undamaged stress tensor; once the damage variable D becomes 1, the material has no longer the load-carrying capacity.

The importance of applying the damage evolution law is shown in Figure 6.5. The graph shows the behavior of the material in the damage situation presence. In the absence of damage evolution law, the stress-strain curve will continue the rising manner after the onset of the damage as shown with the dash line; while by considering the damage evolution law in the analysis the stress should be reduced as shown with the solid line. As shown in Figure 6.5 the damage effect is

appeared into the two forms of elastic properties degradation and softening of the yield stress.

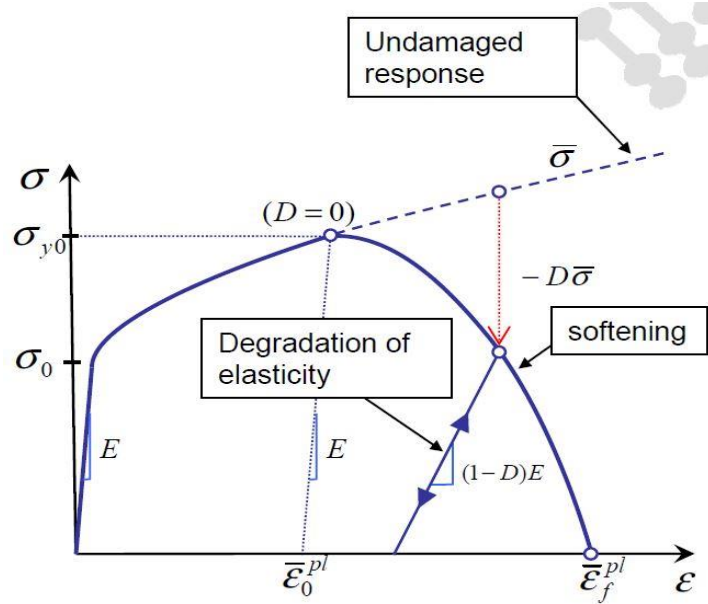


Figure 6.5: Material stress-strain curve regarding to progressive damage degradation [23]

As shown in Figure 6.5, σ_{y0} and $\bar{\epsilon}_0^{pl}$ are the yield stress and equivalent plastic strain at the onset of damage respectively while $\bar{\epsilon}_f^{pl}$ is the equivalent plastic strain at failure. Due to dependency of the equivalent plastic strain at failure as the damage occurs to the element characteristic length, it is not possible to consider the $\bar{\epsilon}_f^{pl}$ as a material parameter in the damage evolution law; however it is possible to consider the equivalent plastic displacement, \bar{u}^{pl} , or fracture energy dissipation, G_f , as the damage evolution law material parameter [27]. This technique reduces the mesh dependency by expressing the stress-strain behavior in terms of stress-displacement format. The idea was taken from estimating the dissipated energy during the opening of one unit area of crack; in this way by implementing this technique to the finite element method for the element with characteristic length of L the fracture energy can be calculated by the Eq. 6.6:

$$G_f = \int_{\bar{\epsilon}_0^{pl}}^{\bar{\epsilon}_f^{pl}} L \sigma_y d\bar{\epsilon}^{pl} = \int_0^{\bar{u}_f^{pl}} \sigma_y d\bar{u}^{pl} \tag{Eq. 6.6}$$

where \bar{u}^{pl} is the equivalent plastic displacement after the damage onset; so before the damage initiation $\dot{\bar{u}}^{pl}$ is 0 while after the damage initiation it becomes $L\dot{\bar{\epsilon}}^{pl}$.

The material damage variable with respect to the equivalent plastic displacement is evaluated in different forms of linear, tabular and exponential. It is important to mention that if the plastic displacement at failure, \bar{u}_f^{pl} is defined as 0, then the sudden failure of material is expected.

If the damage variable is linearly evolved then the damage variable increasing rate can be defined as below in Eq. 6.7:

$$\dot{d} = \frac{L\dot{\bar{\epsilon}}^{pl}}{\bar{u}_f^{pl}} = \frac{\dot{\bar{u}}^{pl}}{\bar{u}_f^{pl}} \quad \text{Eq. 6.7}$$

where the material stiffness is fully degraded when the $\bar{u}^{pl} = \bar{u}_f^{pl}$.

If the damage variable is exponentially evolved by the exponent factor of α with respect to the effective plastic displacement then the damage variable can be calculated based on the effective plastic displacement at failure as in Eq. 6.8:

$$d = \frac{1 - e^{-\alpha\left(\frac{\bar{u}^{pl}}{\bar{u}_f^{pl}}\right)}}{1 - e^{-\alpha}} \quad \text{Eq. 6.8}$$

It is also possible to define the damage evolution parameter based on the dissipated fracture energy per unit area during the damage process indicated by G_f . The damage variable with respect to the fracture energy can be evolved linearly and exponentially. In the case of linear damage evolution based on Eq.6.7 the equivalent plastic displacement at failure can be calculated as a terms of the dissipated fracture energy and the yield stress as in Eq.6.9:

$$\bar{u}_f^{pl} = \frac{2G_f}{\sigma_{y0}} \quad \text{Eq. 6.9}$$

If the damage variable then evolved exponentially, the damage variable is calculated as in Eq. 6.10:

$$d = 1 - \exp\left(-\int_0^{\bar{u}^{pl}} \frac{\bar{\sigma}_y \dot{\bar{u}}^{pl}}{G_f}\right) \quad \text{Eq. 6.10}$$

6.2.2 Simulation of progressive failure analysis of composite structures in ABAQUS

The same constants are required to capture the elastic behavior of the composite material. In order to model the damage initiation of composite material using Hashin's theory [28-30], it is necessary to define the material's strength parameters; while fracture toughness energies are required to model the damage evolution of composite material. The theories related to estimate the damage initiation and evolution of composite material are presented at the following sections.

6.2.2.1 Modeling damage initiation of composite materials

Abaqus predicts the damage initiation of composite materials based on the theory presented by Hashin [29, 30]. This theory is capable of predicting the damage initiation, which refers to onset of the material stiffness degradation, considering the failure modes of fiber and matrix in tension and compression directions as follows in Eqs. 6.11-6.14:

$$\text{Fiber tension mode } (\hat{\sigma}_{11} \geq 0) \quad F_f^t = \left(\frac{\hat{\sigma}_{11}}{X^T} \right)^2 + \alpha \left(\frac{\hat{\tau}_{12}}{S^L} \right)^2 \quad \text{Eq. 6.11}$$

$$\text{Fiber compression mode } \hat{\sigma}_{11} < 0 \quad F_f^c = \left(\frac{\hat{\sigma}_{11}}{X^C} \right)^2 \quad \text{Eq. 6.12}$$

$$\text{Matrix tension mode } \hat{\sigma}_{22} \geq 0 \quad F_m^t = \left(\frac{\hat{\sigma}_{22}}{Y^T} \right)^2 + \left(\frac{\hat{\tau}_{12}}{S^L} \right)^2 \quad \text{Eq. 6.13}$$

Matrix compression mode $\hat{\sigma}_{22} < 0$

$$F_m^c = \left(\frac{\hat{\sigma}_{22}}{2S^T} \right)^2 + \left[\left(\frac{Y^C}{2S^T} \right)^2 - 1 \right] \frac{\hat{\sigma}_{22}}{Y^C} + \left(\frac{\hat{\tau}_{12}}{S^L} \right)^2 \quad \text{Eq. 6.14}$$

where X^T and X^C are longitudinal tensile and compressive strength respectively; Y^T and Y^C are transverse tensile and compressive strength respectively; S^T and S^L are longitudinal and transverse shear strength respectively. α is the representative of shear stress contribution to the fiber tensile initiation criterion. $\hat{\sigma}_{11}$, $\hat{\sigma}_{22}$ and $\hat{\tau}_{12}$ are the representative of the effective stress tensors. At the above-mentioned relations $\alpha=0$ and $S^T=Y^C/2$ if the damage initiation criterion specified by Hashin and Rotem [29] and α equals to 1 if the initiation criterion is based on Hashin [30].

The effective stress tensors is calculated by multiplying the true stress into the damage operator as in Eq. 6.15:

$$\hat{\sigma} = M\sigma \quad \text{Eq. 6.15}$$

where

$$M = \begin{bmatrix} \frac{1}{(1-d_f)} & 0 & 0 \\ 0 & \frac{1}{(1-d_m)} & 0 \\ 0 & 0 & \frac{1}{(1-d_s)} \end{bmatrix}$$

where d_f , d_m and d_s are the damage variable for fiber, matrix and shear damage respectively and related to the tension and compressive damage modes according to the following relations (Eqs. 6.16-6.18):

$$d_f = \begin{cases} d_f^t & \text{if } \hat{\sigma}_{11} \geq 0, \\ d_f^c & \text{if } \hat{\sigma}_{11} < 0, \end{cases}$$

$$d_m = \begin{cases} d_m^t & \text{if } \hat{\sigma}_{22} \geq 0, \\ d_m^c & \text{if } \hat{\sigma}_{22} < 0, \end{cases}, \quad \text{Eqs. 6.16-6.18}$$

$$d_s = 1 - (1 - d_f^t)(1 - d_f^c)(1 - d_m^t)(1 - d_m^c)$$

6.2.2.2 Modeling damage evolution of composite materials

The behavior of the composite material after the onset of the damage is specified through the damage evolution law. The damage elasticity matrix shown by C_d is calculated according to Eqs. 6.19-6.20 [23]:

$$\sigma = C_d \varepsilon \quad \text{Eq. 6.19}$$

$$C_d = \frac{1}{D} \begin{bmatrix} (1-d_f)E_1 & (1-d_f)(1-d_m)v_{21}E_1 & 0 \\ (1-d_f)(1-d_m)v_{12}E_2 & (1-d_m)E_2 & 0 \\ 0 & 0 & (1-d_s)GD \end{bmatrix} \quad \text{Eq. 6.20}$$

where D is equal to:

$$D = 1 - (1 - d_f)(1 - d_m)v_{12}v_{21}$$

d_f and d_m are representative of fiber and matrix damage variables respectively and d_s is the shear damage variable that calculated based on Eq. 6.21:

$$d_s = 1 - (1 - d_f^t)(1 - d_f^c)(1 - d_m^t)(1 - d_m^c) \quad \text{Eq. 6.21}$$

As mentioned before, due to dependency of the equivalent plastic strain at the damage onset to the element characteristics length, the damage constitutive law is expressed as stress-displacement. The equivalent stress versus equivalent displacement at the linear damage evolution process is shown in Figure 6.6. In Figure 6.6 leg OA is representative of the linear elastic behavior of the material while the leg AC indicates the stiffness degradation of material stiffness through damage evolution process. Point A indicates the onset of material damage (damage initiation point). Any unloading or loading during the damage evolution process (as in point B) will result in moving the graph through the path OB to the origin of the plot. G^c is the fracture energy dissipated in each failure mode calculated as the area under the OAC triangle. δ_{eq}^0 is the initial equivalent displacement at which the damage initiation criterion is satisfied for a specific failure mode and it depends on elastic properties and strength parameters of the material. δ_{eq}^f indicates the equivalent displacement when the material stiffness is completely degraded in a specific failure mode and depends on the G^c as shown in Eq. 6.22:

$$\delta_{eq}^f = \frac{2G^c}{\delta_{eq}^0} \quad \text{Eq. 6.22}$$

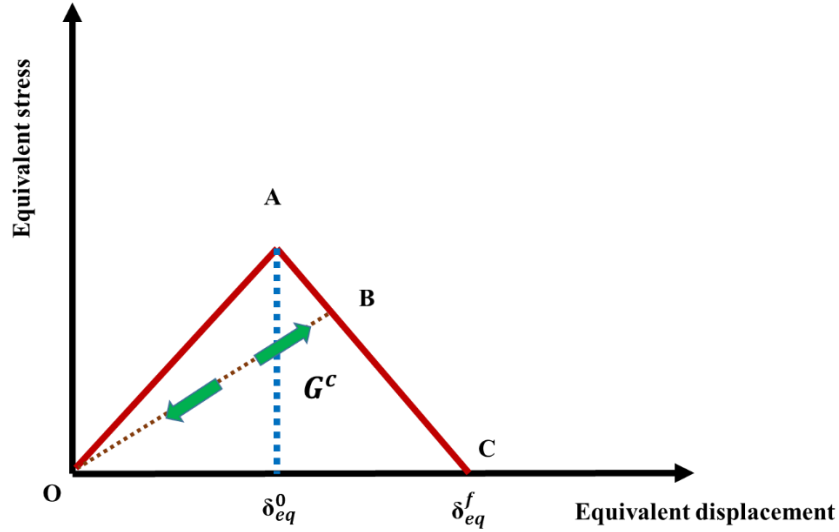


Figure 6.6: Schematic of composite stress-strain curve in linear damage evolution [23]

The equivalent displacement and stress for each failure mode are calculated according to Eqs. 6.23-6.30:

Fiber tension mode ($\hat{\sigma}_{11} \geq 0$):

$$\delta_{eq}^{ft} = L^c \sqrt{\langle \varepsilon_{11} \rangle^2 + \alpha \varepsilon_{12}^2} \quad \text{Eq. 6.23}$$

$$\sigma_{eq}^{ft} = \frac{\langle \sigma_{11} \rangle \langle \varepsilon_{11} \rangle + \alpha \tau_{12} \varepsilon_{12}}{\delta_{eq}^{ft} / L^c} \quad \text{Eq. 6.24}$$

Fiber compression mode $\hat{\sigma}_{11} < 0$:

$$\delta_{eq}^{fc} = L^c \langle -\varepsilon_{11} \rangle \quad \text{Eq. 6.25}$$

$$\sigma_{eq}^{fc} = \frac{\langle -\sigma_{11} \rangle \langle -\varepsilon_{11} \rangle}{\delta_{eq}^{fc} / L^c} \quad \text{Eq. 6.26}$$

Matrix tension mode $\hat{\sigma}_{22} \geq 0$

$$\delta_{eq}^{mt} = L^c \sqrt{\langle \varepsilon_{22} \rangle^2 + \varepsilon_{12}^2} \quad \text{Eq. 6.27}$$

$$\sigma_{eq}^{mt} = \frac{\langle \sigma_{22} \rangle \langle \varepsilon_{22} \rangle + \tau_{12} \varepsilon_{12}}{\delta_{eq}^{mt} / L^c} \quad \text{Eq. 6.28}$$

Matrix compression mode $\hat{\sigma}_{22} < 0$

$$\delta_{eq}^{mc} = L^c \sqrt{\langle -\varepsilon_{22} \rangle^2 + \varepsilon_{12}^2} \quad \text{Eq. 6.29}$$

$$\sigma_{eq}^{mc} = \frac{\langle -\sigma_{22} \rangle \langle -\varepsilon_{22} \rangle + \tau_{12} \varepsilon_{12}}{\delta_{eq}^{mc} / L^c} \quad \text{Eq. 6.30}$$

At the above-mentioned equations L^c is the characteristic element length and the symbol $\langle \rangle$ represents the Macaulay bracket operator defined as $\langle x \rangle = \frac{1}{2}(x + |x|)$; $\forall x \in \mathbb{R}$.

Generally as the material damage initiates ($\delta_{eq} \geq \delta_{eq}^0$), the damage variable for each mode is calculated as in Eq. 6.31:

$$d = \frac{\delta_{eq}^f (\delta_{eq} - \delta_{eq}^0)}{\delta_{eq} (\delta_{eq}^f - \delta_{eq}^0)} \quad \text{Eq. 6.31}$$

The clearer of the Eq. 6.31 concept is indicated in Figure 6.7 as below:

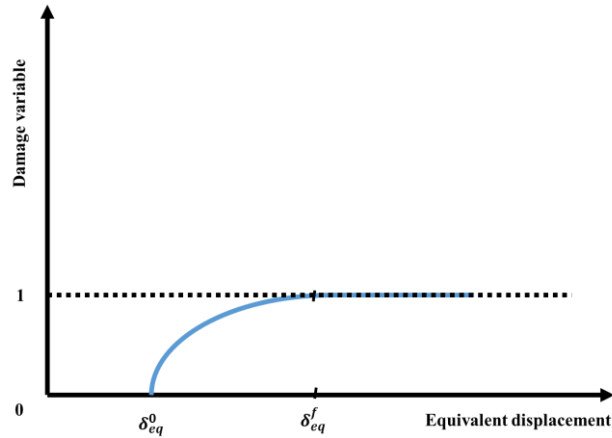


Figure 6.7: Damage variable definition based on equivalent displacement [23]

6.2.3 Modeling crushable foam in ABAQUS

The foam material is designed in ABAQUS as an elasto-plastic material; In order to model the elasticity behavior of the foam material the elastic Young's modulus and Poisson's ratio are required.

6.2.3.1 Defining yield surface

In order to simulate the plasticity behavior of the foam structures in ABAQUS, two hardening models are available; the volumetric and isotropic hardening models. The hardening models use a yield surface which is a Von Mises circle in the deviatoric stress plane and an ellipse in the meridional (p-q) stress plane. In the volumetric hardening model, the hydrostatic tension loading point at the yield ellipse is fixed while the compressive plastic strain controls the evolution of the yield surface as shown in Figure 6.8. On the contrary, the isotropic hardening model uses the yield ellipse centered at the origin of the p-q stress plane and as it evolves the original height to width ratio of the ellipse is fixed based on the model developed by Deshpande and Fleck [31] for the metallic foams as shown in Figure 6.9. Due to the fact that hardening models must describe the uniaxial compression yield stress as a function of the corresponding plastic strain, true stress and plastic strain should be calculated by Eqs. 6.32-6.33 [32]:

$$\sigma_{\text{True}} = \sigma_{\text{Eng}} (1 + \varepsilon_{\text{Eng}}) \quad \text{Eq. 6.32}$$

$$\varepsilon_{\text{Plastic}} = \text{Ln} (1 + \varepsilon_{\text{Eng}}) - \frac{\sigma_{\text{True}}}{E} \quad \text{Eq. 6.33}$$

where σ_{Eng} and σ_{True} are the engineering and true stresses respectively while ε_{Eng} and $\varepsilon_{\text{Plastic}}$ are the engineering and plastic strains respectively. In the present work the volumetric foam hardening method has been used to model the plasticity behavior of the foam structures.

The yield surface for volumetric hardening model is defined as a function of pressure and Mises stresses shown at Eq. 6.34:

$$f(p, q) = \sqrt{q^2 + \alpha^2 \left(p - \frac{p_c - p_t}{2} \right)^2} - \alpha \frac{p_c + p_t}{2} = 0 \quad \text{Eq. 6.34}$$

where the pressure (p) and Mises (q) stresses are defined as below:

$$P = -\frac{1}{3} \text{tr}(\bar{\sigma}) \quad \text{Eq. 6.35}$$

$$q = \sqrt{\frac{3}{2} \bar{\sigma}^D \cdot \bar{\sigma}^D} \quad \text{Eq. 6.36}$$

$\bar{\sigma}^D$ is the deviatoric stress defined as:

$$\bar{\sigma}^D = \bar{\sigma} + pI \quad \text{Eq. 6.37}$$

And α is the shape factor of the yield ellipse representative of the vertical and horizontal axes relative magnitude depending on the initial yield stress in uniaxial compression (σ_c^0), the initial yield stress in hydrostatic compression (p_c^0) and the yield strength in hydrostatic tension (p_t) calculated based on Eq. 6.38:

$$\alpha = \frac{3k}{\sqrt{(3k_t + k)(3 - k)}} \quad \text{Eq. 6.38}$$

where k and k_t defines as; $k = \frac{\sigma_c^0}{p_c^0}$ and $k_t = \frac{p_t}{p_c^0}$.

6.2.3.2 Flow potential

The plastic strain rate is defined based on the volumetric hardening model as in Eq. 6.39:

$$\dot{\varepsilon}^{pl} = \dot{\varepsilon}^{pl} \frac{\partial G}{\partial \bar{\sigma}} \quad \text{Eq. 6.39}$$

where G is the flow potential and defined by Eq. 6.40,

$$G = \sqrt{q^2 + \frac{9}{2} p^2} \quad \text{Eq. 6.40}$$

The equivalent plastic strain rate is defined as Eq. 6.41 and related to the rate of axial plastic strain in uniaxial compression by Eq. 6.42.

$$\dot{\varepsilon}^{pl} = \frac{\bar{\sigma} \cdot \dot{\varepsilon}^{pl}}{G} \quad \text{Eq. 6.41}$$

$$\dot{\varepsilon}^{pl} = \sqrt{\frac{2}{3}} \dot{\varepsilon}_{axial}^{pl} \quad \text{Eq. 6.42}$$

6.2.3.3 Hardening model

As it is clear in Figure 6.8 the yield surface intersects the p-axis at $-p_t$ and p_c . While p_t remains fixed during the material plastic deformation, p_c changes as the material density changing. As the yield surface evolution is expressed by the hydrostatic stress axis size, $p_c + p_t$, it can be a function of the volumetric compacting plastic strain, $-\varepsilon_{vol}^{pl}$ as in Eq. 6.43 [23]:

$$p_c(\varepsilon_{vol}^{pl}) = \frac{\sigma_c(\varepsilon_{axial}^{pl}) \left[\sigma_c(\varepsilon_{axial}^{pl}) \left(\frac{1}{\alpha^2} + \frac{1}{9} \right) + \frac{p_t}{3} \right]}{p_t + \frac{\sigma_c(\varepsilon_{axial}^{pl})}{3}} \quad \text{Eq. 6.43}$$

It is worth to mention that during the uniaxial compression in the volumetric hardening model, $\varepsilon_{axial}^{pl} = \varepsilon_{vol}^{pl}$, so the input data for the model would be uniaxial compression stress vs axial plastic strain.

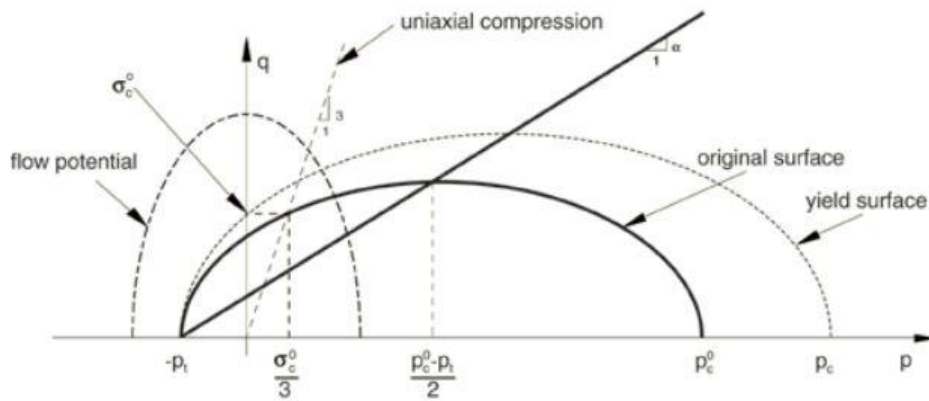


Figure 6.8: Crushable foam model with volumetric hardening: yield surface and flow potential in the p-q stress plane [23, 31]

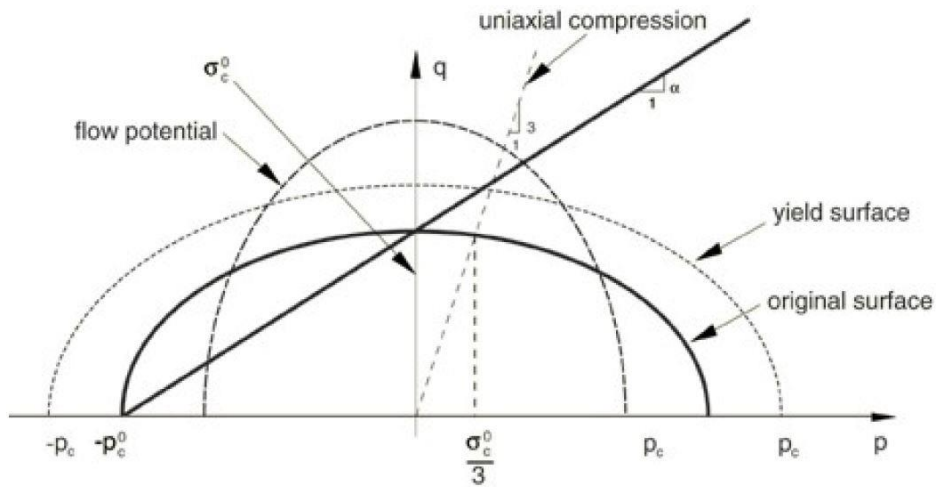


Figure 6.9: Crushable foam model with isotropic hardening: yield surface and flow potential in the p - q stress plane [23, 31]

6.3 Progressive failure analysis of tubes at three-points bending loading

In order to study the energy absorption efficiency of the sandwich structure, three-points bending test of tubes will be performed as a component test. Three-points bending test helps to study the behavior of different structures under the loading with respect to their energy absorption capacity. In this part crashworthiness performance of the steel, composite and composite foam-filled tubes will be studied. Tubes specifications are as follows:

- Tube diameter: 30 mm
- Tube wall thickness: 1.2 mm
- Tube length: 200 mm
- Puncher diameter: 10 mm

The tube supporting pins are constraint in all degrees of freedom while the loading pin constraint in all direction except in loading direction as shown in Figure 6.10.

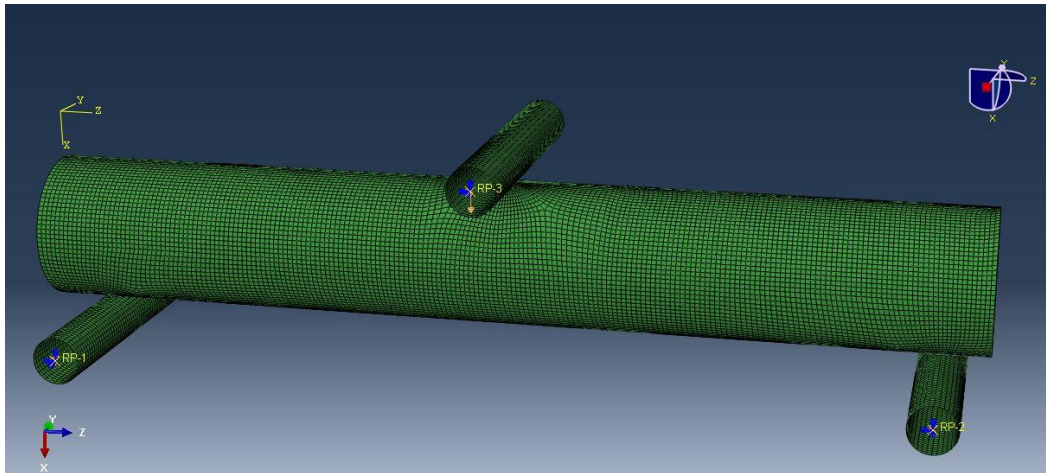


Figure 6.10: Tube three-points bending test configuration

6.3.1 Progressive failure analysis of thin-walled steel tube

The elastic material properties of AISI 1045 steel is presented in Table 6.3. Johnson-Cook plasticity model is implemented to investigate the plastic behavior of the steel tube through the deformation. The Johnson-Cook plasticity model constants are presented in Table 6.4.

Table 6.3: Steel AISI 1045 material properties [33]

Material properties	AISI 1045
Density (Kg/m^3)	7800
Young's modulus (GPa)	200
Poisson's ratio	0.3
Specefic heat ($\text{J/Kg}^\circ\text{C}$)	434
Thermal conductivity ($\text{W/m}^\circ\text{C}$)	47.8
Expansion ($\mu\text{m/m}^\circ\text{C}$)	11

Table 6.4: Johnson-Cook plasticity model constants [34]

Material	A (MPa)	B (MPa)	n	c	m	T_m ($^\circ\text{C}$)	T_0 ($^\circ\text{C}$)
1045 Steel	553	600	0.23	0.012	1.0	1460	20

The Jonson-Cook damage law parameters to study the damage initiation of the steel tube is presented in Table 6.5.

Table 6.5: Johnson-Cook damage law parameters [34]

Damage law parameters	d₁	d₂	d₃	d₄	d₅
AISI 1045 steel	0.06	3.31	-1.95	0.002	0.61

As mentioned before instead of defining the damage evolution of metallic structures based on the equivalent plastic strain, damage evolution is defined based on the equivalent plastic displacement after the damage onset. In this way the equivalent plastic displacement is defined by multiplying the element characteristic length to the equivalent plastic strain at failure.

The energy absorption capacity of the tube is reported by a load-displacement curve and mesh sensitivity analysis is performed using the mesh size of 1-5 millimeters in Figure 6.11. It is important to mention that the results are reported using the Butterworth filter to eliminate the curves oscillations. The deformed shape of the steel tube under the bending load is shown in Figure 6.12 and 6.13.

The behaviour of the tubes when a bending load is applied, is given by the superposition (or the concurrence) of a local (denting) and a global (bending) mode of deformation. After the top surface of the tube imposed by the bending load, denting occurs; this denting deformation is growing both in the transversal and in the axial directions and the local diameter of the tube is progressively reduced (flattening of the tube cross-section). Finally at the last phase of deformation, the tube is undergone the global bending and load reaches a maximum value after which the tube becomes unstable and the deformation proceeds with the load decreasing [35]. As it is clear in Figure 6.12, when the steel tube plastically deforms the plastic hinge appears in the tube and absorbs high amount of energy.

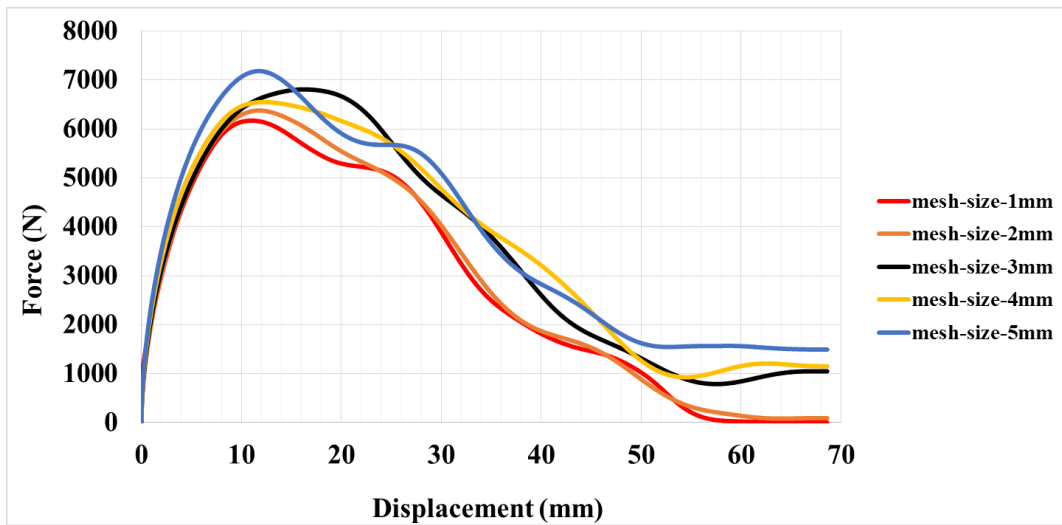


Figure 6.11: Mesh sensitivity analysis of steel tube

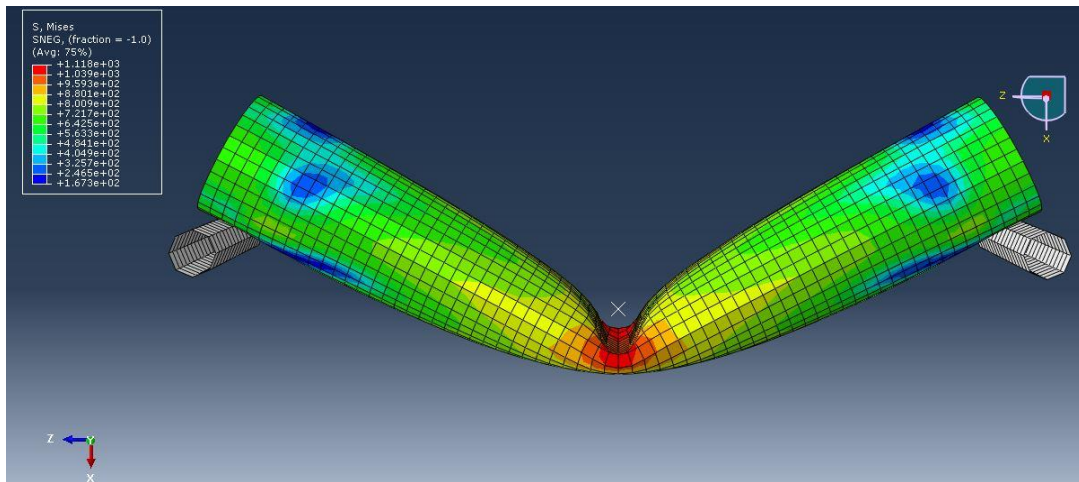


Figure 6.12: Metallic tube deformation under bending load-front view

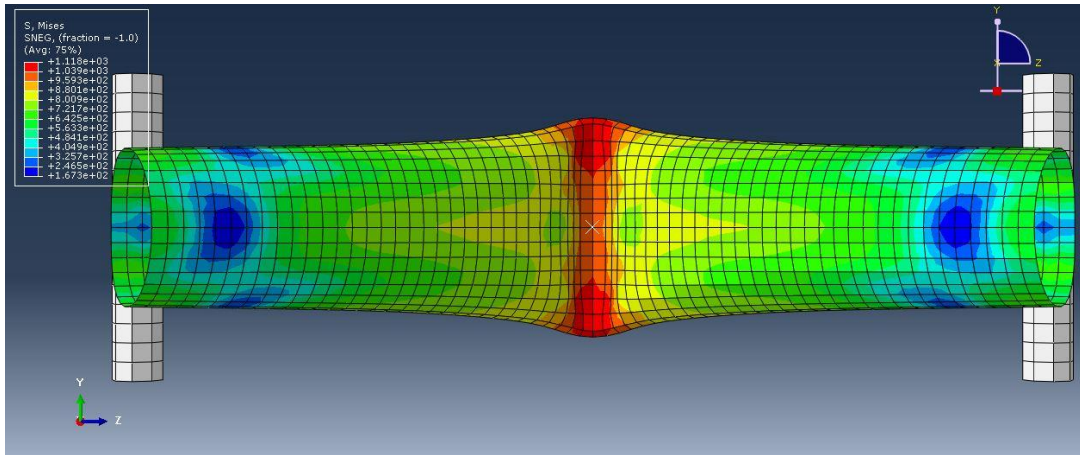


Figure 6.13: Metallic tube deformation under bending load-top view

6.3.2 Progressive failure analysis of thin-walled composite tube

The composite cylindrical tube is made of four unidirectional carbon/epoxy fiber orientated in cross-ply configuration with the total thickness of 1.2 mm as shown in Figure 6.14.

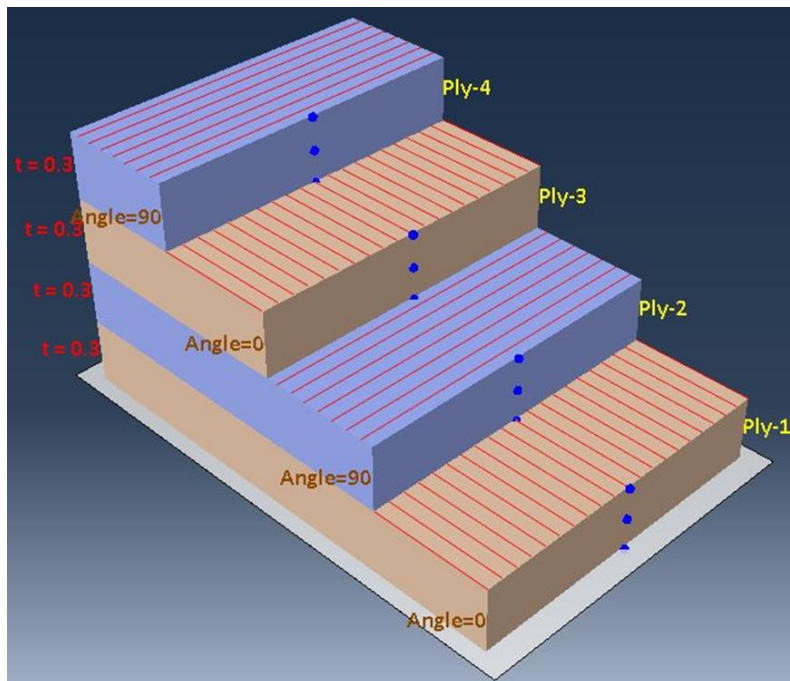


Figure 6.14: Composite lay-up configuration

In order to predict the damage initiation and evolution of composite material as mentioned before, it is necessary to insert the elastic material properties, strength parameters and fracture toughness energies of composite material as input data into the ABAQUS as presented in Tables 6.6-6.8.

Table 6.6: Composite elastic properties [36, 37]

E₁ (GPa)	E₂ (GPa)	ν_{12}	G₁₂ (GPa)	G₁₃ (GPa)	G₂₃ (GPa)
171.420	9.080	0.32	5.290	5.290	5.290

Table 6.7: Strength parameters of composite material [36-38]

X_T (MPa)	X_C (MPa)	Y_T (MPa)	Y_C (MPa)	S_L (MPa)	S_T (MPa)
2326.2	1200.1	62.3	199.8	92.3	92.3

Table 6.8: Fiber and matrix fracture toughness energies in both tensile and compressive directions [39]

G_{ftc} (KJ/ m²)	G_{fcc} (KJ/ m²)	G_{mtc} (KJ/ m²)	G_{mcc} (KJ/ m²)
81.5	106.3	0.2774	0.7879

Energy absorption capacity of the composite tube in terms of force-displacement curve is reported in Figure 6.15.

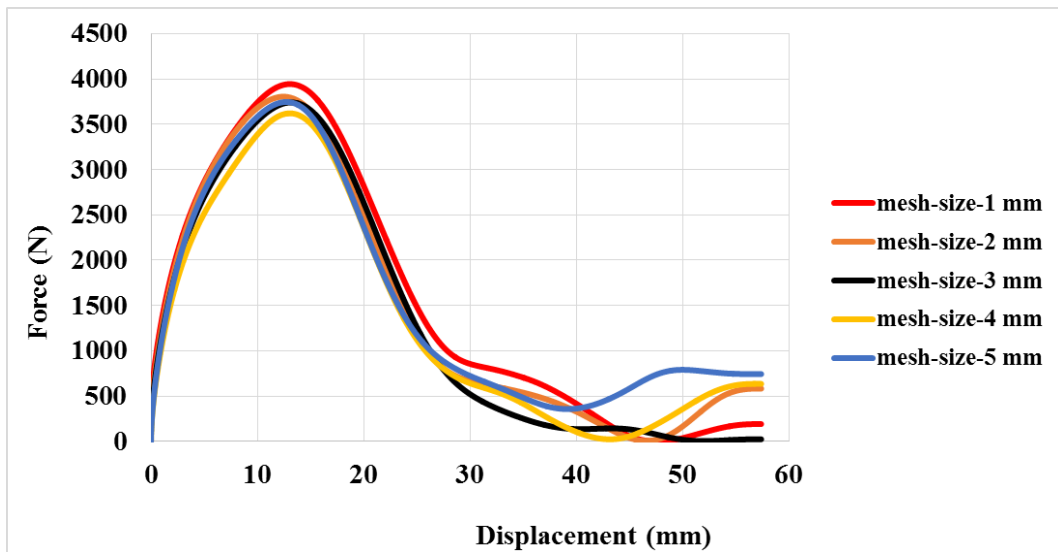


Figure 6.15: Mesh sensitivity analysis of composite tube

After 7.397 mm of vertical displacement, damage initiation values became 1 in matrix and fiber of the 4th layer in both tensile and compressive directions and the layer fracture initiated as shown in Figures 6.16-6.19.

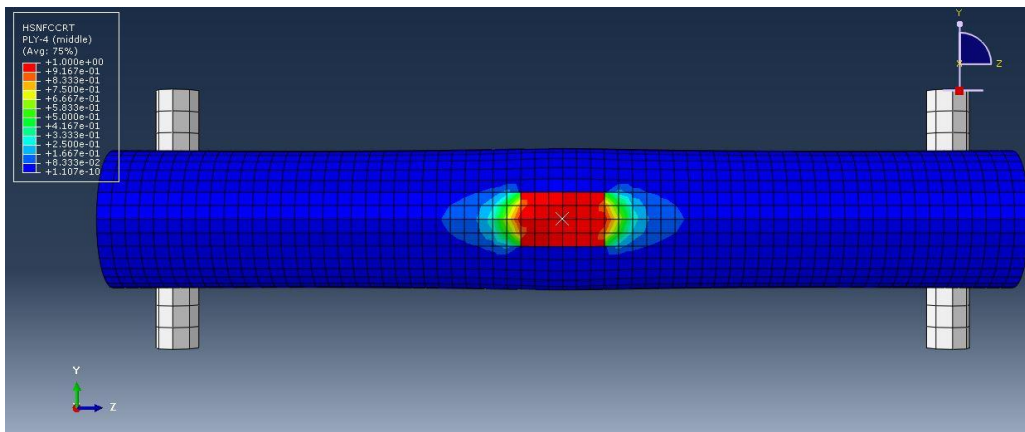


Figure 6.16: Value of Hashin's fiber compressive damage initiation criterion of 4th layer (HSNFC CRT)

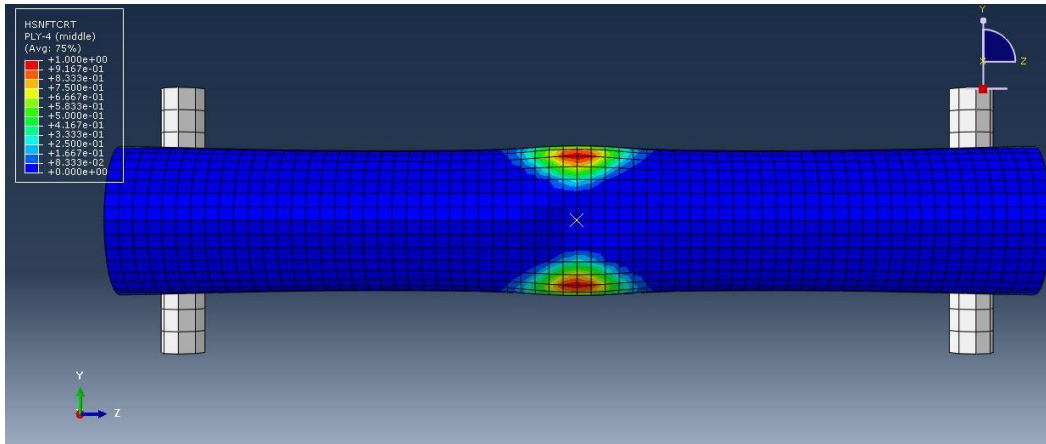


Figure 6.17: Value of Hashin's fiber tensile damage initiation criterion of 4th layer (HSNFTCRT)

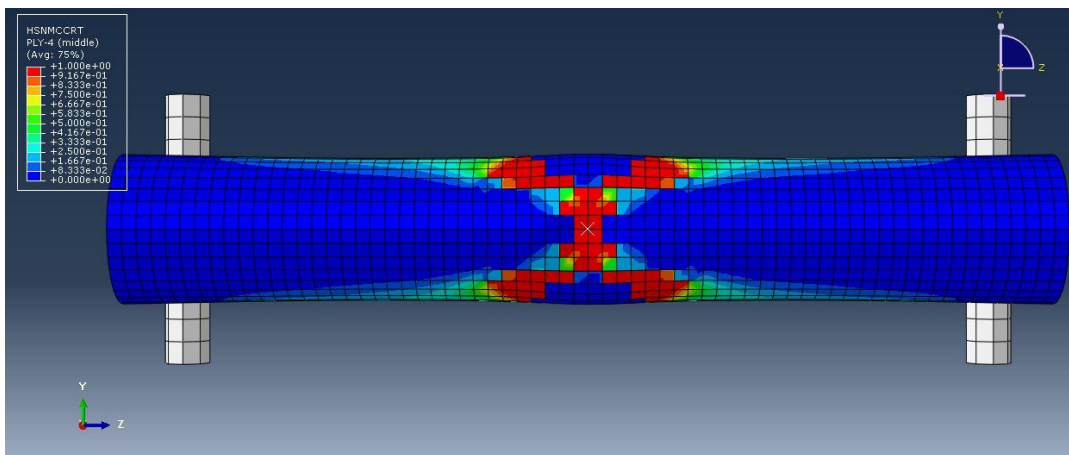


Figure 6.18: Value of Hashin's matrix compressive damage initiation criterion of 4th layer (HSNMCCRT)

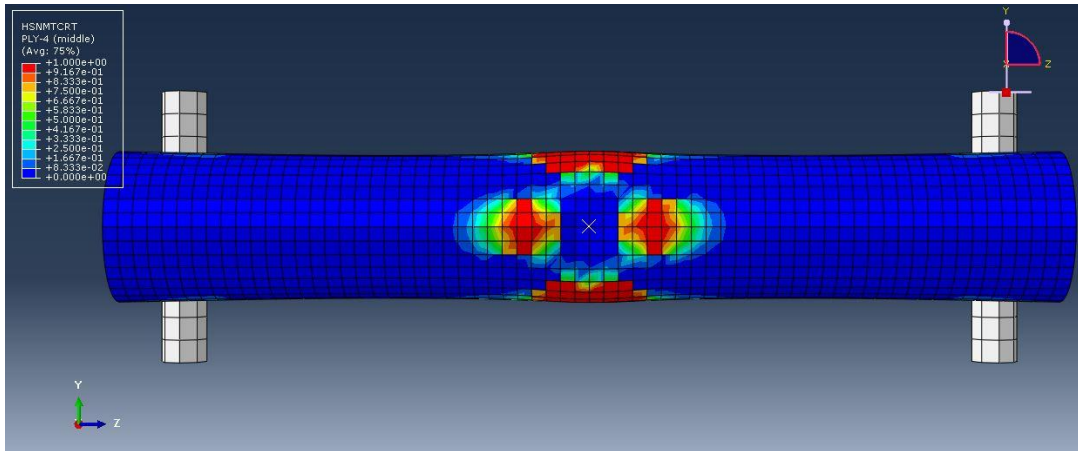


Figure 6.19: Value of Hashin's matrix tensile damage initiation criterion of 4th layer (HSNMTCRT)

The damage propagation modes of fiber and matrix in the fourth layer through the loading resulting in failure of the fourth layer are presented in Figure 6.20-6.24. This procedure continues until the first layer of composite tubes fails and catastrophic failure occurs.

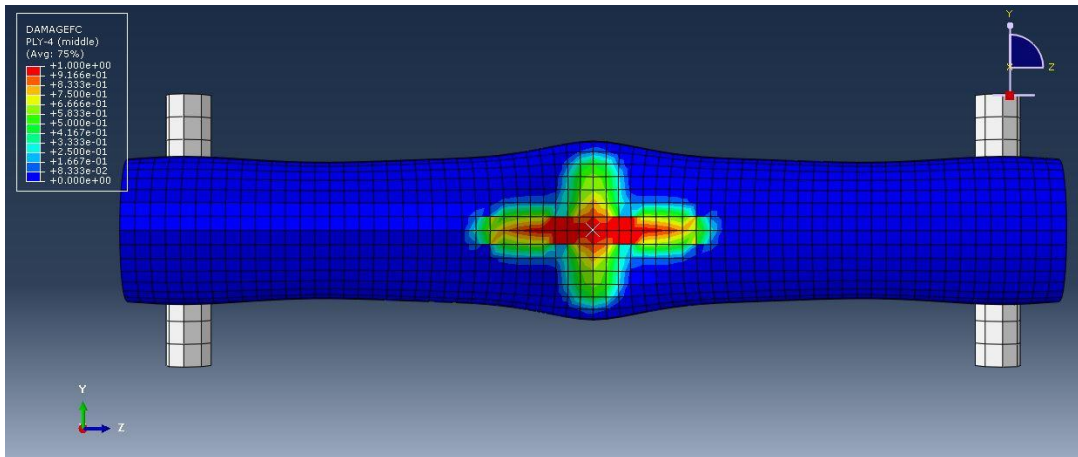


Figure 6.20: Value of fiber compressive damage variable of 4th layer (DAMAGEFC)

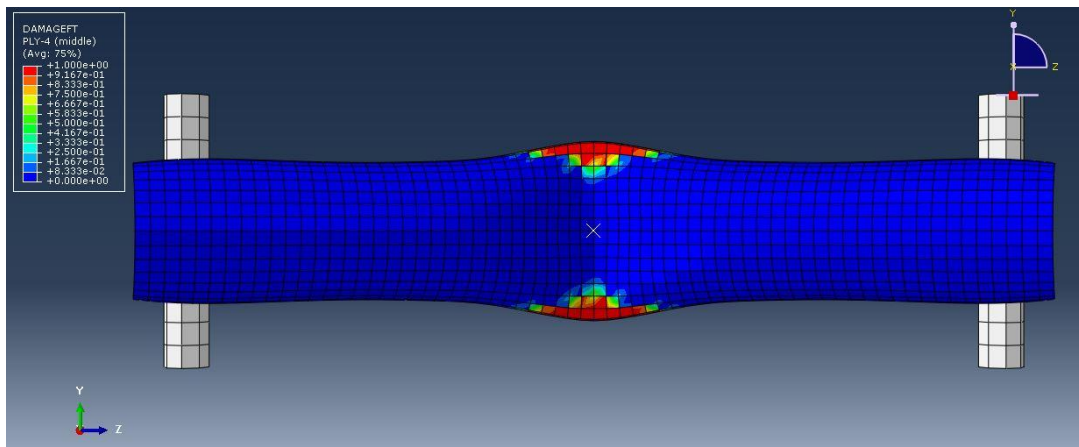


Figure 6.21: Value of fiber tensile damage variable of 4th layer (DAMAGEFT)

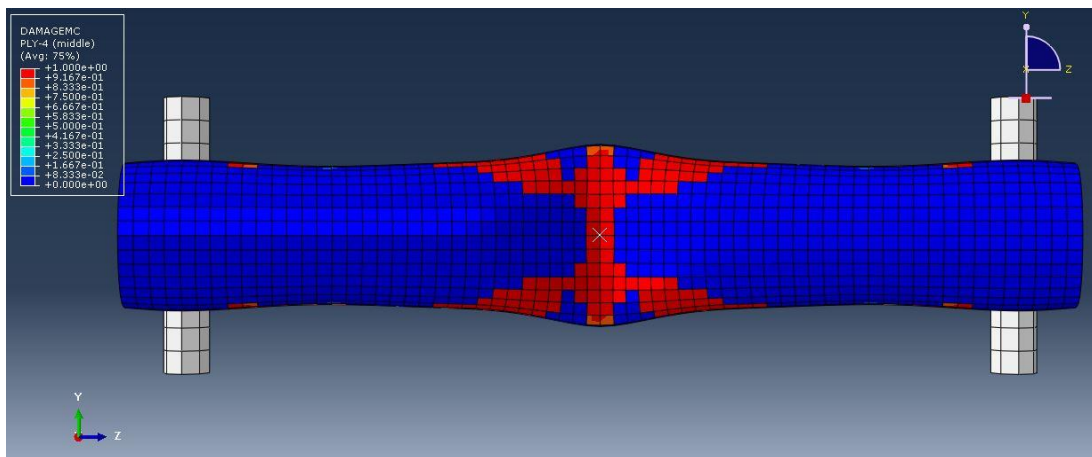


Figure 6.22: Value of matrix compressive damage variable of 4th layer (DAMAGEMC)

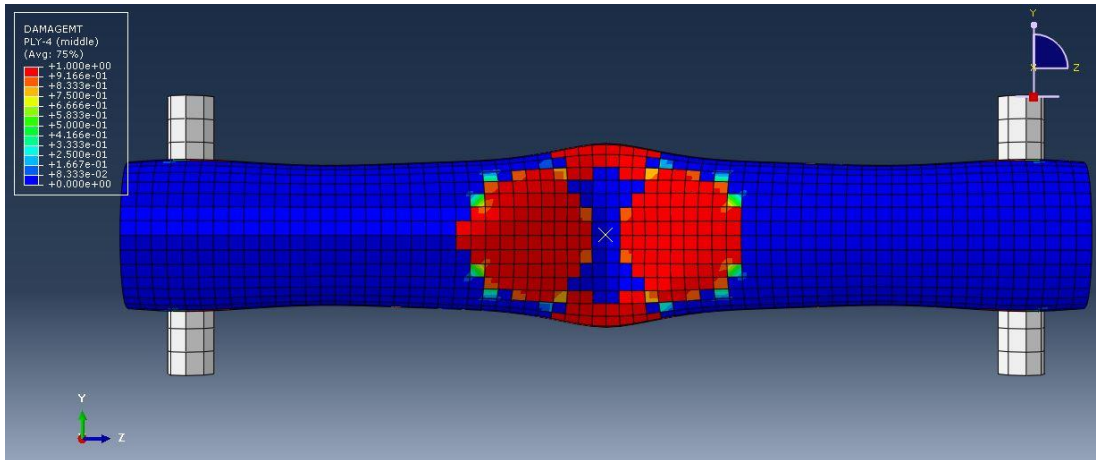


Figure 6.23: Value of matrix tensile damage variable of 4th layer (DAMAGEMT)

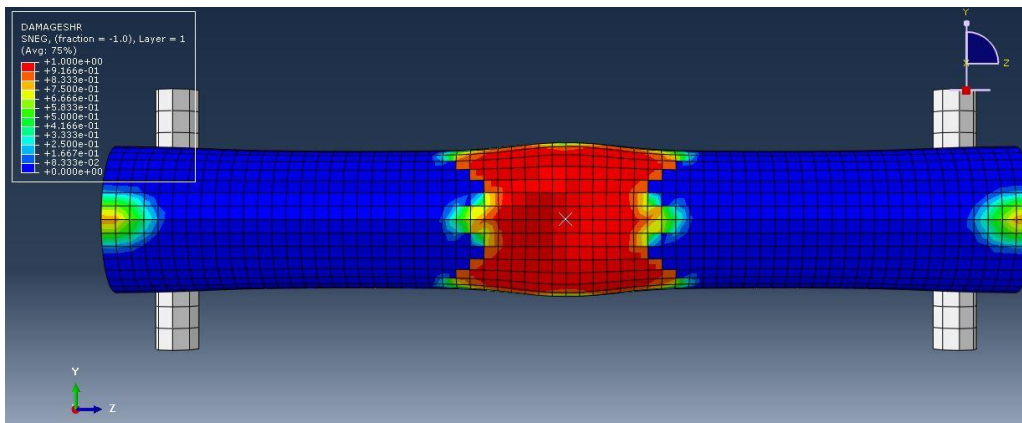


Figure 6.24: Value of shear damage variable of 4th layer (DAMAGESHR)

6.3.3 Progressive failure analysis of composite foam-filled tube

Composite foam-filled (crushable foam core) tube has been tested in three-points bending analysis. The composite material properties, lay-up orientation and thickness are the same as what has been used for the three-points bending test of composite tube while the foam core is made of Expanded Polypropylene (EPP) with the density of 45 Kg/m³. EPP is a plastic structural foam suitable for crashworthiness problems since it is light and able to absorb large amount of

energy [40]. The SEM picture of EPP foam internal structure is shown in Figure 6.25 and the structure of the composite foam-filled tube is shown in Figure 6.26.

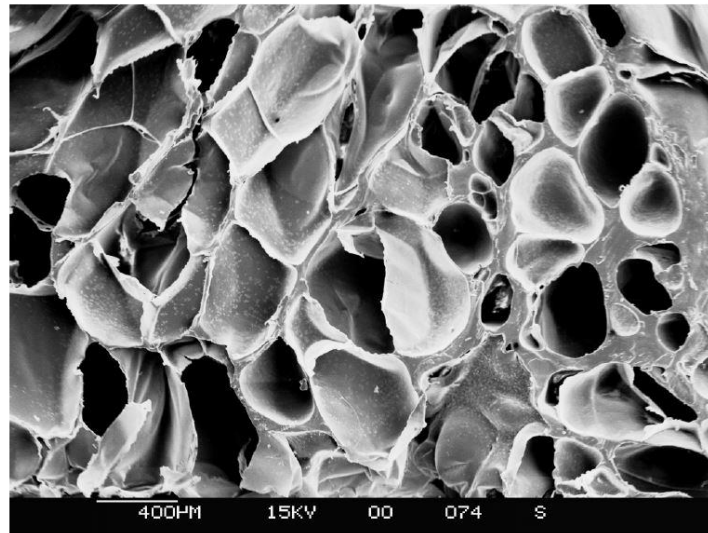


Figure 6.25: SEM picture of EPP foam internal structure [40]

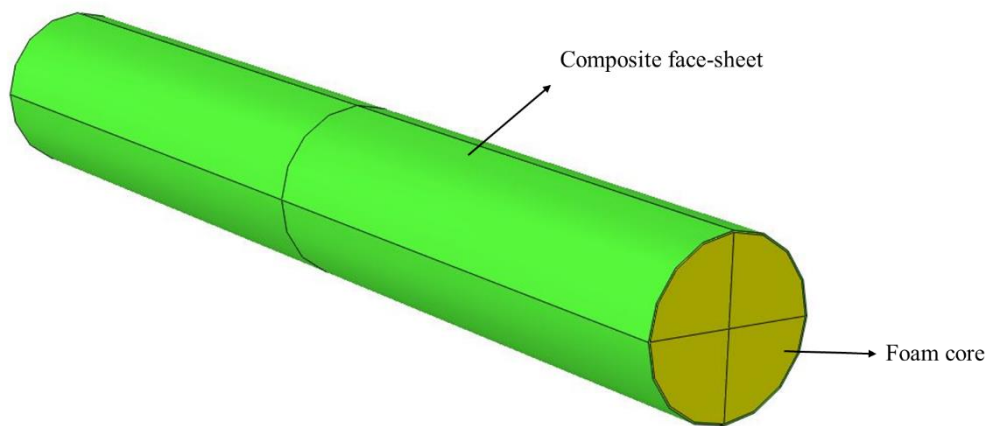


Figure 6.26: Schematic of composite foam-filled tube

Generally, compression is the main mode of deformation for foams since they are weak against shear or tension [41]. When foams are under compressive force, three phases are detectable in their stress-strain curves as shown in Figure 6.27. At the first phase, linear compression occurs followed by the plateau phase determining the mechanical behavior of the foam. The ideal foam is the foam

which has long plateau region due to higher energy absorption ability and controllable reaction stress. The last phase is densification which is a nonlinear compression. Using the same foam base material, foam with higher density has higher plateau strength and higher amount of absorbed energy [42].

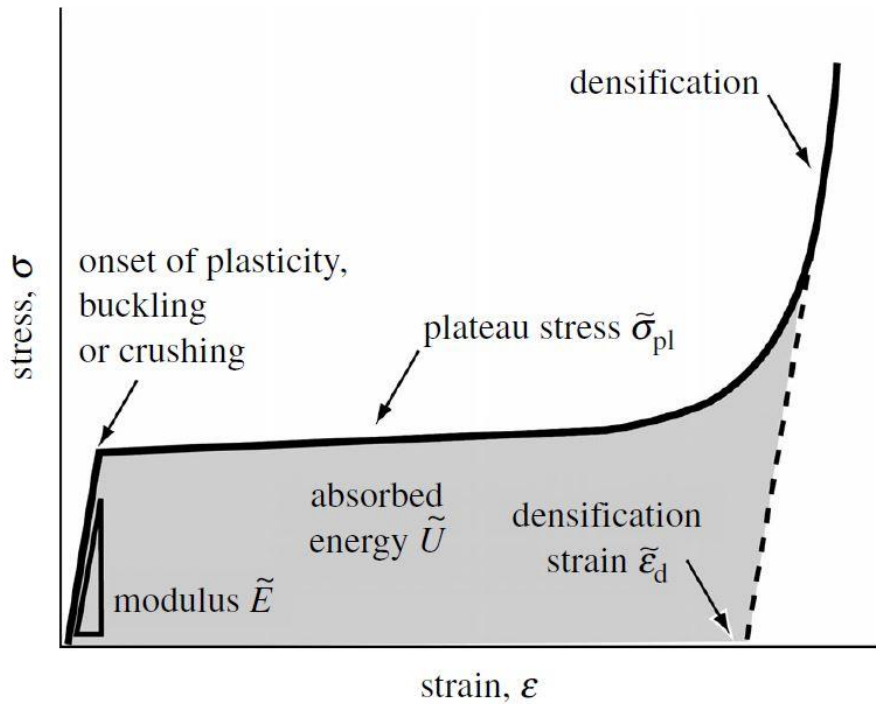


Figure 6.27: Typical stress-strain curve of foam structure under the compression load [43]

The uniaxial test data of the foam material with the density of 45 Kg/m^3 obtained from the ASTM D1621-94 carried out by [44] as shown in Figure 6.28 and Table 6.9. There is a relation between the compressive Young's modulus and the density according to Gibson equation [45] as shown in Figure 6.29; hence the Young's modulus for the EPP 45 Kg/m^3 and Kg/m^3 are determined as 2.1 and 5 MPa respectively. However, during the three-points bending test the foam core of 45 Kg/m^3 density has been tested. During the compression test, neither lateral displacement nor cross section changes are expected: so the Poisson's ratio is almost zero for crushable foam [13].

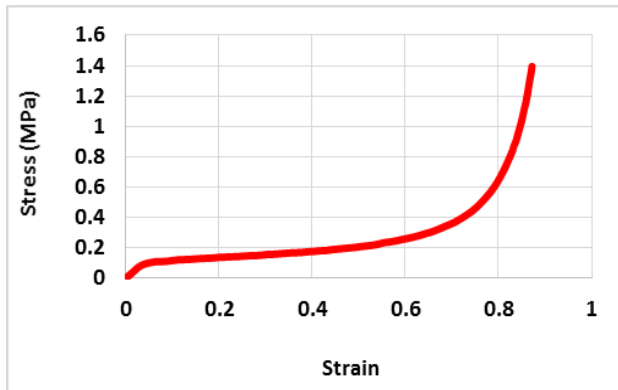


Figure 6.28: EPP foam 45 Kg/m³ stress-strain curve [44]

Table 6.9: Stress vs. strain

Strain	Stress (MPa)
0	0
0.015	0.038
0.05	0.1
0.3	0.16
0.5	0.2
0.6	0.26
0.7	0.37
0.8	0.63
0.83	0.9
0.85	1
0.86	1.18
0.87	1.39

Then by having engineering stress and strain, the equivalent plastic strain can be estimated based on Eqs. 6.32-6.33 can be obtained.

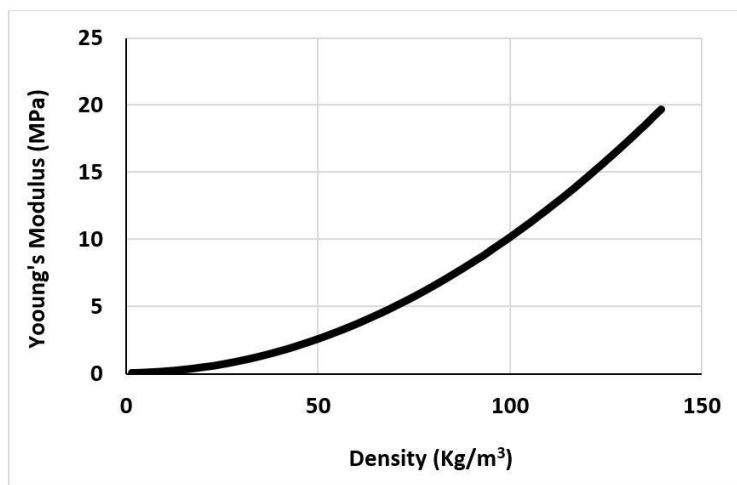


Figure 6.29: EPP foam density vs. compressive Young's modulus [44]

As the composite foam-filled tube is inserted under the bending load, firstly the composite face-sheet takes under pressure results in failure of composite layers one after each other with the same manner of the composite tube and then the stress will be transferred to the foam core leading to compression of the foam core. The damage initiation modes based on the Hashin's failure criteria for the

matrix and fiber in both tensile and compressive directions and the damage propagation modes of the composite material through the loading are almost the same as the ones in bending of composite tube. The deformed shape of the foam core with respect to the volumetric compacting plastic strain, presented by PEEQ in Abaqus, is shown Figure 6.30.

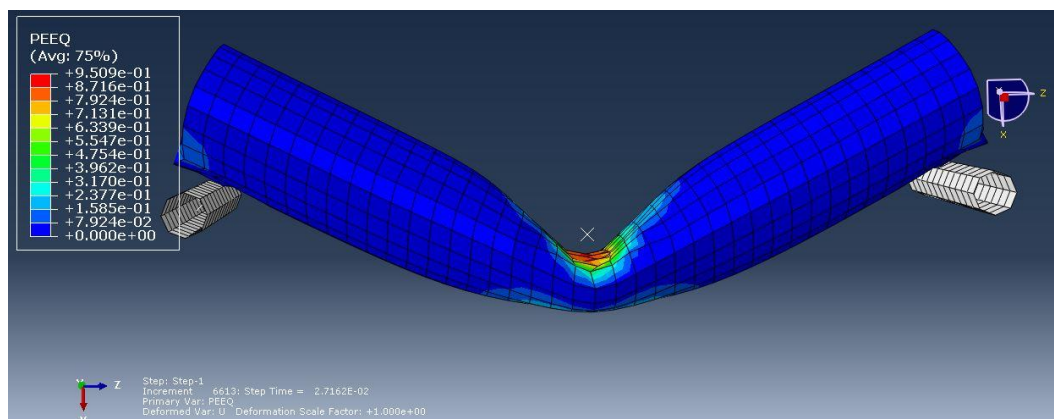


Figure 6.30: Deformed shape of the foam core

Due to the fact that the volumetric hardening model has been used to model the foam structure, PEEQ has the same concept with the $-\varepsilon_{vol}^{pl}$ presented at the theory section. In other words, PEEQ is representative of the initial volumetric compacting plastic strain plus to the volumetric compacting plastic strain during the analysis [23].

6.3.4 Comparison of the tubes performance with respect to materials energy absorption

The energy absorption capacity of tubes is evaluated through the force-displacement curves as shown in Figure 6.31. As it is presented in Figure 6.31, the metallic tube absorbs the highest amount of energy due to the ability for plastic deformation while the composite and composite foam-filled tubes absorb much lower energy. Comparing the absorbed energy values of composite and composite foam-filled tubes (composite= 77.1 J and composite foam-filled =101.2 J) it is noted that using composite foam-filled tube improves the energy absorption capacity of the composite tube by 31%. This result confirms the efficiency of the composite-foam structure in comparison with the composite one through the crashworthiness analysis and the same idea will be implemented for improving the vehicle roof structure performance in the full model at the next section.

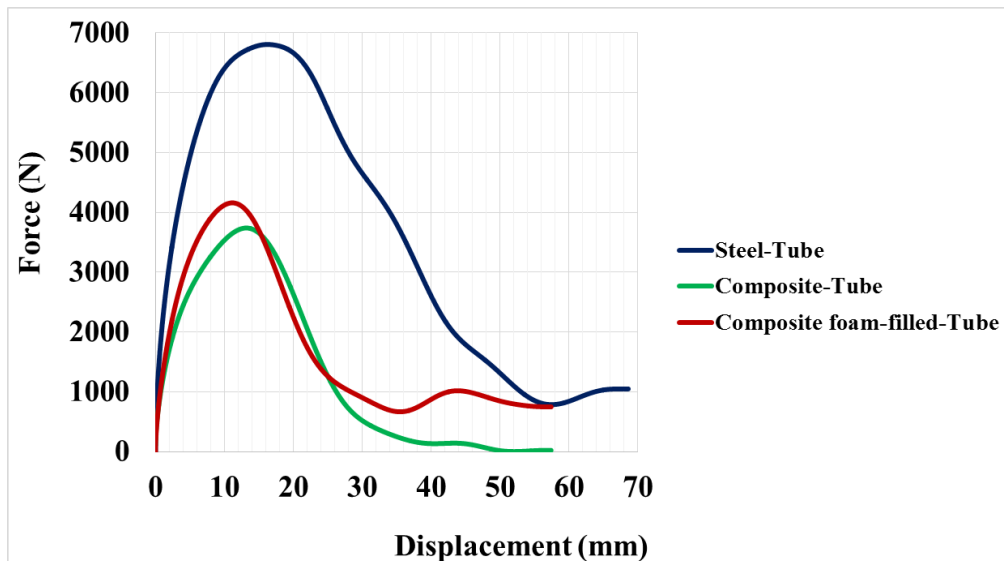


Figure 6.31: Comparison of tubes energy absorption

6.4 Test procedure and development of full vehicle finite element model

The experimental procedure is implemented according to FMVSS 216 test. Based on FMVSS 216 [2], a flat rectangular rigid plate with the dimensions of 1829 mm by 762 mm applies the intended load in the specified direction on the vehicle roof structure while the floor is clamped and constrained in all the degrees of freedom as shown in Figure 6.2. The rigid plate should be oriented in the way that its longitudinal axis is below the 5 degrees of the horizontal (pitch angle) and its transverse axis is below the 25 degrees of the vertical (roll angle) of the centerline. The rigid plate lower surface must be in contact with the vehicle roof centerline at the initial position and is placed at the 254 mm from the forward most point of roof centerline. Based on the standard, the load is applied to the vehicle roof with the velocity of no more than 13 mm/s in maximum 120 seconds. The experimental test configuration including load case and boundary condition are shown in Figure 6.32.



Figure 6.32: FMVSS 216 experimental test configuration [2]

The numerical modeling is the same with the experimental procedure except for the rigid puncher velocity and that is directly determining the simulation process time. The finite element model of TOYOTA YARIS 2010 has been provided from the National Crash Analysis Centre (NCAC) at George Washington University in the United States [46]. Some modifications such as deletion of unnecessary parts for roof crush modeling (e.g. Tires), and addition of the windscreen model and of sufficient constraints between the components of the model have been done. Figure 6.33 shows the finite element model of the vehicle that consists of 974388 elements and 1009131 nodes with the loading and boundary condition.

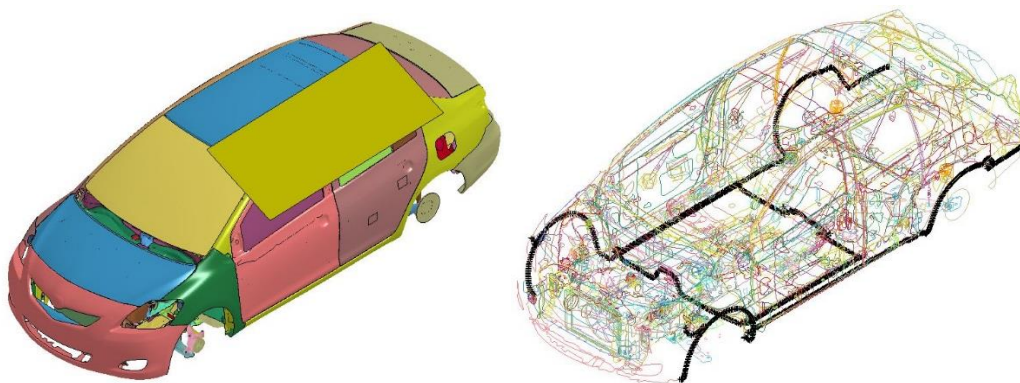


Figure 6.33: Load case and boundary condition

Due to the very high computational cost for modeling quasi-static tests with the LS-DYNA explicit package in actual process time, the simulation is

performed by the rigid plate velocity higher than in the physical test but in very small period of time. In order to prevent instabilities causing by small step size during the analysis, mass scaling method is used to increase the time step size in each cycle by adding artificial mass to the model.

To define the normal direction for the rigid plate is one of the difficulties in modeling the roof crush test. The mathematical method for defining the normal plane has been presented at [47]. The rigid puncher normal plane is obtained after the reference coordinate system rotates about the two planes of Z-X and Z-Y by the rotation angles of β and α respectively as shown in Figures 6.34 and 6.35. The final normal plane is calculated by Eqs. 6.44-6.55:

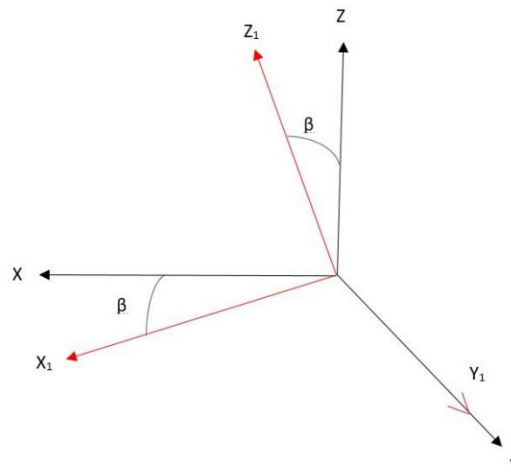


Figure 6.34: Reference coordinate system rotating about the Z-X plane

$$X = X_1 \cos \beta + Z_1 \sin \beta \quad \text{Eq. 6.44}$$

$$Y = Y_1 \quad \text{Eq. 6.45}$$

$$Z = Z_1 \cos \beta - X_1 \sin \beta \quad \text{Eq. 6.46}$$

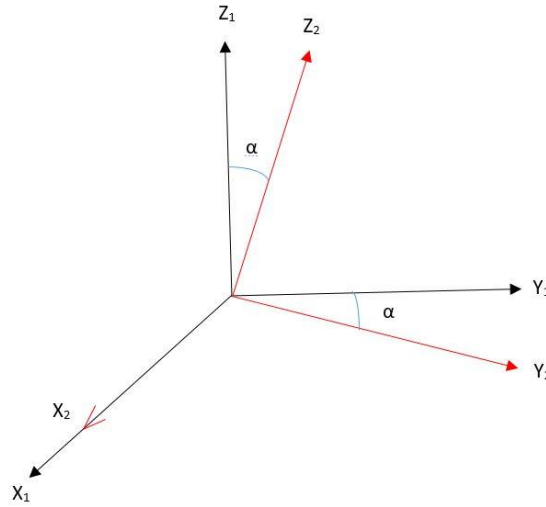


Figure 6.35: Reference coordinate system rotating about the Z-Y plane

$$X_1 = X_2 \quad \text{Eq. 6.47}$$

$$Y_1 = Y_2 \cos \alpha + Z_2 \sin \alpha \quad \text{Eq. 6.48}$$

$$Z_1 = Z_2 \cos \alpha - Y_2 \sin \alpha \quad \text{Eq. 6.49}$$

$$X = X_2 \cos \beta + Z_2 \cos \alpha \sin \beta - Y_2 \sin \alpha \sin \beta \quad \text{Eq. 6.50}$$

$$Y = Y_2 \cos \alpha + Z_2 \sin \alpha \quad \text{Eq. 6.51}$$

$$Z = Z_2 \cos \alpha \cos \beta - Y_2 \sin \alpha \cos \beta - X_2 \sin \beta \quad \text{Eq. 6.52}$$

$$X \sin \beta + Z \cos \beta = Z_2 \cos \alpha - Y_2 \sin \alpha \quad \text{Eq. 6.53}$$

$$Z_2 = X \cos \alpha \sin \beta + Z \cos \alpha \cos \beta + Y \sin \alpha \quad \text{Eq. 6.54}$$

$$\bar{n} = \{ \cos \alpha \sin \beta, \sin \alpha, \cos \alpha \cos \beta \} \quad \text{Eq. 6.55}$$

$$\beta = 5^\circ, \alpha = 25^\circ$$

$$\bar{n} = \{0.079, 0.42262, 0.90286\}$$

where β and α are pitch and roll angles respectively.

Different types of windshield laminated glass strategy are presented in Figure 6.36 by [48]. Windscreens have been modeled with single layer shell elements using ‘Mat_Laminated_Glass’. The windshield consists of two glass layers bonded with PVB. Using ‘Mat_Laminated_Glass’ to model the windshield, it is possible to capture the failure of glass layers based on predefined fracture plastic strain but failure modeling of the innermost polymer is not feasible. Due to this fact, although failure occurs in glass layers, the windshield failed elements are not deleted from the model. The main material properties of glass and PVB are presented in Table 6.10.

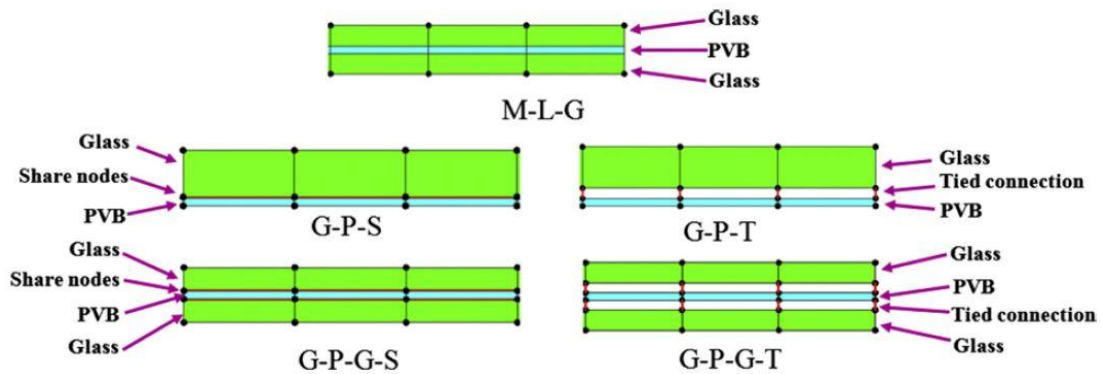


Figure 6.36: Different methods to model the windshield laminated glass [48]

Table 6.10: Glass and PVB main material properties [48]

	ρ (Kg/m ³)	E (GPa)	ν	Failure plastic strain
Glass	2500	74	0.227	0.001
PVB	1100	2.6	0.435	-

Mat_Rigid (MAT20) has been used to model the rigid plate while Boundary_Prescribed_Motion_Rigid has been used to apply the load to roof structure. Automatic contact surface to surface between the rigid plate as the master surface and the roof structure as the slave surface has been used to model the contact and to extract the reaction force history. MAT24, Mat_Piecewise Linear Plasticity, has been used to model the steel roof with the thickness of 1.2 mm. MAT24 is an elasto-plastic material model that can consider the failure based on the equivalent plastic strain and capable of taking into account the strain-rate effects by using the Cowper-Symonds model, which scales the yield strength.

The two types of non-linear element formulations 2 and 16, named “Belytschko-Tsay” shell element and “Fully Integrated Shell Element” respectively, have been used to model the roof panel. Possible Hourglass (HG) modes, which are nonphysical, zero-energy modes of deformation, should be taken under careful control using hourglass control algorithms [49].

6.5 Material selection for sandwich solution

The sandwich solution is made of two composite face-sheets and a foam core. The composite consists of four layers of unidirectional carbon fiber in cross-ply format and Expanded Polypropylene (EPP) with the different densities of 45 and 70 Kg/m³ are used as cores. The schematic of sandwich structure is shown in Figure 6.37. The material properties of Carbon/Epoxy fiber are presented in Tables 6.11 and 6.12. While the composite face-sheet basic thickness is $t=0.6$ mm, the thickness of the foam is constant ($T=25$ mm).

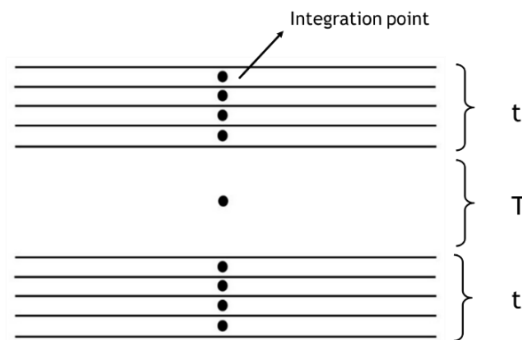


Figure 6.37: Schematic of sandwich panel

Table 6.11: Composite material elastic properties [50, 51]

	ρ (Kg/m ³)	E_1 (GPa)	E_2 (GPa)	ν_{12}	G_{12} (GPa)	G_{23} (GPa)	G_{13} (GPa)
Carbon/Epoxy -Unidirectional	1520	127	8.41	0.0205	4.21	4.21	4.21

Table 6.12: Strength parameters of composite [50, 51]

	X_t (MPa)	X_c (MPa)	Y_t (MPa)	Y_c (MPa)	S (MPa)
Carbon/Epoxy –Unidirectional	2200	1470	48.9	199	154

Wide range of information about different composite material models in LS-DYNA has been presented at previous chapters. Mat54/55 has been selected to model the composite face-sheets due to the ability of this model to capture the failure for unidirectional composite fibers. The thickness of both composite face-sheets is 0.6 mm; complete information about the modeling of unidirectional composite fiber has been presented at previous chapters.

There are different material models available to model the foam structure in LS-DYNA. Comparison of material models for modeling foam structure along with their application is presented in Table 6.13 based on the manual and material model help [52, 53].

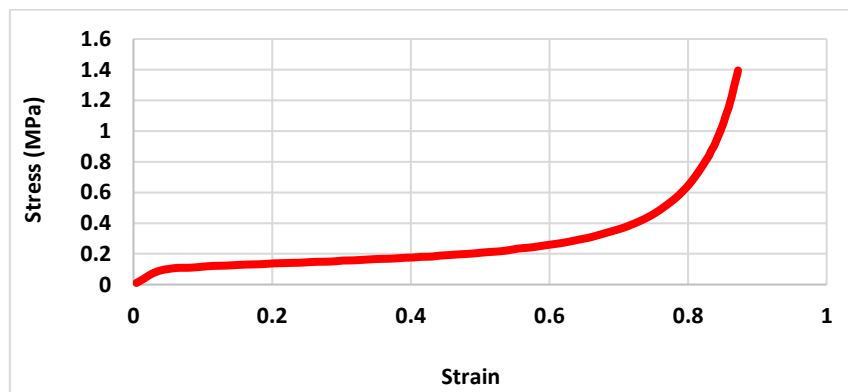
Table 6.13: LS-DYNA available foam material models [52, 53]

Material Card	Failure Consideration	Strain-rate Effects	Typical Applications
MAT53	No	No	Used to model polyurethane foam for automotive applications
MAT57	Yes	Yes	Used to model urethane foam for seat cushions and padding on the side impact dummies (SID)
MAT61	No	Yes	Used to model viscoelastic bodies such as foams.
MAT62	No	Yes	Used to model CONFOR foam on the ribs of side impact dummy
MAT63	No	No	Used for foams in impact applications where cyclic behavior is unimportant.
MAT73	Yes	Yes	Used to model low Density Urethane Foam in seat cushions, padding on the side impact dummies, bumpers and interior foams.
MAT75	No	Yes	Used to model isotropic crushable foams
MAT83	Yes	Yes	Capable of rate effects consideration for low and medium density foams.
MAT142	No	No	Used to model low density, transversely isotropic crushable foams to enhance automotive safety in low velocity (bumper impact) and medium high velocity (interior head impact and pedestrian safety) applications.
MAT144	No	Yes	Used to model isotropic crushable foams with strain rate effects.
MAT154	Yes	No	Used to model aluminum foam
MAT163	No	Yes	Used to model crushable foam with optional damping, tension cutoff, and strain rate effects.
MAT177	No	No	Used to model highly compressible foam
MAT178	No	Yes	Used to model highly compressible foam with strain rate effects
MAT179	Yes	Yes	Used to model highly compressible synthetic foam that are used in some bumper designs.

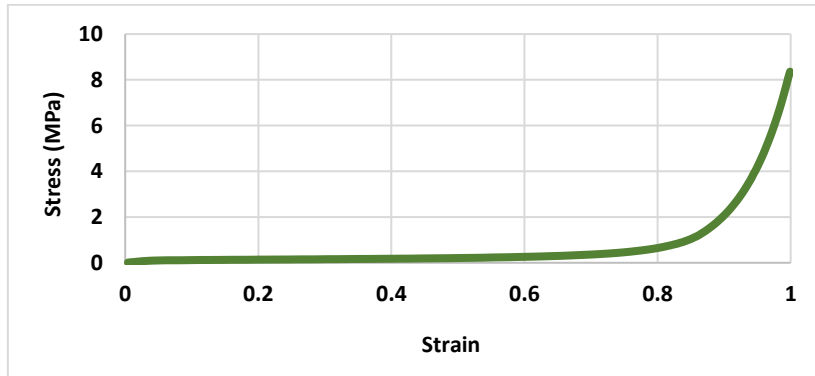
MAT63 (Mat_Crushable_Foam) has been selected to model the foam core. This material model specifically is used for crashworthiness applications where cyclic behavior is unimportant [53]. This material model is not capable of considering strain-rate effects and need extra keyword command to capture the failure. In order to capture the realistic mode of foam failure, it is necessary to use the keyword Mat_Add_Erosion. This option can predict the foam failure based on plastic strain and tensile stress [54]. Tetrahedron solid elements with one integration point have been used to model the foam core.

Hourglass control algorithm type 2 has been applied to control the hourglass energy [55]. Instead of adhesive joints (that hugely increase the computational cost) to attach composite face-sheets to the foam core, Contact_Tied_Nodes_To_Surface has been applied. The contact between the foam core and the composite face-sheets has been detected using Contact_Automatic_Surface_To_Surface.

There are few challenging difficulties in modeling foam structures under compressive force. When foam is under compression load, large deformation occurs and may cause the “negative volume error”. In order to solve this problem it is recommended to extend the initial stress-strain curve specifically at large strains [56]. The original and extended forms of the stress-strain curves for the two selected types of foam are presented in Figures 6.38 and 6.39.

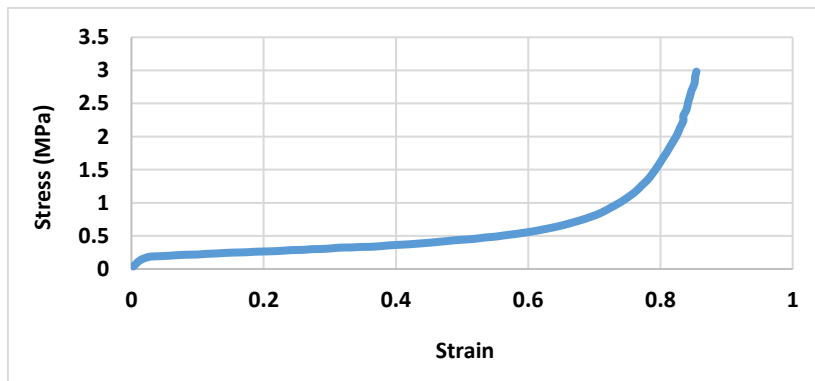


a. Original curve [44]

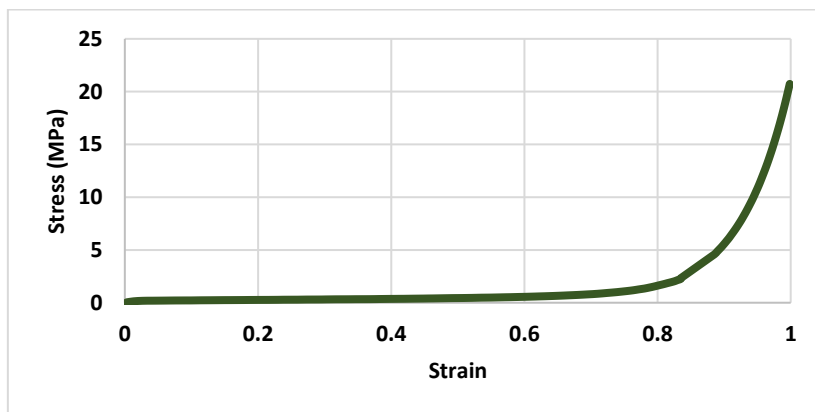


b. Extrapolated curve

Figure 6.38: a. Original and b. exponentially extrapolated stress-strain curves for EPP 45 Kg/m³



a. Original curve [44]



b. Extrapolated curve

Figure 6.39: a. Original and b. exponentially extrapolated stress-strain curves for EPP 70 Kg/m³

Another difficulty in modeling foam structure is penetration of elements into the neighbor elements. To avoid this problem the use of the contact interior type 2 option is needed. This option can handle the elements penetration problems in both compression and shear modes [54]. In the case of modelling a sandwich structure, it is generally recommended to activate the laminate shell theory option. This option corrects the wrong assumption of constant shear strain through the thickness of the shell; this parameter is very important when modelling sandwich structure because it helps to prevent a too stiff behavior of the structure.

6.6 Results and discussion

As a first step, the analysis of the response dependency on velocity has been performed to find out the effects of the increment of the rigid plate speed on the vehicle body stiffness; then the windscreens contribution to the vehicle stiffness has been assessed. Then after the energy absorption capability of the main parts of vehicle Body-In-White (BIW) components has been investigated and at last the results for different proposed designs are presented and discussed.

6.6.1 Velocity dependency

In order to decrease the computational time and cost the loading velocity increased in each step. There is a scale for increasing the velocity based on energies ratio comparison. According to [19] during the quasi-static analysis the ratio of kinetic energy to strain energy should be preserved less than 15%.

To analyze the speed dependency, the initial velocity (846.6 mm/s) of rigid plate has been progressively increased by 50% in each step. Results of vehicle roof structure velocity dependency are presented in Figure 6.40 by means of force-displacement diagrams for the normal production (steel) solution. As it is clear in Figure 6.40, by increasing the rigid plate initial velocity the peak load and energy absorption are increased.

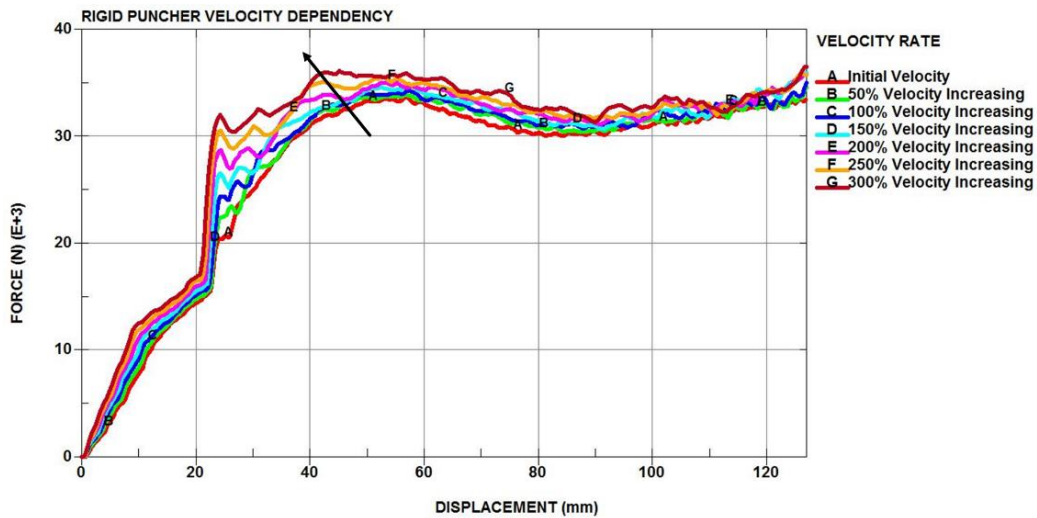


Figure 6.40: Dependency on velocity of the roof crush response.

Although all the curves obtained for the different speeds are quite similar in their trend and almost converging at the right extremity of rigid plate displacement, fluctuations appeared and curves progressively lost the smoothness due to resonance caused by higher velocity. Since the target displacement for the puncher is set to 127 mm, the velocity of 846.6 mm/s (that is the base one) is selected. Although it is possible to use higher velocities in order to decrease the simulation time, the observed force oscillations will make the analyses convergence much more difficult and may hidden other relevant effects.

6.6.2 Windscreens contribution to the vehicle roof structure strength

The effects of the front and rear windshields and of the side-screens on the vehicle roof structure strength are shown in Figure 6.41, again by means of force-displacement diagrams. As it reported in Figure 6.41, three analyses situations have been considered one without any screens, another one without front and rear windshields and the third one without side-screens and results have been compared with all screens situation. It comes out that while the front and rear windshields have high influence on the vehicle roof structure strength, the side-screens have small effects on the total strength. In the case of no windscreens the peak load is reduced of 42% and this confirms the important role of the windscreens in vehicle roof structure strength.

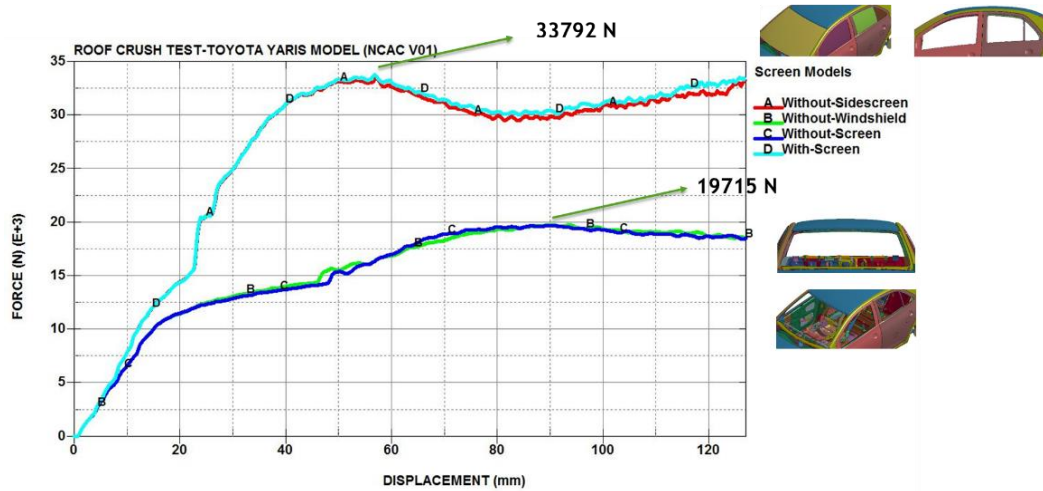


Figure 6.41: Windscreens effect on vehicle roof structure strength in roof crush test

6.6.3 Comparison of the main vehicle BIW components energy absorption

The main parts of BIW structure involved in roof crush test, consists of 31 parts subdivided into the six main categories of A-Pillars, B-Pillars, C-Pillars, roof panel, roof rails and side panels. However, other parts of the chassis also absorb energy during the test which are not of this research interest. As it is clear from the diagram of Figure 6.42, side panels absorb the highest amount (about 50%) of energy during the roof crush test. The rest of absorbed energy is subdivided between B-pillars, roof panel, roof rails, A and C-Pillars. The roof panel absorbs around 12% just by itself and this proves the importance of the roof panel in the crushing test.

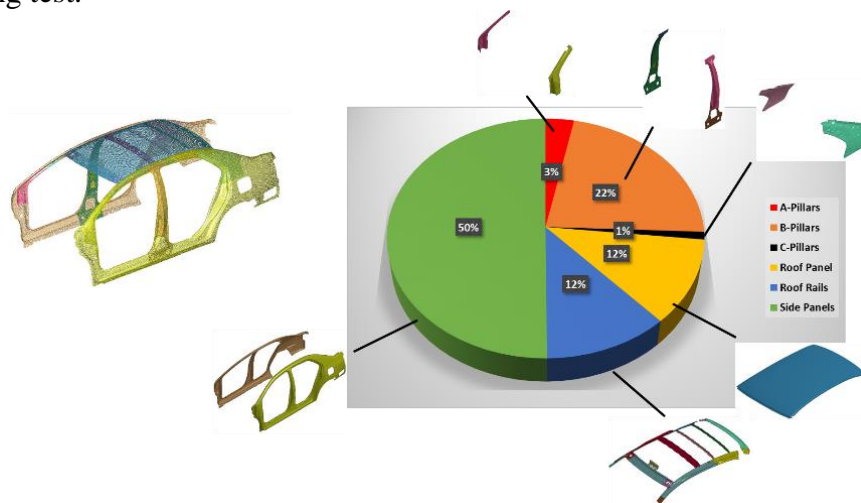


Figure 6.42: Energy distribution in BIW components during the roof crush test

6.6.4 Comparison of stiffness response between different designs of the roof panels

Different types of the roof panel design are proposed in Figure 6.43. Type 1 is the steel normal production solution, type 2 is the composite solution that consists of one composite shell with 1.2 mm thickness, type 3 is the composite sandwich solution with two composite skins (0.6 mm thickness each) and a full foam core, type 4 is the sandwich solution with three longitudinal foam strips, type 5 is the sandwich solution with four longitudinal foam strips, type 6 is the sandwich solution with two longitudinal and one middle transverse foam strips and, finally, type 7 is the sandwich solution with two longitudinal and two transverse foam strips. At the first step the sandwich structure design is made with the EPP 45 Kg/m³ foam core.

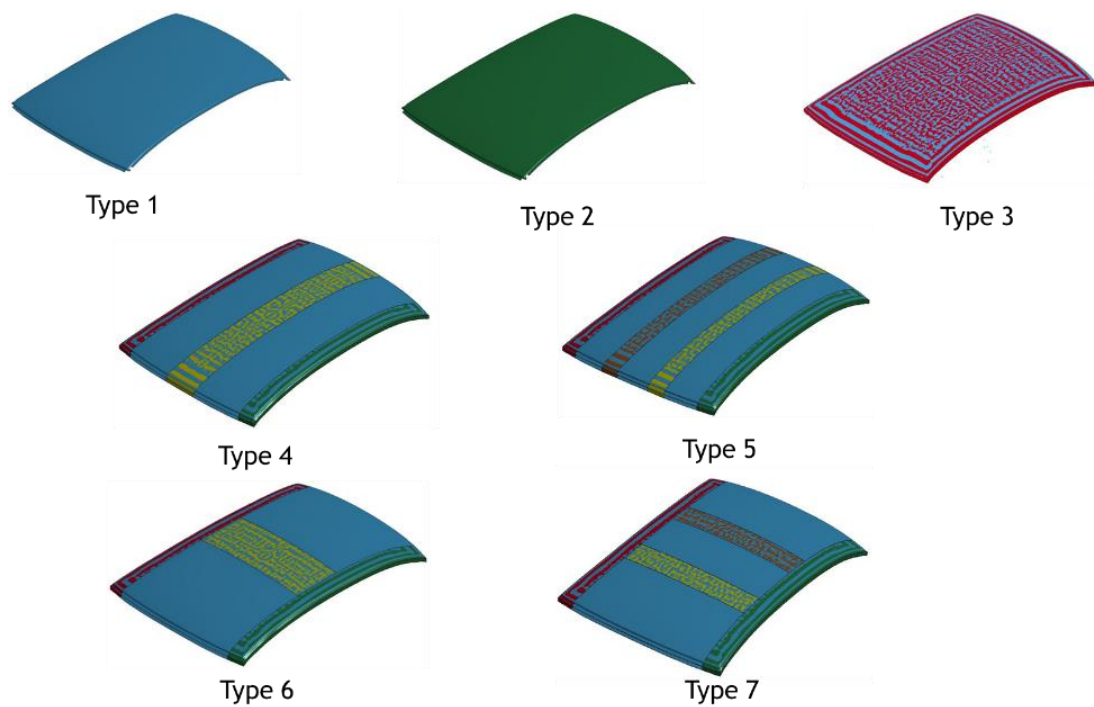


Figure 6.43: Roof panel solution configurations

The comparison of load-displacement curves for different configurations is presented in Figure 6.44. When the roof structure is under compressive force, it deforms elastically up to the about 50 mm of the rigid puncher displacement. In the range between 50 and 60 mm of displacement the maximum of the reaction

force is reached. After that, by continuing the loading, local panel buckling failures and screens deformation begin and all the curves exhibit a decreasing trend. It can be noticed that the steel roof panel curve, due to the material ability of plastic deformation, exhibits force values higher with respect to the other curves and this confirms the highest amount of its energy absorption. All the curves are included into a narrow band, the maximum force and the absorbed energy values are very similar.

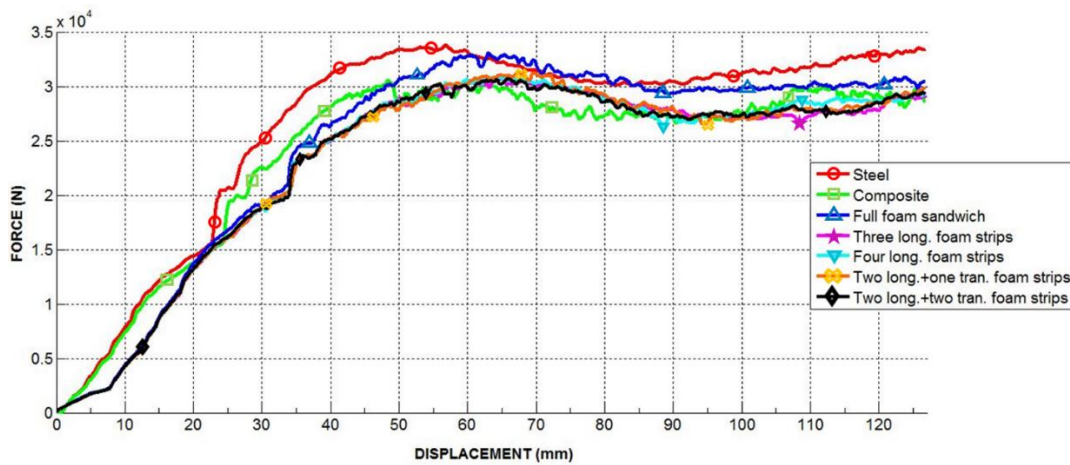


Figure 6.44: Roof crush resistance comparison for the different solutions

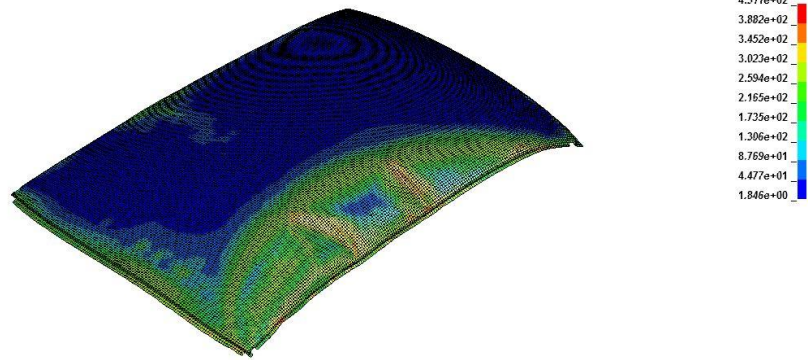
The deformed shape of vehicle roof structure is compared in Figure 6.45 with the picture of the NHTSA test result [57]: the deformed shapes are in good agreement. The deformed shape of the steel roof panel is shown in Figure 6.46.a; the maximum equivalent stress at the roof panel is 431 MPa which is larger than the yield strength of the considered steel (220 MPa) and therefore the roof has been submitted to a quite large plastic deformation.



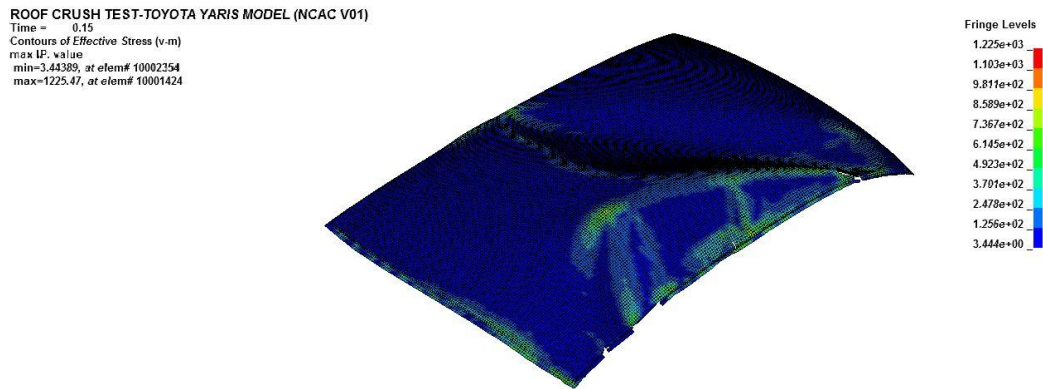
Figure 6.45: Comparison of real and FEM roof crush test

In the case of the full composite roof panel, a rupture occurs at the roof panel edge due to its lower strength and the curve falls instantly with higher amplitude in comparison with the other curves exactly before reaching to displacement of 60 mm as shown in Figure 6.44. As the rupture occurred, the failed roof panel elements are deleted based on the predefined failure criterion as shown in Figure 6.46.b.

ROOF CRUSH TEST-TOYOTA YARIS MODEL (NCAC V01)
Time = 0.15
Contours of Effective Stress (v-m)
max IP value
min=1.84592, at elem# 2674415
max=431.078, at elem# 2661236



a. Steel roof panel



b. Composite roof panel

Figure 6.46. a. Steel and b. composite roofs deformation

The solution type 3 shows a more regular deformation path along with higher energy absorption with respect to the solution type 2. When the solution type 3 is under the compressive force, at first some cracks are appeared at the face-sheet and some elements at the longitudinal edge of roof are deleted; then the foam core is submitted to pressure, rupture occurs at the structure and elements are deleted as shown in Figure 6.47.



a. Outer face-sheet cracking b. Foam core compression c. Foam failed elements

Figure 6.47. Solution type 3 deformation and failure.

According to Figure 6.44, although the other sandwich solutions behave similarly and absorb nearly the same amount of energy, sandwich solutions have different mass. The total absorbed energy, maximum force and solution mass are presented in Table 6.14.

Table 6.14. Solution results comparison (45 Kg/m³ foam core) Part I

Solution	Absorbed Energy (kN.m)	Maximum Force (kN)	Mass (Kg)
Type 1	3.40	33.8	15.69
Type 2	3.06	30.6	3.03
Type 3	3.14	33.1	4.80
Type 4	2.95	31.0	3.73
Type 5	2.96	30.9	3.73
Type 6	2.97	31.3	3.65
Type 7	2.96	30.7	3.65

The deformed shape of foam cores for the other different solutions are shown in Figure 6.48, on the left the deformed shape and on the right the failed elements of the foam core. In the case of solution types 4 and 5, the foam strip at the passenger side remains intact while the failure occurs at the other foam strips (driver side) made visible by the blue elements. In the cases of configuration types 6 and 7, the transverse foam strips remain intact but the failure occurs at both the side foam strips.



a. Type 4

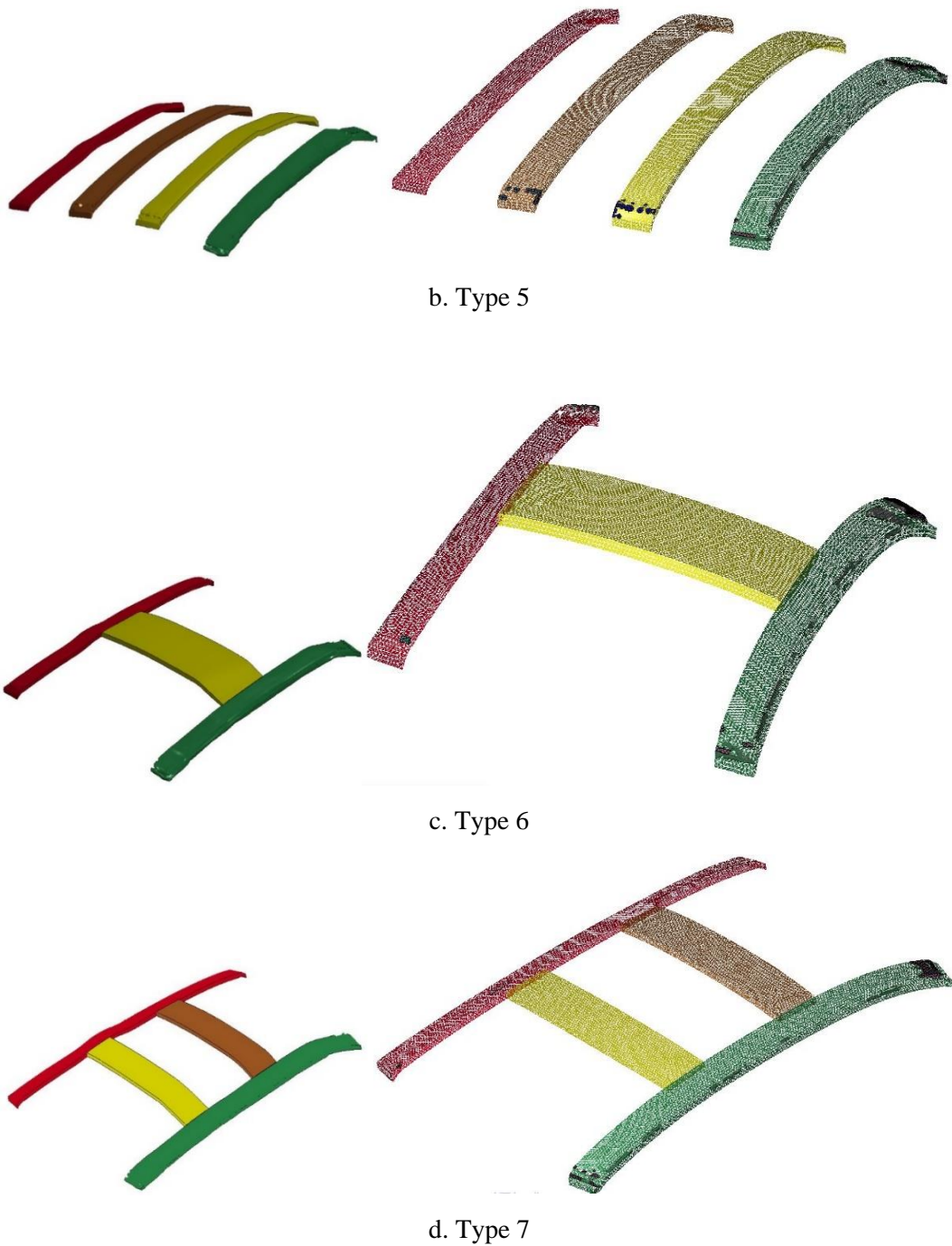


Figure 6.48. Solutions a. Type 4- b. Type 5- c. Type 6- d. Type 7 deformation and failure

There should be a trade-off between the absorbed energy and roof panel mass to identify the most efficient design. In order to have an optimum design in the

case of roof crush test, the strength to weight ratio (SWR) for vehicles is defined. Strength-to-weight ratio is defined as the proportion of the maximum force to the vehicle weight. The SWR and roof panel mass reduction percentages for all solutions are reported in Table 6.15. It is clear that steel panel (solution type 1) has the highest SWR and then the full foam sandwich solution. The best solution among the sandwich solutions with strips foam is sandwich type 6 due to its higher SWR.

Table 6.15: Solution result comparison (45 Kg/m³ foam core) Part II

Solution	Strength-to-Weight ratio (SWR)	Panel Mass Reduction Percentages (%)
Type 1	3.087	-
Type 2	2.827	80.71
Type 3	3.053	69.42
Type 4	2.862	76.23
Type 5	2.853	76.24
Type 6	2.890	76.76
Type 7	2.835	76.75

At the second phase, the same sandwich solutions but with higher density (EPP 70 Kg/m³) foam cores have been tested. The load-displacement curves for different solutions with higher density foam core are presented in Figure 6.49. The complete results for absorbed energy value, SWR and mass report are presented in Tables 6.16 and 6.17. Based on the results presented in Table 6.16, the energy absorption capacity is improved for all the material solutions by applying the higher density foam core.

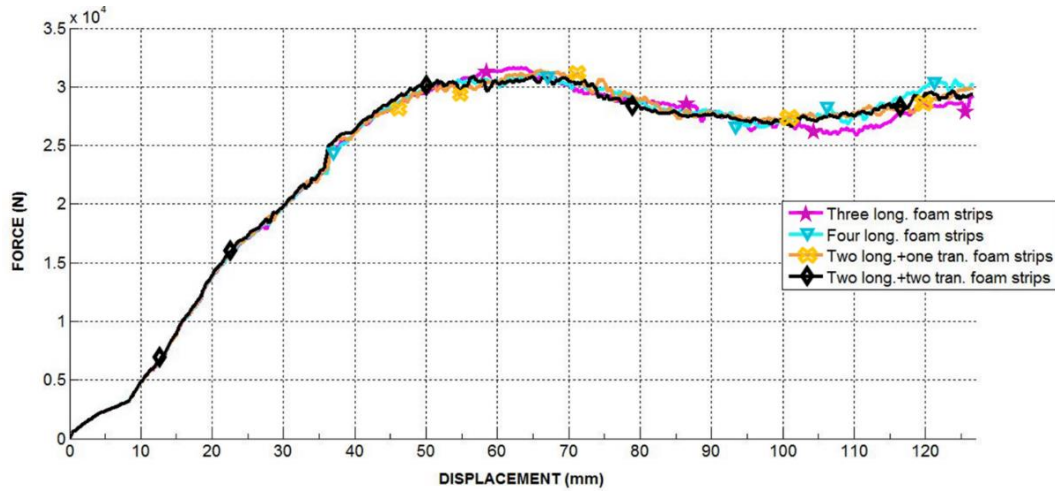


Figure 6.49: Roof crush resistance comparison for the solutions with EPP 70 Kg/m³ foam core

Although the roof panels mass increased by applying the higher density foam cores in the sandwich solutions, SWR increased. This means that increasing roof panel mass using sandwich solutions with higher density foam cores is an effective method due to the foam contribution to energy absorption. Although using the solution type 4 resulting in higher strength-to-weight ratio in comparison with the other sandwich solutions, still there is a considerable difference for this value between sandwich solutions and the steel one.

Table 6.16: Solution result comparison (70 Kg/m³ foam core) Part I

Solution	Absorbed Energy (kN.m)	Maximum Force (kN)	Mass (Kg)
Type 4	2.98	31.6	4.12
Type 5	3.01	31.2	4.12
Type 6	3.01	31.4	3.99
Type 7	3.01	30.9	3.99

Table 6.17: Solutions results comparison (70 Kg/m³ foam core) Part II

Solution	Strength-to-Weight ratio (SWR)	Panel Mass Reduction Percentages (%)
Type 4	2.917	73.74
Type 5	2.880	73.74
Type 6	2.898	74.57
Type 7	2.852	74.57

At the next step, Inspiring from the method presented at [30] for increasing the composite layer thickness, composite face-sheets thickness increased from 0.6 mm to 0.8 mm. The optimized results related to sandwich designs with the face-sheets of 0.8mm and foam core of 70 Kg/m³ density are presented in Figure 6.50 and Tables 6.18 and 6.19. As it is clear in Figure 18 and Table 9, by increasing the face-sheets thickness, the values of maximum force and absorbed energy increase resulting in strength-to-weight ratio raising. According to Table 10 using the optimized solution type 6 reduces the vehicle roof panel mass by 68% (from 15.7 Kg to 5 Kg), while due to its equal SWR value to the steel solution it has almost the same structural performance with the steel ones and is introduced as the best solution.

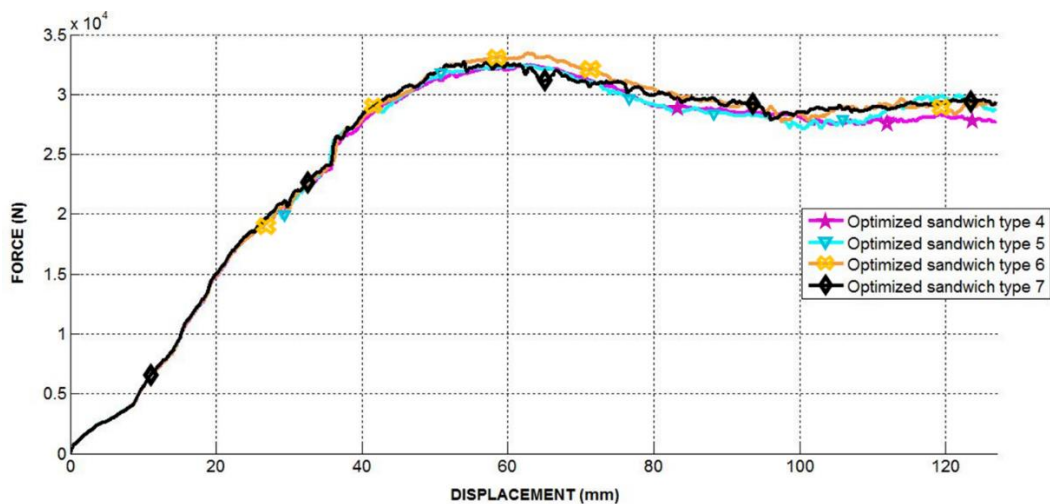


Figure 6.50: Roof crush resistance comparison for the solutions with EPP 70 Kg/m³ foam core and face-sheets thickness of 0.8 mm

Table 6.18. Solution result comparison (70 Kg/m³ foam core-0.8 mm face-sheets thickness) Part I

Solution	Absorbed Energy (kN.m)	Maximum Force (kN)	Mass (Kg)
Type 4	3.11	32.4	5.13
Type 5	3.13	32.4	5.13
Type 6	3.19	33.5	5.00
Type 7	3.17	32.8	5.00

Table 16.19. Solution result comparison (70 Kg/m³ foam core-0.8 mm face-sheets thickness) Part II

Solution	Strength-to-Weight ratio (SWR)	Panel Mass Reduction Percentages (%)
Type 4	2.993	67.30
Type 5	2.987	67.30
Type 6	3.087	68.13
Type 7	3.021	68.13

6.7 Conclusions

In this chapter, an innovative design solution for the vehicle roof structure has been developed and tested in rollover crash analysis. Progressive failure analysis of thin-walled tubes made of steel, composite and composite foam-filled materials have been done through the three-points bending test. Modes of tubes deformation and failure have been presented for different solutions. Results revealed although composite and composite foam-filled solutions absorbed lower amount of energy, as it was expected, composite foam-filled solution increased the composite tube energy absorption by 31%. After proving the efficiency of composite-foam design; the same idea is implemented on the vehicle roof panel during the roof quasi-static crush test.

The considered new solution consists of a sandwich structure with unidirectional carbon/epoxy composite face sheets and EPP foam core. Structural analysis has been developed by means of numerical simulation. Before initiating to analyze the sandwich roof structure, speed dependency test has been

implemented on the steel roof structure and the appropriate test velocity for the rigid puncher has been selected. In particular, it has been pointed out that high test velocities added instabilities to the analysis. Then the effects of front, rear and side-screens on the total vehicle roof structure strength have been tested and it was shown that while front and rear windshields have high influence on the vehicle roof structure strength, side-screens have small effects on the total strength. The next step was aimed to determine the importance of roof panel among the main parts of BIW structure in the perspective of the energy absorption. It has been shown that the roof panel by itself absorbs about 12% of the total vehicle roof structure energy, in case of rollover accident.

After having implemented the roof crush analysis with the sandwich structures panel, it was observed that although all sandwich solutions have absorbed less energy than the metallic roof solution and have slightly lower SWR, they give very large contribution to roof panel mass reduction from 70% to 77%. After the trade-off between the energy absorption, mass and feasibility of the design the sandwich solution type 6 was introduced as the optimum geometrical design. At the second step the foam core density of all sandwich solutions was increased from 45 Kg/m³ to 70 Kg/m³. The new results revealed that the increasing of the foam core density has direct relation with energy absorption capacity and SWR. Again although the solutions absorbed energy were less than the traditional design (except the full-foam sandwich panel solution), they gave a contribution of 73% to 75% to vehicle roof panel mass reduction, still there was considerable difference between the steel and sandwich solutions structural performance. At the final step, the face-sheets thickness was increased from 0.6 mm to 0.8 mm to evaluate the effect of the increasing the layer thickness. Results revealed that, the optimized sandwich solution type 6 with the face-sheets of 0.8 mm and foam core of 70 Kg/m³ density reduces the vehicle roof panel mass by 68% while it has almost the same structural performance with the steel solution.

Part of the work described in this chapter has been published in “Development of an innovative design of a composite-sandwich based vehicle roof structure, 2017 [58]”.

6.8 References

- [1] <http://www.iihs.org/iihs/topics/t/general-statistics/fatalityfacts/state-by-state-overview/2010> (Accessed at December 2016).

- [2] Federal Motor vehicle Safety Standard No. 216 - Roof Crush Resistance. CFR 49 571.216, October 1997.
- [3] SAE J996, "Inverted Vehicle Drop Test Procedure," August, 1967.
- [4] SAE J2114, "Dolly Rollover Recommended Test Procedure," February 2011.
- [5] Federal Motor vehicle Safety Standard No. 216 - Roof Crush Resistance. CFR 49 571 and 585, Docket No. NHTSA-2009-0093.
- [6] Gatilao, F., Roesser, G., & Reaume, B. (2010). An Overview of FMVSS 216a-Roof Crush Resistance Testing. SAE Paper No. 2010-01-1020.
- [7] Mamalis, A., Manolakos, D., Ioannidis, M., & Papapostolou, D. (2005). On the crushing response of composite sandwich panels subjected to edgewise compression: Experimental. *Composite Structures*, 71(2), pp. 246-257.
- [8] Harte, A., Fleck, N. A., & Ashby, M. F. (2000). Energy absorption of foam-filled circular tubes with braided composite walls. *European Journal of Mechanics-A/Solids*, 19(1), pp. 31-50.
- [9] Tuwair, H., Hopkins, M., Volz, J., ElGawady, M. A., Mohamed, M., Chandrashekhara, K., et al. (2015). Evaluation of sandwich panels with various polyurethane foam-cores and ribs. *Composites Part B: Engineering*, vol. 79, pp. 262-276.
- [10] Tarlochan, F., Hamouda, A., Mahdi, E., & Sahari, B. (2007). Composite sandwich structures for crashworthiness applications. *Proceedings of the Institution of Mechanical Engineers, Part L: Journal of Materials Design and Applications*, 221(2), pp. 121-130.
- [11] Zhang, Z., Liu, S., & Tang, Z. (2010). Crashworthiness investigation of kagome honeycomb sandwich cylindrical column under axial crushing loads. *Thin-Walled Structures*, 48(1), pp. 9-18.
- [12] Zangani, D., Robinson, M., & Gibson, A. (2007). Progressive failure of composite hollow sections with foam-filled corrugated sandwich walls. *Applied Composite Materials*, 14(5), pp. 325-342.

- [13] Shah, Q. H., & Topa, A. (2014). Modeling large deformation and failure of expanded polystyrene crushable foam using LS-DYNA. *Modelling and Simulation in Engineering*, vol. 1, pp. 1-7.
- [14] Li, Z., Zheng, Z., Yu, J., & Guo, L. (2013). Crashworthiness of foam-filled thin-walled circular tubes under dynamic bending. *Materials & Design*, vol. 52, pp. 1058-1064.
- [15] Steeves, C.A., & Fleck, N.A. (2004). Collapse mechanisms of sandwich beams with composite faces and a foam core, loaded in three-point bending. Part II: Experimental investigation and numerical modelling. *International Journal of Mechanical Sciences*, 46(4), pp. 585-608.
- [16] Rizov, V., Shipsha, A., & Zenkert, D. (2005). Indentation study of foam core sandwich composite panels. *Composite Structures*, 69(1), pp. 95-102.
- [17] Flores-Johnson, E., & Li, Q. (2011). Experimental study of the indentation of sandwich panels with carbon fiber-reinforced polymer face-sheets and polymeric foam core. *Composites Part B: Engineering*, 42(5), pp. 1212-1219.
- [18] Mao, M., Chirwa, E., & Chen, T. (2007). Reinforcement of vehicle roof structure system against rollover occupant injuries. *International Journal of Crashworthiness*, 12(1), pp. 41-55.
- [19] Pan, F., & Zhu, P. (2011). Design optimisation of vehicle roof structures: Benefits of using multiple surrogates. *International Journal of Crashworthiness*, 16(1), pp. 85-95.
- [20] Kulkarni, S.C., & Marks, M. (2011). Thermoplastic Roof Crush Countermeasure Design for Improved Roof Crush Resistant to Meet FMVSS-216. SAE Paper No. 2011-01-1119.
- [21] Pathare, R., & Mansour, M. (2009). Automotive Roof Crush, Structural Foam Enhancement Solution. SAE Paper No. 2009-01-0371.
- [22] Bambach, M. (2014). Fiber composite strengthening of thin steel passenger vehicle roof structures. *Thin-Walled Structures*, vol. 74, pp. 1-11.
- [23] D. Systèmes, Abaqus 6.12: Analysis user's manual, Providence, RI: Dassault Systèmes Simulia Corp.

- [24] Johnson, G.R., and Cook, W.H. (1985). Fracture Characteristics of Three Metals Subjected to Various Strains, Strain rates, Temperatures and Pressures. *Engineering Fracture Mechanics*, 21(1), pp. 31–48.
- [25] Hooputra, H., Gese, H., Dell, H., and Werner, H. (2004). A Comprehensive Failure Model for Crashworthiness Simulation of Aluminium Extrusions. *International Journal of Crashworthiness*, 9(5), pp. 449–464.
- [26] Johnson, G.R., and Cook, W.H. (1985). Fracture Characteristics of Three Metals Subjected to Various Strains, Strain rates, Temperatures and Pressures. *Engineering Fracture Mechanics*, 21(1), pp. 31–48.
- [27] Hillerborg, A., Modeer M., and Petersson, P.E. (1976). Analysis of Crack Formation and Crack Growth in Concrete by Means of Fracture Mechanics and Finite Elements. *Cement and Concrete Research*, vol. 6, pp. 773–782.
- [28] Camanho, P.P., and Davila C.G. (2002). Mixed-Mode Decohesion Finite Elements for the Simulation of Delamination in Composite Materials, NASA/TM-2002-211737, pp. 1–37.
- [29] Hashin, Z., and Rotem, A. (1973). A Fatigue Criterion for Fiber-Reinforced Materials. *Journal of Composite Materials*, vol. 7, pp. 448–464.
- [30] Hashin, Z. (1980). Failure Criteria for Unidirectional Fiber Composites. *Journal of Applied Mechanics*, vol. 47, pp. 329–334.
- [31] Deshpande, V.S., and Fleck, N.A. (2000). Isotropic Constitutive Model for Metallic Foams. *Journal of the Mechanics and Physics of Solids*, vol. 48, pp. 1253–1276.
- [32] Ghamarian, A., Zarei H.R., Abadi M.T. (2011). Experimental and numerical crashworthiness investigation of empty and foam-filled end-capped conical tubes. *Thin-Walled Structures*, 49(10), pp. 1312–1319.
- [33] Ozel, T., and Zeren, E. (2005). Finite Element Modeling of Stresses Induced by High Speed Machining with Round Edge cutting Tools, *International machining and Engineering Congress and Exposition*, Orlando, Florida, November 5-11.
- [34] Duan, C.Z., Dou, T., Cai, Y.J, and Li, Y.Y. (2009). Finite Element Simulation and Experiment of Chip Formation Process during High Speed

Machining of AISI 1045 Hardened Steel. *International Journal of Recent Trends in Engineering (IJRTE)*, 2(1), pp. 46-50.

[35] Mamalis, A.G., Manolakos, D.E., Ioannidis, M.K., & Kostazos, P.K. (2006). Bending of cylindrical steel tubes: numerical modelling. *International Journal of Crashworthiness*, 11(1), pp. 37-47.

[36] Standard test method for tensile properties of polymer matrix composite materials, ASTM D 3039/D 3039M-00. West Conshohocken (PA), USA: American Society for Testing and Materials (ASTM).

[37] Standard test method for in-plane shear response of polymer matrix composite materials by test of a $\pm 45^{\circ}$ laminate, ASTM D 3518/3518M-94. West Conshohocken (PA), USA: American Society for Testing and Materials (ASTM).

[38] Standard test method for compressive properties of unidirectional or cross-ply fiber-resin composites, ASTM D 3410-87. West Conshohocken (PA), USA: American Society for Testing and Materials (ASTM).

[39] Camanho, P.P., Maimí, P., Dávila, C.G. (2007). Prediction of size effects in notched laminates using continuum damage mechanics. *Composites Science and Technology*, 67(13), pp. 2715–2727.

[40] Belingardi, G., Duella, R., and Caminiti, A. (2002). Optimal choice of the foam design parameters in order to meet the HIC index limit of the FMVSS201 standard. *Proceedings of the 2002 IBEC Conference, Paris, France, Paper 2002-01-2095*.

[41] Croop, B., Lobo, H., & Data point Labs, N. (2009). Selecting material models for the simulation of foams in LS-DYNA. *Proceedings of the 7th European LS-DYNA Conference, Dynamore Gmbh, Salzburg, Germany*.

[42] Belingardi, G., Duella, R., & Caminiti, A. (2002). Optimal Choice of the Foam Design Parameters in Order to Meet the HIC Index Limit of the FMVSS201 Standard. *SAE Paper No. 2002-01-2095*.

[43] Ashby, M.F. (2006). The properties of foams and lattices. *Philosophical Transactions. Series A, Mathematical, Physical, and Engineering Sciences*, 364(1838), 15-30.

- [44] Avalle, M., Belingardi, G., & Ibba, A. (2007). Mechanical models of cellular solids: Parameters identification from experimental tests. *International Journal of Impact Engineering*, 34(1), pp. 3-27.
- [45] Gibson, L.J., Ashby, M.F. *Cellular solids. Structure and properties*. Cambridge: Cambridge University Press; 1997.
- [46] NCAC. Finite element model archive. National Crash Analysis Centre, George Washington University. <http://www.ncac.gwu.edu/vml/models.html> (Accessed May 2014).
- [47] Mao, M., Chirwa, E., Chen, T., & Latchford, J. (2004). Static and dynamic roof crush simulation using LS-DYNA3D. *International Journal of Crashworthiness*, 9(5), pp. 495-504.
- [48] Peng, Y., Yang, J., Deck, C., & Willinger, R. (2013). Finite element modeling of crash test behavior for windshield laminated glass. *International Journal of Impact Engineering*, vol. 57, pp. 27-35.
- [49] <http://www.dynasupport.com/howtos/element/hourglass> (Accessed July 2014).
- [50] Tomblin, J., Sherraden, J., Seneviratne, W., Raju, K.S. A-basis and B-basis Design Allowables for Epoxy-based prepreg Toray T700SC-12K-50C/#2510 Plain Weave Fabric. AGATE-WP3.3-033051-131; September 2002.
- [51] T700SC 12K/2510 Plain Weave Fabric. *Composite Materials Handbook (CMH- 17)*, vol. 2. Rev. G. [chapter 4.2.38].
- [52] LS-DYNA Keyword User's Manual - Volume II. Material Models. Version R7.0. Livermore Software Technology Corporation, February 2016.
- [53] Ls-dyna theory manual, Hallquist J. O. (Ed.), California: Livermore Software Technology Corporation, 2006.
- [54] M. S. Matthew Barsotti. (2010). Comparison of FEM and SPH for modeling a crushable foam aircraft arrestor bed, in *Proceedings of the 11th International LS-DYNA Users Conference*, vol. 16, pp. 37–54.
- [55] Weimar, K., and Day, J. "Negative volumes in brick elements," 2003, <http://www.dynasupport.com/howtos/element/negativvolumes- in-brick-elements>.

[56] S. Bala, "Best practices for modeling recoverable low density foams-by example," 2006, <http://blog2.d3view.com/bestpractices-for-modeling-recoverable-low-density-foams-by-example/>. (Accessed June 2015).

[57] NHTSA TestC0438. Toyota Yaris 4-door sedan with 5° pitch, 25° roll. National Highway Traffic Safety Administration (NHTSA), Vehicle Research and Test Center (VRTC), Ohio, USA; 2007.

[58] Borazjani, S., & Belingardi, G. (2017). Development of an innovative design of a composite-sandwich based vehicle roof structure. *Composite Structures*, vol. 168, pp. 522-534.

Chapter 7

Assembly challenges of vehicle composite roof panel

7.1 Challenging issues of composite car roof panel production

The most challenging issues of applying composite material in automotive industry that should be take into consideration are: production challenges, assembly challenges and cost of the material.

The production challenges of composite material are such as process cycle time and designing complex geometries with different aesthetic. Assembly challenges are including the difficulties of hybrid joining (Estimating the differential of thermal expansion differentiation between composite roof and the steel body shell to determine adhesive properties, elongation and thickness) methods and at last, cost of the composite parts production. The cost of producing composite parts are including the cost of raw material, cost of composite production line, cost of materials waste during the production and cost of applying automation in the production line [1].

7.2 Important notes on designing composite roof panel and attaching process to vehicle chassis

The perfect examples of using composite roof panel are in Alfa Giulia QV and BMW M3 [2, 3]. The roof is manufactured during the autoclave process which is 1.2 mm thick and reduces the roof panel mass by 60% in comparison with the steel solution. The composite lay-up orientation and number of plies depend on the desired performance with the minimum panel weight. As it shown in Figure 7.1, plies are positioned in the panel area with the high chance of bending and deformation which results in reducing the material waste, cost and weight of the roof structure. Applying carbon fiber with high Young's modulus satisfies the roof efficiency requirement along with the huge mass reduction. However, there should be always a trade-off between the type of fiber and the related costs [1].

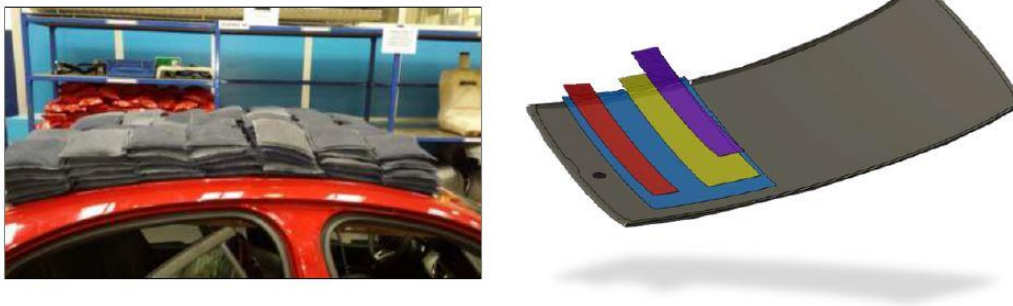


Figure 7.1: Roof fiber lay-up orientation [1]

Using adhesive materials as shown in Figure 7.2, the composite roof panel is attached through the automated process to the vehicle chassis.

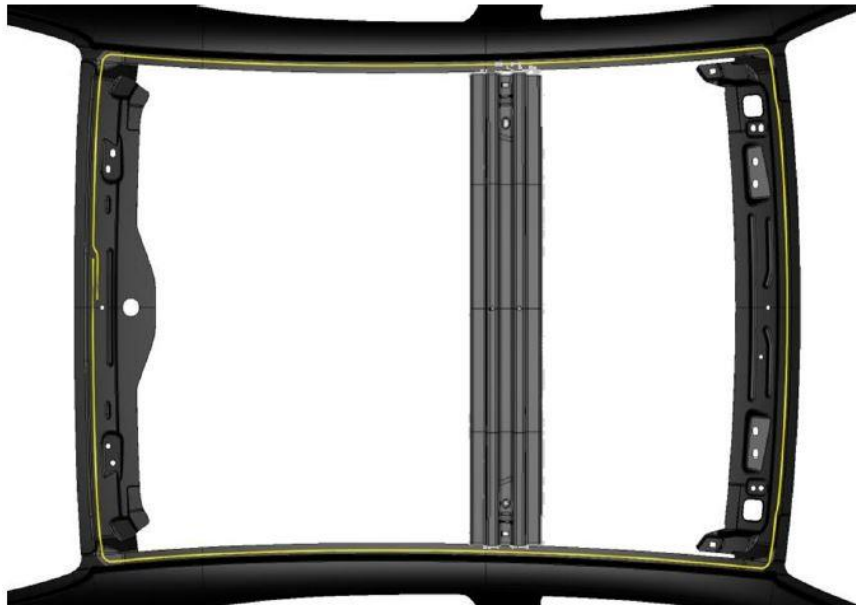


Figure 7.2. Adhesive path on the roof panel [1]

In order to have a successful bonding process, the roof is painted after the scuffing and cleaning process. Of one the most important strategy to guarantee the minimum thickness of adhesive material is using small feet present in the lower perimeter of the roof as shown in Figure 7.3 [1].

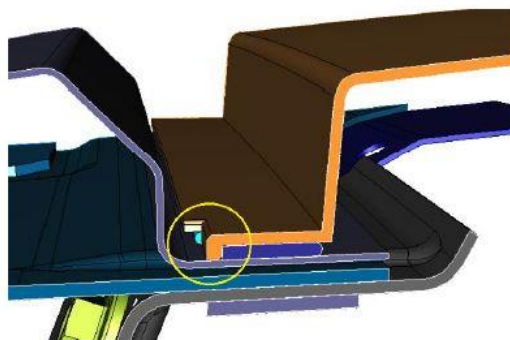


Figure 7.3. Roof feet [1]

7.3 Composite roof panel assembly process

As mentioned before, adhesive material should be inserted to the roof edge and the vehicle body before the body painting process to have a successful hybrid bonding as shown in Figure 7.4 [1].

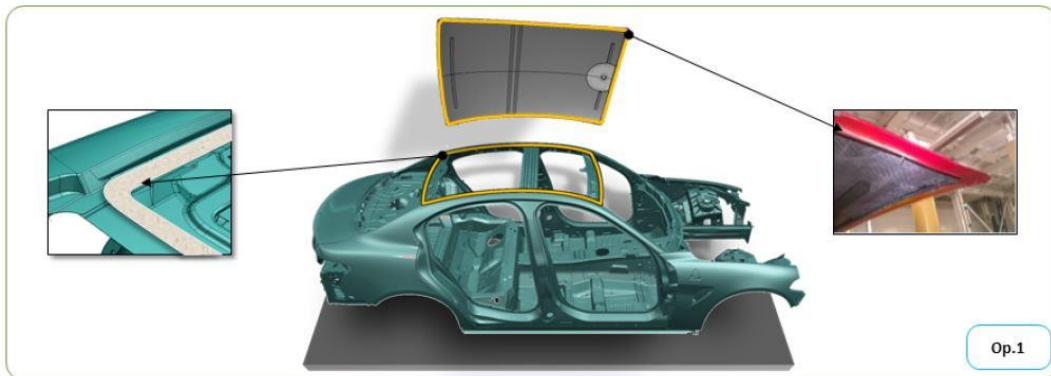


Figure 7.4. First step of pre-assembly of roof panel [1]

Although the painting line of the chassis and roof panel is the same, the oven cure temperature and time are different as shown in Figure 7.5. At the fourth stage the adhesive tape is removed and the roof is assigned to the chassis body as shown in Figure 7.5. At the fifth stage, return tools are used to avoid the direct contact of both surfaces as shown in Figure 7.5. At the sixth stage, the spacers which were placed at the previous stages is removed by an operator as shown in Figure 7.5.

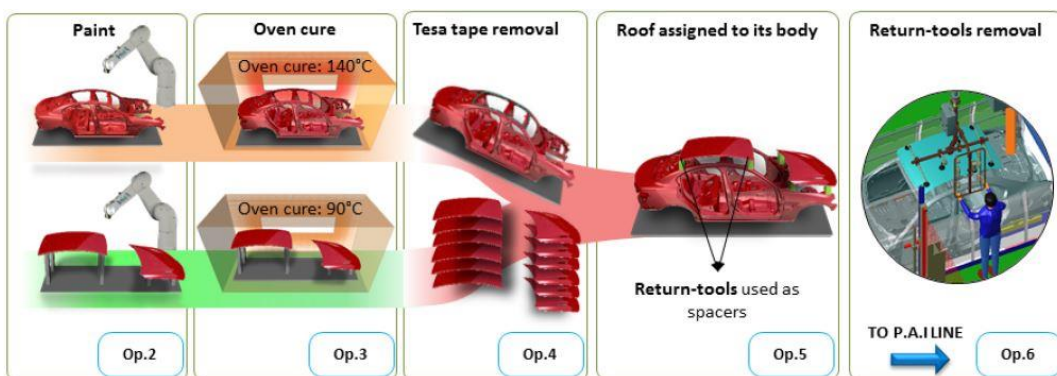


Figure 7.5. Pre-assembly process of roof panel [1]

From this stage the assembly process is automated; at stage 7 and 8 industrial robots are used to clean the vehicle chassis and roof respectively as shown in Figure 7.6. At stage 9 as shown in Figure 7.6, the adhesive material is distributed through the car body by the robot with another end effector.



Figure 7.6. Automated assembly first steps [1]

Using another robot with Infra-Red heaters griper as shown in Figure 7, accelerates the polymerization process of the adhesive material in stage 10. Accurate roof positioning on the chassis is implemented using robots with the laser sensors at stage 11 as shown in Figure 7. At the last stage heating process of the adhesive material is performed as shown in Figure 7 [1, 2].

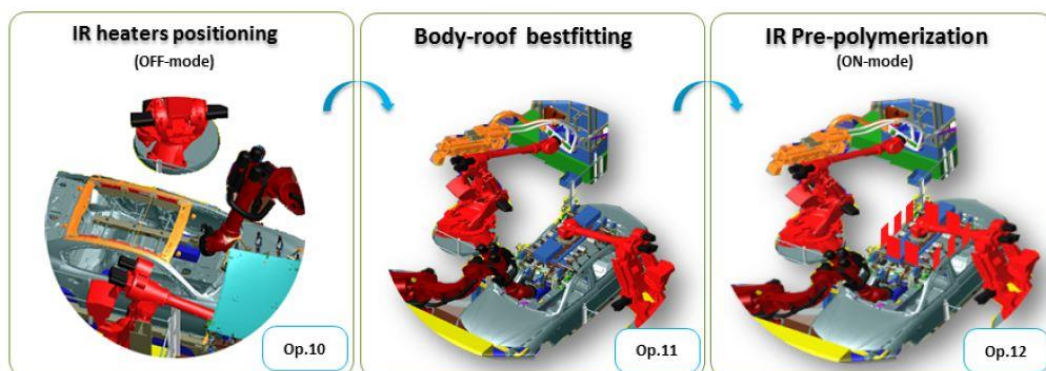


Figure 7.7 Automated assembly second steps [1]

7.4 Conclusion

In this chapter, the most challenging difficulties of the vehicle composite roof panel during the assembly process have been discussed shortly. Important key points regarding to composite lay-up orientation, bonding techniques and assembly process of composite panels have been described.

7.5 References

- [1] Chiapparo, S., CFRP (Carbon Fiber Reinforced Plastics) Best practices, applications and transformation processes assessment for automotive mass production, Master thesis, 2017.
- [2] Jacob, A. (2010). BMW counts on carbon fibre for its megacity vehicle. *Reinforced Plastics*, 54(5), pp. 38-41.
- [3] Lukaszewicz, D. (2013). Design drivers for enhanced crash performance of automotive CFRP structures. 23rd International Technical Conference on the Enhanced Safety of Vehicles (ESV), (13-0302).

Chapter 8

Conclusion

8.1 Overview of the thesis objectives

Based on high interest of vehicle manufacturers in producing light-weight cars, this research was dedicated to design the car body components reducing the vehicle weight while preserving the structural efficiency of the vehicle body structure. In order to achieve this goal, the vehicle roof structure (as the target vehicle body structure) was tested, redesigned and improved through various types of analyses. Different types of analyses have been performed using light-weight materials of aluminum, composite and sandwich to improve the efficiency of the vehicle roof structure. The performance of the designed roof structure was tested through the three main analyses of vehicle chassis stiffness, vehicle frontal crash and roof crush test numerically.

8.2 Findings

The first phase of the analysis is evaluating the stiffness of the vehicle chassis with respect to different material properties of the roof structure. Firstly, it has been tried to develop a benchmark with respect to the most important factors of designing automotive panels based on the primary and modified thicknesses of panels. At the second step, chassis load path analyses during the bending and torsion loadings have been implemented using SSSs method and finite element method. The vehicle chassis loading distribution has been determined and the dissipated forces values through the roof structure have been estimated and compared for the both methods. The results have shown big differences due to simplicity of SSSs method in comparison with the real model. At the third step,

stiffness analyses including modal analysis, as well as quasi-static bending and torsional analyses have been implemented on the chassis with the roof panel made of steel, aluminum and composite materials. Modal analysis results showed that there are not considerable differences between the chassis material solution in aspect of first bending and torsional frequencies. Static stiffness results proved that chassis bending stiffness values are pretty close for all the material solutions while there are considerable differences between the chassis torsional stiffness values. The chassis with the steel roof panel has the highest torsional stiffness value while the chassis with glass fiber/epoxy composite has the lowest value. In order to have a trade-off between the chassis mass and stiffness, light-weight index has been defined. The aluminum as well as the two carbon fiber composite solutions have lower light-weight indexes. It is important to mention that roof panels made of aluminum and carbon fibers reduced the panel mass by 32 % and 40% respectively with respect to the steel solution. At the third step, thicknesses of roof panels except for the steel solution, have been increased based on the cubic root of the rate of their Young modulus to the steel one and all the analyses have been performed again. Chassis torsional stiffness values increased by increasing roof thickness considerably, while light-weight index decreased by increasing roof thickness and roof panels' mass have been reduced by 25% and 38% for aluminum and composite solutions respectively.

At the second phase of the analysis, the behavior of vehicle roof structure during the frontal crash with the specific focus on the material solutions and roof shell thickness has been studied. At the first step, roofs with the same thickness and different material solutions have been examined. Results for two of the selected sections prove that, as it was expected, the traditional solutions of steel and aluminum absorb more energy than the composite ones during the crash. This is due to their ability of large plastic deformation. At the second step, the thickness of roof has been increased according to the equal bending stiffness criteria, i.e. proportionally to the ratio of material Young modulus. After repeating the crash analyses, energy-absorption capacity of roof system has been raised around 9% for the aluminum and 4% for the unidirectional carbon fiber solutions and the ability of roof panel for deformation has been improved. Based on the presented results for modified panel thickness, aluminum and unidirectional carbon fiber solutions it comes out that the composite solutions give comparable stiffness. Although with lower energy absorption capacity of the roof in comparison with the steel solutions but they have large contribution, up to 40%, to the weight reduction of vehicle roof panel along with the acceptable structural performance. Therefore composite material solution can be a valuable substitution for the steel roof panel.

At the third phase of the research, an innovative design solution for the vehicle roof structure has been developed and tested in rollover crash analysis. After determining the performance of tubes, made of steel, composite and composite foam-filled solutions, under the three points bending test and proving the efficiency of composite-foam design; the same idea is implemented on the vehicle roof panel during the roof quasi-static crush test. The new solution consists of a sandwich structure with unidirectional carbon/epoxy composite face-sheets and expanded polypropylene (EPP) foam core has been developed by means of numerical simulation. Speed dependency test has been performed on the steel roof structure at the first place and the appropriate test velocity for the rigid puncher has been selected. It has been pointed out that high test velocities added instabilities to the analysis. Then the effects of front, rear and side-screens on the total vehicle roof structure strength have been analyzed and it was shown that while front and rear windshields have high influence on the vehicle roof structure strength, side-screens have small effects on the total strength. The next step was aimed to determine the importance of roof panel among the vehicle roof structure in the perspective of the energy absorption. It has been shown that the roof panel by itself absorbs about 12% of the total vehicle structure energy, in case of rollover accident. After having implemented the roof crush analysis with the sandwich structures panel, it was observed that although all sandwich solutions have absorbed less energy than the steel roof solution and have slightly lower strength-to-weight ratio (SWR), they give very large contribution of 70% to 77% to roof panel mass reduction. After the tradeoff between the energy absorption, mass and feasibility of the design the sandwich solution the optimum geometrical design has been selected. The effects of increasing foam core density on the energy-absorption capacity of the sandwich solution was investigated by testing foam cores with different densities. The new results revealed that the increment of the foam core density has direct positive relation with energy absorption capacity and SWR. Again although the solution absorbed energy was less than the traditional design (except the full-foam sandwich panel solution), they gave a great contribution of 73% to 75% to vehicle roof panel mass reduction, still there was considerable difference between the steel and sandwich solutions structural performance. At the final step, the face-sheets thickness was increased from 0.6 mm to 0.8 mm to evaluate the effect of the increment of the layer thickness. Results revealed that, the optimized sandwich solution with the face-sheets of 0.8mm and foam core of 70 kg/m³ density reduces the vehicle roof panel weight by 68% while it has almost the same structural performance as the steel solution.

At the last phase of the research, challenges and difficulties of assembling of vehicle composite roof panel in the production have been pointed out and discussed.

Evaluating the behavior of the vehicle roof structure made of different solutions with various configurations under distinct analyses of stiffness and crashworthiness helps to improve the vehicle roof structure performance.